An investigation of the active galaxies M82 and NGC 5128

Neasa Foley

An Investigation of the Active Galaxies M82 and NGC 5128.

Neasa Foley

June 2, 1995

A thesis submitted to the University of Durham
for the degree of Doctor of Philosophy.

Abstract

In this thesis we present multi-waveband imaging polarimetry and spectropolarimetry of the starburst galaxy M82 and multi-waveband imaging polarimetry of the active galaxy NGC 5128. A review of previous studies of these galaxies is given. The imaging polarimetry of M82 in broadband filters reveals a polarization pattern that is due to scattering of light from the galactic disk and a nuclear starburst component. The Hα filter polarimetry shows a centrosymmetric pattern from the nuclear component only. The spectropolarimetry of the southern filaments of M82 shows evidence for a mixture of scattering and intrinsic emission from the walls of a superwind blown cavity. Only the Hα systemic component of M82 is seen in polarized intensity, the blueshifted component is due to intrinsic emission only. NGC 5128 displays a polarization pattern in its dust lane which is produced by extinction due to aligned non-spherical dust grains in a magnetic field. The wavelength dependence of the polarization in the dust lane is found to follow a Serkowski curve in the central regions.

Contents

List of Figures

List of Tables

Preface

The work carried out in this thesis is a report of three years of research carried out by the author while a member of the Polarimetry Group in the Department of Physics at the University of Durham. This included one year full-time study as a privately supported student and two years part-time study as a member of staff, employed as Experimental Officer on the Polarimetry SERC grant. The work is chiefly the authors original work with the exception of the Hα and continuum maps of M82 in Chapter 3, which were published by Dr. S. M. Scarrott, Dr. N. Eaton and Dr. D. J. Axon prior to my joining the group.

The NGC 5128 data were obtained at the SAAO 40″ by the author, Dr. T. M. Gledhill and Dr. R. D. Wolstencroft in 1992 and the M82 spectropolarimetry data were obtained at the WHT by the author, Dr. Axon and Mr. W. J. Henney in 1991. The M82 data was observed at the JKT in 1990 by Drs. Scarrott, Eaton and Axon, and I would like to thank those concerned for helping me to obtain the data.

The M82 observations were made on an observing run awarded to Dr. D. J. Axon, Prof. J. Hough, Dr. S. M. Scarrott and Dr. M. E. Bailey. The NGC 5128 observations were made on an observing run awarded to Dr. S. M. Scarrott and Dr. R. D. Wolstencroft. Their permission has been obtained to publish the results in this thesis or the data taken during these observing runs.

Chapter 1

Introduction to Polarimetry

1.1 The Polarization of Light

Light is a transverse electromagnetic wave. This means it has certain properties: an electric vector and a magnetic vector both mutually perpendicular to each other and to the direction of propagation. An ordinary light source consists of a large number of randomly oriented atomic emitters, each radiating a very short polarized wavetrain. Measured light consists of a summation of millions of these wavetrains so the overall polarization state changes in a completely unpredictable fashion and at so rapid a rate as to make the measurement of any single resultant polarization state impossible. This is known as *natural* light or *unpolarized* light, which is a misnomer since the light is actually composed of a rapidly varying succession of different polarization states. It is conventional to use the electric or $\underline{\mathbf{E}}$ vector to refer to the direction of the polarization.

One can mathematically represent natural light in terms of two arbitrary, incoherent, orthogonal, linearly polarized waves of equal amplitude (i.e. waves for which the relative phase difference varies rapidly and randomly). Figure 1.1a shows a representation of a light wave. Natural light consists of an infinite number of these light waves and the polarization state can be represented as in Fig. 1.1b. Known as a sectional pattern, it is the path one would see traced out by the $\underline{\mathbf{E}}$ vector, if one looked along the propagation direction, i.e. the z-axis, and for natural light we see an infinite number of paths with no fixed pattern, or a random distribution of paths with no fixed directional preference.

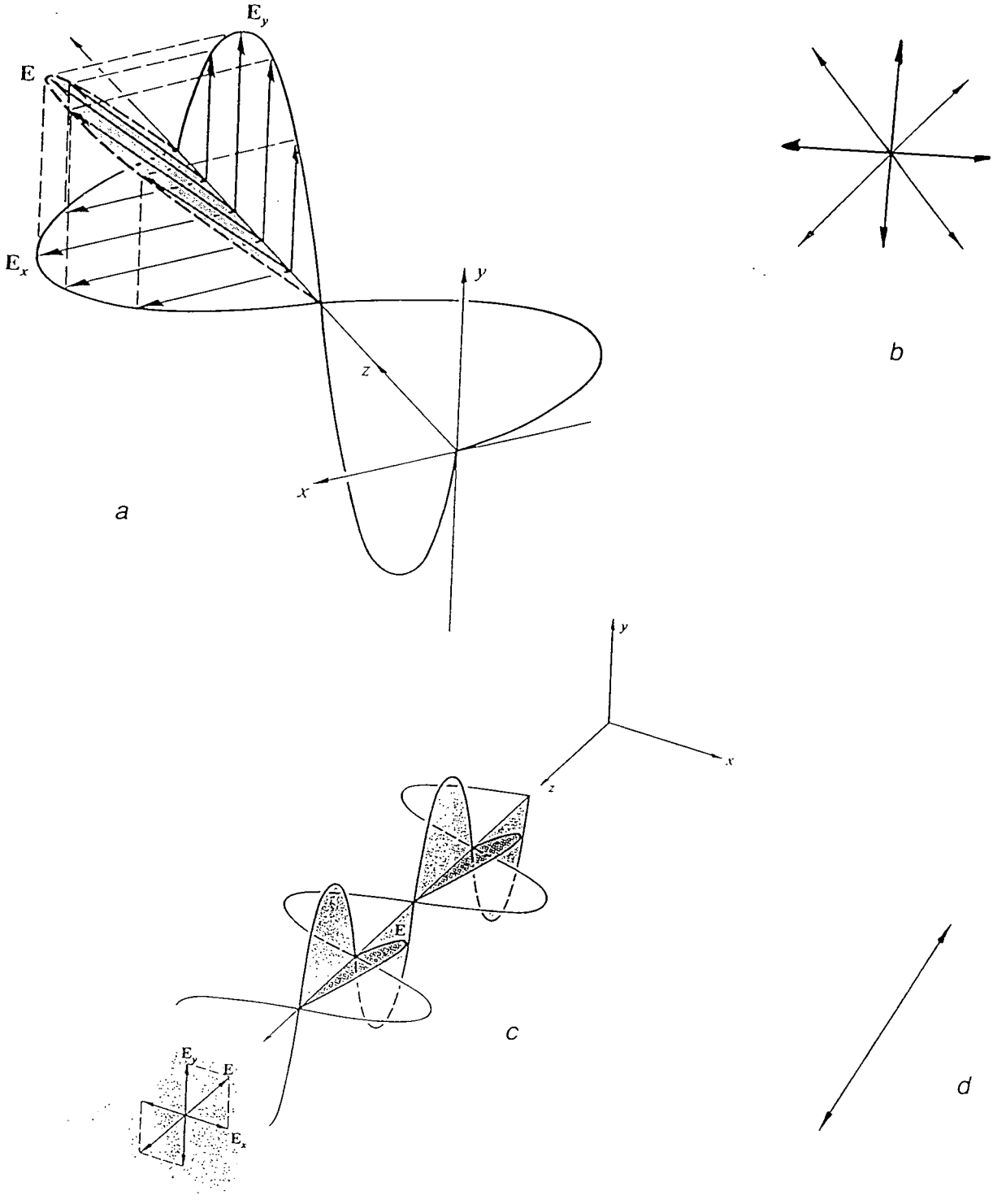

Figure 1.1: (a) Representation of light as two orthogonal waves E_x and E_y. (b) Sectional diagram of an unpolarized light wave.(c) Representation of linear polarized light as two orthogonal waves (d) Sectional diagram of a linear (plane) polarized light wave. (Figures taken from Hecht & Zajac (1974)).

1.1.1 Linear, circular and elliptical polarization

For a plane monochromatic wave with angular frequency ω and wave number k which is propagating in the z direction in a non-absorbing medium, the electric field is given by

$$E = E_x \cos(kz - \omega t) + E_y \sin(kz - \omega t).$$

The real vectors E_x and E_y are independent of position. The electric field vector at any point lies in a plane, the normal to which is parallel to the direction of propagation. In a particular plane (i.e. z = 0), the tip of the electric vector traces out a curve:

$$E(z = 0) = E_x \cos \omega t + E_y \sin \omega t.$$

This is an ellipse known as the vibration ellipse. If $E_x = 0$ (or $E_y = 0$), the vibration ellipse is just a straight line and the wave is linearly polarized. The vector E_y then specifies the direction of vibration. If $|E_x| = |E_y|$ and $E_x.E_y = 0$, the vibration ellipse is a circle, this is known as circularly polarized light. In general $|E_x| \neq |E_y| \neq 0$ and the light is elliptically polarized. If the phase difference between the two components, known as γ, is $+90°$ then one has right-handed circularly polarized light. If γ is $-90°$ one has left-handed circular polarization. If γ is $0°$ or $\pm 180°$ one has linear polarization. Usually $E_x \neq E_y$ and γ has any value between 180° and –180°, and one gets elliptical polarization.

Figure 1.1c shows the pattern of the electric vectors for linearly polarized light and Fig. 1.1d shows the sectional diagram. Circular polarization is a specific case where the amplitudes of the orthogonal waves are equal and the phase difference difference between the two states is constant and equal to $\pi/2$. This results in the $\underline{\mathbf{E}}$ vector describing a circle within the x-y plane as the wave propagates. Most light is elliptically polarized, with the orthogonal waves being of unequal amplitudes and the phase difference varying from 0 to π. The electric vectors and sectional diagram for circular polarization are shown in Fig. 1.2a and b.

1.2 Stokes Parameters

The polarization state of a light wave can be completely described using four parameters known as Stokes parameters. They are mentioned only briefly here but a full treatment

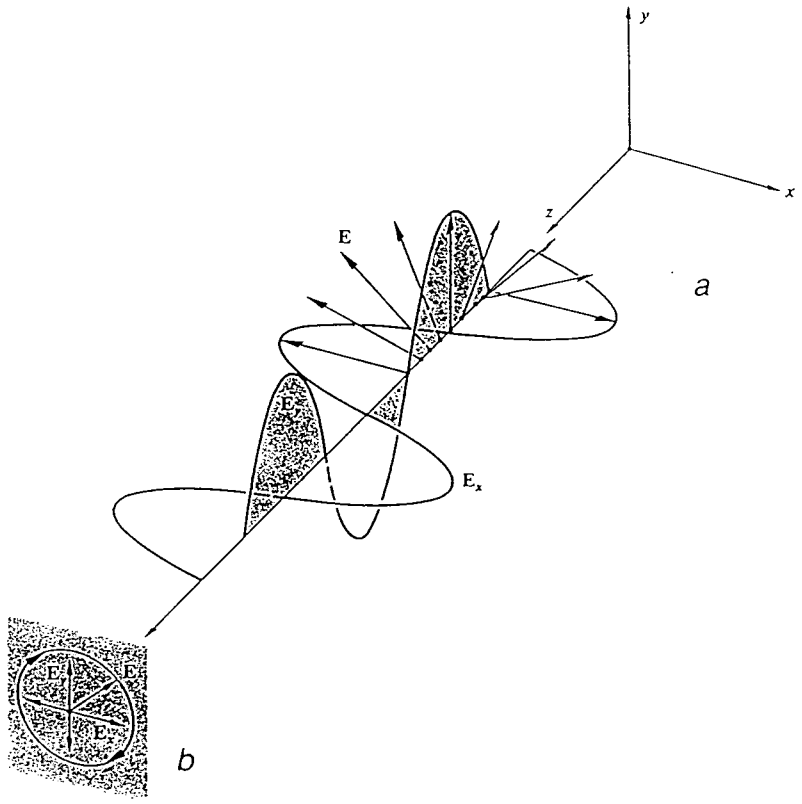

Figure 1.2: (a) Representation of circular polarized light as two orthogonal waves (b) Sectional diagram of a circular light wave. (Figures taken from Hecht & Zajac (1974)).

of Stokes parameters can be found in any optics book e.g. Hecht & Zajac (1974). The four Stokes parameters are known as I, Q, U and V, and correspond to four time-averaged intensities, the average being taken over a time period long enough to permit practical measurement. I corresponds to the intensity of the light beam, Q to the horizontal preference of the $\underline{\mathbf{E}}$ vector, U to the +45° preference and V to the circular polarization right handedness preference, relative to some Cartesian coordinate system. Thus for a negative Q value, the $\underline{\mathbf{E}}$ vector is preferentially vertical, for a negative U value it is preferentially at -45° and for a negative V value it has preferentially left handed circular polarization.

They are equivalent to the following expressions,

$$I = E_x E_x^* + E_y E_y^*,$$

$$Q = E_x E_x^* - E_y E_y^*,$$

$$U = E_x E_y^* + E_y E_x^*,$$

$$V = i(E_x E_y^* - E_y E_x^*),$$

where * means the complex conjugate.

The Stokes parameters can be described by a Stokes vector, $\underline{\mathbf{S}}$ = (I, Q, U, V). For unpolarized light the Stokes vector would be $\underline{\mathbf{S}}$ = (1, 0, 0, 0). For monochromatic light the Stokes parameters are related to each other by the equations

$$(Polarized\ Intensity)^2 = Q^2 + U^2 + V^2$$

$$I^2 \geq Q^2 + U^2 + V^2.$$

For linearly polarized light, $V = 0$, i.e. there is no element of circular polarization and thus

$$PI = \sqrt{Q^2 + U^2},$$

$$P(\%) = \frac{Polarized\ Intensity}{Total\ Intensity} \times 100,$$

and

$$\theta = \tan^{-1} \frac{U}{Q},$$

where θ is the polarization angle, i.e. the orientation of the $\underline{\mathbf{E}}$ vector to a chosen frame of reference. In astronomy, this reference frame is usually North. Stokes vectors are a useful tool since for independent light beams they are additive.

1.3 The Durham Imaging Polarimeter

The Durham Imaging Polarimeter consists of an optical imaging polarimeter with a GEC CCD camera and a number of controlling computers, which travels to observatories around the world and is used to measure the linear polarization of astronomical objects, ranging from comets to quasars. The polarimeters internal optical components include a Wollaston prism, a super-achromatic half-wave plate and focusing optics, controlled by a PC running under the Unix operating system. The CCD camera has a blue-sensitive coating and is read using the IMAGER program of Dr. C. MacKay (Wright & MacKay 1981). The polarimeter itself uses a revised version of control programs written by Mr. D. Stockdale. The data can be stored on disk or exabyte. A customised software package (DIPS) is used to reduce the data on its return to Durham. The original algorithms were devised by Dr. R. Warren-Smith, further additions were made by Dr. P. Draper and Dr. C. Rolph and the entire suite of programs were re-written by Dr. T. Gledhill to run in the Starlink ADAM environment. The polarimeter, its principles and operations are described in detail in Warren-Smith (1978), Scarrott *et al.* (1983), Draper (1988) and Scarrott (1991).

1.4 Astronomical Causes of Polarization

We are interested in the occurrences of polarized light in an astronomical context. There are a number of causes including synchrotron radiation, scattering of light from small particles and extinction by aligned dust grains. These are described below, as are the ways of differentiating between them. Synchrotron polarization is not of direct relevance to the work in this thesis and will therefore be described only briefly.

1.4.1 Synchrotron

In the case of synchrotron radiation, relativistic charged particles (electrons) in a magnetic field move around the field line in a spiral fashion and emit radiation within a cone. Because the electrons are constrained to move around the field line, we see the radiation they emit as polarized. Synchrotron radiation is mostly seen at radio wavebands, but has been observed at optical wavelengths, notably in the Crab Nebula and the jets of M87 and 3C273. The electric vector of the polarized emission lies perpendicular to the direction of the magnetic field projected onto the plane of the sky. High values between 50 and 100%

are often obtained which depend on the spectral index of the radiation. A mathematical treatment of the polarization of synchrotron radiation can be found in Longair (1981).

1.4.2 Scattering

The removal of energy from an incident light wave and the subsequent re-emission of that energy is known as scattering. The photon interacts with the bound electron cloud of an atom or molecule, imparting energy to the atom. This energy is subsequently dissipated as photon emission.[1] At frequencies above or below resonance the electrons vibrating with respect to the nucleus may be regarded as oscillating electric dipoles and as such they re-radiate electromagnetic energy at a frequency which coincides with that of the incident light.

In astrophysical contexts, scattering occurs mostly from atomic particles (electrons) or dust grains. Polarization caused by scattering has been found in many astronomical objects such as reflection, bipolar and cometary nebulae (NGC 2261 – Scarrott, Draper & Wolstencroft 1989, Pars22 – Scarrott, Draper & Tadhunter 1993, GGD30 – Foley *et al.* 1993), comets (Austin – Eaton, Scarrott & Gledhill 1992, Okasaki-Levy-Rudenko – Eaton, Scarrott & Wolstencroft 1991) and galaxies (M82 – Scarrott, Eaton & Axon, 1991, NGC 1808 – Scarrott *et al.* 1993).

Scattering is usually divided in two different types, Rayleigh scattering and Mie scattering, although Rayleigh scattering is merely a specific case of Mie scattering where the scattering particle size is much much less than that of the wavelength of the incident light. Mie scattering is scattering where the particle size is approximately equal to the wavelength of the incident light.

Rayleigh Scattering

For Rayleigh scattering, the percentage polarization can be expressed as

$$P(\%) = \frac{1 - \cos^2\theta}{1 + \cos^2\theta},$$

where θ is the scattering angle i.e. the angle through which the incident light is deflected. If light is scattered by a small angle it is said to be forward scattered and

[1]Note that we are at all times talking about elastic or coherent scattering i.e. the frequency of the scattered light is the same as that of the incident light.

scattered by a large angle (greater than 90°) it is said to be backscattered. If a sufficiently small sphere is illuminated by unpolarized light, the scattered light is 100% polarized at a scattering angle of 90°. This is analogous to complete polarization upon reflection of unpolarized light on a plane interface at the Brewster angle. The scattered light is usually polarized perpendicular to the scattering plane therefore P is almost always positive. One can refer to polarization as negative in certain situations where the scattering angle becomes parallel to the scattering plane. The degree of polarization is a function of the scattering angle of the light, and maximum values of polarization are achieved at angles close to 90°.

Mie Scattering

Mie scattering theory permits a more realistic treatment of scattering where the particle size is approximately equal to the wavelength of the incident light. In 1908, Mie solved Maxwells equations for electromagnetic wave propagation from particles of arbitrary size in the case of smooth homogeneous spheres. One defines the scattering functions of spheres in terms of a dimensionless parameter x where

$$x = \frac{2\pi a}{\lambda},$$

and a complex refractive index m where

$$m = \sqrt{k - \frac{2i\sigma\lambda}{c}},$$

where a is the diameter of the particles, λ is the wavelength of the light, k is the dielectric constant of the sphere material and σ the conductivity of the sphere material. Detailed treatment of Mie scattering theory can be found in Van der Hulst (1957), with further details in Chandrasekhar (1960), Warren-Smith (1978) and Bohren & Huffman (1983).

Figure 1.3a shows the polarizations expected for all scattering angles for Rayleigh scattering and for Mie scattering, with different distributions of grain sizes. For Rayleigh scattering, polarization is symmetric around at scattering angle of 90° but for Mie scattering, the polarization becomes stronger at back scattering angles, with increasing particle size distribution. Figure 1.3b shows the variations of intensity for scattering light with increasing scattering angle for Mie scattering and Fig. 1.3b shows the variations of intensity for Rayleigh scattering.

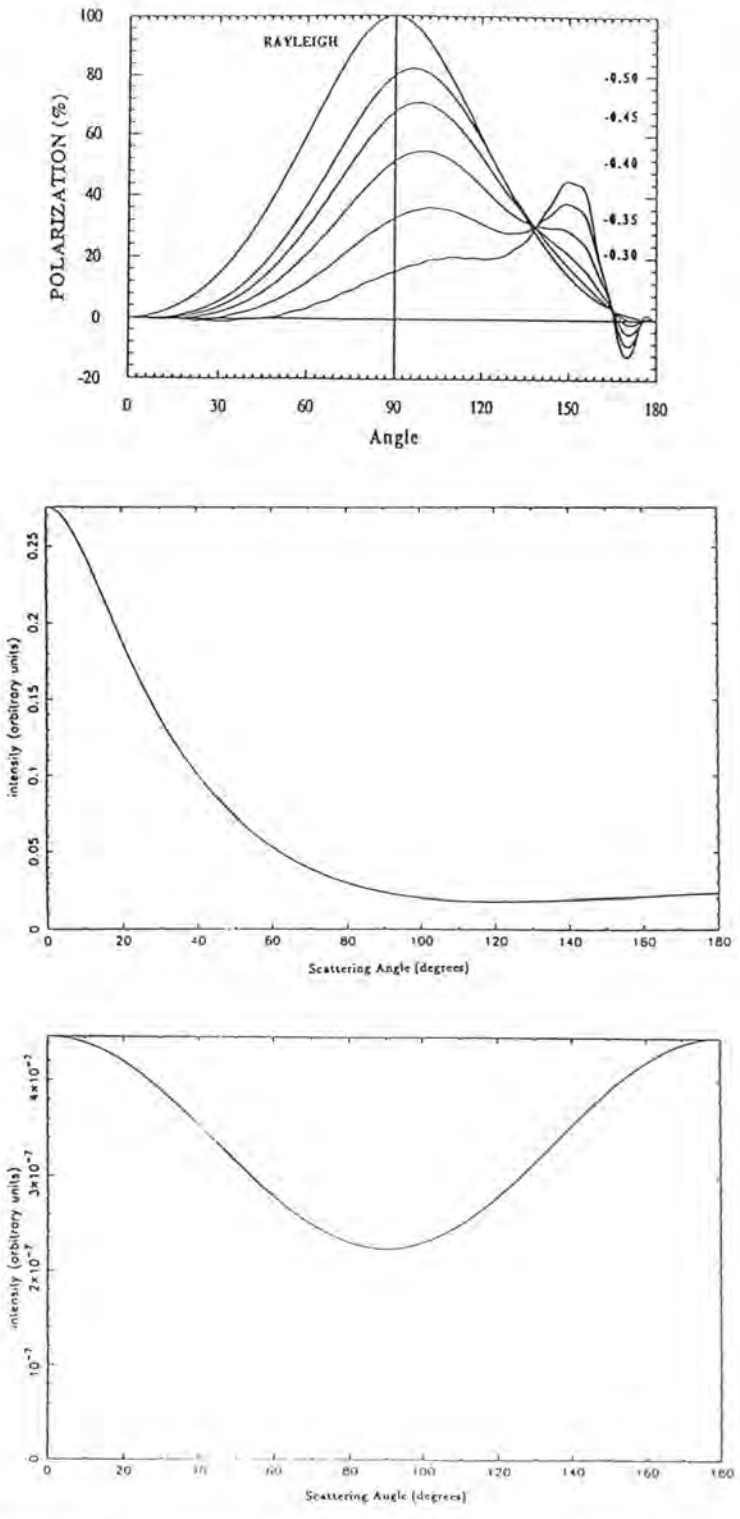

Figure 1.3: (a) Percentage polarization versus scattering angle expected for Rayleigh scattering and Mie scattering with different grain size distributions, (b) Intensity versus scattering angle for Mie scattering for a particular grain size distribution, (c) Intensity versus scattering angle for Rayleigh scattering.

1.4.3 Extinction by Aligned Grains

In reality, few grains are perfect spheres. The interstellar medium is filled with non-spherical dust grains and light which scatters off such a grain will have one polarization state enhanced over the other due to selective extinction. However, if the dust grains are aligned randomly the polarization states will also occur randomly and no net polarization will be observed.

A process known as the Davis-Greenstein effect can cause spinning, non-spherical grains in a magnetic field to align their axis of rotation with the magnetic field lines. The alignment of the dust grains allows a cumulative effect to occur where the selective extinction of many aligned dust grains are summed, so that the emerging light is polarized parallel to the magnetic field. The wavelength dependence of polarization caused by extinction by aligned grains follows a distinctive curve known as the Serkowski curve. This effect will be discussed in greater detail in Chapter 4. Objects which display polarization patterns symptomatic of extinction by aligned dust grains include M51 (Scarrott, Ward-Thompson & Warren-Smith, 1987) and M104 (Scarrott, Rolph & Semple, 1991).

1.5 M82 and NGC 5128

The astronomical objects discussed in this thesis are both unusual, active galaxies. Messier 82 is a starburst galaxy which has a highly active central region. Long filaments are visible in the light of Hα along its minor axis and may be the result of a giant explosion in its centre. It is an extremely dusty galaxy, and any internal optical structure is masked by this dust. Previous studies have found it have high polarization and it is an ideal candidate for the study of polarization caused by scattering from dust.

NGC 5128 (Centaurus A) is a large elliptical galaxy bisected by a broad dust lane. It is well-studied at most wavelengths and has been found to have an unusual polarization pattern indicative of extinction by aligned grains.

In Chapter 2 we will discuss previous studies of M82 and their results and in Chapter 3 we will present results from multi-waveband imaging polarimetry studies of this galaxy, and a spectropolarimetric study of the southern minor axis as well as a scattering model of M82. In Chapter 4 we will discuss previous studies of NGC 5128 and possible grain alignment mechanisms in the dust lane. In Chapter 5 we will present results of a multi-

waveband study of NGC 5128. In Chapter 6 we will summarize the conclusions reached in this thesis.

Chapter 2

Previous Studies of M82

2.1 Introduction

M82 has been described as the prototype starburst galaxy. Classed as Irregular Type 2 (Sandage, 1961), it presents an edge-on appearance and is shrouded in dust. Although it is only 3.3 Mpc distant (Freedman and Madore, 1988) no visual features such as stars are resolvable, unlike its larger nearby companion M81, a spiral galaxy with distinct and well-resolved stars which is only 65kpc away from M82[1]. It possesses unusual Hα filaments which protrude from the galaxy along its minor axis. Initial theories suggested the filaments were the result of a massive explosion in the nuclear region but the vast number of studies of M82, over 200 papers in the last 25 years, have drawn a picture of a highly disturbed galaxy with a very high rate of supernova (SN) explosions occurring in its central regions. In this chapter we will review starburst galaxies, some of the M82 studies and the conclusions which have been drawn from them.

Starburst galaxies have certain properties which include high IR luminosity, intense localized star formation and outflow from the starforming region (a galactic superwind). A number of galaxies have been found that fulfill these requirements (Heckman, Armus and Miley (1990), Terlevich *et al.* (1992), Forbes *et al.* (1992), Van der Werf *et al.* (1993)). These galaxies include M82, NGC 253, NGC 3079, NGC 4945, NGC 6240 and Arp 220.

A large percentage ($> 70\%$) of all luminous IR galaxies are interacting or merging. Starburst models for luminous IR galaxies interpret the starburst as a direct result of the

[1] centre to centre in projection

interaction. In order to produce the luminosity of FIRGs, star formation rates would have to be so high as to exhaust the gas in less than a Hubble time which implies relatively short bursts of star formation are required, hence the starbursts.

A superwind results when the kinetic energy in the ejecta supplied by SNe and the winds from massive stars in a nuclear starburst is efficiently thermalized. This means that the collisions of intersecting supernova remnants (SNRs)/winds convert the kinetic energy of ejecta into thermal energy via shocks, with little energy lost to radiation because of the very high post-shock temperatures and low densities. The collective effect of the SN and stellar winds then creates a bubble of very hot gas with a pressure that is much larger than its surroundings. As the bubble expands and sweeps up ambient gas it rapidly enters the radiative phase which occurs when the radiative cooling time of the ambient material, that is its shockheating, becomes shorter than the winds expansion time scale.

Superwinds create extensive shocks in the halo which is seen as a diffuse emission region and also in the formation of an intricate network of tenuous emission line (especially in Hα) filaments extending many kpc from the centrally located starburst. Evolutionary models of starburst nuclei predict the formation of a thin dense shock-ionized shell surrounding a hot cavity. The shell gradually expands perpendicular to the galactic plane, until it finally breaks open at the top. The shell evolution is determined by the SN rate and the time scale. If the SN rate is high the shell will expand quickly, elongate and break open at the top. If the SN rate is low, the expansion will be slow and the shell will remain smaller and nearly spherical. A recent paper by Heckman, Lehnert and Armus (1994) deals with the basic physics and astrophysics of superwinds including momentum and energy input in starbursts. They include simple models of hydrodynamics and radiation, conditions for driving superwinds and the effect of clouds.

Optical spectra of far-IR galaxies support the superwind model in which the kinetic energy provided by the SN and winds from massive stars in a central starburst drive a largescale outflow that can shockheat and accelerate ambient interstellar or circumgalactic gas.

Superwinds are energetically adequate to power both the observed optical and X-ray nebulae, and the relative emission line intensities and their radial variations are consistent with ionization by wind-driven shocks but not photoionization by O stars or an active galactic nucleus (AGN).

2.2 Polarization studies

Since we will be examining M82 in polarized light in Chapter 3, we will begin by looking at previous polarization studies. Initial polarization measurements were made by Elvius (1962, 1967, 1969) as part of her program of polarization studies of extragalactic objects, and she found that the outer parts of the galaxy showed linear polarization. She suggested that the filaments were illuminated by the scattering of light by dust in the filaments.

M82 was then mapped by Lynds and Sandage (1963) who noticed that the filaments were most luminous in Hα light. They suggested that M82 was the site of a giant explosion with matter being blown out along the minor axis. Synchrotron emission similar to that causing polarization in the filaments of the Crab Nebula was proposed as the polarization mechanism. Solinger (1969) proposed that the centrosymmetric pattern of the polarization vectors was due scattering of light from a Seyfert-like nucleus at the centre of the explosion by free electrons behind the shock front. Visvanathan and Sandage (1972) examined the polarization angles in patches of the filaments and concluded that synchrotron was not responsible for the polarization since the polarization angles were at right angles in the centre of the galaxy and not perpendicular to the filaments. They measured the wavelength dependence of polarization in patches of the filaments and concluded that the polarization was independent of wavelength, leading them to believe that it was the result of free electron scattering.

The optical (Hα, NII and SII) velocity profiles of M82 (Heckathorn 1972) showed that gas was infalling on one side of the galaxy and outflowing on the other. This meant that the filaments could not be due to a simple explosion in the centre of the galaxy where scattered light would be redshifted on both sides, nor could they be due to an implosion or infalling gas on both sides since scattered light would be blueshifted on both sides. Elvius (1972) suggested a model whereby M82 is moving as a whole through a surrounding medium containing some kind of particles which scatter the light from the bright nucleus assumed to exist in the centre of M82. The blueshift is caused by a velocity gradient arising from interaction between the gas and the galaxy. Mathis (1973) modelled scattering by dust in the filaments and tried to mimic the Visvanathan and Sandage (1972) wavelength independence by using Oort–van der Hulst dust grain mixtures. A composite of 2 or 3 distributions with many more small (approximately Rayleigh limit) grains than large particles appeared to be the best such model.

Solinger and Markert (1975) modelled the polarization pattern expected from Rayleigh

scattering of light from a point source embedded in a circular disk and calculated that most of the scattered continuum light comes from the galactic disk and not the nucleus. Schmidt, Angel and Cromwell (1975) made the first photographic polarimetric map of M82 and this showed that the scattered continuum in the halo does indeed originate in the galactic disk and is not from a bright nucleus. They realised that the filaments might be quite strongly polarized themselves after the subtraction of the smooth halo polarization.

A polarization map in the B waveband was presented by Bingham *et al.* (1976), based on the results of Pallister (1976), made with an electronographic camera. This again showed the smooth scattering pattern over the galactic halo. They pointed out that central features at other wavelengths (e.g. radio, infrared etc.) were not coincident on one 'special' position.

Solinger, Morrison and Markert (1977) proposed that there was no concrete evidence for an explosion in M82 and that the galaxy is in fact immersed in and drifting through an immense thin intergalactic dust cloud associated with the M81 group (see Section 2.3.) They compared the core of M82 at radio, IR and optical wavelengths with similar data for our Galaxy and concluded that the central luminosity can be explained by copious star formation, stellar emission, SN and stellar wind interactions and that there is no need for a massive explosion.

Instead of a set of concentrated, rapidly moving filaments, they suggested a near-uniform volume through which the galaxy drifts slowly. They also introduced the notion of "star-spiders[2]" as an illumination method for the filaments. The dust particles act as "co-moving mirrors" thus explaining the blue and redshifted light. The velocities seen in the filaments are only Doppler shifted reflections of disk emission which arise from the combination of normal rotation and steady drift through the cloud. They calculate that a relative cloud/disk velocity of 100 – 200km/sec is needed.

M82s surface brightness, disk luminosity distribution and central core luminosity are similar to those of a small spiral but the internal dust pattern within its disk has no visible trace of a spiral pattern. The disk edges seem to have no supergiants, which can be individually resolved in M81. The internal dust is so mottled that it cannot hide all such stars if they were present. They conclude that M82 is an interloper in the M81 group

[2]A temporary gap in the dust/gas cloud surrounding the bright nucleus allows a beam of light to be emitted, and this light travels out, illuminating a portion of the dust in its path. It is similar to the Jacobs Ladder effect seen when the sun is hidden by patchy cloud.

and point to the presence of NGC 3077, another visually disturbed and dusty galaxy as evidence that some kind of interaction has taken place. Perkins (1978) calculated the polarization values based on the model of Solinger, Morrison and Markert (1977).

Chesterman and Pallister (1980) presented a linear polarization map of M82 in the R waveband. The orientation of the vectors did not differ significantly from those of the B map of Bingham *et al.* (1976) but the percentage polarization, P(%), is smaller in R than in B. They compared P(%) measured along the minor axis and found that the SE side of the galaxy is more highly polarized than the NW side in both colours, this was more noticeable in B. The SE side displayed a wavelength dependence, with B polarizations up to twice that of the R polarizations. This disagreed with the Visvanathan and Sandage (1972) theory of electron scattering. Wavelength dependence could not be measured on the NW side because of high noise levels. They modelled M82 as a tilted system with the NW side inclined towards us by 8 – 10°. Dust is distributed symmetrically with respect to the plane of the galactic disk. Light from the bright central regions of the galaxy scattered by dust particles to the SE of the galaxy may reach the observer directly but light scattered by dust particles to the NW must pass through the galactic disk where it will be attenuated before reaching the observer. It becomes mixed with unscattered light and the polarization is diluted. The results of their model give values for the polarization values which were similar to those observed, and to those expected from a point source in an infinite cloud with a constant density of Rayleigh scatterers.

Recently, Scarrott, Eaton and Axon (1991) presented a linear polarization map of M82 in Hα. They found a centrosymmetric pattern with polarization levels of up to 30% in the filaments and concluded that in Hα, M82 is a giant bipolar reflection nebula. A map of M82 in Hα light is shown in Fig. 2.1 and is overlaid with a map of the Hα polarization vectors. The centre of their polarization pattern appears to be a point source at R.A.(1950) = $9^h\ 51^m\ 42^s.1 \pm 0^s.4$, Dec.(1950) = $69°\ 55'\ 1'' \pm 2''$ and is not coincident with features at other wavelengths which will be discussed later on in this chapter. They see part of the filaments in polarized light which implies that at least part of the filamentary structure is due to scattered light.

2.3 Interaction between M82, M81 and NGC 3077

Cottrell (1977, 1978) suggested that Irregular Type 2 galaxies are the result of binary collisions between normal galaxies. These collisions have induced tidal interactions be-

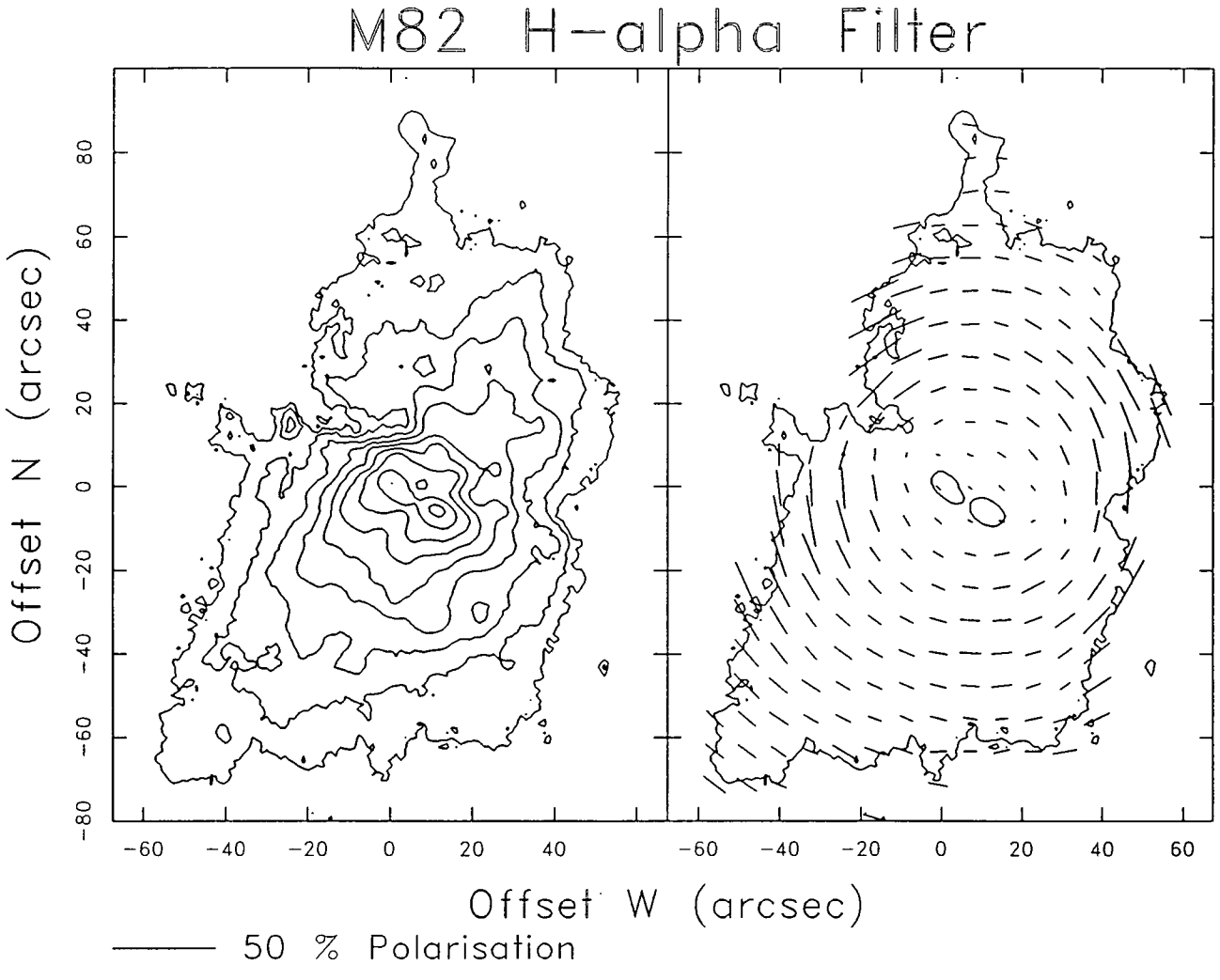

Figure 2.1: A Hα contour map of M82 overlaid with a map of the polarization vectors (Scarrott, Eaton and Axon (1991)).

tween the galaxies causing an influx of dust and gas into the nuclear regions leading to star formation. The tidal interactions take the form of either mass transfer or removal of angular momentum from gaseous components so that they can fall into the central regions of the galaxy.

Bridges of emission connecting M81 with M82, NGC 3077 and NGC 2976 have been found in HI (Gottesman and Weliachew 1977), as has a common envelope of neutral hydrogen and HI (Van der Hulst 1978, 1979, Crutcher *et al.* 1978, Appleton *et al.* 1981)

Getov and Georgiev (1989) found an extended low brightness structure enveloping the bright galaxies. It coincided with the radio structure in that region and they found evidence for optical bridges connecting M81 with NGC 3077 and NGC 2976. They also found a bridge of bright spots connecting the SE region of M82 and the north part of M81. They theorised that this was star formation brightness in clumps of gas connecting the two galaxies.

Thronson, Wilton and Ksik (1991) examined the interaction between NGC 3077 and M81 and concluded from the star formation rates that an interaction had taken place between these two galaxies. Although the total mass of gas in NGC 3077 and M82 is roughly similar, M82 seems to be more effective at turning this gas into molecular material, perhaps because M82 is a disk galaxy with a bar but NGC 3077 is elliptical.

The activity in M82 most likely results directly or indirectly from dynamical interaction with intergalactic matter in the M81–M82 group of galaxies. Although the cause and effect processes are not known in detail, infalling matter could plausibly trigger the first of successive "waves" of star formation through the resulting shock caused by its collision with the interstellar matter near M82's nucleus.

2.4 Spectroscopic studies and superwinds

O'Connell and Mangano (1978) examined the structure, kinematics and emission-line spectra in the central regions of M82 and at the base of the Hα filaments. They examined in detail the optical knots, the brightest of which are relatively young compact starclusters (blue globulars). Massive HII regions are seen in M82's nuclear region. The fact that they are optically visible means they are probably foreground objects in the nuclear region. The emission line velocity fields showed that these knots did not display the characteristic line broadening of a Seyfert nucleus and the disparity in their velocities showed that they

are separate objects and not the same object with a foreground dust field. The inner Hα filaments are in the immediate vicinity of Knot A (the brightest) and are not merely seen in projection. Figure 2.2 shows the positions of Knots A, C and E and the optical kinematic centre on a contour map of Hα. O'Connell and Mangano (1978) found that, outside the central 2kpc, the current star formation rate is abnormally low for a spiral galaxy. However the central region has had very active star formation in the last 10^8 years with central star clusters A, C and E being the youngest. A fresh supply of gas must have entered the central 1kpc during the last 10^8 years in order to fuel this star formation. Although M82 appears abnormally dusty, the mass of dust is not unusual for a late-type galaxy. The dust is conspicuous because it is dispersed through the galaxy and not confined to the plane of the galaxy.

Spectra of the Hα and NII emission lines across the minor axis of M82 showed unusual splitting of these lines which appear to form a complete hollow ellipse (Axon and Taylor, 1978). They interpreted this as the filaments forming an expanding cone and the emission being confined to the surface of this cone. The magnitude of the velocity splitting reaches a maximum of 250km/sec. They suggested that the observed filamentary emission is intrinsic and unpolarized but is superimposed on a weaker diffuse and highly polarized scattered component.

Williams, Caldwell and Schommer (1984) imaged spectrophotometric observations of Hα in M82. They obtained a series of images of Hα at different velocities showing the filaments and their velocities clearly. The overall velocity field is clearly not that of a disk in circular rotation. Some of the filaments have discrete velocities clearly separated from the smooth weaker Hα halo emission in their immediate neighbourhood. The Hα morphology follows that of the HI (Cottrell, 1977) and they suggest that the original source of the gas may have been a tidal encounter with M81 as modelled by Killian and Gottesman (1979). Some of this gas has been captured in essentially polar orbits, leading to the large-scale behaviour seen in the HI observations. Dissipative processes led to infall of some of this material which has produced a burst of star formation in the central regions in the last 10^8yr. This large star-formation rate has in turn produced a considerable number of SN explosions which has lead to ejection (the inner filaments) and powered the radio continuum, IR and X-ray emission.

The dust travelling with the HI in the polar orbits is responsible for much of the scattered polarized light and the diffuse Hα radiation and therefore the systemic difference of 80km/sec between the HI radial velocity and the Hα velocity may be due to the motion

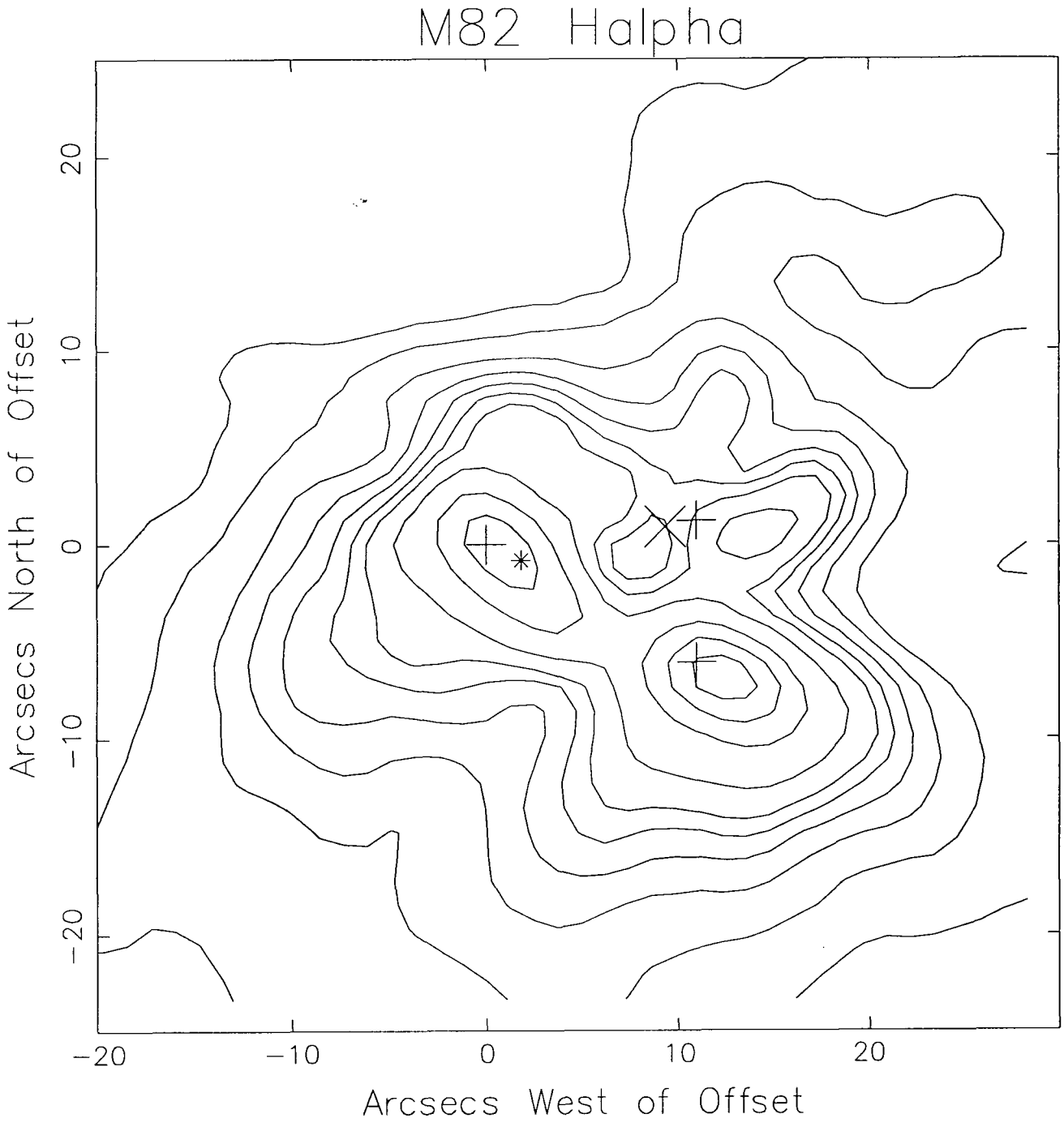

Figure 2.2: The centre of the Hα contour map of M82. The centre of the polarization pattern is indicated by ×, Knots A, C and E of O'Connell and Mangano (1978) are indicated by + and the optical kinematic centre is indicated by ∗.

of this gas perpendicular to the line of sight, i.e. infall. This dust will act as the moving mirrors (see Section 2.2), moving towards the central Hα source on both sides of the plane of the galaxy thus blueshifting this radiation and causing the offset between the HI and Hα velocities.

Chevalier and Clegg (1985) modelled the wind from a starburst nucleus. If most of the SN energy input is thermalized, a strong wind is driven out of the region. The wind is probably so fast that gravitational forces are not involved. The interaction of the wind with clouds can give rise to streaming motions and X-ray emission. The wind is expected to create a hole in any diffuse gas in which the galaxy is embedded.

MacCarthy, Heckman and van Breugel (1987) used the ratio of the SII lines to derive the variation of electron density with radial distance from the centre of M82 and NGC 253. They applied the Chevalier and Clegg model to both galaxies. For M82 the observed winds are highly bipolar and there is evidence for collimation in the flows in the X-ray and emission line data. The CO annulus of molecular gas (see Section 2.8) in the central few hundred parsecs of M82 may provide the nozzle that collimates the bipolar outflow. The outflowing wind presumably collides with ambient clouds in the galaxy halo. The winds ram pressure will drive fast shocks into low density clouds producing X-ray emission, and slow shocks into high density clouds producing optical line emission. The model predicts that the total pressure in the wind should decrease roughly with radial distance as r^{-2}. MacCarthy, Heckman and van Breugel's (1987) measurements of the pressure in the emission line filaments are consistent with this prediction. Moreover, the emission line spectra of the filaments are similar to the model spectra of shock-heated gas.

Upon encountering the outflowing wind, the infalling clouds of material will be shock heated to high temperatures. The more tenuous clouds will suffer high velocity shocks and may thus contribute some or all of the diffuse soft X-ray emission. Denser clouds will be heated to temperatures of the order of 10^5K, thus giving rise to the observed optical emission lines as they cool to $\sim 10^4$K. Visvanathan and Sandage (1972) noted that the constant ratio of Hα to NII would support scattering as being the dominant process. MacCarthy *et al.* (1987) found a weak but real variation in the Hα to NII ratio. Also the strong spatial variations in the other line ratios, especially the SII lines clearly argue that scattering cannot be the dominant process in the central 500pc.

Bland and Tully (1988) examined the Hα split lines and found that they reach a maximum separation of $\sim$ 350km/sec at a radius of 60″ out along the minor axis. The filaments lie along the surfaces of two elongated bubbles which are roughly perpendicular

to the galactic disk. If the galaxy is tilted by 8° with the NE side pointing towards us then the filaments define a bipolar outflow from the central region with the southern bubble moving towards us (Fig. 2.3). The southern bubble reaches a maximum opening angle of $\sim$ 35° at a radius of $\sim$ 65″. The brighter branch of the Hα line lies near the systemic velocity which implies that one side of the bubble is almost in the plane of the sky and the fainter branch of the Hα line is blueshifted on the southern side and redshifted on the northern, with systemic velocity at the nucleus.

Over the smooth halo they found that the NII/Hα ratio and velocity dispersion of the emission lines is constant. This implies that the light has been scattered uniformly into our line of sight. This scattered light explains the appearance of the broadband polarimetric images which show a smooth circularly symmetric halo centered on the nucleus. If the filaments are unpolarized the intrinsic polarization from the halo may be as high as 50%.

Bland and Tully (1988) concluded that they had strong evidence that M82 is a scaled up bipolar reflection nebula. Numerous SN explosions ($0.1\mathrm{yr}^{-1}$, Rieke *et al.* 1980) have heated the gas and dust in the nuclear region and this matter expands and is channeled out along the minor axis because it is confined by the gaseous disk surrounding the nuclear region (see Sections 2.8 and 2.6). Bland and Tully (1988) suggested that the broadline and continuum emissions arise from reflection in a halo of dust particles that scatter light escaping preferentially along the poles from the nuclear starburst. In this model the scattered light component is the source of the linear polarization observed about the galaxy. As the bubble sweep out only a fraction of the halo volume the polarized halo is evident even along the minor axis. Bland and Tully (1988) expected the filaments to show essentially no linear polarization once the influence of the halo is removed. However intrinsic polarization of up to 30% has been found in the filaments by Scarrott, Eaton and Axon (1991).

Tomisaka and Ikeuchi (1988) modelled galactic scale bipolar outflows from the nucleus of a starburst galaxy and applied it to M82. A large wind bubble, $\sim$ 100 – 200pc in the nuclear region, results from frequent SN. By 2D hydrodynamical simulations they found that hot matter heated by the SN explosions interacts with ambient interstellar matter and forms a wind bubble structure i.e. a hot cavity and a surrounding cooled shell. The bubble gradually elongates with expansion perpendicular to the galactic disk. Finally the shell is broken near the top and hot matter in the cavity is collimated and accelerated upwards. Hot gas can go up to 1 – 2kpc above the plane. This corresponds to X-ray emission extending perpendicularly to the galactic disk in M82. A further cooled

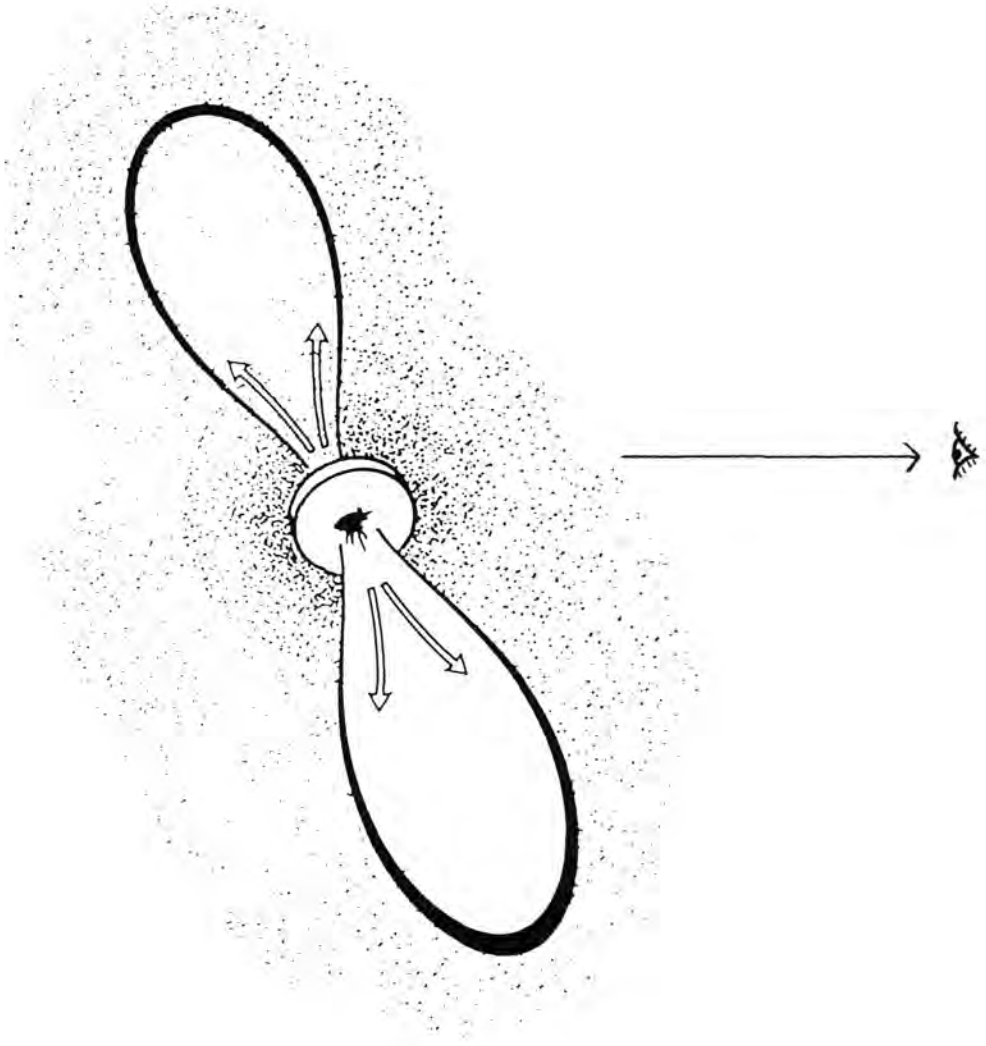

Figure 2.3: Schematic diagram of minor axis bubbles. The northern part of the galactic disk is inclined towards us, so the southern minor axis bubble is also inclined towards us.

shell is formed near the disk plane seems to correspond to a CO spur extending into the halo region of M82.

Gotz *et al.* (1990) undertook a spectroscopic investigation along the major axis of the galaxy and examined the H, He, O, N and S emission lines and the Hα and Na D absorption lines. Absorption lines trace the rotation curve of stars in the disk of M82 and the emission lines come from HII regions in the inner and outer starburst zone. The emission lines showed two components separated by 270km/sec in the central region, over 50″ parallel to the major axis i.e. split lines along the *major* axis as well as the minor axis. One component is from HII regions in the galactic disk, the other is from the starburst wind. The molecular ring is surrounded by a split-line emission zone of diameter 760pc ($\pm$ 25″) near the major axis, inside of which is presumably the blowout of the hot superwind.

The starburst wind sweeps out clouds from the disk, accelerating them to terminal velocities and giving rise to H_2 lines (on the inner edge of the molecular ring), X-rays (in tenuous clouds in the hot wind) and near-IR/optical/near-UV emission lines in the denser clouds in the wind (the filaments). The emission line gas in the wind region may result from the heating of cool dense clouds embedded in the hot outflowing wind, or from the cooling of entrained material on the outer surfaces of the wind bubble. Their results provide kinematic evidence that much of the visible ionized gas is actually outside the starburst region, in fact in HII regions external to the main CO peaks. The same is true for the ionized gas in the wind at 150pc above the plane which seems to be at larger radii than the molecular ring. This is predicted by the model with the magnetic field. They also measure (i) the electron densities in the disk HII region and at the rim of the flow, (ii) the rotation curve of the ionized gas in the central region, and the stellar population in the galactic disk, and (iii) the visual extinction near the major axis (see Table 2 in Gotz *et al.* 1990).

Gotz *et al.* (1990) derived a total mass of $2.9 \times 10^9 M_\odot$ for the central 3.3kpc diameter and argue that the major axis split lines have a different origin from the split lines along the minor axis. The first component's velocities are characteristic of HII regions and molecular clouds rotating in the plane of the galaxy while the second component's velocities are from the far side of the outflow in the starburst wind. In contrast to the disk the wind does not have a large amount of matter in molecular form.

The velocity of the hot 10^8K starburst wind may be 2000km/sec as in the Chevalier and Clegg model, but they only detect the cooler 10^4K denser debris (the Hα clouds) which is carried along and accelerated by the wind to an outflow terminal velocity of 600

$\pm$ 200 km/sec at the rim of the blowout cone. The clouds' terminal velocities are relative to their local velocities in the galaxy prior to acceleration so an observer sees their flow velocities superimposed on the rotation of that part of the galaxy from which the clouds originated. The full opening angle of the outflow cone is 30°. The split line profiles are observed in lines at the red end of the spectrum (Hα, SII, NII) possibly because the far side has more extinction in the emission lines at shorter wavelengths.

Heckman, Armus and Miley (1990) discuss at length the superwind model and apply it to a number of starburst galaxies including M82. They obtained optical spectroscopy of 14 far-IR galaxies and the data supports a superwind model in which the kinetic energy provided by supernovae and winds from massive stars in a central starburst drives a largescale outflow that can shock-heat and accelerate ambient interstellar matter of circumgalactic gas. Blown-out bubbles are observed in a number of these galaxies, including M82, NGC 253, NGC 4945, NGC 3079 and Arp 220.

The SIII/Hα flux ratio has been mapped by Waller, Gurwell and Tamura (1992). They suggest that the regions with higher SIII/Hα flux ratios are tracing larger amounts of reddening and hence obscuration of ionized dust. The geometry of this ratio map is consistent with the model of a circumnuclear ring of obscuring dust that is highly inclined to the line of sight. The lack of far-side obscuration is due to the far-side dust lying behind most of the ionizing gas. One can see that the regions of strongest extinction coincide with ridge lines in the CO emission and with extensions in the 10.8μm emission. The correspondence is restricted to the north of the major axis where the emitting CO gas and emitting/obscuring dust are in the foreground.

McKeith *et al.* (1994) observed near-IR emission and absorption lines along M82's major axis and found radial velocity-position curves that differ markedly from the lines at visible wavelengths. They find identical rotation for gas and stars contrary to previous results. They argue that the rotation derived from emission and absorption lines at visible wavelengths refer to outer regions of the galaxy since at those wavelengths the central disk is obscured by dust.

2.5 X-ray studies

The X-ray emission in M82 is characterised by the presence of diffuse radiation containing strong point-like sources whose X-ray luminosity, if arising from a single point, is much

higher than previously observed from objects other than AGNs. Such very luminous X-ray sources have been proposed as black hole candidates since the sources are radiating at far above the Eddington limit for a solar mass object.

An image of M82 in soft X-rays (Watson, Stanger and Griffiths 1984) obtained on the Einstein Observatory Imaging Proportional Counter (*EOIMC*) and Einstein Observatory High Resolution Imager (*EOHRI*) showed a complex central region with several unresolved sources and a halo of patchy diffuse emission extending for several arcseconds along the minor axis both NW and SE. This diffuse emission was more profuse on the SE side and lies along the same region as the Hα filaments in the optical. The X-ray halo appears to be correlated with the Hα filaments implying there is some physical relationship between the two. Watson, Stanger and Griffiths (1984) suggested that the X-ray emission from the halo is due to thermal emission from hot (10^7K) gas but this raises a problem since dust could not exist in these regions for very long because the dust grains would be destroyed very quickly in the hot plasma. They suggest that the filaments are formed in older SNR when radiative losses lead to rapid cooling and hence fragmentation of the denser parts of the shock front. The existence of the X-ray emission and the dust can be reconciled if the the X-ray emitting gas and the cold dust occupy spatially distinct regions. These X-ray sources are shown in Fig. 2.4 along with the SNRs of Kronberg, Biermann and Schwab (1985).

The X-ray interpretations of Kronberg, Biermann and Schwab (1985) from *ROSAT* and *EOHRI* data show that the X-ray emission clearly originates outside the inner M82 nucleus. This was the first galaxy to show substantial X-ray emission away from the stellar disk. The peak of the X-ray emission coincides approximately with the SNR 41.9+58 (see Section 2.7) but uncertainties do not permit a definite identification. The perpendicular features extend 53″ south and 22″ north of the centre, along the minor axis. A component of the X-ray distribution appears to coincide with the radio and 10μm complexes. It is stronger to the east and appears to be concentrated on the line defined by the compact radio sources (Kronberg, Biermann and Schwab, 1985) which is a few arcseconds below the centre line of the overall radio complex. This suggest recent activity is centered there.

The bulk of the diffuse X-ray emission is generated by the off-axis component to the south which coincides approximately with the inner optical filaments. The X-ray extension has a P.A. of 170°. This is almost perpendicular to the radio axis and forms a 54° halfwidth cone whose apex is at or near SNR 41.9+58. This cone contains most of the southern plateau of X-ray emission as well at the strong Hα filaments. The minor

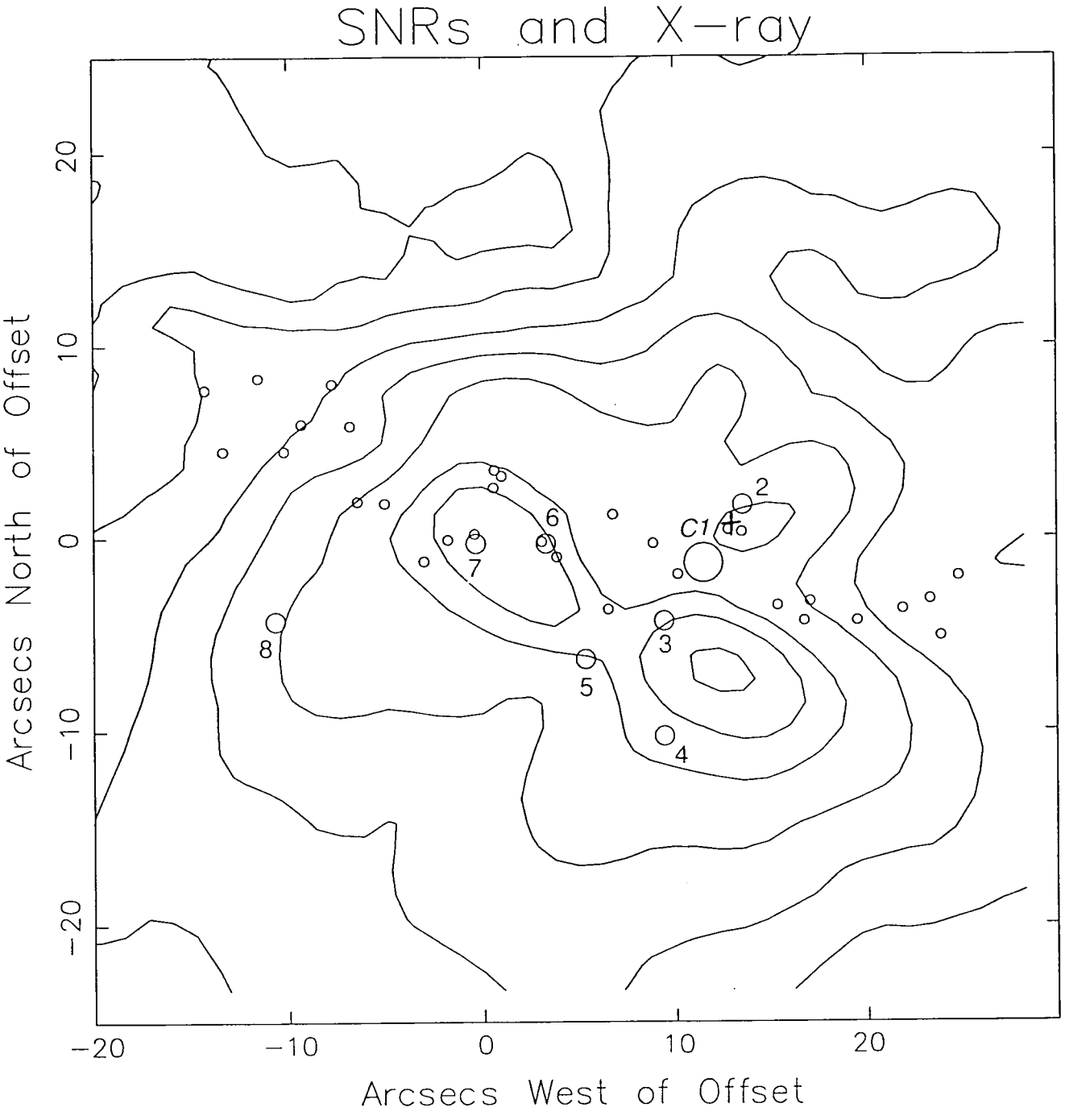

Figure 2.4: A Hα contour map overlaid with the positions of supernova remnants (Kronberg, Biermann and Schwab, 1985) and X-ray hotspots (Watson, Stanger and Griffiths, 1984). The SNRs are indicated by o and the X-ray hotspots by O. SN 41.9+58 is indicated by O. X-ray source 1 is not shown because it is a considerable distance from the other sources at this scale. The X-ray source labelled C1 is source 1 of Collura *et al.* (1993).

axis emission extends out to 9 arcsecs from the nucleus compared to only 5 arcsecs on the major axis (Fabbiano, 1988), obtained on the *EOIPC* in the 0.2 – 3.5KeV energy range and the *EOMPC* (Monitor Proportional Counter) in the 1 – 15 KeV energy range.

Schaaf *et al.* (1989) observed M82 using *EXOSAT* in the low energy range 0.06 – 2KeV and the medium energy range 1 – 15 KeV. The low energy results confirmed those of Watson *et al.* (1984) and Fabbiano (1988). They concluded that the radio halo was consistent with the SN rate implied by the radio source population. They proposed a tunnel network similar to that of Cox and Smith (1974) for our Galaxy and think that a blowout from these tunnels is imminent. There is a difference between the X-ray and radio morphologies. The X-ray emission is perpendicular to the galactic disk but the radio emission is confined to it. Schaaf *et al.* (1989) conclude that inverse Compton scattering of relativistic electrons and far-infrared photons may provide a considerable part of the entire X-ray luminescence beyond the soft energy band. Away from the nucleus however, free-free emission is more likely to dominate.

Collura *et al.* (1994) report variability from 2 of the point sources using *ROSAT* and *EOHRI*. Since emission from sources appearing point-like at a few arcsecs resolution might actually be due to a multiplicity of distinct sources, the study of variability may be crucial in constraining the contribution of individual sources to the observed emission. Source 1 (labelled C1 in Fig. 2.4) is either a compact X-ray binary or a combination of several binaries. The amplitude variation is strong evidence for an individual source in which case it is a massive compact object. Source 2 is an individual source of $20M_{\odot}$ which makes it the most luminous X-ray binary yet known and a black hole candidate. They postulate that it could be a background AGN microlensed by the nuclear region of M82.

2.6 Infrared Studies

One characteristic of a starburst galaxy is that it is extremely luminous in the IR. M82 ($L_{IR} = 3 \times 10^{10}\ L_{\odot}$) emits over 80% of its total flux at wavelengths greater than 3μm. Rieke *et al.* (1980) in their seminal paper mapped M82 and NGC 253 at 2.2 and 10.6μm. For M82, comparison of the 10.6μm map with the 6cm radio map of Hargrave (1974) showed a striking resemblance adding weight to the suggestions that there is a connection between nonthermal radio emission and IR emission from galactic nuclei (Fig. 2.5). The structure at 2.2μm is very different from that at 10.6μm. There is a clear nucleus at R.A.(1950) = $9^h\ 51^m\ 43^s.85 \pm 0^s.3$, Dec.(1950) = $69^\circ\ 55'\ 1''.0 \pm 1''.5$ and the map

suggest the presence of a smooth disk of stars centered on the nucleus, viewed edge-on and with a slightly brighter stellar population or less foreground extinction to the east of the nucleus than to the west. No feature on the 10.6μm map coincides with the 2.2μm nucleus. It is clear from the general shapes of the IR spectra that the middle- and far-IR fluxes are predominantly thermal re-radiation by dust. The 10.6μm map is very similar to the 20μm map and the 58μm map of Telesco and Harper (1980). The far-IR source coincides with that at 10μm. In addition to the far-IR luminosity, a significant amount of the direct output of the red giants in M82 must escape in directions roughly perpendicular to the plane. Rieke *et al.* (1980) calculate a lower limit on the extinction of the central regions of $A_v \approx 25$. The CO bands in the near-IR spectrum demonstrate that the flux from 1 – 2.5μm is dominated by the output of late-type stars.

Rieke *et al.* (1980) modelled M82 extensively using the available data and got the best agreement between their calculations and the observed data when (i) the starburst model has an initial mass function (IMF) with a lower mass limit of $\sim 3M_\odot$, (ii) star formation is very efficient; about 50% of available material has been converted into stars over the last $\sim 10^8$yr and (iii) the starburst lasts $\sim 2 \times 10^7$ to 1×10^8yr: more than one such starburst phase can occur.

They calculate a SN rate of 0.3 SN/yr and suggest that a substantial part of the X-ray emission probably originates in collapsed stellar and SNRs. The 10.6μm map presumably indicates the locations of the most recent star formation which contains OB stars, while the 2.2μm indicates the locations of the red giants and supergiants. Since the red and supergiants are older than the O and B stars, the maps may be showing that star formation has spread outward from the nucleus and is no longer centrally concentrated. A burst of star formation triggered by an encounter with M81, is able to match all the observed parameters for M82. The model of Rieke *et al.* (1980) can account simultaneously for the nonthermal radio flux, the large luminosity (predominately in the IR), the large flux from red giants and supergiants seen at 2.2μm, the UV required to excite the X-ray flux and the non-circular motions of the interstellar gas.

The CII integrated emission (158μm) and continuum emission (Crawford *et al.* 1985, Lugten *et al.* 1986) have peaks at the 2.2μm nucleus and extend along the major and minor axes. The continuum is similar to the mid- and far-IR maps of Rieke *et al.* (1980) but the line emission shows more extent along the minor axis. CII line is a tracer of molecular clouds and not of atomic hydrogen clouds or tenuous intercloud gas. The 158μm emission comes from warm dense gas at the surfaces of molecular clouds which

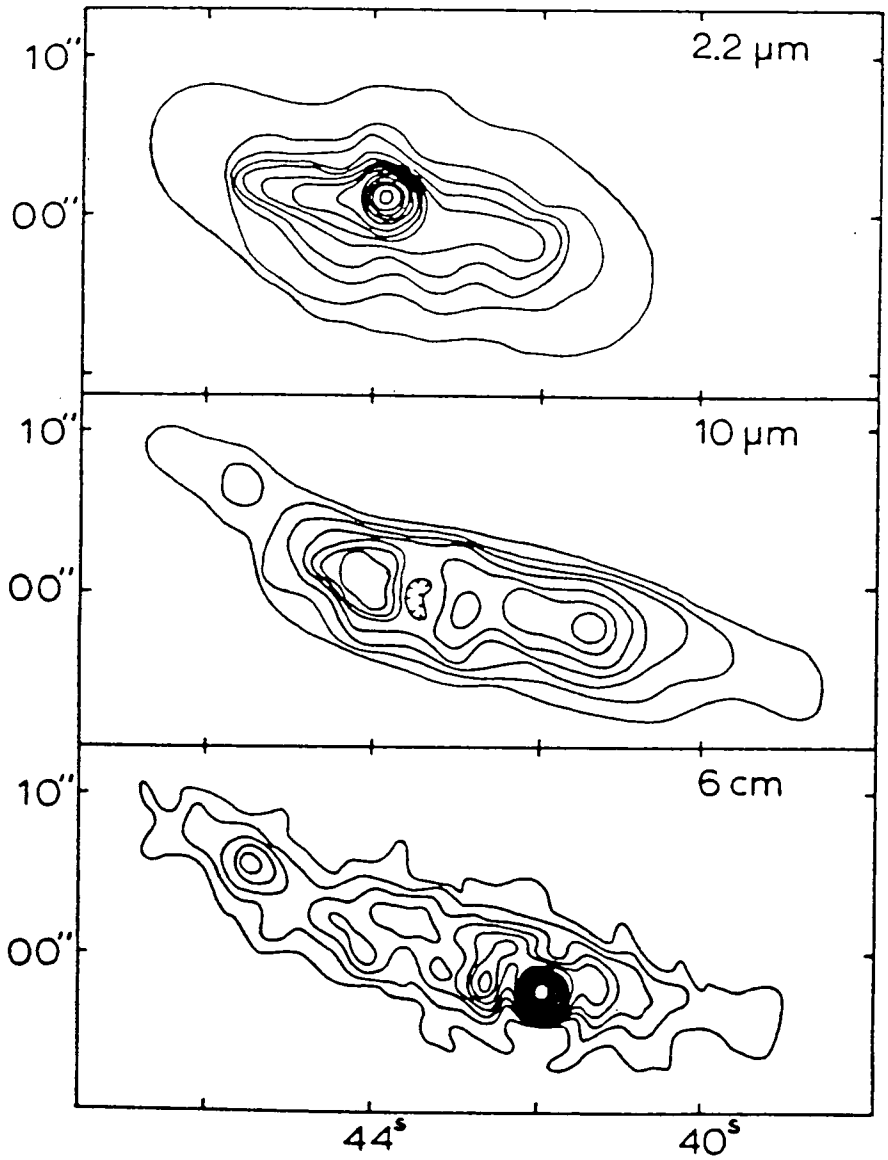

Figure 2.5: The 2.2 and 10.6μm maps from Rieke *et al.* (1980) and the 10.6cm map from Hargrave (1974).

are exposed to UV light from embedded OB stars or galactic interstellar radiation fields. This may be evidence of significant emission several hundreds parsecs above and below the plane of M82 in the region of the filaments. Much of the far-IR line emission originates in the inner rotating ring. From the volume filling factor they estimate that the emission probably comes from a large number of small clouds, thin sheets or filaments with large ratios of surface area to volume.

Telesco (1988) reviewed the significance of the IR observations in terms of star formation. Most of the observed C^+ resides in warm dense zones just outside HII regions in molecular clouds i.e. at HI–HII interfaces. The CII 158μm line is a tracer of UV radiation in the 912 – 1101Å range implying that young stars are common throughout M82s interstellar medium, emitting UV radiation on much of the gas. From near IR emission lines from H_2 one can calculate the mass of shock-heated gas. Because H_2 cools to less than 1000K in about 2yr, the rate at which H_2 is being shocked in M82 is about $400 M_\odot yr^{-1}$. Comparing this mass to the total gas masses, if these rates are sustained over 10^5 – 10^6yr, a mass equivalent to the total gas mass must be shocked.

Nonthermal radio continuum and dust-emitted IR fluxes are correlated for large, heterogenous samples of galaxies. This correlation reflects the coexistence of the young stars powering the infrared luminosity with other Population I objects, especially Type 2 SN which generate high-energy electrons and synchrotron emission. The IR luminous region of M82 is coincident with bright, nonthermal radio emission in which are embedded about 40 radio point sources. The starburst model of Rieke *et al.* (1988) implies a SN rate of $0.2 - 0.3 yr^{-1}$ and should result from a stellar population sufficient to emit the observed IR luminosity. However the SN rate may not be sufficient to account for the observed radio flux. The centre of M82 emits radio flux which requires a SN rate of $\sim 5 yr^{-1}$. Also the SN rate may not be high enough to account for the synchrotron emission, but SN rates and particle acceleration may be different in active star forming regions than they are in the Galactic and extragalactic sample that are usually taken as representative. Star formation maintained at these rates will exhaust all of the gas in many active star-forming galaxies in a time much less than the apparent age of the galaxy. Telesco suggests that galaxies may experience short-term fluctuations in their star formation rates over much of their lives: a galaxy could experience as many as 15 'bursts' over 10^9yr if each active star forming phase lasted $\sim 2 \times 10^7$yr.

Interacting galaxies are several times more likely to have nuclear activity or a burst of star formation, (Verter and Rickard 1989) probably as a result of tidal effects on

the central gas orbits. Maps of the centre of M82 at 10μm, 19.5μm and 30μm (Dietz *et al.* 1989, Telesco, Decher and Joy 1989) showed the two peak nature of other IR studies. The double-peaked structure is thought to correspond to a warm ring of dust or spiral arms viewed edge-on. Dietz *et al.* (1989) made IR polarization measurements in J, H and K at the K1 and K2 peaks of Dietz *et al.* (1986) and concluded that both intrinsic and interstellar polarization components could be found in K2, the intrinsic component perhaps being due to scattering by dust which surrounds a luminous source within K2. The two CO peaks of Lo *et al.* (1987) lie outside the IR peaks (see Section 2.8). The 10–100μm emission is from heated dust and colour trends result from spatial variations in mean temperatures of the IR-emitting dust along the line of sight. To explain the colour variations small hot grains must be assumed to account for the IR energy distribution. These small grains may consist partly or mostly of PAHs (polycyclic aromatic hydrocarbons).

Much of the starburst region may be depleted of the smallest grains relative to the surrounding galaxy because the calculated UV flux is very strong. In effect the starburst is embedded in a halo which has a much higher content of small grains. The UV energy density in the halo is high enough to noticeably heat the grains but not high enough to destroy them. This UV radiation probably originates from massive stars embedded in the halo. Because the starburst region contains abundant molecules one might expect that many of the small grains reside in dense clouds and are therefore shielded from the intense UV by the neutral atomic and molecular gas, but this appears to be primarily in sheets and filaments (Lo *et al.* 1987, Lugten *et al.* 1986) (see Section 2.8), a geometry which would provide minimum protection to the grains. This differs from Watson, Stanger and Griffiths (1984) who argued that the dust would be quickly destroyed by the UV flux.

Lester *et al.* (1990) presented near-IR spectroscopy in J, H and K bands for the inner 60pc (4″) of the galaxy. They found emission from shocked molecular hydrogen at the core of M82 and it can be understood as originating on the inner edge of the molecular ring that surrounds the starburst. They calculated the IR extinction and found that an unusual IMF is unnecessary if the red starlight from the core is diluted by thermal emission from grains at the long wavelength end of the K waveband. The FeII distribution is spatially similar to the nonthermal radio emission, confirming its association with the SNR.

Telesco *et al.* (1991) mapped M82 at J, H, K, 10.8, 19.2, and 30μm. The appearance at 2μm indicates that a bar $\sim$ 1kpc in length is located at the centre of the galaxy. The

near IR maps show a strong central peak, a secondary peak located $\sim$ 10″W of it and lower level emission along the major axis. The JHK colours are consistent with most of the IR emission originating in a heavily obscured population of red stars (Joy, Lester and Harvey, 1987). Red supergiants may make a significant contribution to the 2μm emission.

Higher optical depth lies along a ridge that is almost parallel with the major axis of IR emission. A comparison between the 2.2μm optical depth and the HI opacity (Weliachew, Fomalont and Greisen 1984) shows that they are strikingly similar. They conclude that the dust responsible for the prominent near-IR absorption is associated intimately with the HI detected in absorption. The kinematic properties of the HI imply it exists near the centre and may be toroidal, which suggests that most of the near IR extinction towards the nucleus originates in dust that is also near the centre and in the toroid. Dust in the outer disk contributes little to the obscuration. A good correlation has been found between the nuclear molecular emission and the optically dark lane, a correlation that would not hold if there were much extinction far from the nucleus. The bar is seen in K as emission wings at $\sim$ 15″ (240pc) radius. Its axis is tilted by 4° with respect to the major axis of the K emission so it may be that the structural major axis of the bar is not in the plane of the sky but is tilted to our line of sight.

The 10, 19 and 30μm emissions show two peaks $\sim$ 10″ apart and embedded in lower level emission. Their maps are comparable with the 58μm maps of Telesco and Harper (1980) and 40 and 100μm maps of Joy, Harvey and Lester (1987). The high-resolution 10–30μm maps indicate reasonably well the distribution of much of the IR luminosity emerging at wavelengths greater than 30μm where the resolution of existing scans is lower. The correlation between the 10μm and the Brγ implies that warm dust is distributed like the ionized gas and supports the conclusion that the IR emitting dust is heated by the same population of young stars that ionize the gas. Carlstrom (1988) concluded that all the 3.3mm continuum is due to bremsstrahlung and is therefore an accurate tracer of the ionized gas in M82. It is difficult to reconcile this with the 10μm emission and the distribution of the Brγ line flux which should also trace the ionized gas. The 3.3mm distribution (see Section 2.9) probably contains emission from cool dust as well as bremsstrahlung, this is especially likely near the 10μm peak where the 45μm emission is very strong.

The two brightest CO peaks are located at larger radii than the IR emission. An extensive region of star formation must be located on the inner side of the molecular toroid and must be participating in the galactic rotation manifested by the molecules. Strong

10–30μm emission is not seen at either of the dominant CO lobes. The western mid-IR peaks are within a few arcsecs of Knot E, secondary K peak, 450μm peak, 41.9+58 and the OH masers. Numerical simulations have shown that galaxies are extremely efficient at forming bars. Once formed these can dramatically influence global gas dynamics and hence large-scale star formation with the generation and maintenance of spiral arms being one important example. The bar was probably formed by the interaction with M81.

Puxley (1991) found that the apparently low extinction toward the nucleus inferred from optical and near IR recombination line and continuum studies ($A_v \sim 5$) can be reconciled with much larger values inferred from mid-IR and longer wavelength measurements ($A_v \sim 25$) if dust and radiating sources are well mixed along the line of sight. If the large extinction derived from long wavelength data attenuates the emission from giant and supergiant stars then the IMF in M82 is difficient in low mass stars.

Telesco and Gezari (1992) obtained high-resolution 12.4μm images of the central regions of M82. They found two prominent lobes separated by $\sim 10''$, equidistant from the central peak at 2μm. The lobes are embedded in a broad ridge of diffuse emission which extends $\sim 20''$ along the major axis. They found no correlation between the IR emission and the young SNRs (seen at 6cm) of Kronberg, Biermann and Schwab (1985). There is considerable small-scale structure indicating several bright clumps less than 20pc in size which may be embedded in giant star clusters. They attribute the high values of the ratio of nonthermal and IR emission near the nucleus and the ratio of IR luminosity to CO luminosity in one of the starburst lobes to disruption of the central region by supernova activity. They argue that the mid-IR-emitting dust is heated by young stars and not by supernova shocks.

McLeod *et al.* (1993) have recently presented near-IR imaging and spectroscopy in J, H and K along the major axis of M82. They find that the extinction cannot be modelled by a simple foreground screen of dust, but more complex models such as a uniform mix of dust and gas, or a non-uniform screen of absorbers can provide a reasonable fit to the observations. For a uniform mix of dust and gas they calculated an extinction of 27 mag.

Gaffney, Lester and Telesco (1993) looked at the velocity dispersion of the stellar component in the nuclear regions of M82. The dispersion is significantly larger than that of the ionized gas in the same region. The near-IR continuum from the central 15pc is dominated by a nuclear bulge population that predates the enveloping starburst. A large fraction of the total mass in the nuclear region is contained in a region smaller than that of the starburst disk. This suggests that the starburst disk, which is a strong source of

K band light, must have a much lower mass-to-light ratio than the nuclear bulge, which supports the theory of Rieke *et al.* (1980) that red supergiants supply most of the K band light there.

Recently, Larkin *et al.* (1994) obtained J, H, K, L′ and Brγ imaging of the central regions of M82. They find further evidence for a stellar bar and conjecture that if we could see M82 face-on we would see the dust confined to two lanes preceeding the bar in its rotation about the nucleus. The strong correlation between the CO(1-0) maps of Carlstrom (1988), and the dust features revealed by the IR colours, suggest they may originate from the same regions within M82. The two Brγ sources are within the CO lobes of Carlstrom (1988). They are roughly coincident with the emission seen at 12.4μm by Telesco and Gezari (1992) which is consistent with the idea that much of the flux from dust heated in ionized regions is re-radiated in the mid-IR range. Figure 2.6 shows the models proposed by Larkin *et al.* (1994) for the geometry of the stellar bar and molecular clouds.

2.7 Radio studies

M82 was initially identified with the nonthermal radio source 3C231 by Lynds (1961). Kronberg, Pritchet and van den Bergh (1972) mapped M82 at 8083MHz (3.71cm) and compared the discrete radio sources they found with IR hotspots and found no detailed correspondence between them. Kronberg and Wilkinson (1975) mapped M82 at 8085MHz and found more discrete components, the brightest of which they called 41.9+58.

Kronberg, Biermann and Schwab (1981) presented radio maps of M82 at 1465-MHz (20.6cm) and 4885MHz (6.1cm), showing a number of SNRs and concluded that an extreme burst of O and B star formation was necessary to account for the radio, IR and X-ray luminosities. They found no significance between their radio peaks and the IR knots of Kronberg, Pritchet and van den Burgh (1972) but they did find a good correspondence between Knot C of O'Connell and Mangano (1978) and a low brightness radio plateau protruding southward of 41.9+58.

Weliachew, Fomalont and Greisen (1984) mapped the HI and OH absorptions at 1667 and 1420MHz, across the central 1kpc of M82. They found that the HI and OH are concentrated in a centrally rotating ring of radius 250pc, thickness $<$ 120pc and with a maximum rotational velocity of 137km/sec. The optical and radio kinematic centres

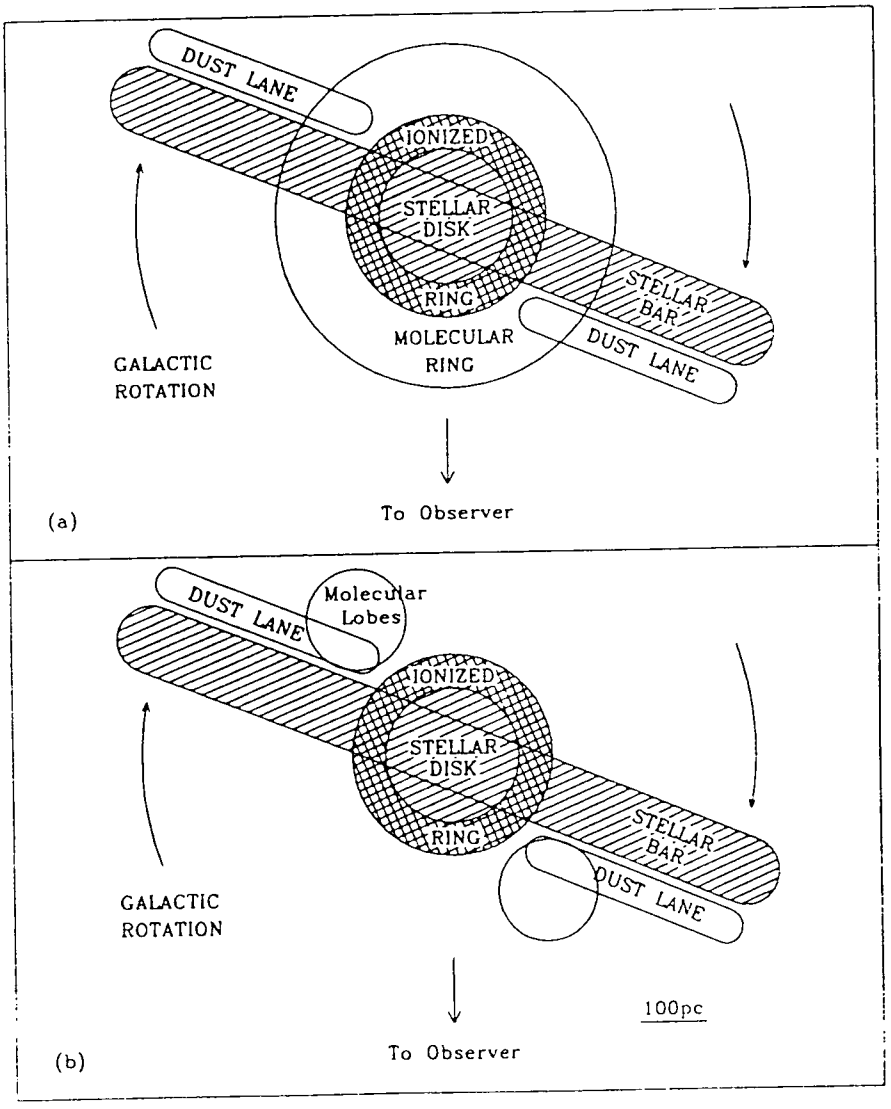

Figure 2.6: Posible models for the face-on geometry of M82 from Larkin *et al.* (1994).

coincide within 20pc of the 2.2μm peak which is consistent with the suggestion of Rieke *et al.* (1980) that the 2.2μm peak is a giant star cluster at the centre of M82. There are two major OH concentrations and these coincide roughly with the HI peaks. Minimum ages derived from kinematics (rotation period of ring is 1.1×10^7yr) and abundances are too small to decide whether the ring formed before or after the interaction with M81. They find OH masers near two extensions from the continuum point source. These extensions may be regions where gas has been ejected from the point source and the resulting compression may create favourable conditions for masing. The OH/HI abundance is near galactic values and suggests that the gas in the ring has already been processed into stars and that the material has galactic metallic abundance, but it does not imply the ring is old.

Unger *et al.* (1984) observed M82 at 408, 1666 and 4995MHz. They found a large number of compact radio sources in the central few hundred pc of the galaxy. Again there is little detailed correspondence between these radio sources and objects seen at other wavelengths. Although the diffuse X-ray source is centered on 41.9+58, the individual X-ray sources (Watson *et al.* 1984) do not have any correspondence. Unger *et al.* (1984) placed an upper size limit of $\sim$ 2pc on the stronger sources and $\sim$ 4pc on the weaker sources, with an upper limit of $\sim$ 1pc on 41.9+58 which has dominated the radio structure for 15 years and so may be atypical. The distribution of the compact radio sources is asymmetric when compared to the low-resolution map of Kronberg, Biermann and Schwab (1981). The stronger sources lie close to the steep gradient on the south side of the plateau while there are no sources on the north. They feel that this reflects the true distribution of the sources and is not an obscuration effect. Both the Hα and the X-ray emissions are stronger to the south and are similarly asymmetric. They suggest a model where the compact radio sources lie within that part of an edge-on ring which is tilted to the south.

From Rieke *et al.* (1980) the 2.2μm emission comes from old red giants close to the dynamical centre and the 10μm arises in hot dust associated with more recent star formation. This implies the region of star formation is moving outward from the centre and the 2.2μm centre is coincident with the kinematic centre. The twin peaks of the far-IR map lie inside the peaks of the HI distribution. The bulk of the diffuse radio source lies inside the inner edge of the HI ring which laterally confines the X-ray emitting gas. The filaments and the SN may be related in that the hot gas responsible for the X-ray emission originates in the SN explosions. Since the gas is laterally confined by the HI ring it is forced to expand along the minor axis. Rapid cooling as it expands into the cool

neutral Hydrogen will give rise to the observed Hα filaments. If there is a greater external pressure in HI to the north, this would account for the asymmetry.

In Kronberg, Biermann and Schwab (1985), higher resolution radio maps at 2, 6 and 21.2cm (14.9, 4.87 and 1.41 GHz) are presented and analysed along with X-ray maps (see Section 2.5). The SNRs are shown in Fig. 2.4, with the X-ray objects of Watson, Stanger and Griffiths (1984) on a contour map of the B waveband. None of these sources displayed any radio polarization. The brightest sources lie along organised quasi-linear features and indicate that the presumed SN and massive star formation occur in a system that has been organised by the dynamics of the inner 300pc region in M82. The optical depth suggested by the OH and HI absorption maps of Weliachew, Fomalont and Greisen (1984) coincide remarkably well with the lower line of radio sources. Their OH maser source 2 coincides with 42.2+59. Each of the 28 radio sources is more radio-luminous (by up to 150 times) than the brightest radio source in our Galaxy. The strongest optical knots have no discernable radio component but the overall boundary of the 10μm emission (Rieke *et al.*, 1980) and the intense 58μm emission (Telesco and Harper, 1980) correspond well to the 6cm map.

If 41.9+58 radiates by incoherent synchrotron radiation then the combination of its radio luminosity, spectral shape, age and size impose severe constraints on its physical properties. They calculate an average expansion speed of $\sim 10^3$km/sec which implies 41.9+58 did not undergo a free expansion in its early phase. This may be typical of a Type 2 SN deep inside a large molecular cloud.

Bartel *et al.* (1987) made 2.3GHz and 8.4GHz observations of 23 'hotspots' in the nuclear region of M82. They obtained the first reliable image of 41.9+58 and got a linear extent of 0.7pc. This implies that an age of approximately 25 years. The other hotspots suggest ages of about 10 to 100 years implying a SN rate of 0.1yr^{-1} for the inner 600pc of M82 with an uncertainty factor of 2. Table 2.1 shows some of the SN rates that have been calculated over the past 20 years.

Seaquist and Odegard (1991) observed M82 in the 6 – 90 cm range. Their most sensitive map (at 20cm) shows a radio halo surrounding the galaxy whose diameter is comparable with the optical extent of the disk (around 8′). They infer that the radio halo has a nonthermal spectrum and is therefore produced by synchrotron radiation. There appears to be some correspondence on a small scale between optical and radio features, in particular there are slight radio enhancements (horns) associated with the optical filaments on the northern side. The filaments and the associated radio emission may be

Author (Year)	SN rate (yr^{-1})
Kronberg and Wilkinson (1975)	0.1
Rieke *et al.* (1980)	0.3
Unger *et al.* (1984)	0.5
Kronberg and Sramek (1985)	0.3–0.2
Kronberg *et al.* (1985)	0.16
Bartel *et al.* (1987)	0.1
Muxlow *et al.* (1994)	0.05

Table 2.1: Supernova rates in the central regions of M82 calculated over the last 20 years

connected with the cone of ejection representing a bipolar outflow from the nucleus. The morphology of the synchrotron halo is however not strictly bipolar but rather more spherically symmetric. The radio brightness distribution at 20cm shows a marked north/south asymmetry with respect to the disk of M82. The lowest contours reveal an extension toward the NE and a sharp gradient towards the south. This is also seen at 90cm. The higher resolution maps show a different asymmetry in the form of a bulge or enhancement in the radio emission along the minor axis to the SE of the disk. The X-ray maps of comparable resolution also exhibit prominent emission on the south side of the disk (Schaaf *et al.*, 1989). Both the radio and the X-ray counterparts are generally coincident with the southern system of optical filaments, which are also more prominent than corresponding features on the north side. They suggest possible physical origins for these asymmetries. The spectral indices imply that synchrotron is responsible and they propose a simple model involving outward convection of relativistic particles with electron energy lost by inverse Compton scattering against IR photons and adiabatic expansion.

Reuter *at al.* (1992) find clear evidence for a vertical magnetic field structure in the halo of M82. Maps at 90, 20, 6 and 3.6cm show a complex morphology of the synchrotron halo encompassing the central starburst region. The halo is characterised by a filamentary structure with prominent gaps located between the filaments. All these features exhibit a preferential orientation normal to the plane of M82 and extend out to 1kpc along the minor axis. There is a prominent synchrotron gap which appears to be associated with a corresponding gap in the distribution of compact non-thermal sources in M82s nuclear region. The conditions for the existence of such filaments and gaps can be explained in terms of plasma convection along a vertical magnetic field in M82s halo. The origin of

the proposed large-scale bipolar field may be a galactic dynamo or a bipolar wind, but a bipolar wind is favoured by the time scale involved.

Recently, Muxlow *et al.* (1994) have published MERLIN images of the central 700pc region of M82. They find over 40 discrete objects, all resolved by a 50milliarcsecond (0.75pc) beam. Most of these sources are SNRs, some displaying shell structure. They calculate a SN rate of 0.05/yr which is lower than previous estimates based on the fact that Kronberg and Sramek (1992) found no new SN in the last decade which implies that the SN rate is not as high as previously calculated. None of the discrete sources found show characteristics of AGNs, radio jets etc. The mean diameters of the SN imply they are a much younger population than that found in our Galaxy or the LMC, with an average age of about 200 years. They note that one of the SN, 42.21+590 is very closer to the centre of the polarization pattern in the Hα map of Scarrott, Eaton and Axon (1991).

Yun, Ho and Lo (1993) have found that there is a triangular central concentration of neutral atomic gas and several long tidal streamers originating from M82. The coincidence of the beginning of the tidal streamer with the flaring of the optical disk as well as the smooth continuum of the disk velocity field into the HI streamer strongly suggest the *tidal* disruption of the disk, contrary to the widely proposed scenario of tidal stripping and gas accretion from M81. Close to the nucleus the HI features are associated with both the optical filament and the dust lanes, and it is suggested that these HI clouds are the sites of reflection and scattering of the light originating in the nucleus.

2.8 Molecular Studies

M82 was the first extragalactic object found to contain CO emission (Rickard *et al.* 1975, Solomon and de Zafra 1975). Knapp *et al.* (1980) observed CO(2 - 1) and found M82 to be optically thin in CO at the systemic velocity in the central region. They found that the relative amounts of stars and gas in the centre of M82 suggested that much of the current star formation is taking place as high-mass stars. Stark and Carlson (1982) also found that the CO emission is optically thin compared to other galaxies. At least some of the CO emission seemed to be spatially extended beyond the optical disk. Their observations suggested a large tenuous halo of molecular material associated with the dust filaments above and below the stellar disk. Table 2.2 lists some of the many molecular studies which have been published in recent years.

Reference	Year	Molecular Transition
Stark & Carlson	1982	$^{12}CO(2-1)$, $^{12}CO(1-0)$, $^{13}CO(1-0)$, $C^{18}O(1-0)$
Sutton Masson & Phillips	1983	$^{12}CO(2-1)$, $(1-0)$
Young & Scoville	1984	$^{12}CO(1-0)$
Oloffson & Rydbeck	1984	$^{12}CO(1-0)$
Lo *et al.*	1987	$^{12}CO(1-0)$
Nakai *et al.*	1987	$^{12}CO(1-0)$
Loiseau *et al.*	1988	$^{13}CO(2-1)$
Carlstrom	1988	$HCN(1-0)$, $HCO^{+}(1-0)$, $CO(1-0)$, 3.3mm
Sofue	1988	Review
Verter & Rickard	1989	$^{12}CO(2-1)$, $(1-0)$ in 17 galaxies incl. M82
Phillips & Mampaso	1989	$^{12}CO(2-1)$
Baan *et al.*	1990	H_2CO, $CS(2-1)$
Turner Martin & Ho	1991	$^{12}CO(3-2)$, $^{13}CO(3-2)$
Wild *et al.*	1992	$^{12}CO(6-5)$, $(3-2)$, $(2-1)$, $(1-0)$
		$C^{18}0(2-1)$, $C^{17}0(2-1)$,
		$HCN(3-2)$, $H^{13}CN(1-0)$, $HCO^{+}(3-2)$
Sofue *et al.*	1992	$^{12}CO(2-1)$
Gusten *et al.*	1993	$^{12}CO(4-3)$

Table 2.2: Recent papers on molecular studies of M82.

The maps of Sutton, Masson and Phillips (1983) are similar in shape and extent to the 10.6μm IR emission (Rieke *et al.* 1980) and 6.1 cm continuum emission (Kronberg, Biermann and Schwab, 1981). Lo *et al.* (1987) mapped ^{12}CO(1 – 0) at high resolution in the central 1kpc of M82. Lo *et al.* (1987) resolved two components; a high central concentration and extended features that may be gas expelled from the central concentration. The maps of the central regions are similar to the 10μm, 6cm and SNRs areas. The CO source, 1.5 by 0.3kpc in extent, is roughly aligned with the disk of the galaxy and has two prominent peaks approximately 25″ apart (Fig. 2.7). These appear on either side of the 2.2μm central source. Lo *et al.* (1987) concluded that there is a stellar bar in the centre of M82, suggested by the distribution and kinematics of the central gas concentration and the 2.2μm light distribution, which may have played an important role in the starburst formation. This was also suggested by Telesco *et al.* (1991) (see Section 2.6).

Sofue (1988) reviewed the molecular studies of M82 up to that point and discussed the possible physical and starburst scenarios in some detail. These included

- the Ring and Outflowing Cylinder model of Nakai *et al.* (1987) where a large fraction of the gas inside the molecular ring (which is circularly rotating) has been blown out of the galactic plane, possibly by a large number of SN explosions.
- Numerical models of this structure including explosion, wind and magnetic models
- Accretion of gas and formation of dense nuclear disk, and bar formation by tidal interaction
- The starburst scenario.

The alignment of the many SNRs with the CO map (although not with the CO peaks) suggest that some large-scale mechanism, in addition to the high surface density of molecules has influenced the recent star formation. The kinematic and structural major axes of the CO are not aligned. Similar misalignment is observed in the velocity field derived from optical emission lines (Heckathorn 1972, O'Connell and Mangano 1978, Williams, Caldwell and Schommer 1984). Thus the observed gas motion cannot be simply that of an inclined circularly rotating disk or ring.

The distribution of ^{13}CO(2 – 1) is quite different from ^{12}CO(2 – 1) and ^{12}CO(1 – 0) (Loiseau *et al.* 1988). The ^{13}CO(2 – 1) map has 3 maxima, 2 correspond to outer maxima found by Lo *et al.* (1987). The central source is the most intense point of the map and appears to correspond to 41.9+58.

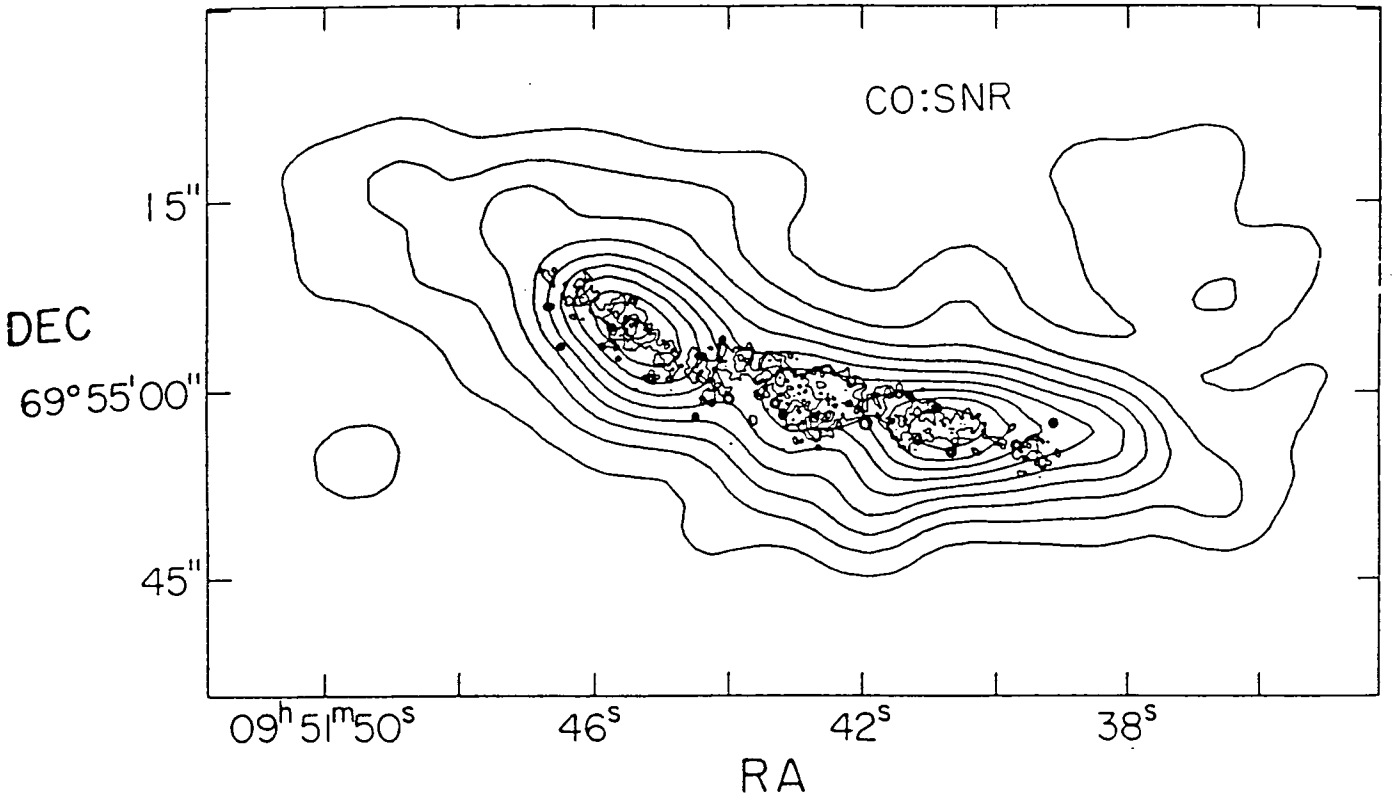

Figure 2.7: A ^{12}CO (1 – 0) map of M82 from Lo *et al.* (1987) overlaid with a contour map of the SNR of Kronberg, Biermann and Schwab (1985).

Because much higher H_2 densities are required to collisionally excite HCN and HCO^+ than CO, and because HCO^+ is highly reactive, maps of these molecules can be used to separate the effects of density, shocks, UV and cosmic rays on the molecular component (Carlstrom 1988). Also, since the 3.3mm emission is due to free-free emission it probes the HII regions associated with the starburst. The map of the 3.3mm emission is similar to the 10μ and 6cm maps. This supports the starburst hypothesis and indicates that high density ionized thermal gas coexists with the molecular gas. The CO map at 8″ resolution is similar to the map of Lo *et al.* (1987). At 5″ resolution a third peak appears near the centre and the map is very similar to the HI absorption map of Weliachew, Fomalont and Greisen (1984). The HCN map has three peaks and an extended spur south of the 2.2μm centre. The HCO^+ has an excess near 41.9+58 which extends southward towards the base of the southern optical filaments. The two western peaks are not as prominent as the CO and HCN ones but the ratio of HCO^+ to CO or HCN is the same as the ratio for the eastern peak. This implies that the HCO^+ western peaks are concealed by excess emission. HCN and HCO^+ require much higher densities than CO to be excited. This implies that a substantial fraction of molecular gas in the central starburst must be in dense clouds. The molecular mass was derived to be $1 \times 10^8 M_\odot$ with a small volume filling factor. The excess HCO^+ emission is well correlated to the base of the optical filaments and the excess X-ray emission. The excess HCO^+ emission near the base of the filaments could be dense molecular gas that has been entrained in the outflow. Alternatively the excess could be from dense high latitude ambient gas with which the outflow is interacting. Although a toroidal distribution of molecular gas is an attractive explanation for collimation of the outflow, the molecular cloud distribution is more complicated than a rotating ring (especially the central peak).

Verter and Rickard (1989) surveyed $^{12}CO(2-1)$ and $^{12}CO(1-0)$ in seventeen IR-luminous galaxies and compared them with M82 to see if M82 is the prototype for IR-luminous galaxies. Many (but not all) IR-luminous galaxies appear to be undergoing tidal interactions. The starburst scenario endorsed by most authors calls for a galactic interaction to cause gas accretion of a circumnuclear disk which somehow triggers a burst of star formation. In most starbursts the gas excitation appears to be dominated by shock heating (as opposed to UV radiation) making them compatible with the supernova-driven wind model of Chevalier and Clegg (1985). McCarthy *et al.* (1987) have shown that this model fits the kinematics, X-ray and optical spectra of M82. Heckman *et al.* (1987) have shown that the IR-luminous galaxies with "tepid" IR temperatures are spectroscopically

very similar to the M82 filaments suggesting that the SN wind scenario applies to these galaxies as a class. The ability of circumnuclear molecular gas to act as a nozzle has been modelled. Observationally, Verter and Rickard measured all the galaxies in their sample to be optically thick so they inferred that the molecular gas ensemble in most starbursts is capable of withstanding the nuclear outflow of the burst without substantial ablation. Their findings cast doubt on M82 as the prototype of the starburst galaxy since it is optically thin.

Phillips and Mampaso (1989) mapped the $^{12}CO(2-1)$ line. This line is significantly stronger than its $^{12}CO(1-0)$ counterpart and has a differing projected spatial distribution. Much of the optically thin emission appears to be concentrated to the north, the X-ray emission is located to the south and it would appear that the two distributions are occupying differing regions of the source, a configuration that would be difficult to explain in terms of the symmetrical outflow structure proposed by Nakai *et al.* (1987). The nature of the X-ray emission is itself a matter of some dispute. The interior asymmetrically located emission constituting the bulk of the flux has been noted to follow a similar distribution to that of the optical source, suggesting that much of the flux may be emerging from an extensive grouping of massive X-ray binaries and population I stars. They propose a model shown in Fig. 2.8 which builds on that of Rieke *et al.* (1980). The HI toroidal structure is a transient disk of accreted material which, through shock compression by incoming material and subsequent large scale gravitational instability and collapse, gives rise to the present narrowly defined regime of intensive starburst activity. They suggest that accretion of material from an enveloping HI cloud may not only explain the central toroidal disk but through its partial dissociation with the starburst radiation field, together with a high inflow velocity range, low metallicity and low density go some way to explaining the high CO line ratios to the north of the core.

A map of $CS(2-1)$ at high resolution in the centre of the galaxy showed two spatially resolved centres of emission which are part of a molecular ring (Baan *et al.*, 1990). Comparisons of the H_2CO and the CS emissions suggest that the H_2CO emission arises from a region $10'' - 15''$ SW of the nucleus.

Turner, Martin and Ho (1991) mapped M82 in $^{12}CO(3-2)$ and $^{13}CO(3-2)$. These higher rotational transitions are more sensitive to warm gas. The map has two peaks similar to the $J = 1 - 0$ components at $\sim 10''$ NE and $10''$ SW of the centre. High temperatures appear to prevail for molecular clouds within the central 500pc. The total mass of H_2 within the central $44''$ is calculated to be $\sim 8 \times 10^7 M_\odot$, or including He, $10^8 M_\odot$.

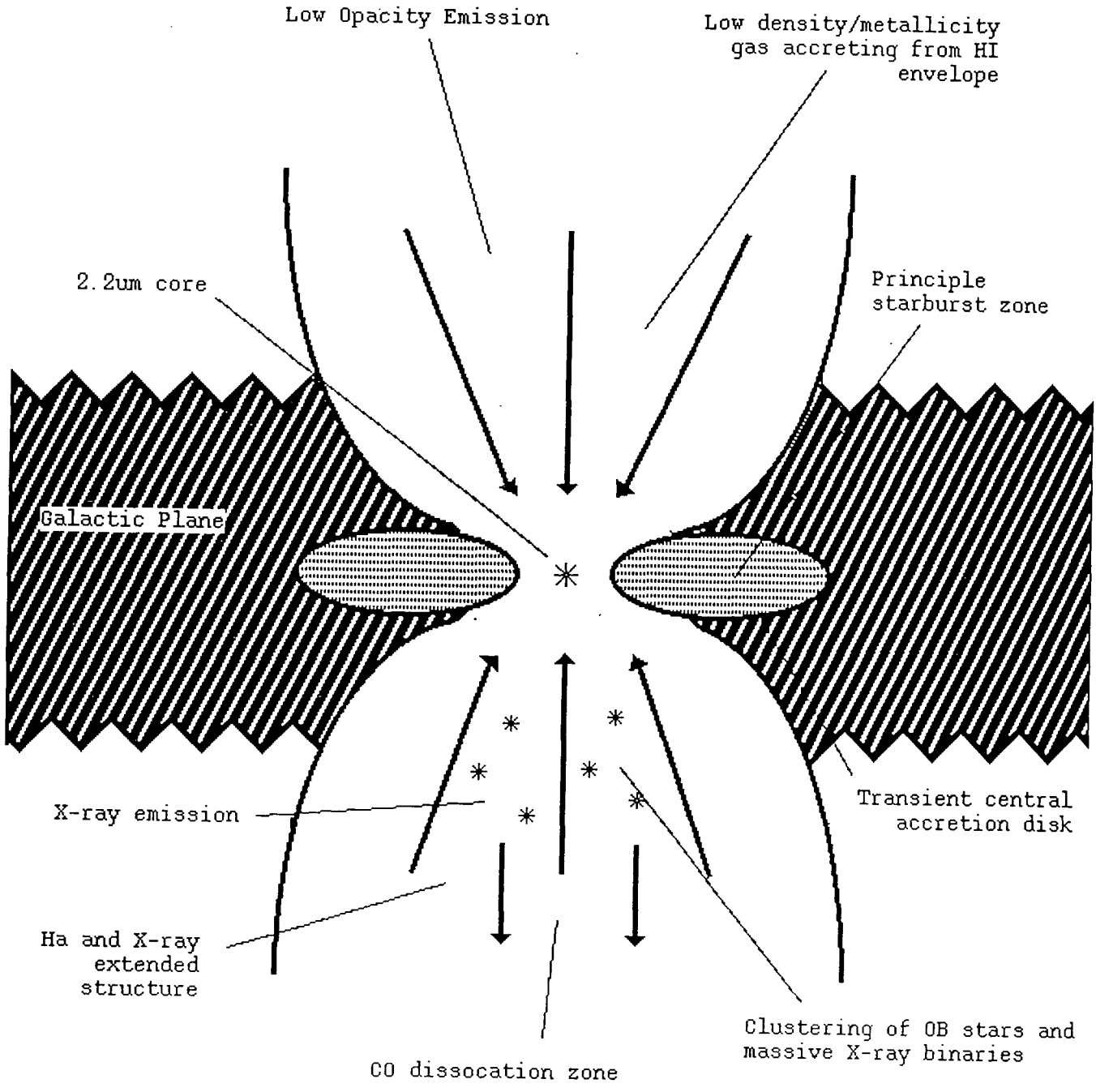

Figure 2.8: The model of M82 suggested by Phillips and Mampaso (1989).

The warm molecular gas is $\sim$ 10% of the total mass within the inner 40″ diameter of M82. An interpretation of this is that the hot gas represents hot cores surrounding a very large number of distributed exciting sources. Sheets and filaments might be believable where the observed wind temperatures and pressures are due to shocks and winds within the starburst. The optical depth of the J = 3 – 2 transition is relatively low.

Wild *et al.* (1992) made a multi-line study of M82 and observed many high-order transitions (Table 2.2). The strong J = 6 – 5 emission clearly indicates the existence of a warm dense molecular gas component in M82 whose large line widths imply that these regions are not confined to a small volume but are distributed throughout M82's nucleus and the gas temperatures are greater than 40K. They find that the ^{12}CO(3 – 2) emission towards the nucleus is weak with respect to the J = 1 – 0 emission. The CO radiation temperature ratios imply that the ^{12}CO emission is optically thick.

Sofue *et al.* (1992) found that the rotation of the molecular disk is Keplerian which suggests the galaxy has no massive halo. The extended molecular halo shows very slow rotation and indicates that the halo gas has been ejected from the central region with conservation of angular momentum.

Atomic carbon has only been found in one other extragalactic object. Schike *et. al.* (1993) have detected it in several places in M82. It is thought to exist primarily in the transition zone between ionized and molecular phases according to current models of photo-dissociation regions. Some of the emission is due to atomic carbon existing within the molecular clouds.

2.9 Millimetre and Sub-millimetre Studies

Sub-millimetre observations trace the distribution of cool dust present in M82. It is generally assumed that this dust component is mixed intimately with molecular gas clouds fueling the extensive star formation and therefore can provide an estimate of the dust mass. The dust may be (i) mixed with the molecular gas, (ii) produced in circumstellar shells of late type giant stars at evolutionary mass loss stages and expelled by strong stellar winds, (iii) condensed out of SN material or (iv) stripped from M81. Calculations of the dust mass vary from $1 \times 10^5 M_\odot$ as a lower limit on the dust mass returned to the interstellar medium in the last 10^8yr (Hughes, Gear and Robson, 1990) to $8.7 \times 10^8 M_\odot$ for the total gas mass in the inner 50″ × 50″ area (Krugel *et al.*, 1990).

Studies at 400μm and 450μm (Jaffe *et al.*, 1984; Smith *et al.*, 1990) found peaks at or near the 2.2μm position. There is no similarity between the distribution of the 9mm emission (Klein, Wielebinski, Morsi, 1988) and the X-ray emission of Kronberg, Biermann and Schwab (1985). The extended emission feature at R.A.(1950) = 9^h 51^m 33^s, Dec.(1950) = 69° 55′ 36″ is roughly coincident with the strongest X-ray source which has been suggested as a blackhole candidate, but this coincidence may be accidental. The 9mm map is in good agreement with 23GHz (1.3cm) map of Kronberg *et al.* (1979).

Most of the 1.3mm flux comes from cool dust in the core of the galaxy (Thronson *et al.* 1989). Smith *et al.* (1990) compared their 450μm map with the ^{12}CO maps. Their map has only one peak, located to the SW of the 2.2μm nucleus, unlike the ^{12}CO maps which show two peaks. They explain their single peak by saying that the two lobes are there but swamped by sub-millimetre emission from the giant star-forming region; some process must be enhancing the ^{12}CO emission in the lobes or depressing it in the interior region. They conclude that the CO and the sub-millimetre emissions cannot *both* be reliable tracers of molecular hydrogen. The intense UV flux in the central starburst region and the detection of CII 158μm emission (Crawford *et al.* 1985) lead them to believe that the CO may originate in warm, dense photodissociation regions at the interface between HII regions and molecular clouds where the gas temperature is much greater than the dust temperature.

Hughes, Gear and Robson (1990) mapped M82 in the central 1kpc at 800μm and 1100μm and found an elongated nucleus with a peak at the 2.2μm nucleus and a halo of dust grains out to 500pc from the plane of the galaxy. The distribution of dust grains in the halo is an important diagnostic of whether inverse Compton scattering emission from far-IR photons scattered off relativistic electrons, or free-free emission from electrons is the dominant process responsible for the X-ray emission. They find that dust grains are transported into the halo along with relativistic electrons, most likely by strong stellar winds from the 10^8 red giants proposed by Rieke *et al.* (1980).

The 450μm data can be compared with the ^{13}CO(2 – 1) data of Loiseau *et al.* (1988) which allows a direct comparison of the molecular gas and the optically thin millimetre/sub-millimetre dust emission. They trace a central clump of gas *and* dust and neither displays the twin peaks of the ^{12}CO. The similarity of the 450 μm structure to the X-ray structure (Watson *et al.*, 1984) suggests that inverse Compton scattering of far-IR and sub-millimetre photons may be an important source of X-ray luminosity. The 1100μm map has a filament extending $\sim$ 600pc south of the galaxy and appears to be

correlated with a strong optical dust lane and an X-ray plume. If the X-ray luminosity is due to inverse Compton scattering of far-IR and sub-millimetre photons from cool dust grains off relativistic electrons in the halo then the need to consider destruction of grains in a hot plasma becomes unnecessary. (Watson *et al.* 1984 thought that the dust and the plasma had to be in different regions, see Section 2.5). They concluded that inverse Compton scattering dominates the X-ray luminosity of M82, particularly in a direction perpendicular to the disk where dust grains are preferentially ejected along the rotational axis of the galaxy where the molecular ring acts as a nozzle.

The close similarity between the spatial distribution of the millimetre and sub-millimetre emission and of the ^{13}CO gas, radio and X-ray continuum emissions demonstrates that the dust distribution is intimately associated with the star-forming nucleus of M82. Sufficient grains are produced in the circumstellar shells of the red giants during a typical starburst episode and are then ejected into the halo. There is some correlation between spur-like features extending perpendicularly out of the plane of the galaxy in the 800μm map and the molecular CO map. This could be the result of "piling up of grains" expelled from the nucleus, adding to a population associated with the molecular ring, to produce the increased column density.

Krugel *et al.* (1990) mapped M82 in 1300μm. They found a pronounced maximum, and a weaker maximum coincident with the 2.2μm peak. There was good agreement between the ^{13}CO(2 - 1) map of Loiseau *et al.* (1988). Carlstrom and Kronberg (1991) obtained high-resolution 3.3mm continuum maps of the central regions of M82. This continuum emission extended for about 35″ along a warped ridge and was similar to results obtained at longer wavelengths such as the nonthermal radio emission and the thermal IR emission. The 3.3mm (92GHz) emission is predominantly free-free emission from evolved HII regions. Most of the neutral gas and dust has been swept into dense shells surrounding the HII regions. The 3.3mm peak coincides with the dense compact recombination line region and with the peak of the far-IR emission. Thus there is substantial star formation over a much larger region than inferred from the optical and X-ray emission. Evidently 'super-bubbles' forming in the outer reaches of the starburst have not yet had time to break out of the plane. This suggests that the starburst has evolved from the core of the nuclear region and is now spreading into the molecular gas at the periphery of the starburst region. Figure 2.9 shows the peaks of the various millimetre and sub-millimetre maps on a Hα contour map of M82.

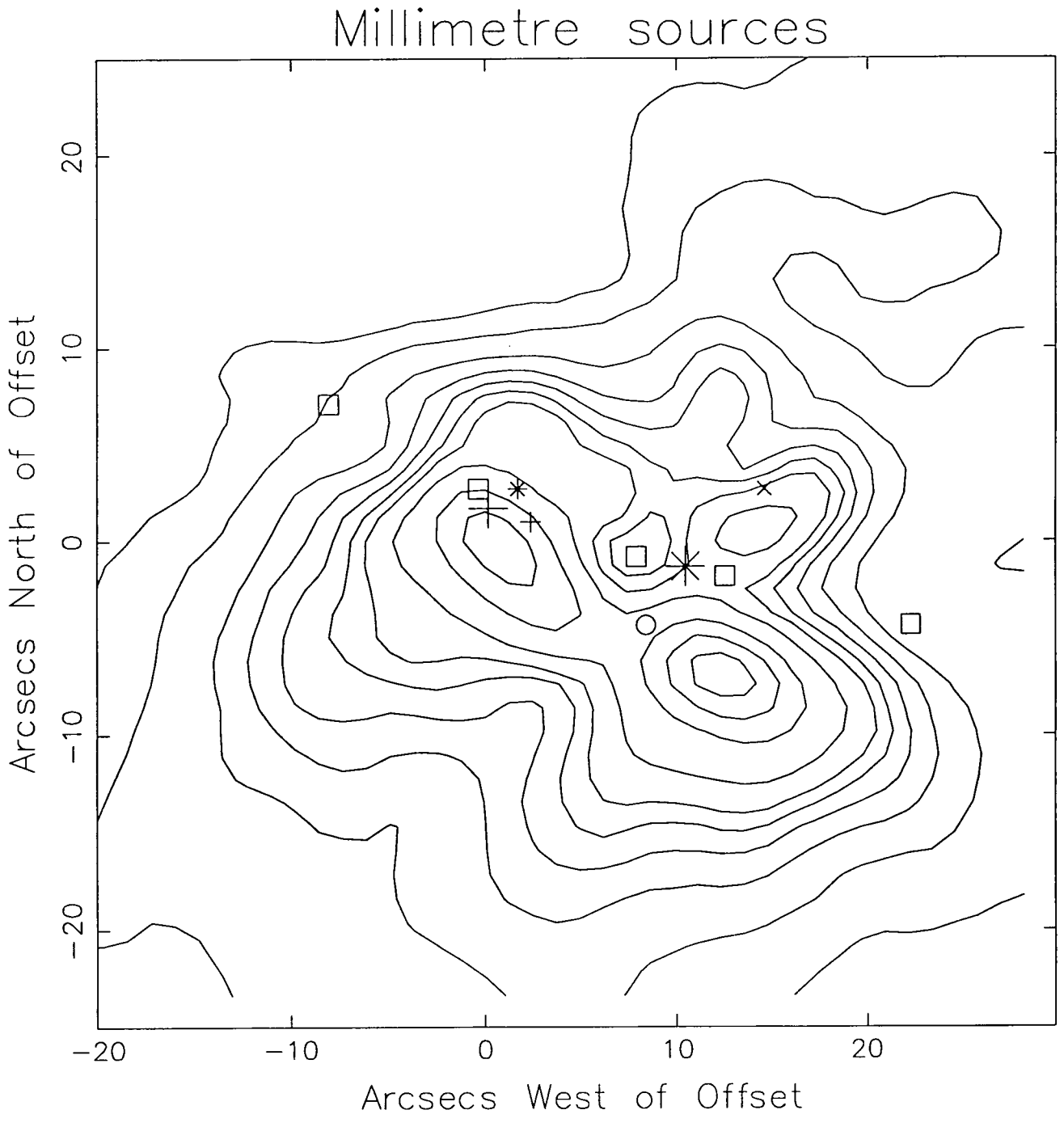

Figure 2.9: A Hα contour map overlaid with millimetre and sub-millimetre features. The 450μm data of Smith *et al.* (1990) is indicated by +. The 1300μm data of Krugel *et al.* (1990) is indicated by o. The 9mm data of Klein *et al.* (1988) is indicated by $\times$. The 3.3mm data of Carlstrom and Kronberg (1991) are indicated by $\Box$. The 800 and 1100μm data of Hughes *et al.* (1990) is indicated by $*$. The 2.2μm data of Rieke *et al.* (1980) is indicated by $+$. SN 41.9+58 of Kronberg and Wilkinson (1980) is indicated by $\ast$.

2.10 Summary

M82 is the classic starburst galaxy with a central star forming region, superwind-blown bubbles along the minor axis and a filamentary halo in Hα. Its polarization pattern shows that in continuum radiation the dusty halo of the galaxy is seen as a giant reflection nebula jointly illuminated by its galactic disk and a central starburst, with a point source illumination within the starburst in Hα.

To summarize the conclusions reached from previous studies, at the centre of M82 lies a region of intense star formation. This starburst nucleus was most probably triggered by infalling gas due to a tidal interaction with M81. Many supernova have, and still are, occurring in this region, throwing off dust and gas which has piled up into a circumnuclear torus. The numerous SN have created a hot cavity in the original molecular disk, now a ring of radius 250pc, as defined by the two main peaks in the CO maps at millimetre wavelengths. The superwind is channelled along the minor axis, blowing the observed bubbles in the galactic dust and gas envelope. These bubbles are hollow with Hα radiation found spectroscopically on their surfaces, the southern-most of which is inclined towards us. There is extended X-ray emission along the southern minor axis which coincides with radio and mid-IR emission. The galaxy appear polarized to quite high levels at optical wavelengths.

Models suggest that the starburst superwind breaks out of the galactic disk giving rise to X-rays and the line emission filaments above and below the plane of the galaxy by collisional shockheating. The starburst core lies in a circumnuclear molecular disk where 10μm, 40μm and Brγ emission are seen in a pair of lobes (possible tangential points to an edge-on ring) flanking the main peak at 2.2μm which is presumably a concentration of stars at the nucleus of the galaxy. The brighter CO peaks are located at larger radii than the IR peaks. The near-IR emission differs from the mid-IR and shows a bar structure, it is similar to the HI opacity. The mid-IR emission is similar to the thermal radio emission. The mid- and far-IR emissions are predominately thermal re-radiation.

The radio emission has a thermal component and lots of non-thermal supernova remnants. The SNRs lie on the southern part of a tilted edge-on ring. The radio halo is comparable in extent with the optical emission and is extended to the SE. No radio polarization is evident. The 3.3mm map is very similar to the 10μm and 6cm maps.

The CO emission has been found to be optically thin unlike any other starburst galaxy. A large fraction of gas inside the circularly rotating ring has been blown out of

the galactic plane by the SNe. The SNR are aligned with the CO axis and the CO peaks near SNR 41.9+58. The CO intensity and the HI column density are very similar. The CO ring is about 400pc in diameter with the $^{13}CO(2-1)$ ring about 470pc in diameter. The stellar bar of K is visible in CO. High density ionized thermal gas coexists with molecular gas. Some CO emission is extended beyond the optical disk. There is an excess in HCO^+ towards the base of the southern optical filaments. The molecular ring exists at higher rotational transitions, indicating temperatures greater than 40K.

Thus we have built up a picture of a very disturbed galaxy at all wavelengths. It has many unusual features including its extremely dusty appearance, the bubbles and the optical filaments along the minor axis, and the many SNRs in its central regions. In the next chapter we will examine optical and spectropolarimetric observations of M82.

Chapter 3

Polarimetric Studies of M82

3.1 Imaging Polarimetry

3.1.1 Introduction and Aims

In this chapter, we will present imaging polarimetry and spectropolarimetry of M82. We are interested in the origin and nature of the polarized light from this galaxy, and in particular the cause of polarized light from the Hα filaments along the minor axis. No other starburst galaxy has such prominent filaments. Some theories suggest that the filaments are illuminated dust that has been blown out of the central star-forming region by numerous supernovae. If the filaments are illuminated blown-out material then we should see polarization of light from the galaxy by scattering off this material, alternatively if the filaments are intrinsically emissive we expect to see little polarization.

3.1.2 Observations

Imaging polarization observations were made on 1990 March 12 – 17 on the William Herschel Telescope on La Palma using the Durham Imaging Polarimeter. The polarimeter (Scarrott *et al.*, 1983; Scarrott 1991) was used with a blue-sensitive coated GEC CCD to make a total of 96 exposures in 4 wavebands. Table 3.1 shows the observations made and the filter responses. Note that the continuum filter is a narrow red continuum filter whose waveband is near that of the Hα filter but does not encompass it. The readout noise of the CCD is typically 7 – 9 electrons per pixel and the effective seeing of the combined data was 2.5 arcseconds. The image scale corresponds to 1.23 arcsecs per pixel.

Filter	B	V	Hα	Continuum
Number of exposures	12	12	36	36
Exposure Time (secs)	600	600	600	600
Peak Response (Å)	4385	5498	6560	6652
Mean wavelength (Å)	4400	5520	6556	6644
Bandwidth FWHM (Å)	1030	860	59	49

Table 3.1: Observation details and filter responses for M82.

3.1.3 Data Analysis

The data were reduced in the standard polarimetry fashion using DIPS, the Durham Imaging Polarimetry Software package. This involved flatfielding the data, aligning the images with each other, estimating the exposure and instrument factors affecting the polarizations and subtracting the background sky component. A detailed discussion of the reduction technique can be found in Warren-Smith (1978), Draper (1988), Scarrott *et al.* (1983) and Scarrott (1991).

When the data had been reduced to give files for each waveband containing all the information necessary to calculate the Stokes vectors for each pixel of the detector, the red continuum C, was subtracted from the Hα plus continuum, Hα+C, to leave the Hα only. This was done by dividing Hα+C data by the C data to calculate a scale factor, taken in the main body of the galaxy disc and not including any part of the filamentary system. This scale factor was applied to each frame of the continuum data before it was subtracted from the Hα+C data. Note that the Hα filter is 59Å wide at FWHM and includes two NII lines. The NII lines contribute less that 40% of the total intensity recorded in the Hα filter.

The arcsecs/pixel scale was calculated using the Right Ascensions and Declination's of stars in the field of M82, and was found to be 1.23″/pix. From these star positions and the image scale, an offset was chosen, Knot A of O'Connell and Mangano (1978), R.A.(1950) = $9^h\ 51^m\ 43.93^s$, Dec.(1950) = 69° 54′ 59.3″, which appears as the left hand bright spot in the very central regions of the galaxy. All maps have North at the top and East at the left unless otherwise indicated, and positions are given in arcseconds North and West of the offset point. Because of the two channel nature of the polarimeter, the light from the bright star BD70578 to the SW of the galaxy has scattered off the grid

edges onto some of the image planes.

To calibrate the data, profiles were taken in the B and V wavebands along the minor axis, passing through Knot A of O'Connell and Mangano (1978), in 12.3″ bins. The intensity in arbitrary units, I, was changed to relative magnitudes by taking $M = -2.5 \times \ln(I)$. These magnitude profiles were compared with those of Artomonov (1978). He had obtained photometric profiles of M82 along the minor axis through the optical bright spot (Knot A). Although there is uncertainty in the size of aperture used to measure his profiles, a comparison was made between the two profiles and is shown in Figs. 3.1a and b. The profiles in Fig. 3.1a are those of the B waveband and those in Fig. 3.1b are of the V waveband. Scaling factors were applied to the B and V data and thus we obtain calibrated intensity maps of the galaxy in these wavebands. From these we can calculate a scale height of 1kpc for the disk of M82 which compares with a value of 1.8kpc calculated by Chesterman and Pallister (1980) and a value of 1kpc calculated by Solinger and Markert (1975).

3.1.4 Results

Figure 3.2 shows a contour map of the B waveband overlaid with a map of the polarization vectors. The polarization pattern is elliptical with increasing polarization as one gets farther from the galaxy. The minor axis of the galaxy appears to be more polarized than the other regions with values of around 40% being reached at about 50″W, 80″N of the centre (about 90″ along the minor axis to the SE of the galaxy.)

Figure 3.3 shows a contour map of the V waveband overlaid with a map of the polarization vectors. This also has an elliptical polarization pattern with features similar to the B waveband map. but the polarization is slightly less, reaching 30% along the SE part of the minor axis.

Figure 3.4 shows a contour map of the red continuum waveband overlaid with a map of the polarization vectors. Again this has an elliptical pattern with higher polarization values along the minor axis. Figure 3.5 shows a contour map of the red continuum plus Hα waveband overlaid with a map of the polarization vectors. The contour image shows the galactic disk, as seen in the C image, but there is an additional component along the minor axis, the Hα filaments. The polarization pattern is elliptical with a strong component along the minor axis.

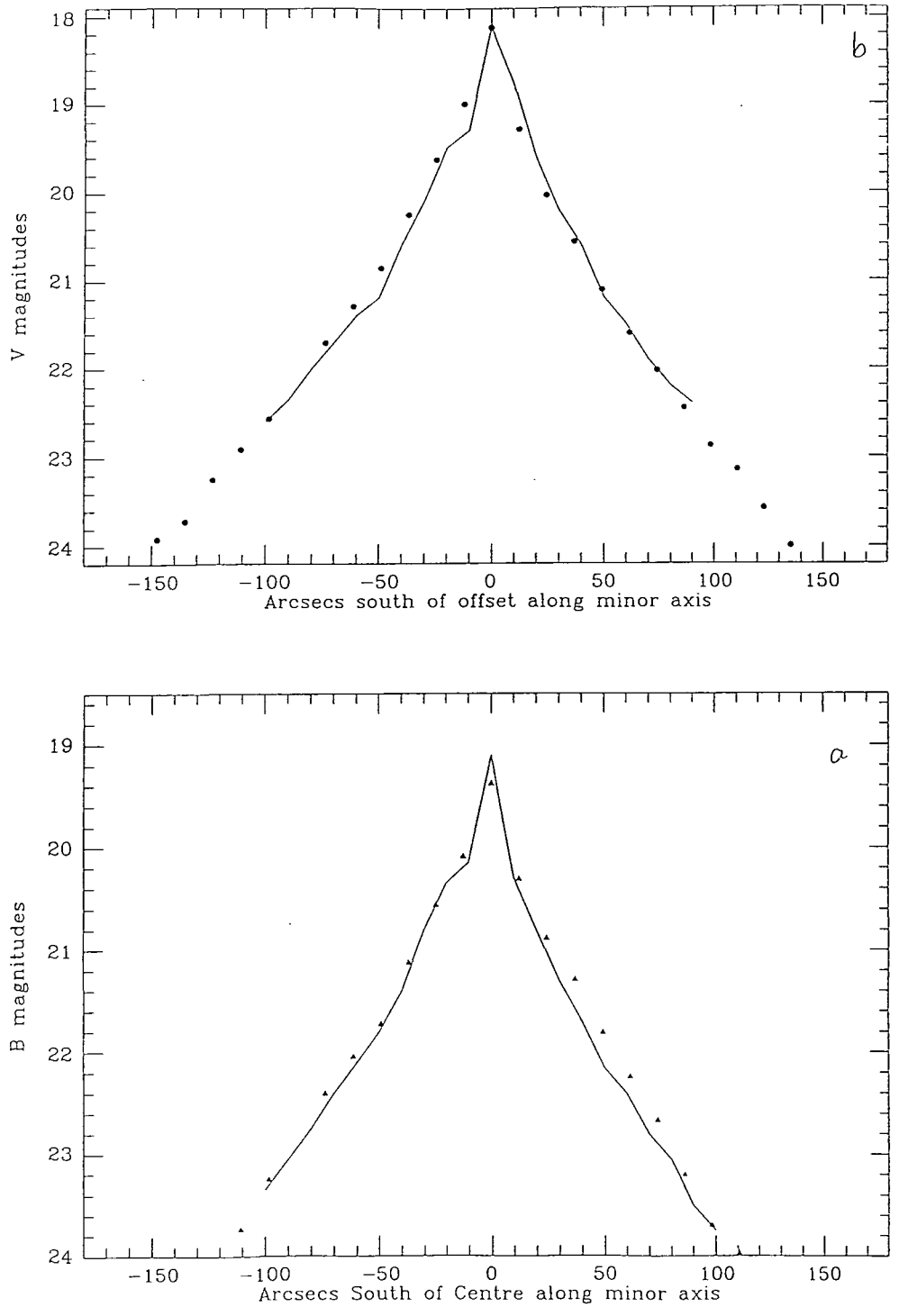

Figure 3.1: (a) The calibration curve of Artomonov (1978) in the V waveband is indicated by the solid line. The circles show the magnitudes of our data having applied a scale factor to them. (b) The calibration curve for the B waveband. The triangles indicate our data.

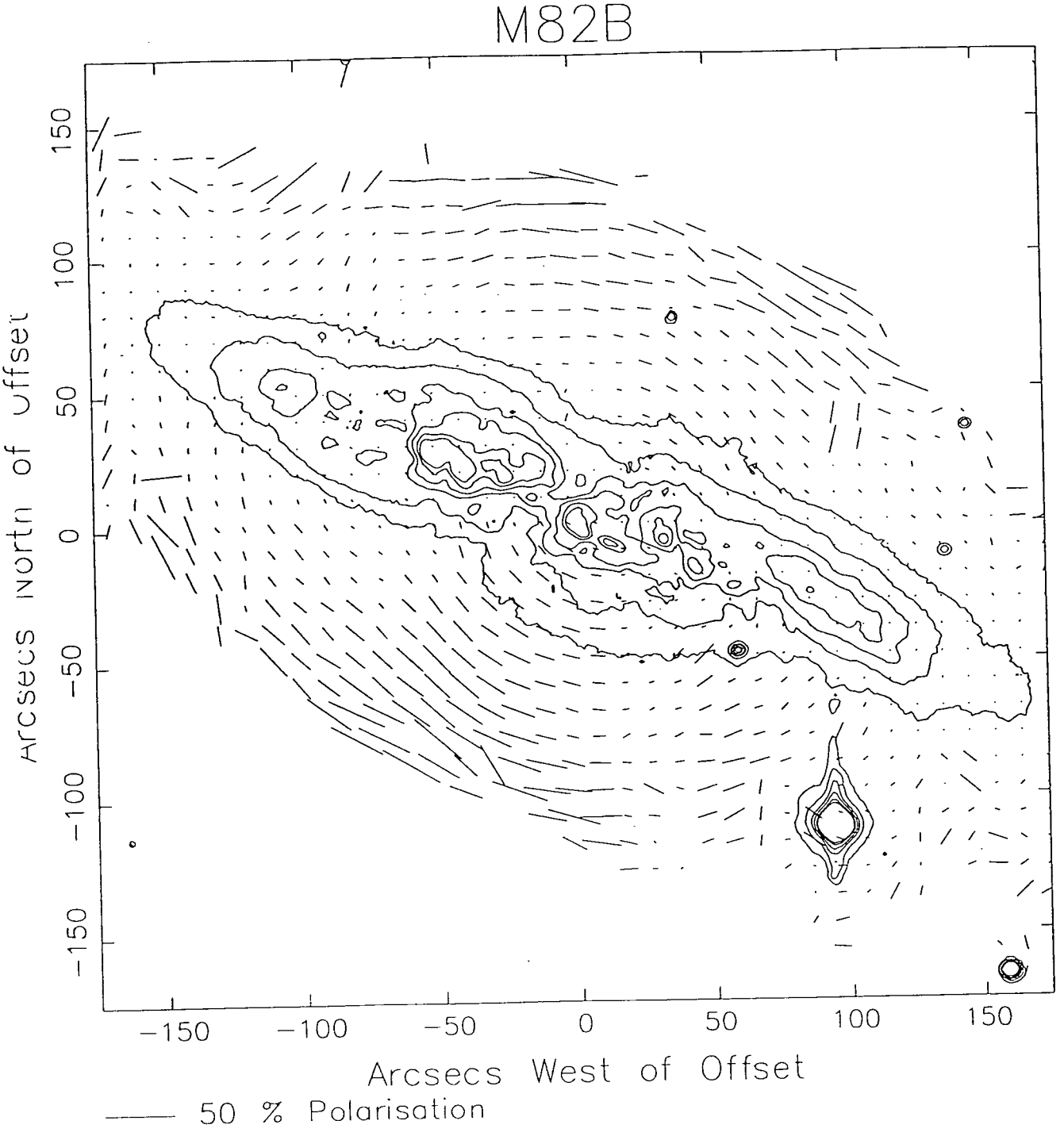

Figure 3.2: A contour map of M82 in the B waveband overlaid with a map of the polarization vectors calculated in 10 by 10 pixel bins, moved 8 by 8 pixels.

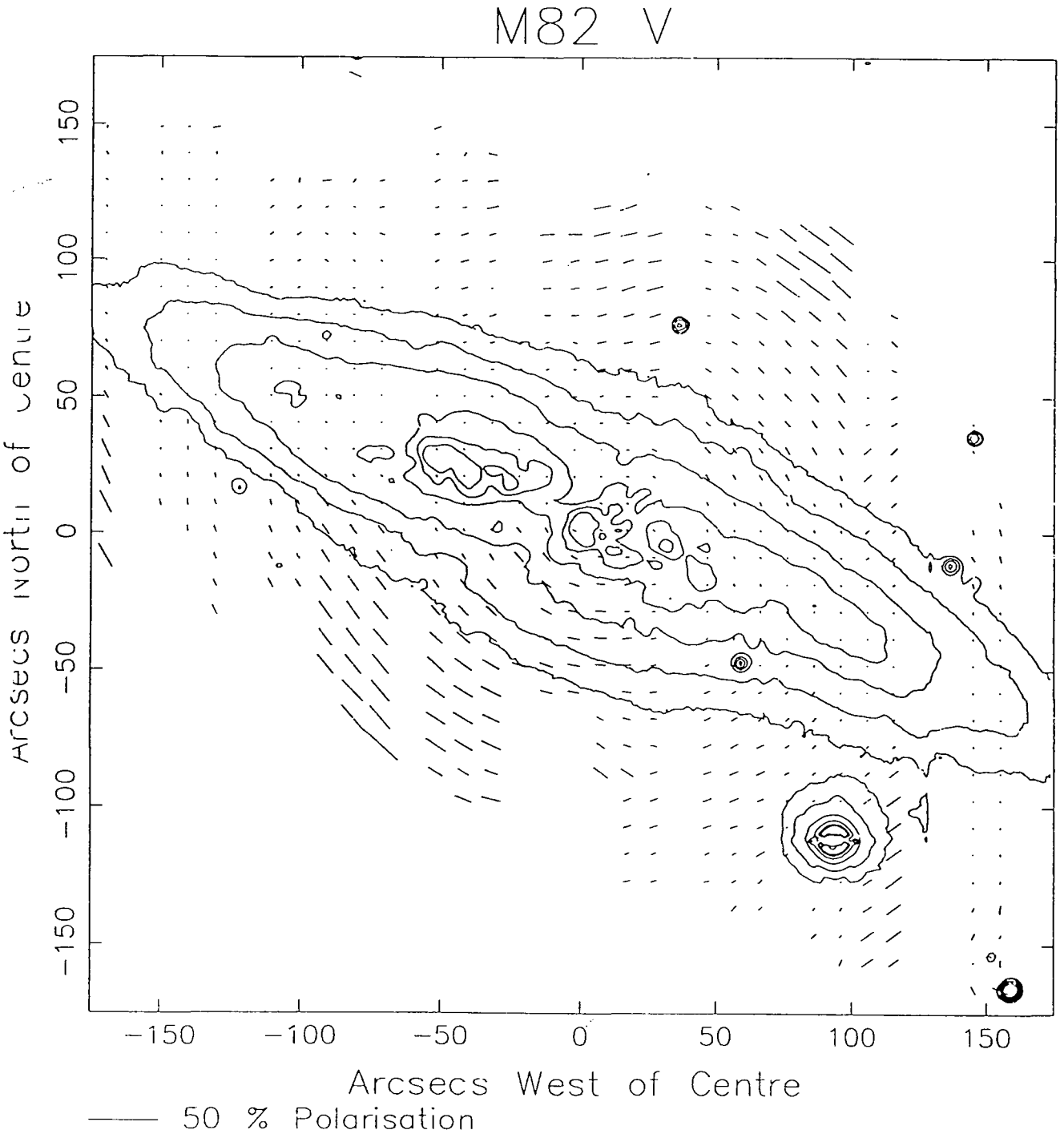

Figure 3.3: A contour map of M82 in the V waveband overlaid with a map of the polarization vectors calculated in 10 by 10 pixel bins, moved 8 by 8 pixels.

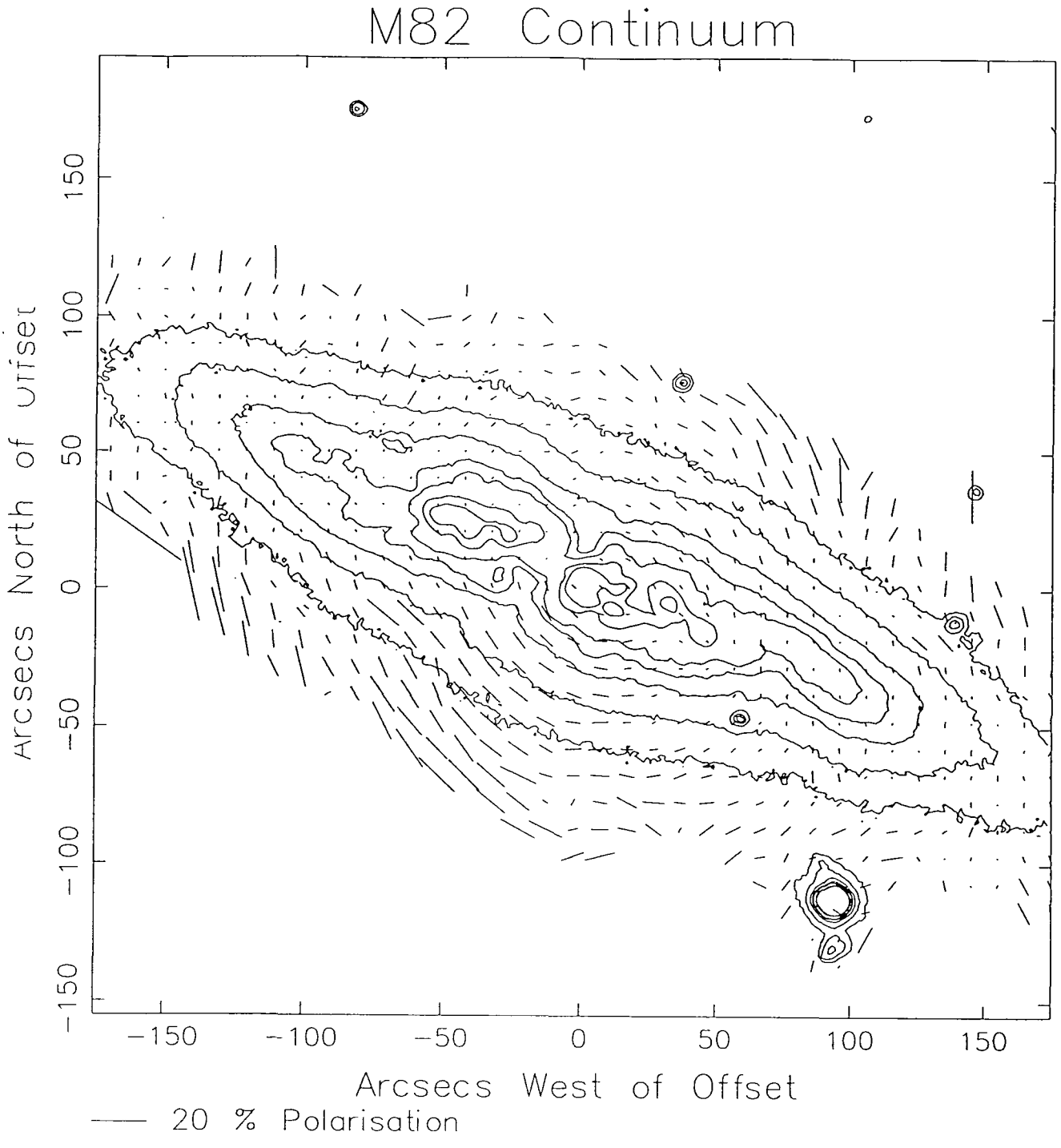

Figure 3.4: A contour map of M82 in the C waveband overlaid with a map of the polarization vectors calculated in 10 by 10 pixel bins, moved 8 by 8 pixels.

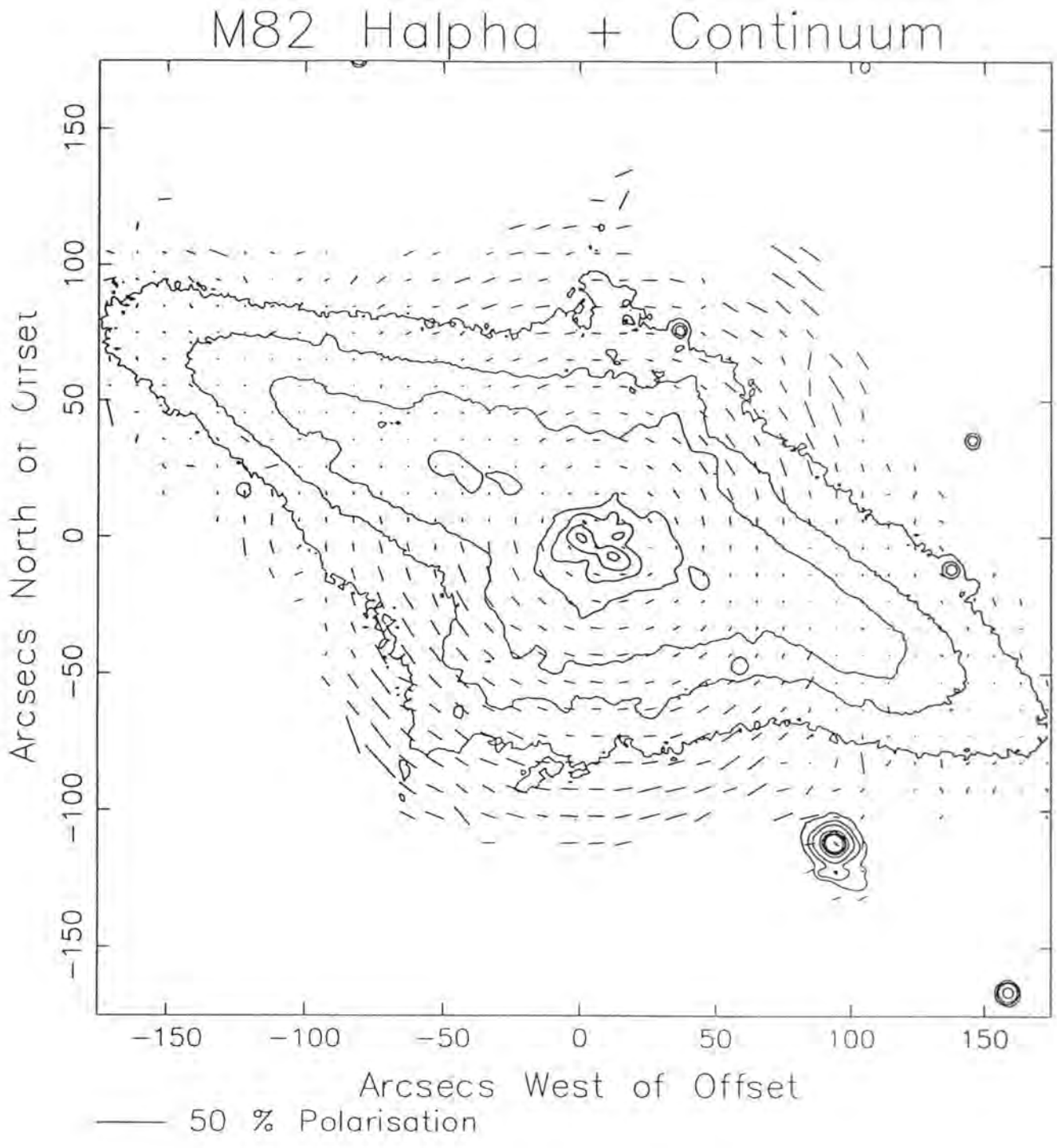

Figure 3.5: A contour map of M82 in the Hα plus continuum waveband overlaid with a map of the polarization vectors calculated in 10 by 10 pixel bins, moved 8 by 8 pixels.

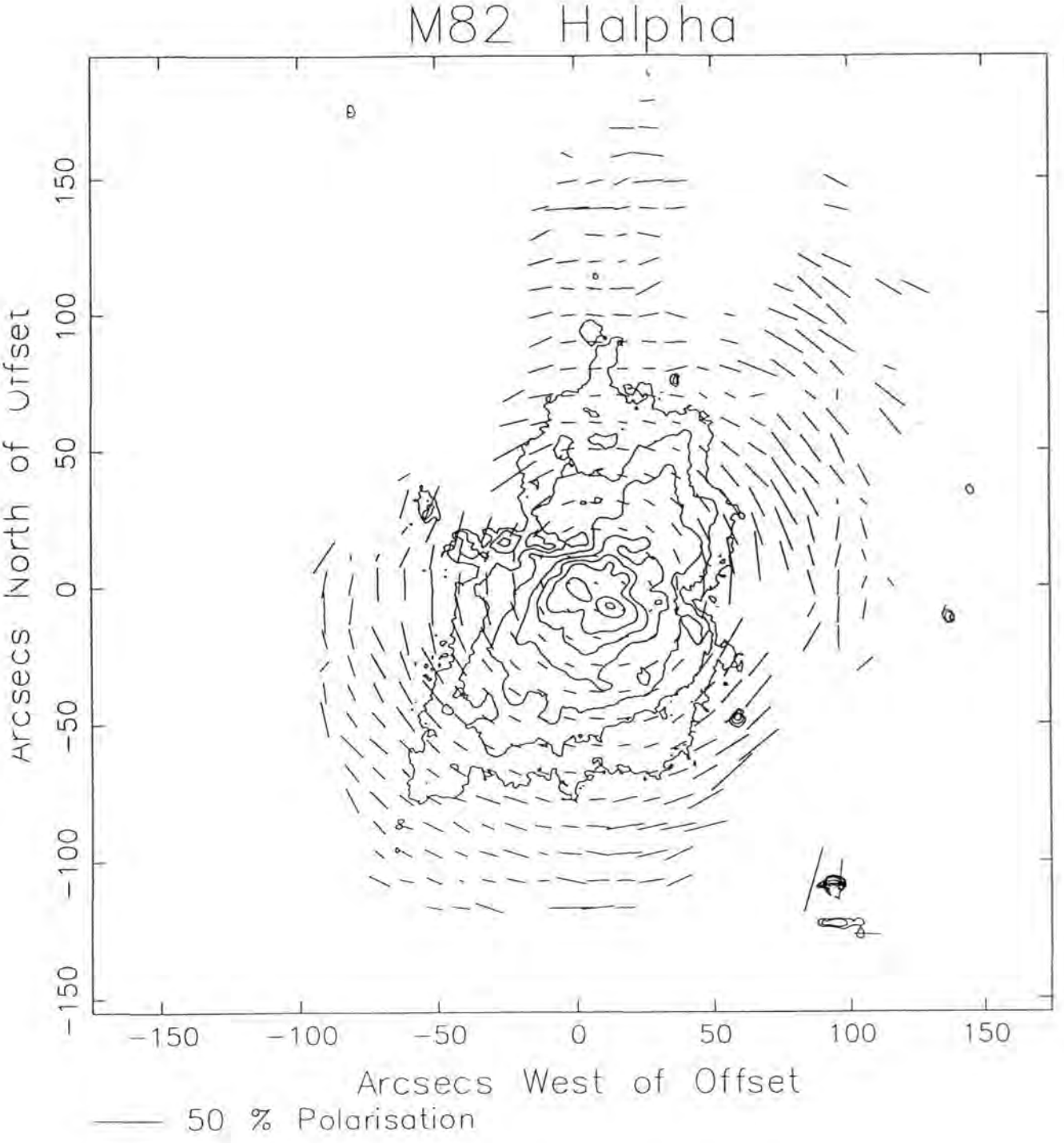

Figure 3.6: A contour map of M82 in the Hα waveband only, overlaid with a map of the polarization vectors calculated in 10 by 10 pixel bins, moved 8 by 8 pixels.

	Ellipse			Normals	
Filters	X_{cen} (pix)	Y_{cen} (pix)	Ellipticity	X_{cen} (pix)	Y_{cen} (pix)
B	173 ± 8	180 ± 5	0.5	172	180
V	172 ± 8	172 ± 8	0.7	171	175
Hα	174 ± 8	171 ± 5	1	173	171
C	170 ± 10	169 ± 12	0.7	172	171

Table 3.2: Centre of polarization pattern calculated by ellipse fitting and by projection of normals.

Figure 3.6 shows a contour map of the Hα waveband only, overlaid with a map of the polarization vectors. The Hα contour image shows that the emission is bipolar in nature with the filaments apparently blown out from the centre. The polarization pattern is circular with values of up to 30% out to 100″. There is little Hα emission from the disk of the galaxy, the majority being confined to the centre and the minor axes. The Hα data were previously presented in Scarrott, Eaton and Axon (1991) but was also reduced by the author for comparison with the rest of the data.

Ellipticity

Two methods were used to calculate the centre of the pattern of polarization vectors. One involved projecting normals from the polarization vectors and calculating their point of intersection, since for polarization by scattering the polarization angle is always normal to the point of origin of the scattered light. The other method involved using a computer program which connected the polarization vectors of a map together to make contours of an elliptical nature. The ellipticity of these contours were then compared to modelled ellipses. The model ellipses were fitted to the data curves by varying their centre and the degree of ellipticity and the best-fit was calculated by minimising a χ-square value calculated by a NAG routine. This was carried out for each wavelength. The Hα pattern was found to be circular, the others having varying degrees of ellipticity, as indicated in Table 3.2. No errors are available for the normals method, but it can be seen that both methods give results which agree well with each other. The change in ellipticity with wavelength reflects the different contributions from the disk and nuclear components.

Wavelength Dependence

A wavelength dependence study of the polarization of M82 was previously carried out by Chesterman and Pallister (1980), as described in Chapter 2. To compare our measurements with theirs, the percentage polarization was measured along the minor axis in 12.3″ (10 pixel) circular apertures, crossing through the centre of the polarization pattern. This was done in the B, V and C filters. Figure 3.7 shows the wavelength dependence of the polarization along the minor axis of M82 and Fig. 3.8 shows where these points were taken on the V waveband intensity map. It can be seen that the polarization on the SE side of the galaxy is greater than that on the NW side in all wavebands. The B polarization is greater than the V polarization which is greater than the C polarization out to 100″ (1.5kpc). No evidence was found for wavelength dependence along the major axis of the galaxy.

Chesterman and Pallister (1980) also found the SE side to be more polarized than the NW side, and the percentage polarization in the B waveband, $P_B(\%)$, to be greater than the percentage polarization in the R waveband, $P_R(\%)$, on the SE side. They proposed a tilted disk model, the essence of which is as follows. Polarized light due to scattering from the southern side of the galaxy can reach the observer directly. Polarized light from the northern side of the galaxy must travel through the disk of the galaxy before reaching the observer and will be attenuated. Light emitted by the galaxy reaches the observer unattenuated from both sides. The addition of redder light intrinsic to the disk leads to the fall off in polarization towards longer wavelengths. Figure 3.9 shows the tilted disk model.

Defining the subscripts as follows, N = North, S = South, I_P = polarized intensity, I_T = total intensity, P = percentage polarization, I_H = intensity component due to scattering before attenuation (from the halo) and I_D =intensity component due to disk, they defined

$$t = \frac{I_{PN}}{I_{PS}},$$

$$b = \frac{I_{TN}}{I_{TS}} = \frac{tI_H + I_D}{I_H + I_D}.$$

If $f = I_D/I_H$, the ratio of disc to scattered intensity, we find

$$b = \frac{t+f}{1+f} \Rightarrow f = \frac{b-t}{1-b}.$$

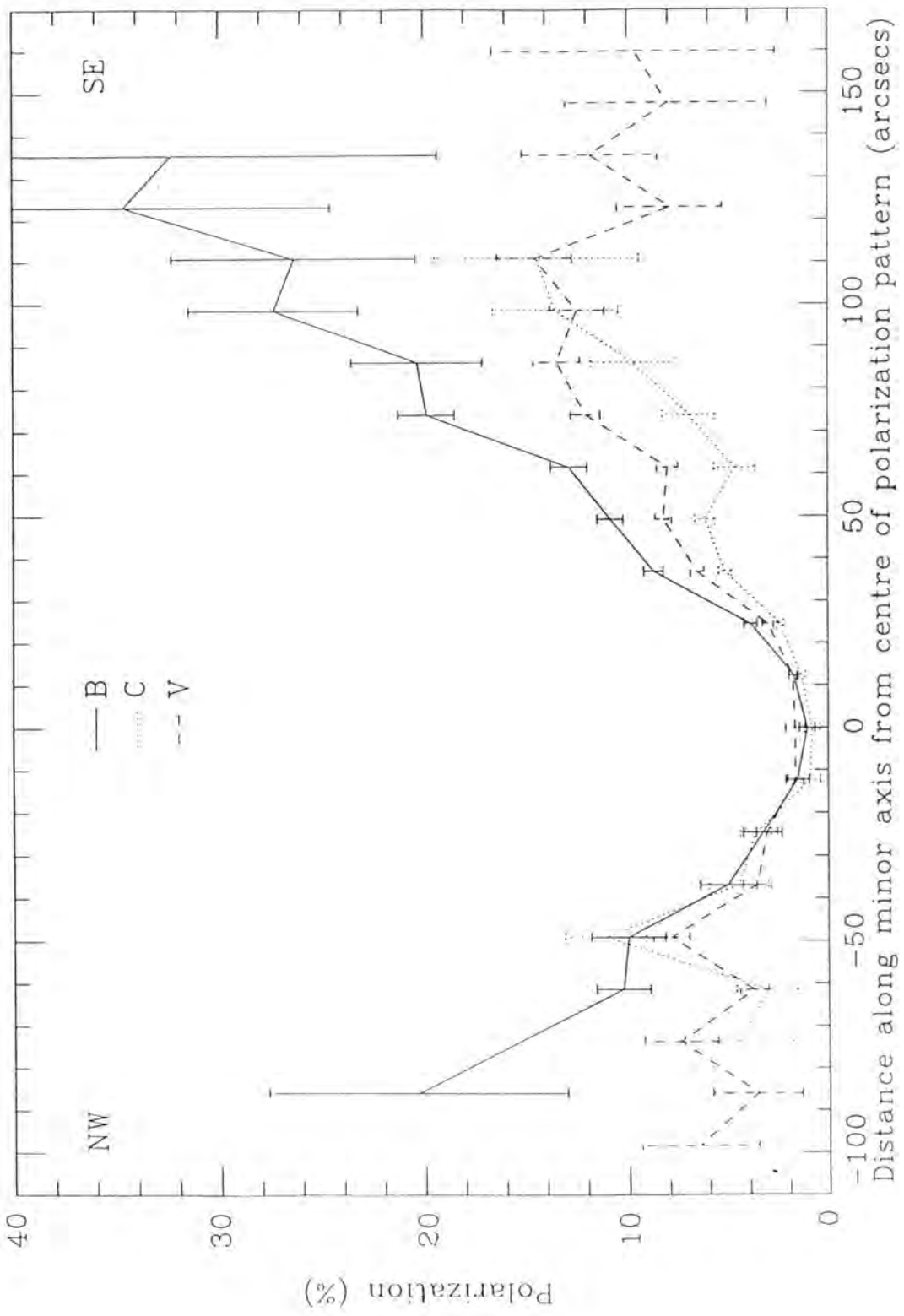

Figure 3.7: Wavelength dependence of polarization along the minor axis of M82 in B, V and C wavebands.

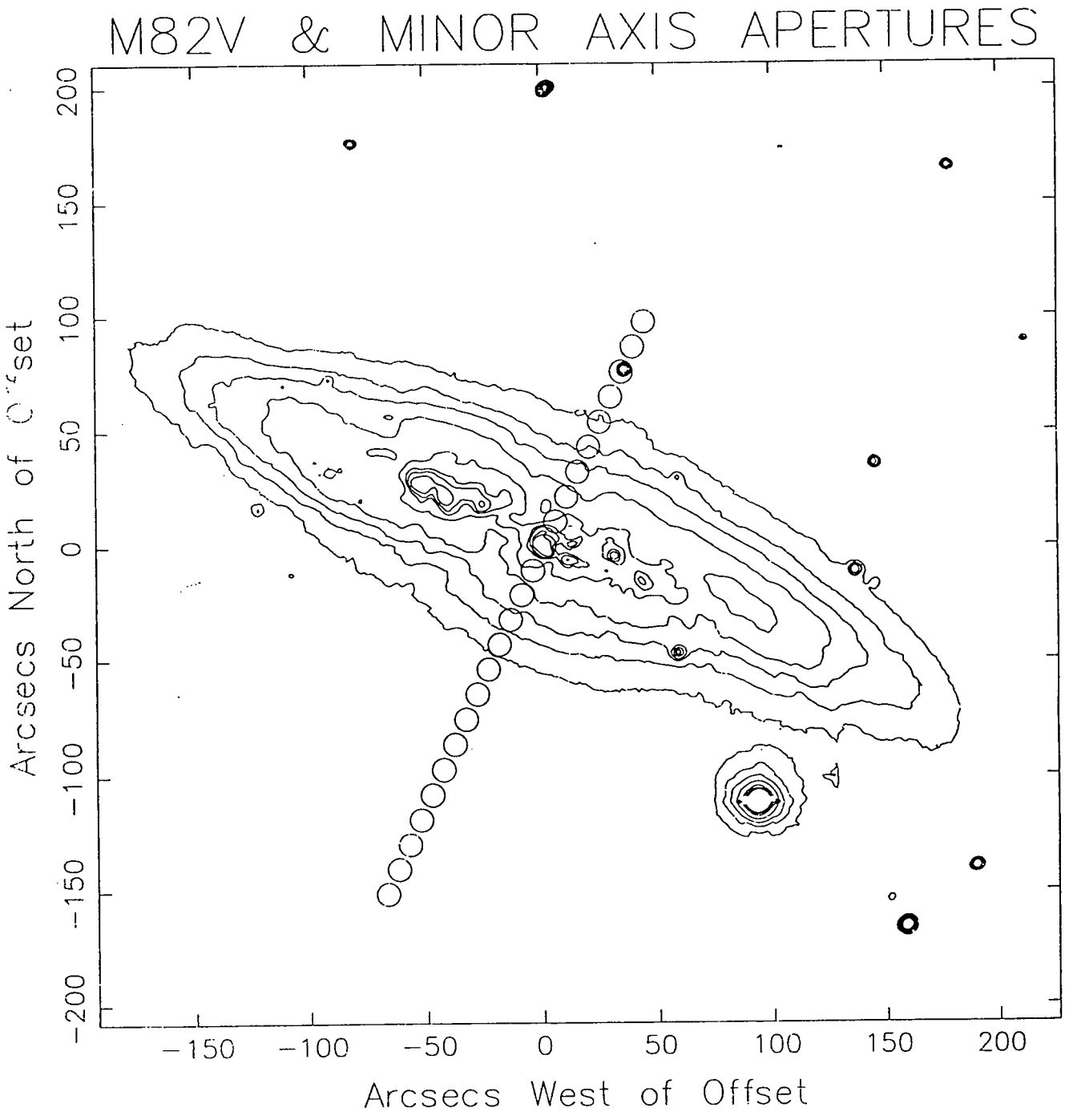

Figure 3.8: A contour image of the V waveband overlaid with the positions of the apertures used to measure the polarizations shown in Fig. 3.7. The apertures shown are circular and 12.3″ in diameter.

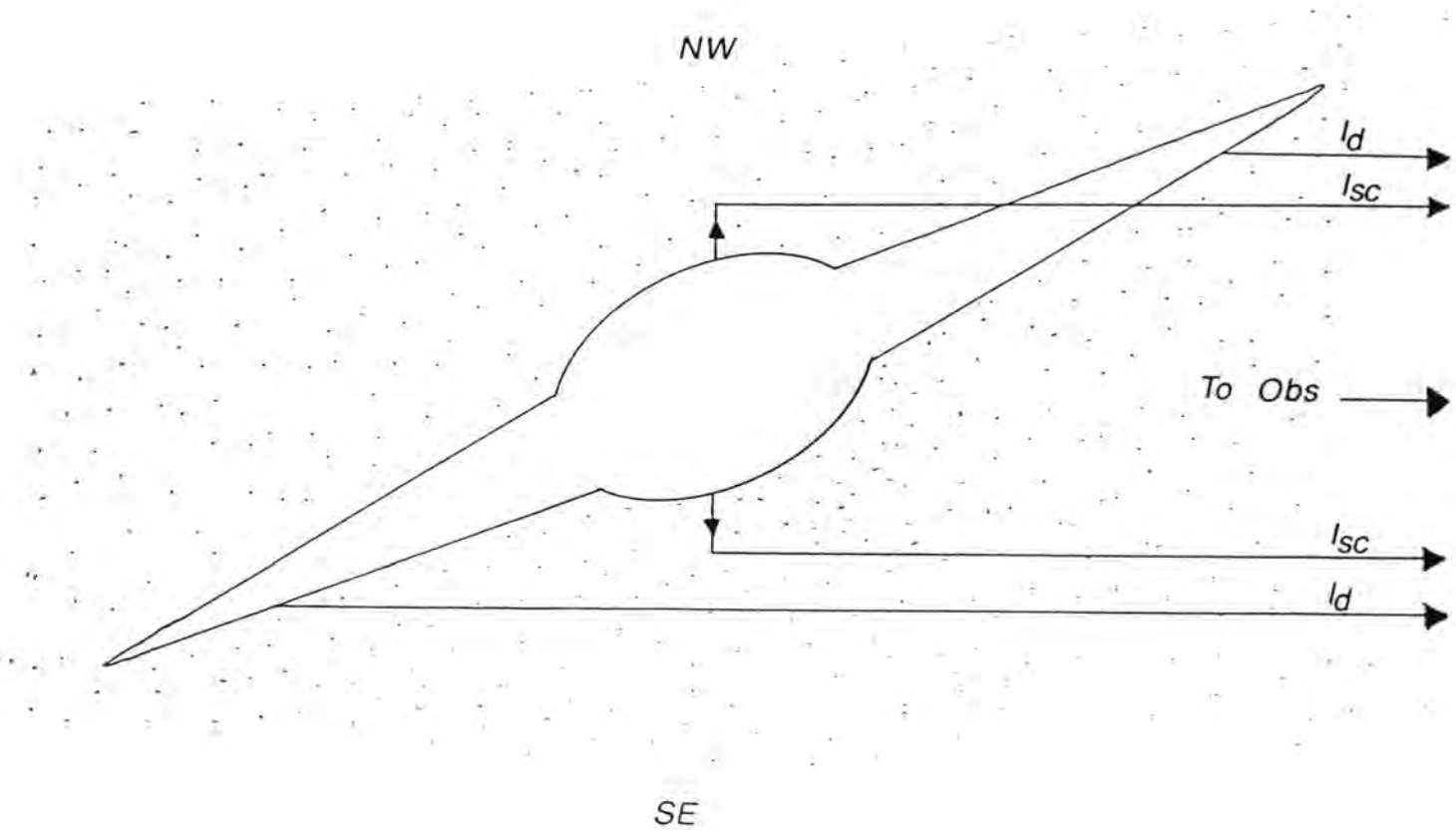

Figure 3.9: A schematic diagram of the tilted disk model of Chesterman and Pallister (1980). I_d is the disk intensity and I_{sc} is the scattered intensity.

Dist. along minor axis (arcsec)	$t = PI_N/PI_S$ [1]			$f = (b-t)/(1-b)$ [2]			$P_H = P_S \times (f+1)$ [3]			τ [4]		
	B	V	C	B	V	C	B	V	C	B	V	C
12.3	0.51	0.77	0.70	1.31	1.13	1.18	20.2 ± 1.1	14.0 ± 0.7	11.2 ± 0.7	0.20 ± 0.03	0.11 ± 0.01	0.16 ± 0.03
24.6	0.17	0.23	0.24	2.06	7.84	1.93	33.2 ± 2.0	72.9 ± 4.9	18.0 ± 1.5	0.77 ± 0.27	0.64 ± 0.19	0.62 ± 0.31
36.9	0.21	0.39	0.35	2.09	1.70	1.80	39.8 ± 2.8	21.7 ± 1.4	13.1 ± 2.9	0.68 ± 0.26	0.41 ± 0.11	0.46 ± 0.27
49.2	0.26	0.47	0.90	2.40	1.68	1.15	67.6 ± 5.3	32.2 ± 2.0	15.0 ± 3.1	0.59 ± 0.18	0.33 ± 0.06	0.05 ± 0.01
61.5	0.42	0.48	0.72	1.84	1.66	1.53	57.7 ± 9.8	35.8 ± 3.1	24.7 ± 5.8	0.38 ± 0.12	0.32 ± 0.07	0.14 ± 0.05
73.8	0.75	1.13	1.31	1.25	0.84	0.47	61.4 ± 10.1	22.9 ± 2.7	19.9 ± 11.1	0.13 ± 0.04	-0.05 ± 0.007	-0.12 ± 0.03
86.1	1.99	0.96	0.73	0.76	1.01	1.11	46.5 ± 11.7	29.2 ± 3.8	30.5 ± 10.9	-0.30 ± 0.07	0.02 ± 0.004	0.14 ± 0.08
98.4	—	2.53	—	—	0.09	—	—	8.6 ± 58.5	—	—	-0.40 ± 0.16	—
110.7	1.11	0.47	—	0.86	1.99	—	60.0 ± 44.7	35.3 ± 10.9	—	-0.04 ± 0.02	0.33 ± 0.22	—
123.0	—	1.43	—	—	0.44	—	—	11.6 ± 41.3	—	—	-0.15 ± 0.11	—
	B		R	B		R	B		R	B		R
30	0.33		0.30	2.6		6.9	27		47	0.49		0.52
60	0.22		0.35	1.1		2.9	33		37	0.65		0.46
90	0.25		—	0.44		—	35		—	0.6		—

Table .3: Parameters relating the tilted disc model at various distances along the minor axis from the optical centre. The upper part of the table refers to this work, the lower part to the results of Chesterman and Pallister (1980).

[1] $t = PI_N/PI_S$, the fraction of light transmitted by the disc.
[2] $f = (b-t)/(1-b)$ where $b = I_N/I_S$; the ratio of disc intensity to scattered intensity on the SE side.
[3] $P_H = P_S \times (f+1)$, percentage of the scattered component of light.
[4] $t = \exp(-\tau')$; $\tau = \tau'/\alpha$; $\alpha = 2.3$.

The optical thickness of the disk, τ' is given by $\tau' = -\ln(t)$, and the optical thickness of the disk normal to its plane is $\tau = \tau'/\alpha$, where α is a factor by which the optical thickness in increased when light is transmitted obliquely. For spiral galaxies of types Sa – Sd, they chose the mean α to be 2.3, and assumed it is constant over wavelength.

The degree of polarization of scattered light before dilution by the halo P_H, can be calculated by

$$P_H = P_S.\frac{I_{TS}}{I_{HS}} = P_S.\frac{I_{DS} + I_{HS}}{I_{HS}} = P_S.(f + 1).$$

Thus, by measuring the intensity, polarized intensity and polarization of the galaxy at equal distances north and south of nucleus along the minor axis we can calculate the optical thickness and the degree of polarization before dilution by the halo. The calculations of Chesterman and Pallister (1980) are compared with ours in Table 3.3. They did not find any variation in optical thickness τ along the minor axis in either waveband, nor did they find any change with wavelength. However, they only had three data points with which to test their models. We find that τ decreases with distance along the minor axis in all colours, and it also decreases as wavelength increases over the 0 – 60″ range. Figure 3.10 shows the variation of τ with distance along the minor axis in the B, V and C wavebands.

Chesterman and Pallister found that P_H in the B waveband increases from 27% to 34.5% between 30 – 90″ and we find it increases from 33% to 46% between these distances. They compared this to light from an extended source, scattered from an large optically thin cloud of Rayleigh scatterers, which will have a polarization value of 33%. They also found P_H in the R waveband decreases from 47 to 37% between 30 – 60″ although they suggest that it may not differ significantly from P_H in the B waveband due to the uncertainties in their measurements. We find it increases from 18% to 24% between these distances.

3.1.5 Discussion

Since the Hα polarization pattern looks similar to that expected from scattering of light from a bright source in a cloud of dust grains, we do not expect to see wavelength dependence of the polarization. If Rayleigh scattering is the polarizing mechanism then blue light is more efficiently scattered than red light by the dust grains, with a dependence

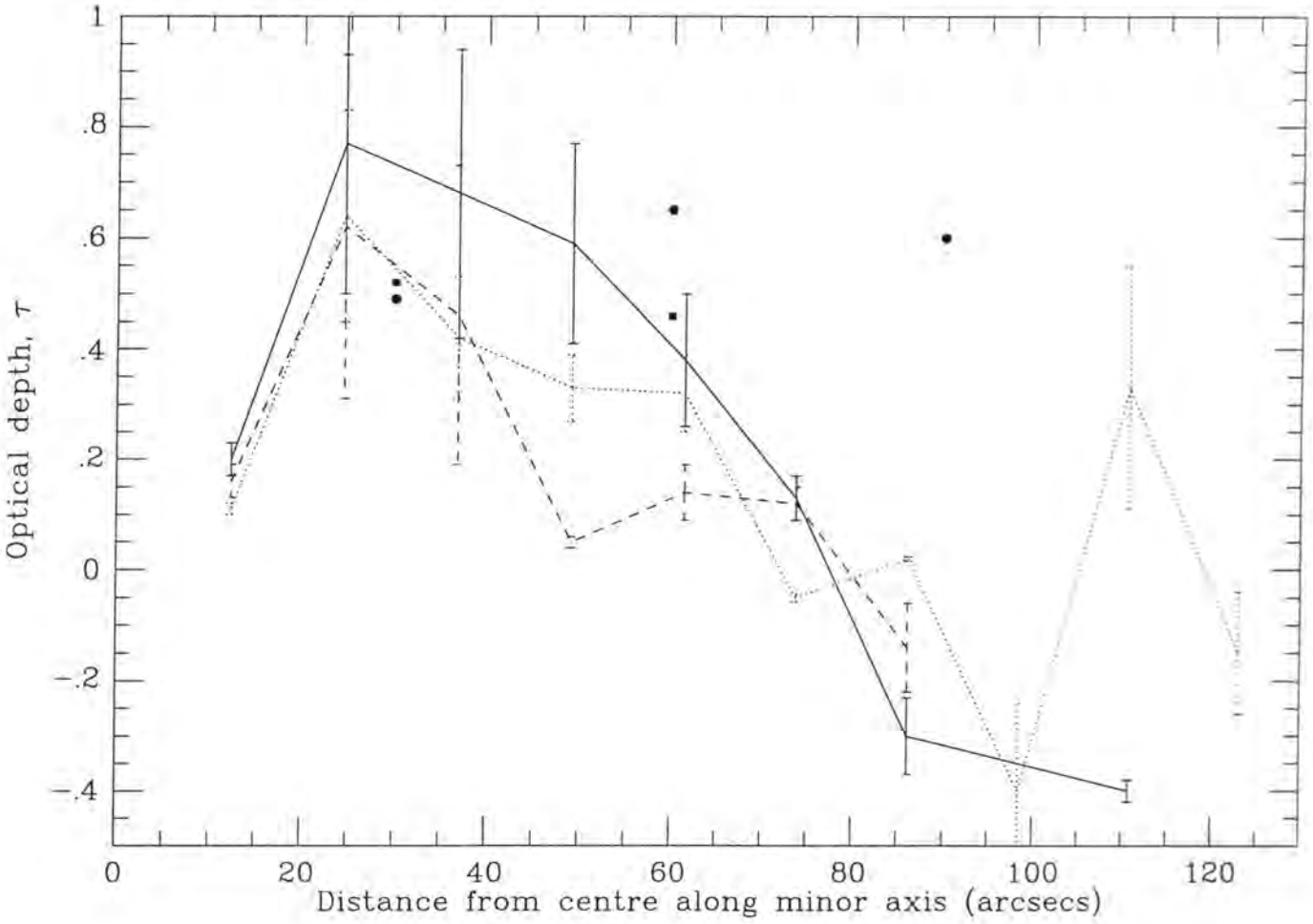

Figure 3.10: Variation of optical thickness τ with distance from the centre of the galaxy, for B, V, and C wavebands. B is indicated by the continuous line, V by the dotted line and C by the dashed line. The B points of Chesterman and Pallister (1980) are indicated by squares and the R points by circles.

that goes as $1/\lambda^4$, but the degree of polarization is the same for all wavelengths. This means that although we see a lower intensity of red light it has the same polarization value as the blue light. In theory this polarization value can reach a maximum of 100% for a scattering angle of 90 degrees, but a more realistic value is about 33% for summing through an infinite cloud of scatterers. For Mie scattering, in general, a wavelength independence of polarization implies a power law distribution of grain sizes (Warren-Smith, 1978).

We must explain the wavelength dependence in a manner that does not involve the scattering. Looking at Fig. 3.7, we see that the wavelength dependence occurs on the southern side of the galaxy only. We have clear evidence of dependence between 20″ – 80″ along the southern minor axis. If the blue and red light are polarized in the same way then the red light must be diluted in some way. Chesterman and Pallister (1980) suggest that the addition of redder light emitted by the galactic disk leads to the fall off in polarization towards the longer wavelengths.

Solinger, Morrison and Markert (1977) modelled M82 as a luminous galactic disk with a bright nuclear source in a cloud of optically thin Rayleigh scatterers. Perkins (1978) also used this illuminating arrangement with a cylinder of dust grains surrounding the galaxy. These models were made before the advent of the superwind theory so any future modelling must take into account the hollow cavities blown into the dust halo, and the scattering geometry this entails. New light is shed upon this scattering geometry by examining the spectrum of the galaxy in polarized light.

3.2 Spectropolarimetry

3.2.1 The aim of the spectropolarimetric observations

Spectropolarimetry helps to distinguish between different polarizing mechanisms occurring in an object. If line and continuum polarizations and polarization angles are the same then both types of radiation travel similar lightpaths and undergo similar scattering or attenuation. Dichroic absorption or scattering of radiation are the most likely mechanisms which have similar line and continuum polarizations, with the absorption and/or scattering taking place outside the line-emitting region. If the line and continuum polarizations are different then either they are produced by different sources or the continuum

Object	HWP Position (degrees)	No. exposures × Length of exposure (secs) Feb 18–19 and Feb 23
M82	0	2 × 900 and 2 × 900
	45	2 × 900 and 1 × 1800
	90	2 × 900 and 2 × 900
	135	2 × 900 and 1 × 1800
Sky	0	2 × 900 and 1 × 900
	45	2 × 900 and 1 × 1800
	90	1 × 900 and 1 × 900
	135	1 × 900 and 1 × 1800

Table 3.4: Spectropolarimetric observations of M82.

radiation undergoes absorption and/or scattering in a manner different from that for the line radiation.

3.2.2 Observations

Spectropolarimetric observations of M82 were made on 1991 Feb 18, 19 and 23 using the ISIS Spectropolarimeter on the 4.2m William Herschel Telescope, La Palma. The red-arm EEV P88200 CCD detector was used to take 14 exposures of the southern filaments of M82 at different half wave plate positions. A long-slit Dekker with 10 apertures was used, with the visible centre of the galaxy in the second aperture of the Dekker. The Dekker was placed along the southern filaments of the galaxy at a position angle of 151°. This Dekker has used to get coverage of the full extent of the filaments. The telescope was offset from the galaxy by 10 arcmins after every exposure and a corresponding sky exposure was taken. Table 3.4 gives details of the observations. The slit-width was 1 arcsec, equivalent to 220 microns. The 1200R grating was used with a centre wavelength at $\lambda\lambda$6563Å. Conditions were not photometric, the humidity was high and consequently the seeing was approximately 1.5″. The offset was accurate to within 0.1″ and the sky variation through each cycle was negligible.

The distance separating the apertures corresponded to 23″ with each aperture being 4″ wide. The filaments stretch for $\sim$ 100″ to both the north and the south of M82 along the minor axis. Figure 3.11 shows the position of the apertures on an Hα contour image

of M82. The apertures are labelled for future reference.

Cosmic rays were removed individually from the raw data frames using FIGARO and the surrounding data was interpolated across the invalid areas, with care being taken not to smear a spectral line across a sky area. The data were calibrated with arc lamp spectra using 2DSPEC and each sky frame was subtracted from its corresponding galaxy frame. The data were then converted to a format suitable for use with the Durham Imaging Polarimeter Software package and reduced in the usual manner (Scarrott, 1991). Data from the three nights were reduced separately and then combined once it had been ascertained that they were in agreement with one another. The data were also reduced without subtracting the sky frames, but instead using modelled flat fields. In this reduction the sky exposures were added together and averaged, and the skylines were blanked out and interpolated over. Left and right-hand apertures were selected for the left and right hand grid images (ISIS was used as a two channel instrument), making sure that no vignetted edges were included. These left and right-hand apertures were then collapsed in the x-direction to one dimension, a line. A surface-fitting program was used to fit curves using various spline points to this line. The fitted curves were then expanded back to the size of the original frame. The mean of each expanded frame was found and they was divided by this value respectively. Reductions then proceeded in the usual manner using these fields as left and right aperture modelled flat fields. The results obtained were, in all cases of the modelled flatfields, found to be worse than those obtained using the sky subtracted data. All the sky vectors were found to have similar position angles implying an incorrectly subtracted sky or an unflat flatfield. For the sky subtracted data, the sky vectors had large polarizations at random polarization angles implying a correctly subtracted sky. The sky fields were examined statistically and compared with the data frames to see whether large fluctuations occurred during the observations. It was found that the sky frame values fluctuate in a similar manner to the galaxy frame values, implying that the sky observations provide an adequate means of flatfielding the data. The number of counts registered in the sky exposures was very small, with an average of 6 counts obtained in a 15 minutes exposures. This was consistent throughout the sky and galaxy observations. The data were also reduced separately using 2DSPEC by Dr. D. J. Axon (private communication) and similar results were obtained. A preliminary discussion of the results were presented by Foley, Scarrott and Axon (1992).

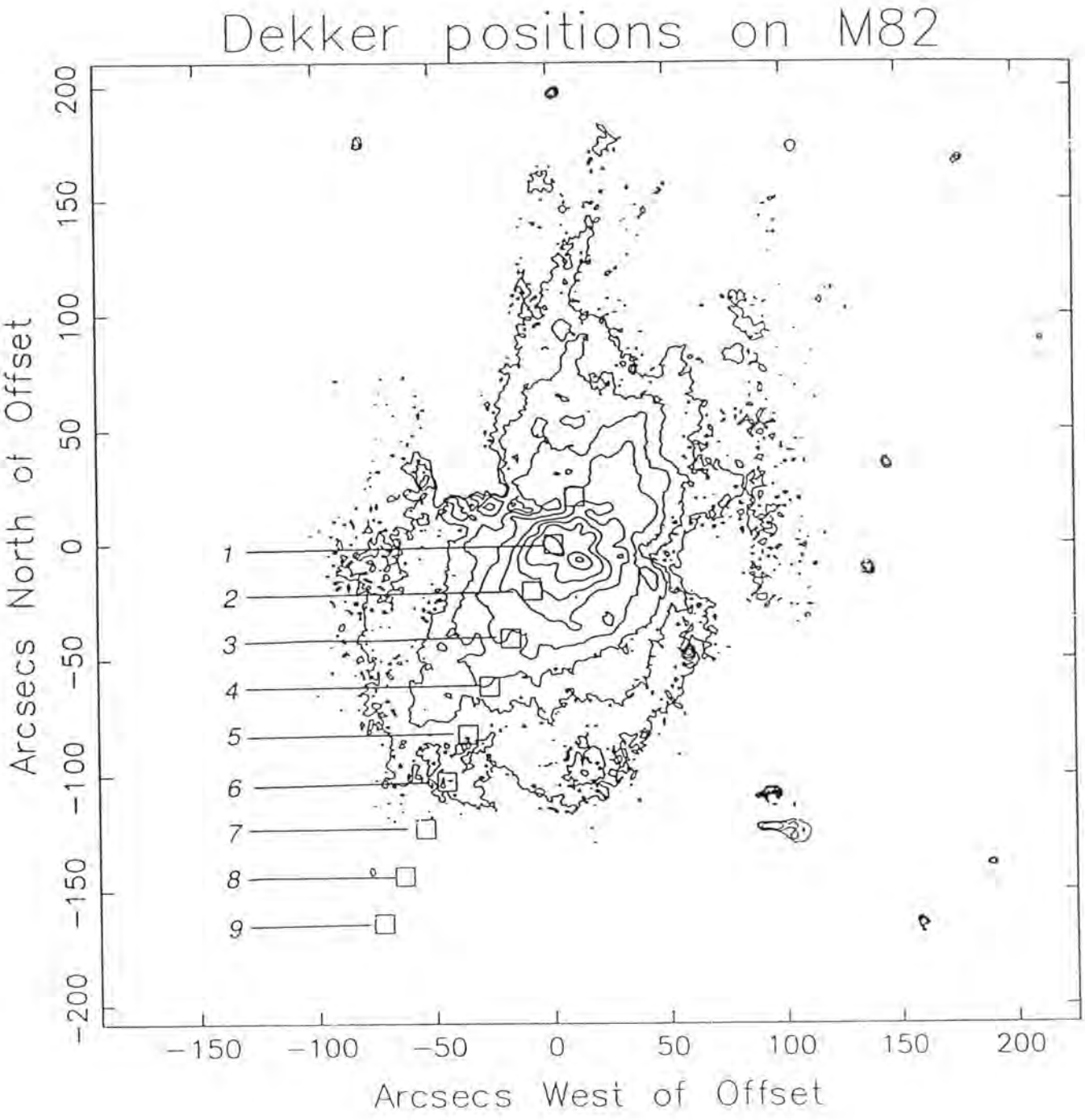

Figure 3.11: Position of spectropolarimetry Dekker apertures shown on a contour map of the Hα data for M82 showing extent of filaments.

3.2.3 Results

Figure 3.12 shows a greyscale intensity image of the spectropolarimetry results. Apertures are numbered from right to left and the two end apertures are ignored since the data they contained was vignetted. The emission lines shown correspond to, from top to bottom, NIIλ6548, Hα, NIIλ6584, SIIλ6717 and SIIλ6731. Splitting in the emission lines is apparent, with the widest splitting being seen in Aperture 4 at 69″S. This is close to the value for maximum splitting found by Bland and Tully (1988) at 60″S, although our apertures do not cover this region. Beyond Aperture 5 there is little signal except for that of the sky lines, the 'closing' of the filamentary bubble having occurred somewhere between Apertures 5 and 6. In these images the stronger component of the line is almost at the systemic velocity of M82 and the fainter component is blueshifted with a maximum velocity separation from the rest velocity of the galaxy of $\sim$ 300km/sec.

In Aperture 1, the lines are at the systemic velocity of the galaxy. The Hα line which is at 6562.81Å in our rest frame has been redshifted to 6567.76Å, giving a redshift of $z = 0.00075$ and a recessional velocity of 230km/sec. As we move outward along the filaments, the two components are both slightly blueshifted with respect to the system velocity. The main intensity peak is very slightly blueshifted (maximum shift is 1.97Å, which equals –90km/sec) and we shall refer to it as the systemic velocity component. In Aperture 4 the maximum splitting for the small intensity peak is 6.4Å or equivalent to –293km/sec and we will refer to it as the blueshifted component. As discussed in Axon and Taylor (1978) and Bland and Tully (1988), at the splitting region we are seeing emission from the surface of a large bubble of dust and gas blown out along the minor axis by a galactic superwind from the starburst region of the galaxy. In Fig. 2.3 we have shown a schematic diagram of M82 and its minor axis bubble as if we were looking at it in the plane of the sky. From the earth, the galactic disc appears to be slightly inclined away from us so the southern bubble is slightly inclined towards us. The back edge of the bubble is almost in the plane of the sky and the front edge of the bubble is pointing towards us. Thus the blueshifted component is light from the front edge of the bubble and the systemic component is light from the back of the bubble.

Figures 3.13 to 3.17 show profiles of the intensity, Stokes parameters Q and U, polarized intensity, percentage polarization and polarization angle along the entire length of Apertures 1 to 5. Figure 3.13 shows the results for Aperture 1 at the centre of the galaxy in the wavelength range 6365–6780Å. The continuum is featureless except for the emission lines, which are, from left to right, NIIλ6548, Hα, NIIλ6584, SIIλ6717 and SIIλ6731. There

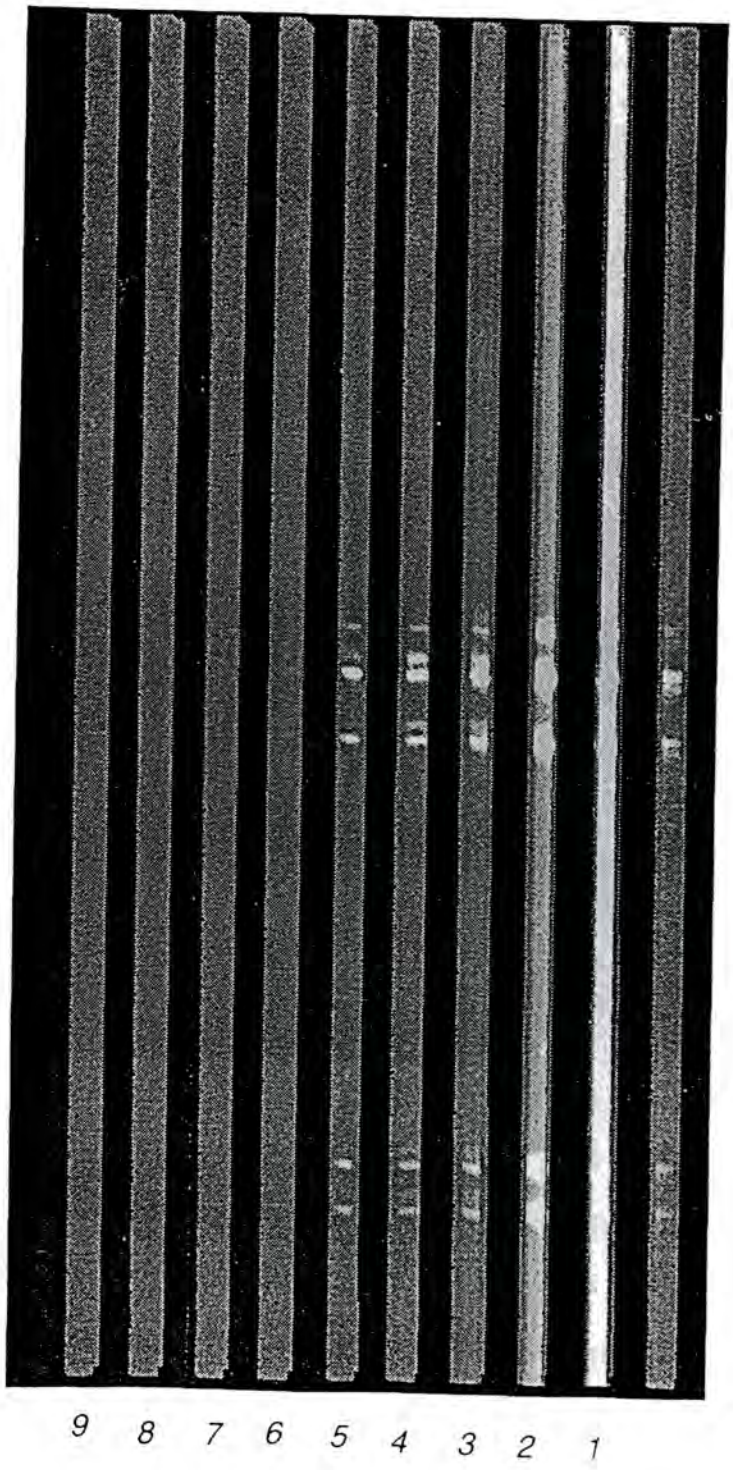

Figure 3.12: Greyscale intensity image of the spectropolarimetry data, showing the full data set.

are corresponding features in Q, U and polarized intensity. The continuum polarization is constant at about 9%, with dips[1] occurring at the positions of the emission lines. There is a trend in the intensity to increase slowly as wavelength increases, as you would expect from the broadband observations. This causes the polarization to decrease as wavelength increases since the polarized intensity is constant. The polarization angle is fairly constant at about 90°.

Figure 3.14 shows the results for Aperture 2 at 23″S. Again, in intensity we see a flat continuum with strong emission lines, which have broadened slightly. Peaks in polarized intensity and troughs in polarization correspond to the intensity peaks. The continuum polarization is at about 14% on average. The polarization angle is fairly constant at about 90°. In Fig. 3.15 we see the results for Aperture 3 at 46″S. The splitting starts to become apparent with a bulge on the blueward side on all the emission lines. Again there are corresponding peaks in polarized intensity, but now we see two dips in the polarization for each emission line. The continuum polarization averages in the range of 40 to 60%.

Figure 3.16 shows the results for Aperture 4 at 69″S. The splitting is most evident in this aperture. Two peaks can be seen for each emission line, the smaller peak is blueshifted and the larger peak is at the systemic velocity. For the systemic velocity line there is a corresponding feature in Q for the Hα and NIIλ6584 lines as well as corresponding peaks in polarized intensity. The continuum polarization is very large, and becomes quite random away from the emission line area. We have not measured anything of significance in the continuum since there is little signal there. The emission line polarizations again show a sharp drop to between 5 and 10%, with two dips for the split lines.

Figure 3.17 shows Aperture 5 at 93″S. The splitting is still apparent but the blueshifted emission lines are very small with respect to the systemic component. The polarized intensity has peaks at the Hα and NIIλ6584 systemic lines. The polarization decreases at the intensity lines, but otherwise has mainly null values since there is not enough signal in the continuum to calculate valid polarizations.

We can focus on the Hα and NII lines in detail. In Fig. 3.18 the emission line results for Aperture 1 are shown with the errors which were modelled from the detector characteristics such as photon statistics and sky subtraction. We see the emission peaks in the intensity corresponding to NIIλ6548, Hα and NIIλ6584 lines, and similar peaks in the polarized intensity. The level of polarization is reasonably constant at all wavelengths

[1]The word *dips* is used in this context to describe the decrease in the percentage polarization corresponding to the emission lines

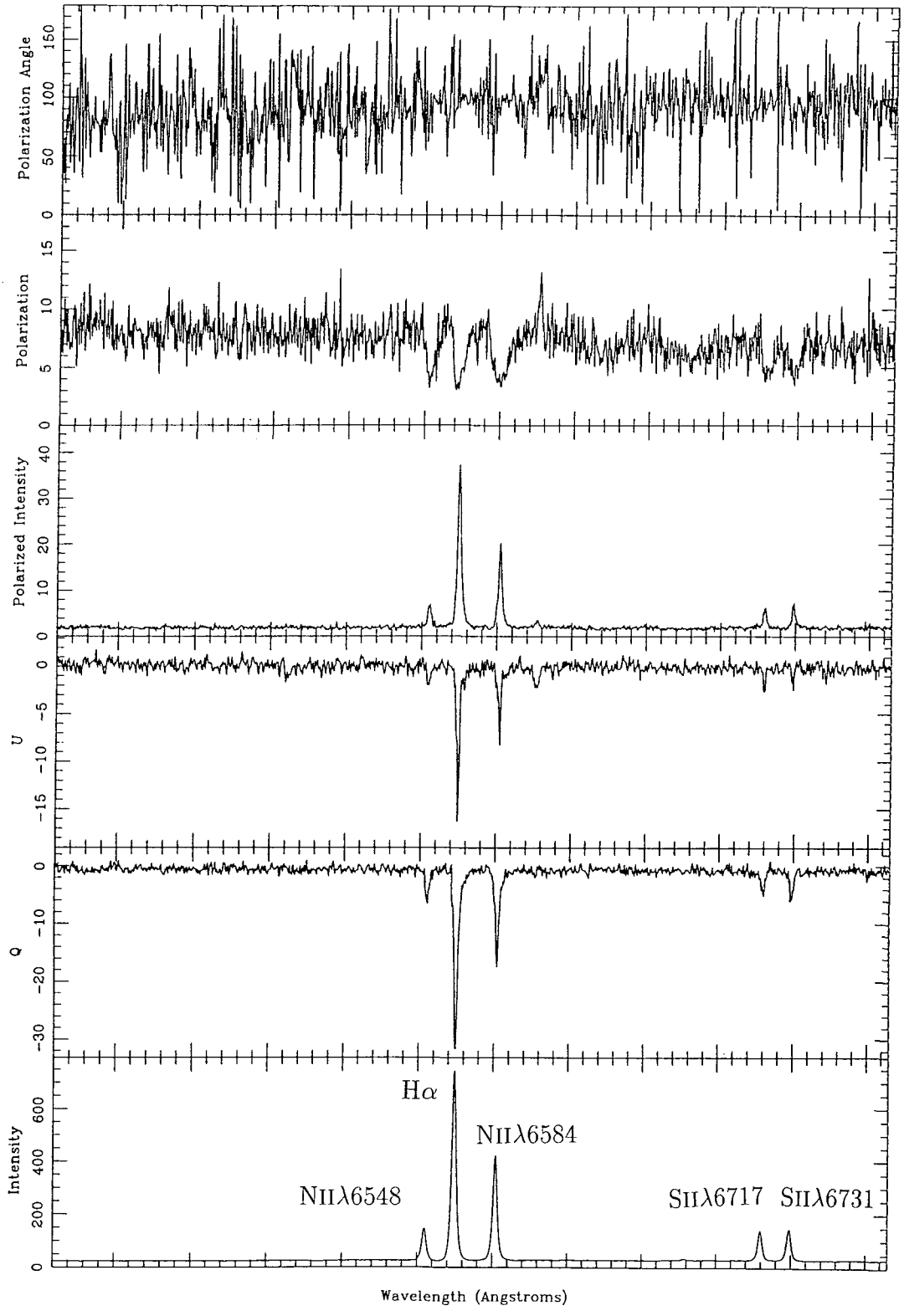

Figure 3.13: Profiles along Aperture 1, showing the intensity, Q, U, polarized intensity, percentage polarization and polarization angle. The emission lines are labelled.

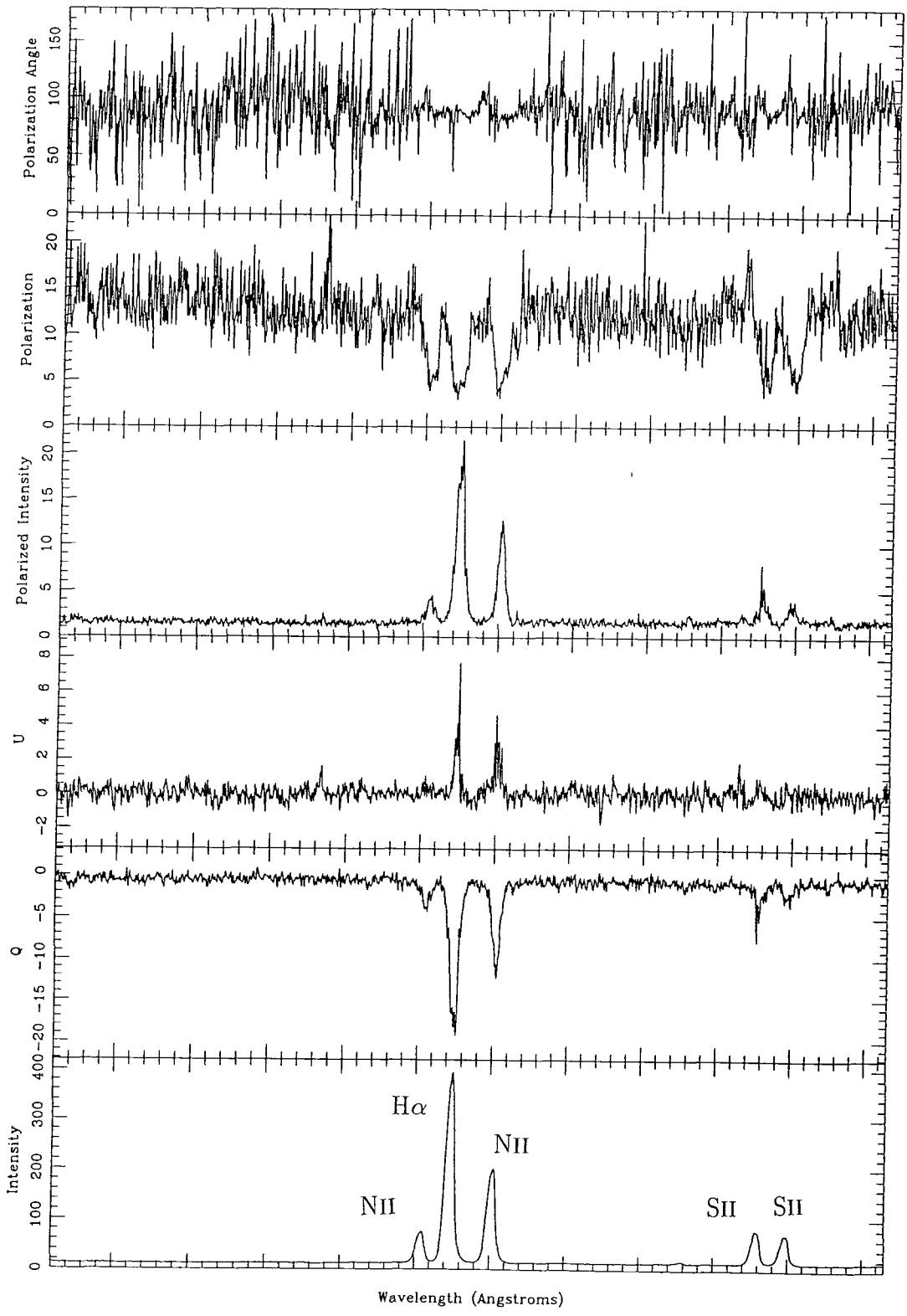

Figure 3.14: Profiles along Aperture 2, showing the intensity, Q, U, polarized intensity, percentage polarization and polarization angle. The emission lines are labelled.

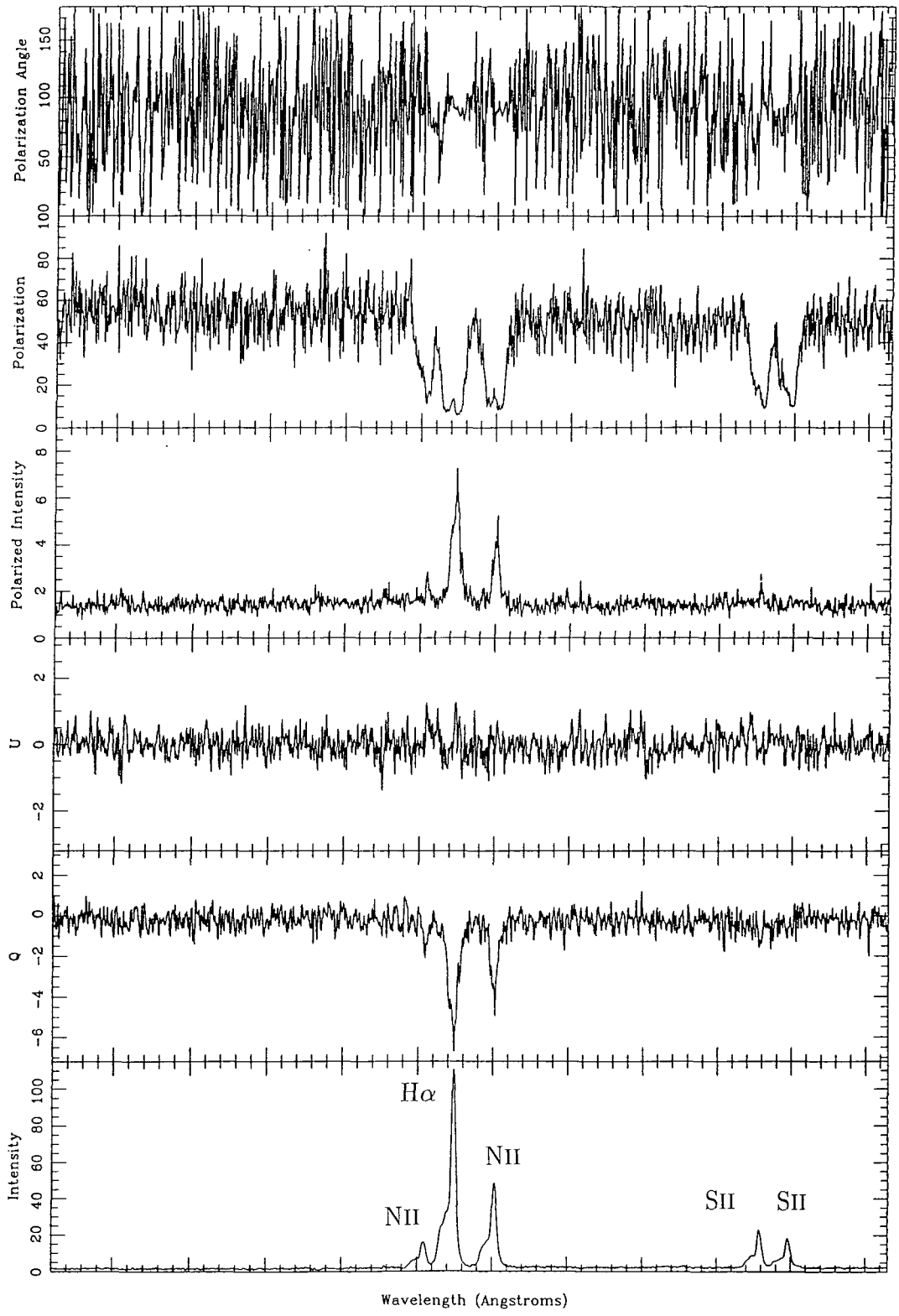

Figure 3.15: Profiles along Aperture 3, showing the intensity, Q, U, polarized intensity, percentage polarization and polarization angle. The emission lines are labelled.

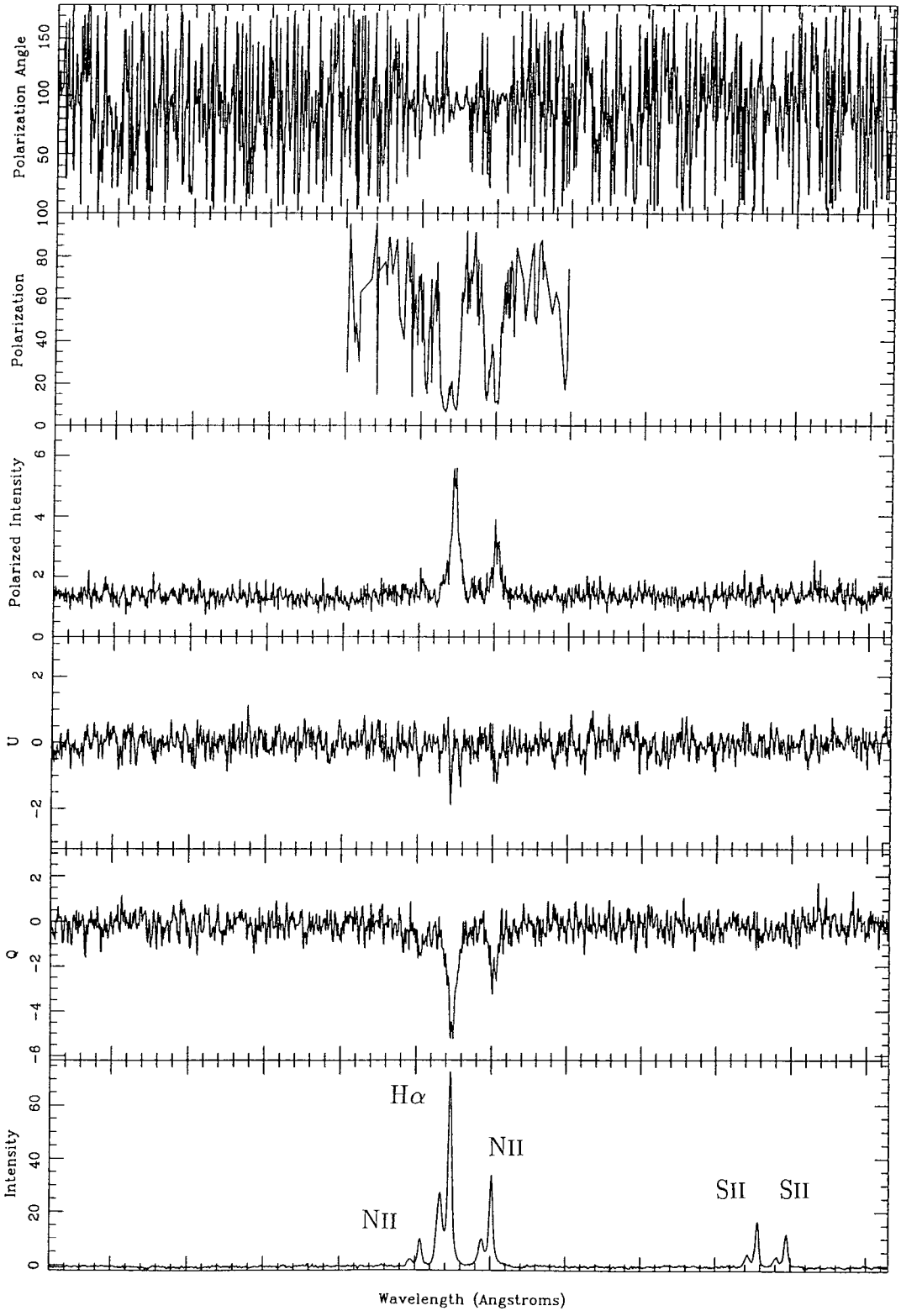

Figure 3.16: Profiles along Aperture 4, showing the intensity, Q, U, polarized intensity, percentage polarization and polarization angle. The emission lines are labelled.

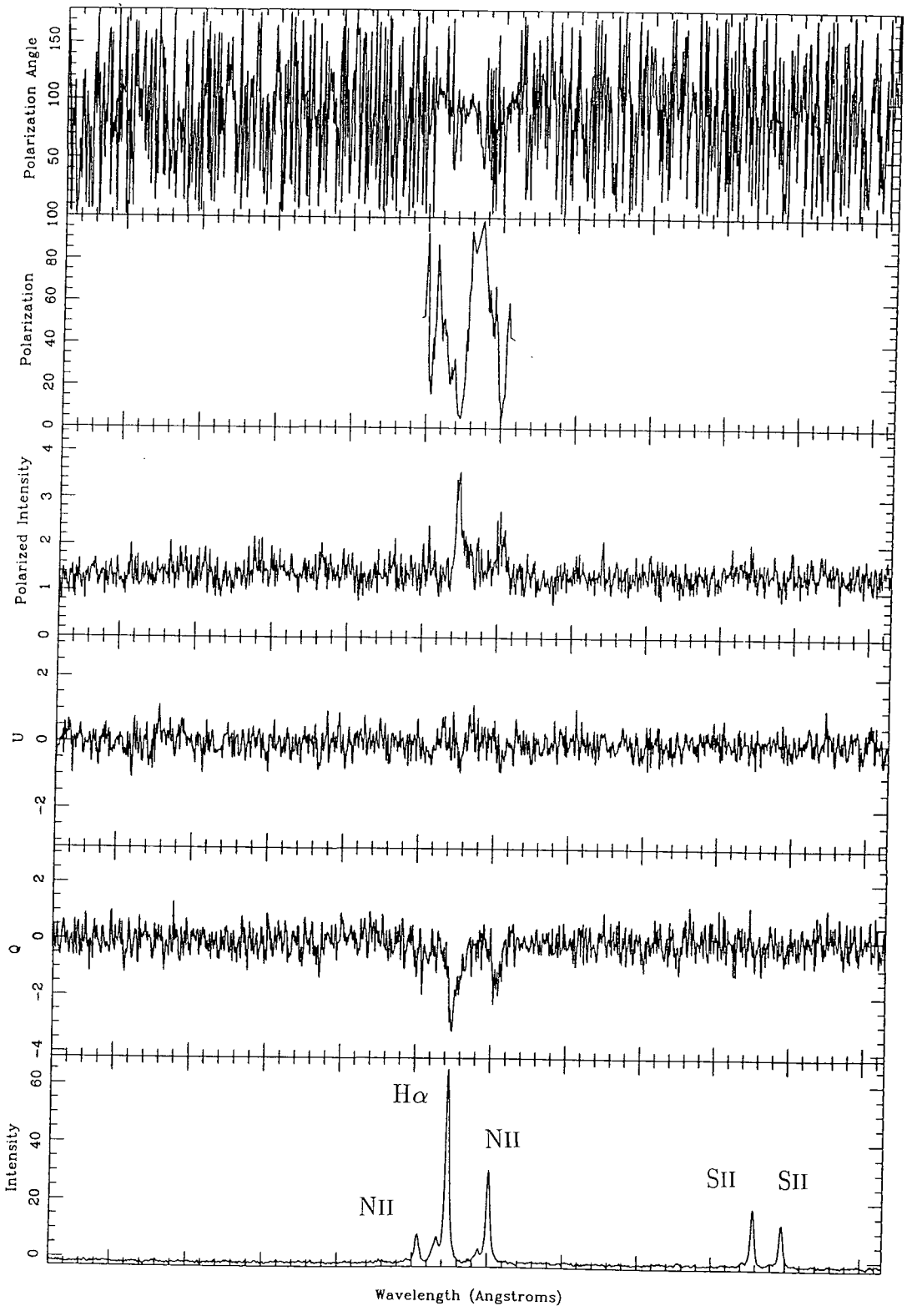

Figure 3.17: Profiles along Aperture 5, showing the intensity, Q, U, polarized intensity, percentage polarization and polarization angle. The emission lines are labelled.

shown, at 9%; this indicates that all components have a contribution of scattered light. The errors on the polarizations are quite large, except at the emission line peaks. Again, we point out that the continuum polarization levels are much too high.

Figure 3.19 shows a profile along Aperture 2, at 23″S from the galactic centre. The shape of the lines has started to change and they are slightly blueshifted. Peaks in intensity and polarized intensity correspond to troughs in polarization, with corresponding features being seen in Q and U. The continuum shows a constant polarization of between 15 to 20% and we can see the depolarizing effect of the emission lines, which reduces the polarization to 5%. The NIIλ6548 peak is just visible above the errors in polarized intensity.

Figure 3.20 shows a profile along Aperture 3, at 46″S from the galactic centre. The line splitting begins to show, with bulges appearing on the blueward side of all three peaks. Again the intensity peak corresponds with the polarized intensity peak, and also with a polarization trough, while a corresponding feature can be seen in Q. The continuum emission is at $\sim$ 60%. We see a large trough at the emission line positions where the polarization is reduced to around 8%. There appear to be two distinct dips in the polarization, one corresponding to the systemic velocity peak and another corresponding to the blue-shifted split line which is just starting to become evident. The NIIλ6548 peak is no longer visible above the errors in polarized intensity and as such we cannot say that we have measured anything of significance there.

Figure 3.21 shows a profile along Aperture 4, at 69″S from the galactic centre. There are two intensity components clearly resolved, 4.55Å apart. In intensity we see the tip of the systemic velocity component in NIIλ6548, and both components in Hα and NIIλ6584. Corresponding features can be observed in Q for the systemic emission lines of Hα and NIIλ6584, as can peaks in polarized intensity. There is not enough signal in the NIIλ6548 polarized intensity for us to have measured anything within errors. We see a peak in polarized intensity at the systemic component of the Hα indicating clearly that this light is scattered but there appears to be no peak in polarized intensity corresponding to the blueshifted Hα peak. We see two distinct dips in polarization, one for the blueshifted line and one for the systemic velocity line, both at around 10%. The continuum polarization fluctuates at about 60%.

Figure 3.22 shows a profile along Aperture 5, at 93″S from the galactic centre. There is still clear splitting between the emission lines but the intensity of the blueshifted line is very much weaker than the other line. The separation between the lines is 4.4Å. The systemic velocity peak in intensity for Hα corresponds to a peak in polarized intensity,

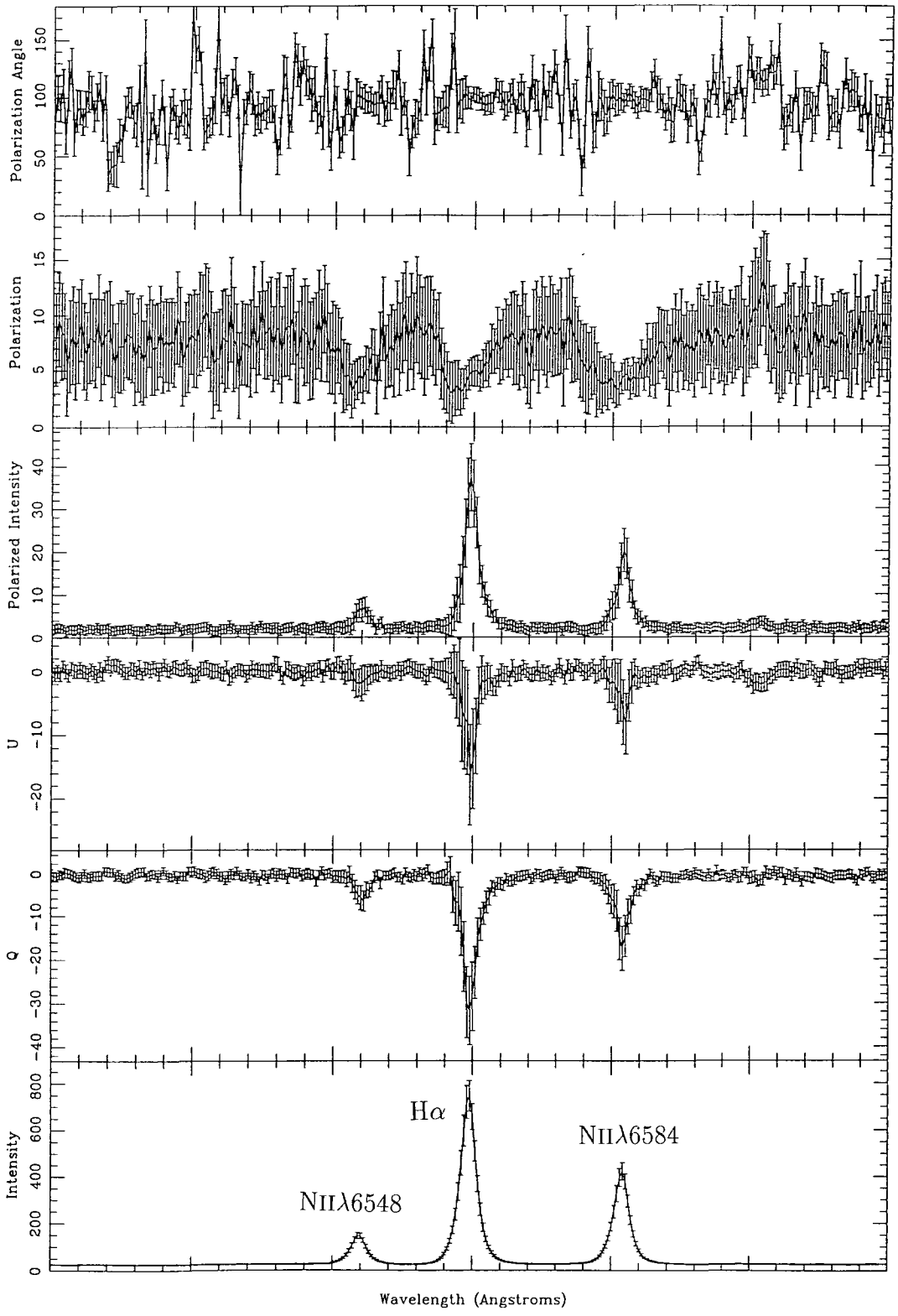

Figure 3.18: Profiles along the emission line region of Aperture 1, showing the intensity, Q, U, polarized intensity, percentage polarization and polarization angle with errors.

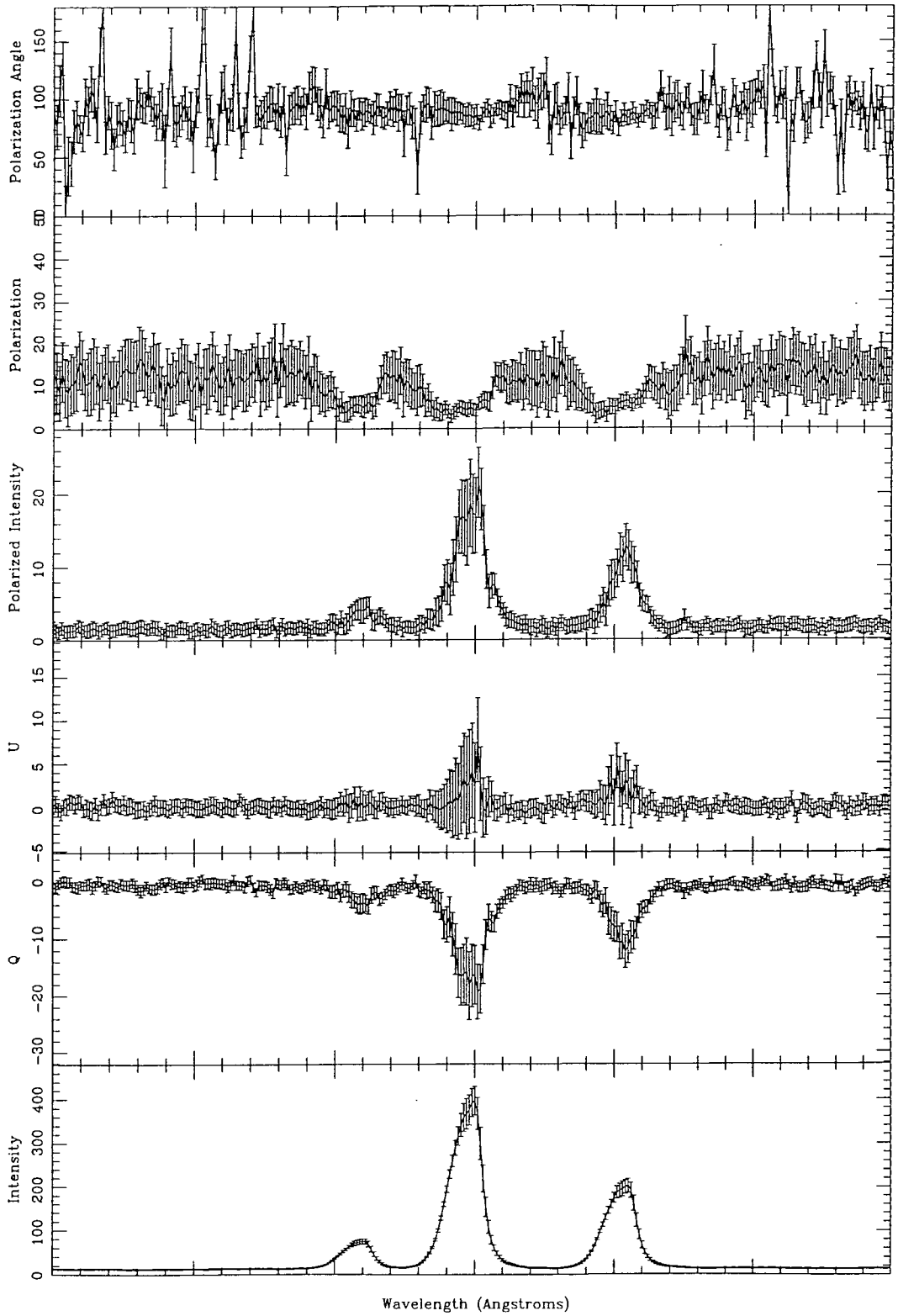

Figure 3.19: Profiles along the emission line region of Aperture 2, showing the intensity, Q, U, polarized intensity, percentage polarization and polarization angle with errors.

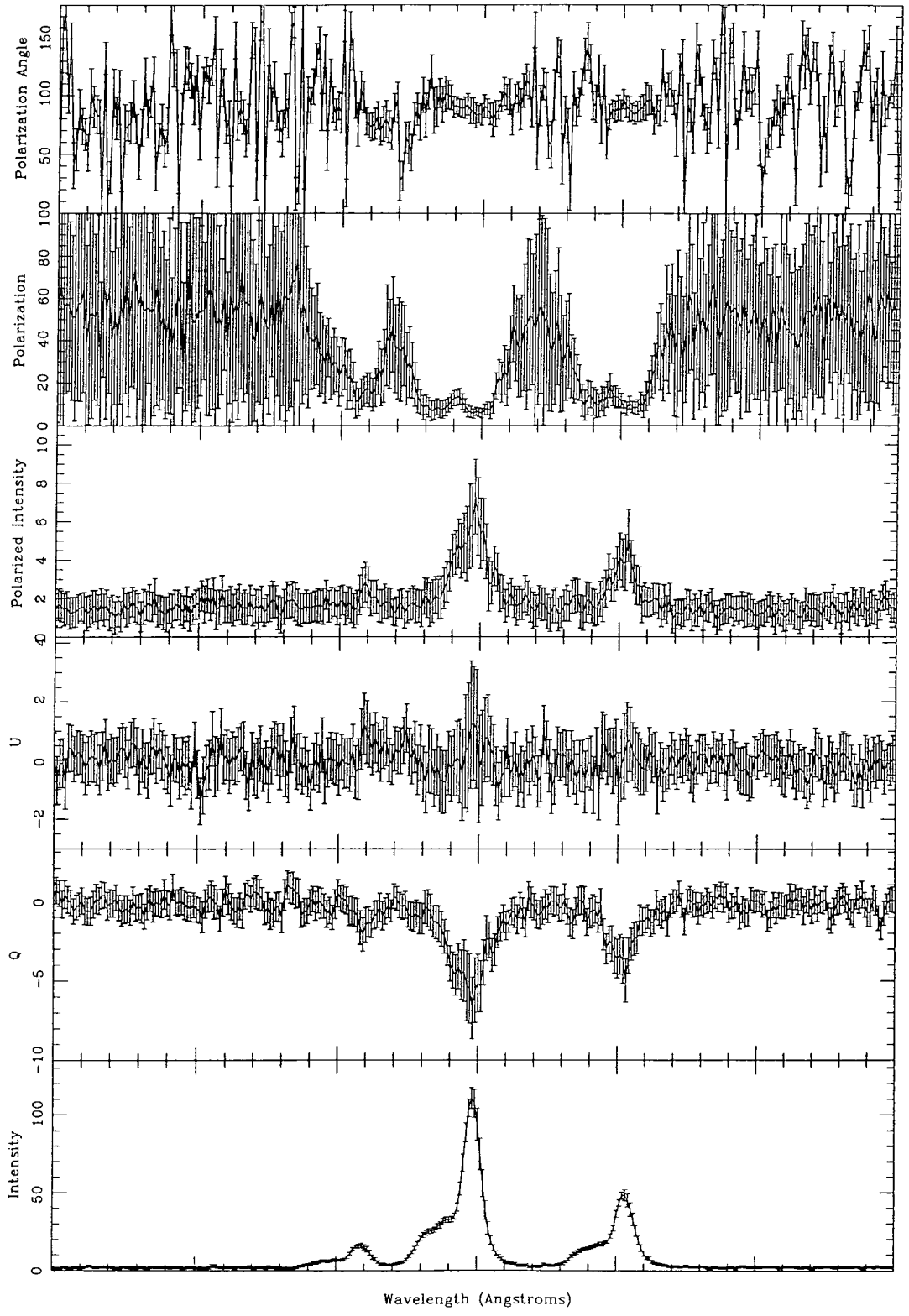

Figure 3.20: Profiles along the emission line region of Aperture 3, showing the intensity, Q, U, polarized intensity, percentage polarization and polarization angle with errors.

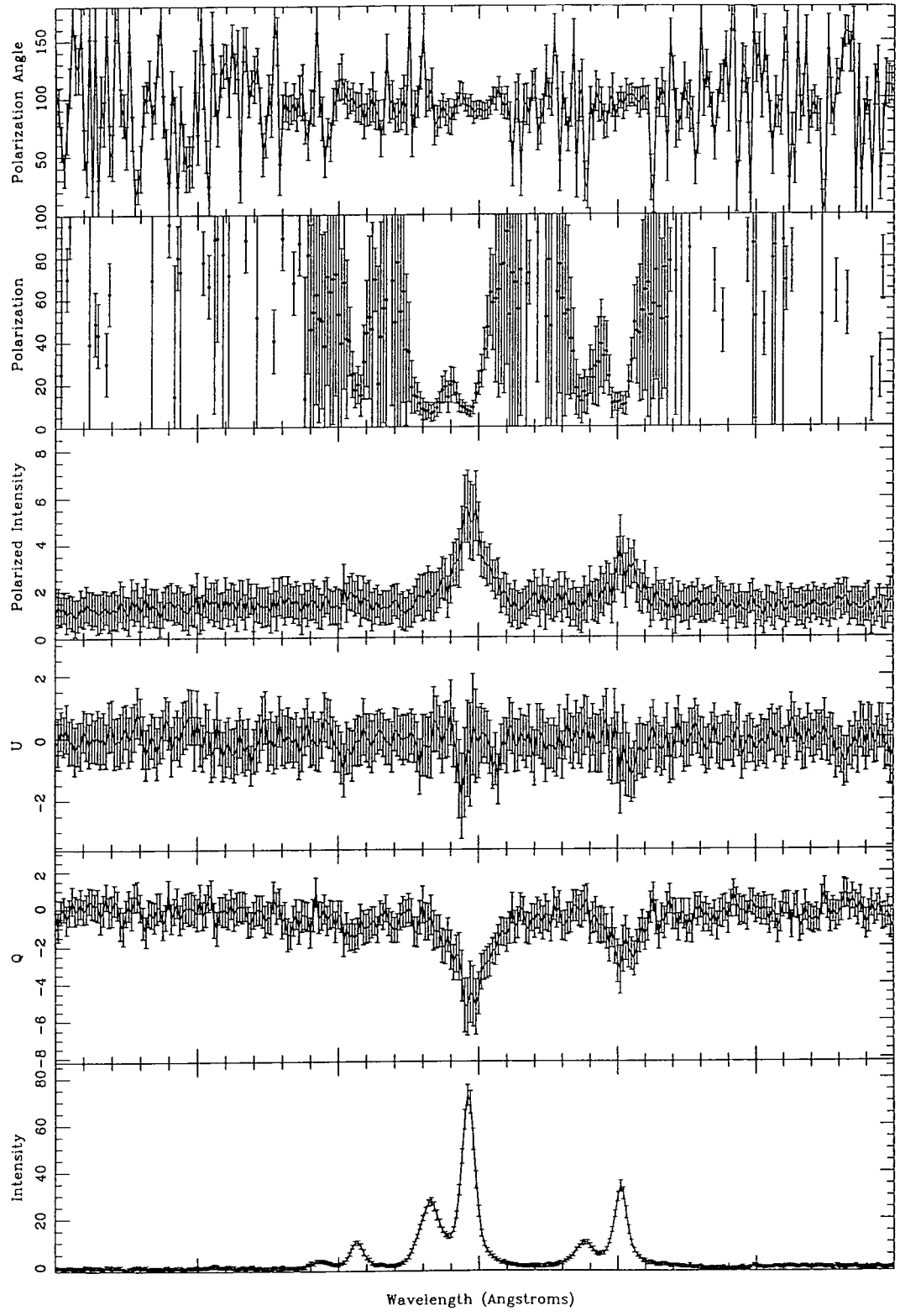

Figure 3.21: Profiles along the emission line region of Aperture 4, showing the intensity, Q, U, polarized intensity, percentage polarization and polarization angle with errors.

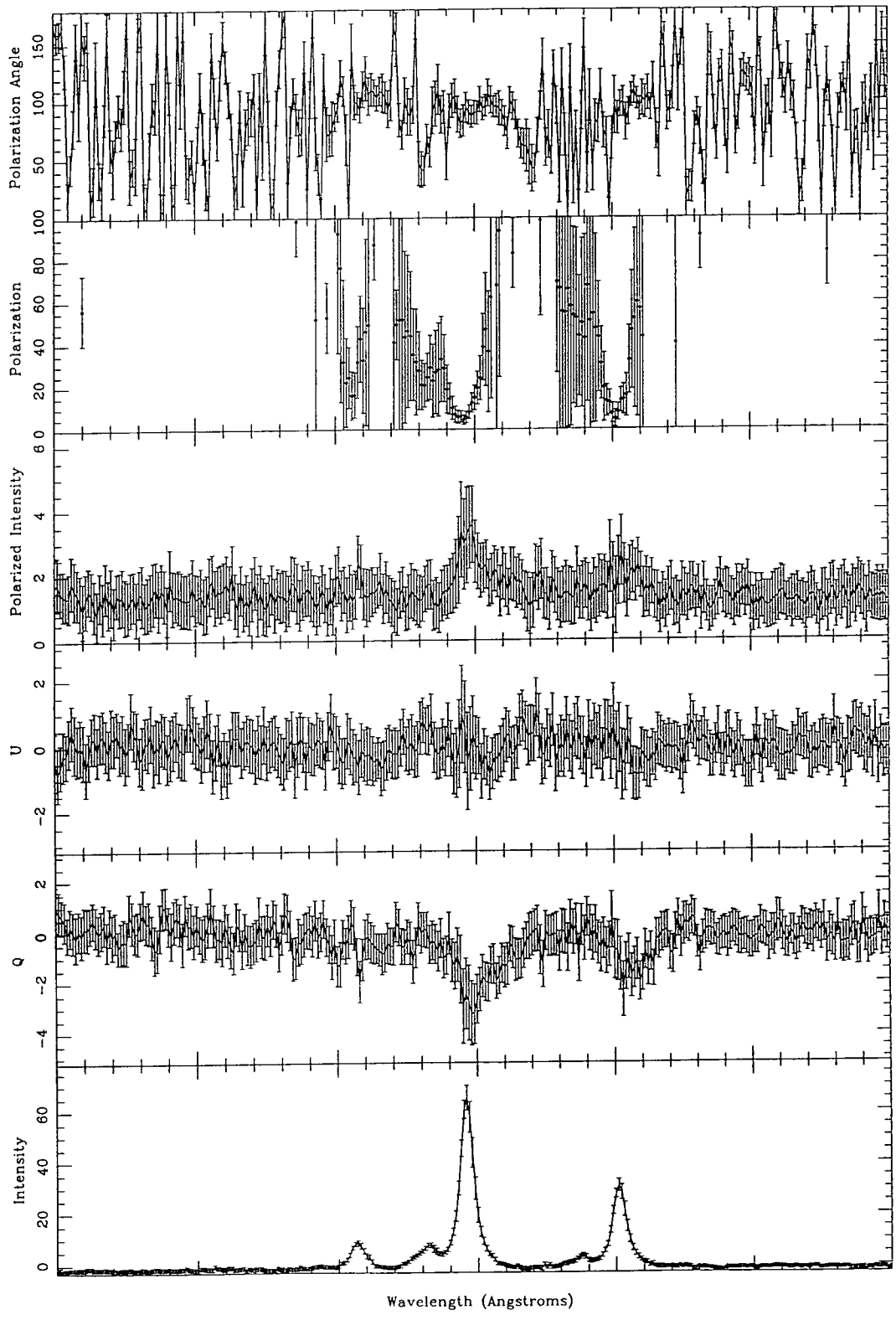

Figure 3.22: Profiles along the emission line region of Aperture 5, showing the intensity, Q, U, polarized intensity, percentage polarization and polarization angle with errors.

while the NIIλ6584 systemic velocity peak is just visible in polarized intensity above the errors. There is a decrease in the polarization to $\sim$ 5% corresponding to the systemic velocity peaks in Hα and NIIλ6584 line. Null values were mostly recorded for the continuum polarization since the continuum has very low intensities. The errors on the continuum polarization are very large, and where measured, it fluctuates between 30 and 100%.

A profile along Aperture 6, at 115″S from the galactic centre showed almost no signal from the emission lines although a faint bump could be seen in the Hα position and in the NIIλ6584 position. No splitting was discernable. There was no detectable signal in polarized intensity and the polarization was almost completely random. Apertures 7, 8 and 9 contained even less signal so none of these data profiles are shown.

3.2.4 Discussion

It is clear that the splitting of the Hα, NII and SII emission lines is due to light coming towards us from the front and back walls of a blown-out cavity. If one looks at Fig. 3.11 again, one can see that the northern filaments appear to describe the edges of a bubble, with one wall at 5″W, 120″N of offset and the other at 50″W, 90″N. The walls of the southern bubble are unclear but the filament at 60″E, 70″S of offset could be one, with a hint of another at 0″W, 70″N. The filaments could then be a result of an effect similar to limb brightening, whereby the edges of a thin luminous body appear to be brighter than the centre because of luminosity summing effects along the lines of sight at the edges. It can also be seen from Fig. 3.11 that the apertures are not directly down the southern filament but rather down the centre of the bubble, sampling the main body of the cavity rather than the edges.

We can think of M82 as having two distinct scattering geometries. One is the "giant bipolar nebula" seen in Hα with the bubbles illuminated by a central Hα source (the starburst) giving the centrosymmetric pattern seen in the imaging polarimetry. This is shown schematically in Fig. 3.23, part (i) showing the edge-on view, part (ii) showing the side-on view and part (iii) showing the view if we were looking down the minor axis.

The other geometry is that of a dusty cloud or halo surrounding the galaxy, with 2 empty bubbles blown in it (if not empty then at least with a much lower dust/gas density or else we would not see such clear splitting in the emission lines). This dust cloud is illuminated by the galactic disk, with a component from the starburst region. It is shown in Fig. 3.24 with (i), (ii) and (iii) as in Fig. 3.23. Old models of M82 used the cloud

of scatterers geometry without the Hα 'holes' in it (Solinger, Morrison & Markert 1977, Perkins 1978), illuminated by galactic disk and a bright point-like nuclear component. The continuum polarization patterns seen in B, V and C can be explained by this simple scattering geometry, and the cavities may be ignored since they comprise only a small fraction of the halo volume.

The Hα emission is seen mainly in the bubbles and along the minor axis. Hα is a major emission of supernovae and young, bright stars, while older, slower evolving stars have a much quieter Hα signal. Previous studies have deduced that there is probably little star formation currently occurring outside the starburst region in M82. Dust is thickly but patchily distributed throughout the galaxy, and we should see such emission if it exists in the main body of the galaxy, through the patchy parts.

Since the dust particles are moving away from the centre of the starburst they see the light from the starburst redshifted. We would expect to see this reflected in a redshifted peak corresponding to the velocity of the particles but this is not observed. Either the angle of the bubble coming out from the galaxy is such that the blueshift caused by this is exactly cancelled by the redshift of the particle velocity or else the dust is not moving at the cavity walls, where the scattering occurs - perhaps because of collisions with other dust. Any intrinsic emission should be at the particle velocity.

We can interpret the spectropolarimetry as follows: at the centre of the galaxy the polarization appears to be due to scattered radiation from a central illuminating source, as indicated by the Hα imaging polarimetry, thus we get a constant polarization within the errors. At 23″S the line polarization starts to become evident as troughs in the continuum polarization and this becomes increasingly evident as we go further out the minor axis.

Radiation is emitted from the surfaces of the blown out bubble, due to the collision of hot, high velocity gas with the walls of the cavity. This shocked emission comes towards us from the front and the back of the bubble, and since the interior of the bubble is hollow, is essentially unpolarized. Thus we get two unpolarized lines which have the effect of reducing the continuum polarization. At 23″S the splitting has only just begun, however at 69″S, for each emission line we have two clear components, scattered light from the central hidden source, and weak intrinsic emission from the walls of the cavity.

The scattered light will have the same velocity component as the dust grain off which it scatters. Thus we should have a scattered component, seen in the polarized intensity, associated with each emission component. The strong systemic component in Aperture 4

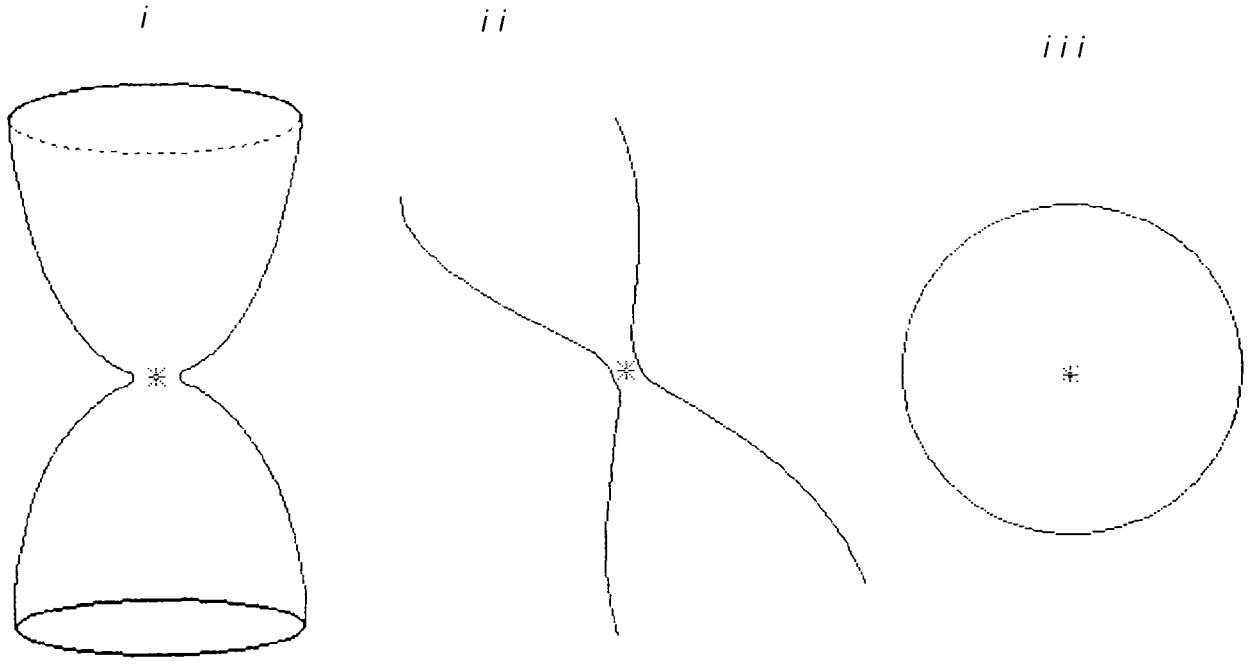

Figure 3.23: Geometry of M82 as seen in Hα. It shows the geometry as seen from (i) our point of view, (ii) an edge-on view and (iii) looking down the minor axis.

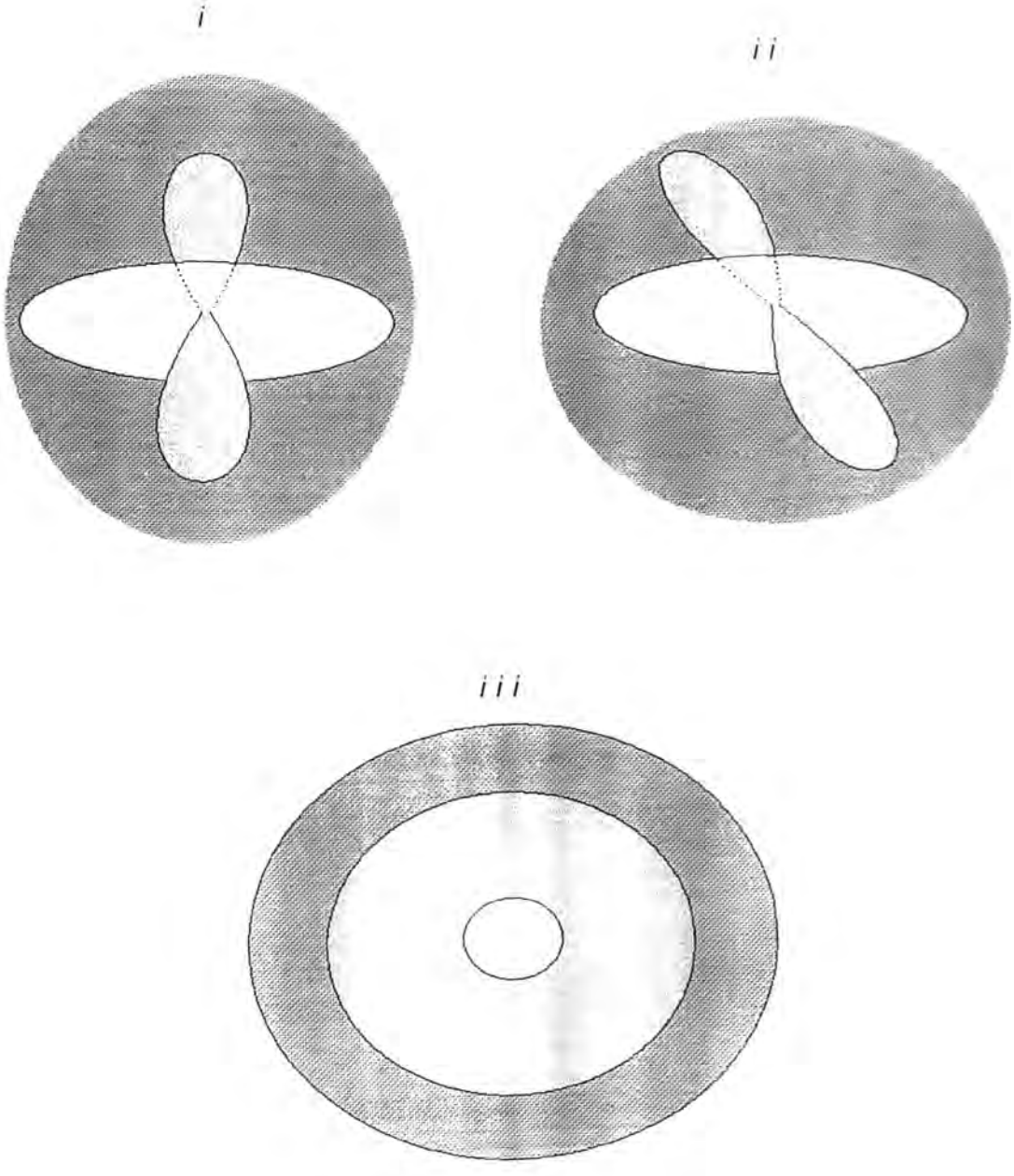

Figure 3.24: Geometry of M82 as seen in continuum. It shows the geometry as seen from (i) our point of view, (ii) an edge-on view and (iii) looking down the minor axis.

is polarized, and therefore contains a scattered component, whereas the weaker blueshifted component is virtually unpolarized indicating that it due to intrinsic emission only.

The X-ray halo appears to be correlated with the Hα filaments implying there is some physical relationship between the two. The collimated superwind from the starburst encounters dense clouds of dust and gas near the nucleus and shocks these clouds out of the nuclear region, heating them to high temperatures. As the starburst continues, the bubble grows, with any blown-out nuclear material colliding with the walls of bubble and causing further shocking. The interior of the bubble contains little material because of this wind. As the bubble expands the density of the walls decreases and the shocks became stronger, giving rise to diffuse X-ray emission. One theory suggests that condensations of material may have gathered on the surface of the bubble due to inhomogeneities, thus causing the filaments, and another is that they were formed in older SN remnants when radiative losses led to rapid cooling and hence fragmentation of the denser parts of the shock front.

High density clouds (the filaments) suffer slower shocks and can be heated to temperatures in the region of 10^5K, giving rise to the observed optical emission lines as they cool to $\sim 10^4$K. The emission line spectra of the filaments have been found to be similar to the model spectra of shock-heated gases. This does not necessarily disagree with the theory that the filaments are seen because of limb brightening effects since the filaments would appear due to a summing of the intensity of the cavity edges, where this hotter shocked gas will be.

Because of the tilt of the bubble, both walls of the cavity will have forward scattered light coming in our direction, with light from the back wall, close to the plane of the sky being scattered through almost 90° into our line of sight. Figure 3.25 shows the scattering angles through which the radiation from the central source will be scattered. We would expect light scattered from the front wall of the cavity to be more forward scattered than light from the back wall (see Fig. 1.3). If we assume the scattering to be Rayleigh scattering only, then we would expect the intensity of the light to increase for the more forward scattered blueshifted component, but the polarization to be weaker than the system velocity component. If we assume the scattering to be Mie scattering for a typical size distribution of scatters (e.g. typical for our Galaxy) then we would expect the intensity for the blueshifted component to increase and the polarization to decrease slightly with respect to the system velocity component. The rate of the increase in intensity and the decrease in polarization will be different for Mie and Rayleigh scattering

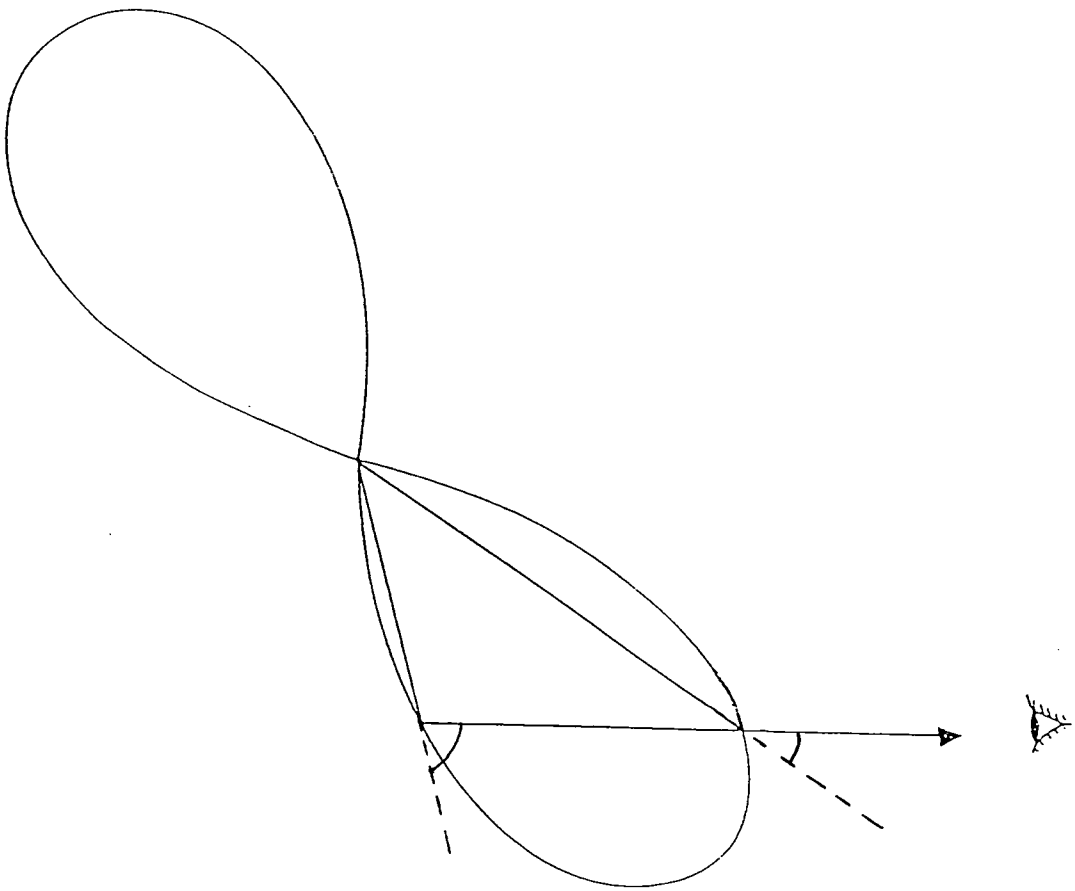

Figure 3.25: Scattering angles undergone by light from central source upon encountering the cavity walls.

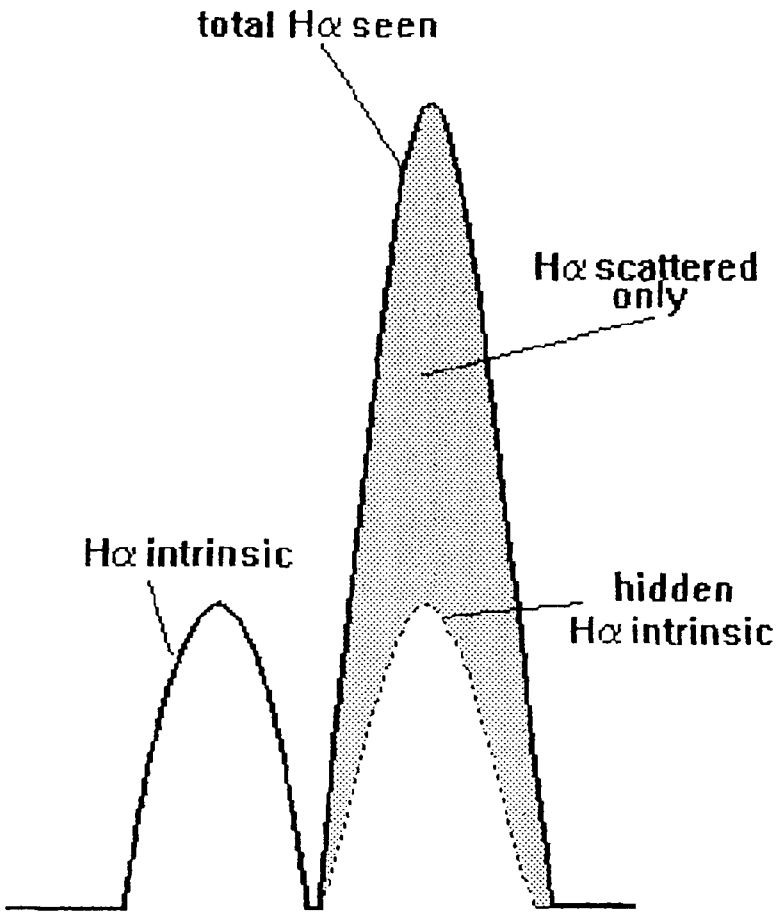

Figure 3.26: Schematic diagram of Hα lines in M82 showing the scattered and intrinsic emission components.

for each aperture, and the average was subtracted from the polarized intensity for that aperture, giving an image for each aperture in polarized intensity which a continuum level which fluctuated about zero. This was then divided by the corresponding intensity image, and the resulting output image was multiplied by 100 to give the percentage polarization values. All values calculated where the intensity was less than 5, or the polarized intensity was negative were discarded and the results are shown in Figs. 3.27 to 3.31. The value of 5 for the intensity cutoff was chosen arbitrarily because it was greater than zero but less than the values found for the emission line peaks. This is a somewhat ad hoc de-biasing method. but nevertheless works effectively.

We can compare Fig. 3.27 for the first aperture with Fig. 3.18. There are identical features in the intensity and polarized intensity, the only difference being that the polarized intensity has a continuum level averaged at zero, as one would expect. The percentage polarization however has a lower level of continuum polarization, a value of 4 – 5% compared with the previous 9%. The Hα and NII polarized intensity peaks do not stand out against the continuum polarization measurements.

The results for Aperture 2 are shown in Fig. 3.28 and should be compared with Fig. 3.19. Again, the intensity and polarized intensity peaks in these diagrams have the same shape, with the polarized intensity continuum level averaged at zero. The Hα polarization drops to 4 – 5%, as do the NII polarizations. This is about the same as the previously found values. The continuum polarization levels fluctuate between 12% to 20% with an average at about 15%, similar to the previous values.

Aperture 3 is shown in Fig. 3.29 which should be compared with Fig. 3.20. The cutoff levels of five units in intensity and zero in polarized intensity start to have an effect in this aperture. This has also occurred to greater effect in Figs. 3.30 and 3.31 and most of the continuum polarization has been removed in this way. The Hα polarization fluctuates within the range 6 – 10% with similar values found at the NIIλ6584 peak and a few values at around 18% for the NIIλ6548 peak. However, this last must be ignored since the polarized intensity for NIIλ6548 is not significantly above the continuum.

Aperture 4 is shown in Fig. 3.30, comparable with Fig. 3.21. In intensity we see the tip of the systemic velocity component in NIIλ6548, both components in Hα, and the systemic component in NIIλ6584. There is not enough signal in the NIIλ6548 polarized intensity for us to have measured anything. We see a peak in polarized intensity at the systemic component of the Hα indicating clearly that this light is scattered. This corresponds with a decrease in the percentage polarization to around 8%. The blueshifted

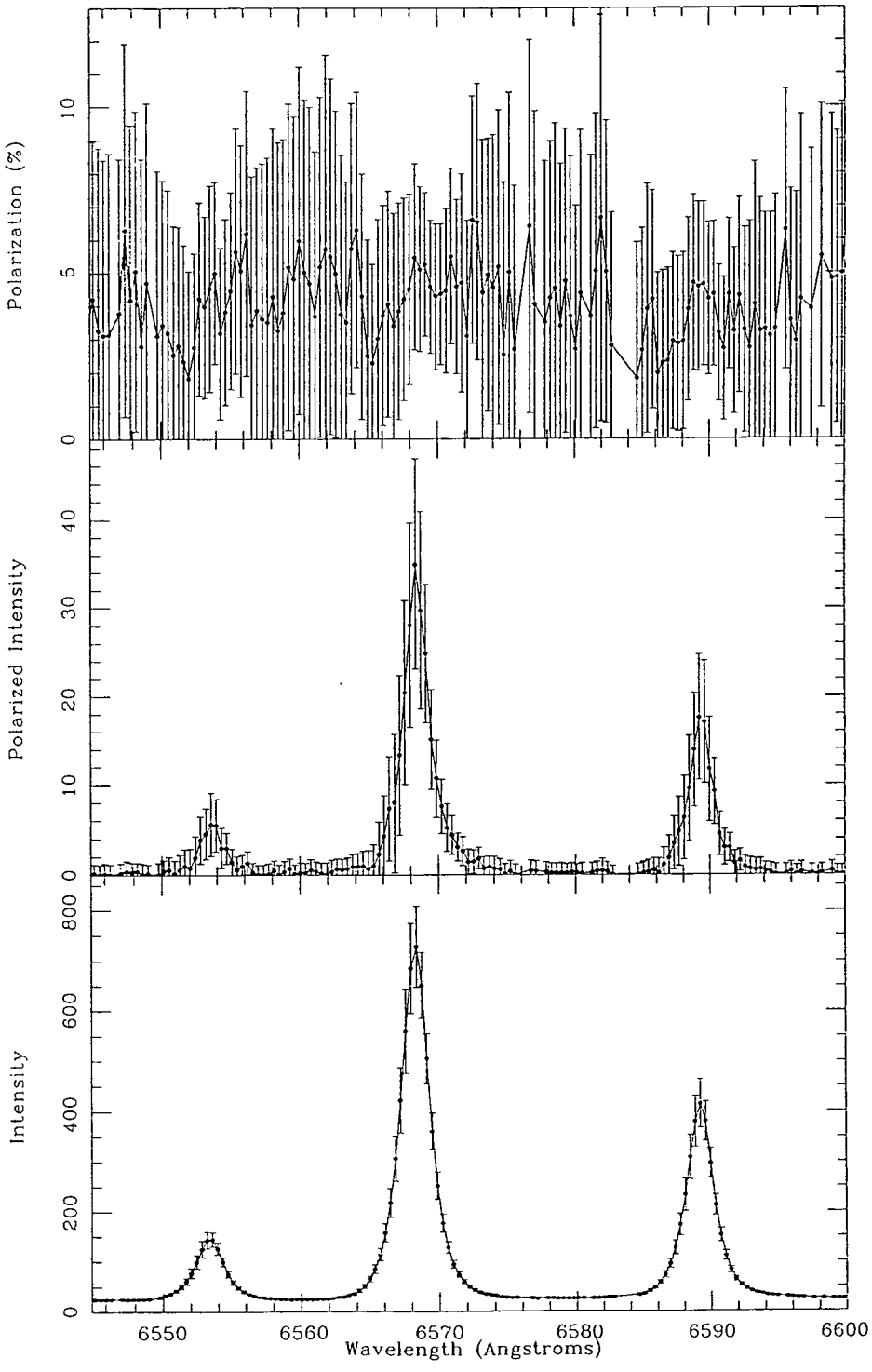

Figure 3.27: Profiles along Aperture 1, showing the intensity, polarized intensity and percentage polarization for the Hα region with the polarized intensity continuum subtracted.

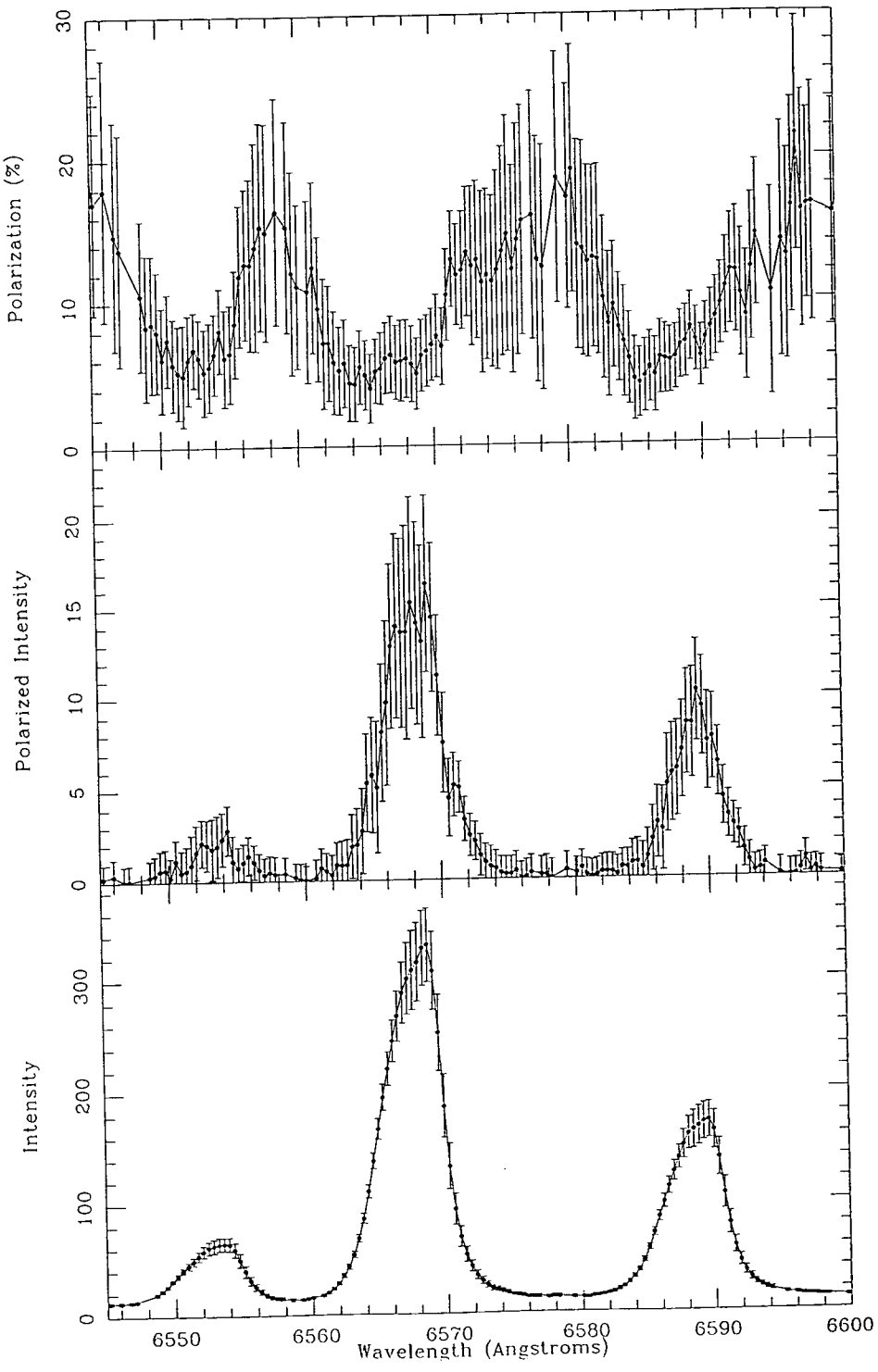

Figure 3.28: Profiles along Aperture 2, showing the intensity, polarized intensity and percentage polarization for the Hα region with the polarized intensity continuum subtracted.

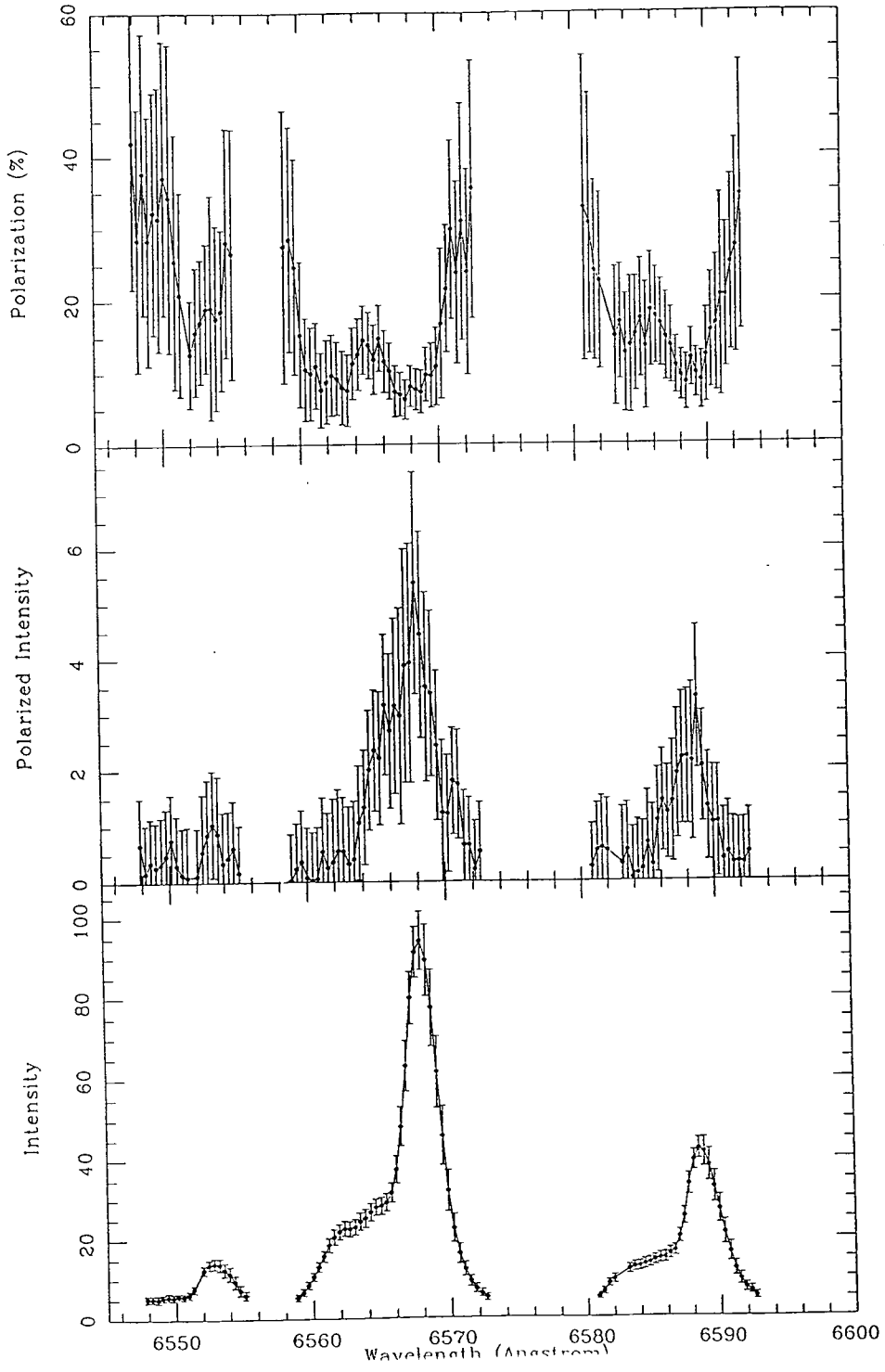

Figure 3.29: Profiles along Aperture 3, showing the intensity, polarized intensity and percentage polarization for the Hα region with the polarized intensity continuum subtracted.

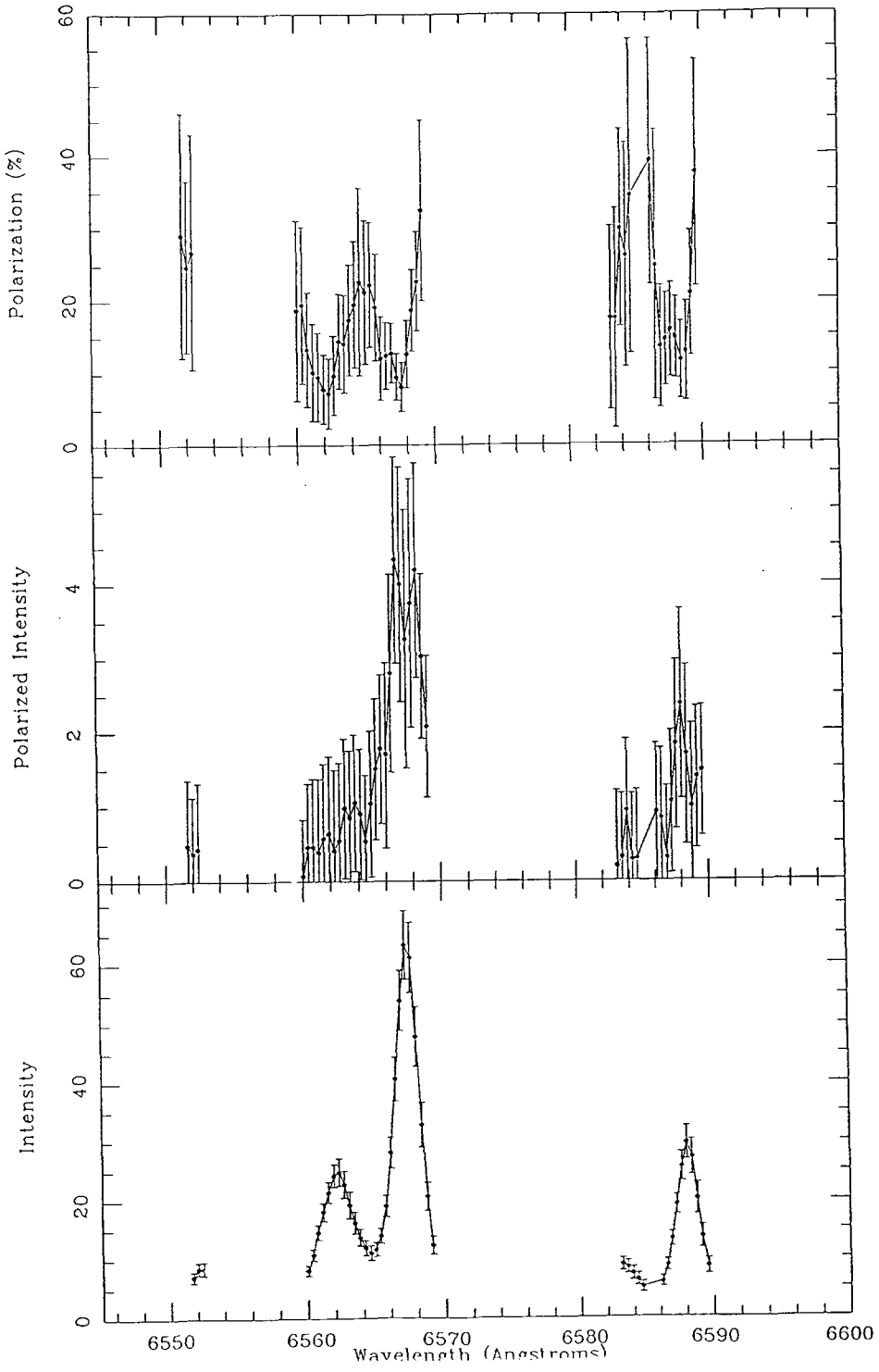

Figure 3.30: Profiles along Aperture 4, showing the intensity, polarized intensity and percentage polarization for the Hα region with the polarized intensity continuum subtracted.

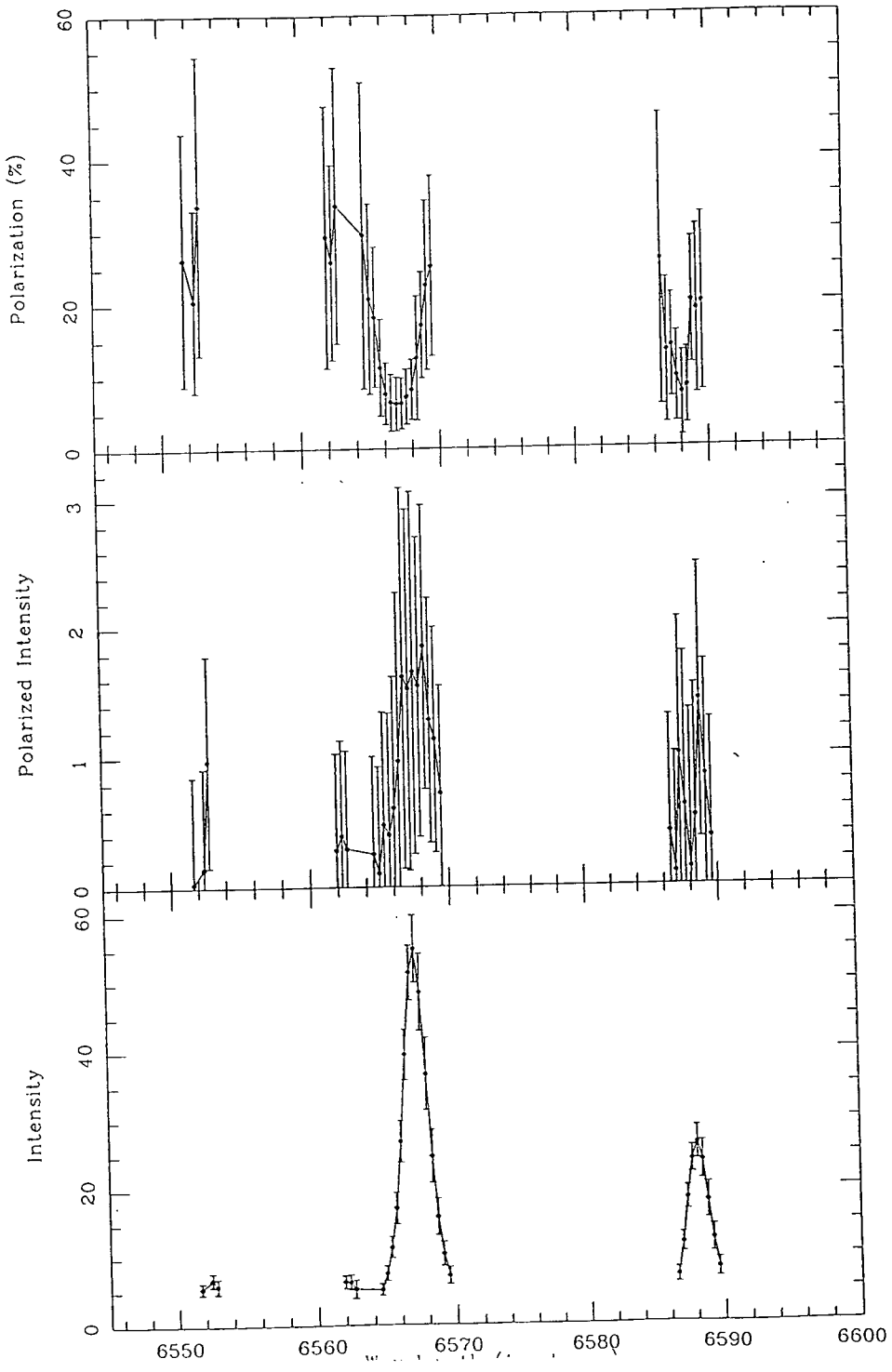

Figure 3.31: Profiles along Aperture 5, showing the intensity, polarized intensity and percentage polarization for the Hα region with the polarized intensity continuum subtracted.

peak does not have a corresponding peak in polarized intensity but there is a decrease to 8% in polarization. Considering the errors, we see that only the systemic peak in Hα is of significance.

Aperture 5 is shown in Fig. 3.31, comparable with Fig. 3.22. Only the systemic velocity peaks of Hα and NIIλ6584 are visible. The polarization values for the Hα is approximately 8%. The rest of the data has been removed by our selection procedure.

3.2.6 Comparison of imaging and spectropolarimetric data

We can compare the polarization values found for the spectropolarimetry with the polarizations from the imaging polarimetry. Table 3.5 shows the polarizations found for the broadband imaging data in a 4″ square aperture, using aperture polarimetry at 0″S, 23″S, 46″S, 69″S, and 93″S along the minor axis, in the continuum, Hα + continuum (Hα filter), and Hα only wavebands. In this table (i) refers to the imaging polarimetry and (s) refers to the spectropolarimetry.

The spectropolarimetric values presented in Table 3.5 were calculated as follows:

1. The Intensity, Q and U Stokes parameters were summed over the wavelength interval corresponding to the FWHM of the Hα filter to give the total I, Q and U for the filter. A polarized intensity and polarization were calculated for the filter using $PI = \sqrt{Q^2 + U^2}$ and $P\% = 100\frac{PI}{I}$. The polarization angles have been calculated using the Q and U values and the errors using $d\theta = \frac{90}{\pi}\frac{dPI}{PI}$.

2. The errors dI, dQ and dU were estimated from the square root of the total I, Q and U.

3. The error on PI and P% were calculated using

$$dPI = \frac{\sqrt{Q^2 dQ^2 + U^2 dU^2}}{PI}$$

and

$$dP(\%) = \frac{100}{I}\sqrt{dPI^2 + \frac{PI^2 dI^2}{I^2}}.$$

The reason PI, P% and P.A. were not merely averaged was because the polarizations calculated that way would be artificially high because of the excess polarized intensity caused by Q and U oscillating about zero. By calculating the total I, Q and U, it was

hoped to smooth out these fluctuations, reducing the calculated polarized intensity and hence the polarization.

However, where Q and U are zero within errors, as in the continuum region, one cannot say that anything has been measured. Because of the positive bias in polarized intensity it is necessary to use another estimator to show that the polarization is unmeasured.

It can be shown (Simmons & Steward, 1985), that where P/σ is less than a threshold value[2] then the estimate for the true polarization is zero. For the maximum likelihood estimator this threshold value is 1.41. By calculating P/σ for each wavelength position along the 5 apertures, it was found that this ratio was only greater than 1.41 in the emission lines, implying that we have only measured valid polarization in these regions. Therefore nothing has been measured in the continuum spectropolarimetry and that part of Table 3.5 was been left blank.

The Hα only polarizations are calculated by subtracting the summed I, Q and U of a continuum region near to, and of a similar width to, the Hα emission lines, from the summed I, Q and U of the Hα lines. The new P% and P.A. are given in the table. Errors were calculated by propagation through the subtraction and then through the polarization equations.

In the imaging polarimetry, the Hα filter contains the Hα light and the NII light as well as the underlying continuum. When the continuum has been subtracted off to give the Hα only, the data still contains the NII lines and any remaining continuum between these lines. Thus we cannot do a direct comparison with the Hα only from the spectropolarimetry.

From Table 3.5 we see that the imaging polarimetry values are quite similar. This is probably because the filters are fairly broad. The continuum light in the filaments falls off rapidly along the minor axis and the errors on the polarization measurements rises rapidly. We can deduce that the continuum light is not emitted intrinsically in the filaments, nor scattered towards us by the filaments because there is no evidence for the existence of filaments in the continuum imaging polarimetry. We must conclude that the continuum light is scattered towards us by the galactic dust halo. In all three cases the

[2]The P in this ratio is calculated using normalized Stokes parameters, $\frac{Q}{I}$, $\frac{U}{I}$.

polarization increases with distance from the nucleus, as one would expect for scattering.

Ap	Hα filter (i)		Continuum filter (i)		Hα only (i)	
	P(%)	Angle	P(%)	Angle	P(%)	Angle
1	1.9 ± 0.2	92.0 ± 2.5	1.9 ± 0.2	86.6 ± 3.4	1.9 ± 0.3	92.3 ± 2.5
2	6.8 ± 0.3	85.6 ± 1.3	6.7 ± 0.7	82.0 ± 3.0	7.1 ± 0.8	87.6 ± 3.3
3	8.4 ± 0.6	82.3 ± 2.0	4.6 ± 1.5	80.8 ± 9.4	9.1 ± 1.6	80.7 ± 9.7
4	10.3 ± 1.3	77.5 ± 3.6	18.7 ± 3.6	83.1 ± 5.4	7.4 ± 3.8	73.7 ± 6.5
5	9.2 ± 3.7	61.4 ± 11.5	17.6 ± 10.4	89.1 ± 16.8	7.7 ± 11.1	45.2 ± 20.5

Ap	Hα filter (s)		Continuum filter (s)		Hα only (s)	
	P(%)	Angle	P(%)	Angle	P(%)	Angle
1	3.6 ± 0.2	98.6 ± 1.2	—	—	4.3 ± 0.6	100.5 ± 4.2
2	5.1 ± 0.2	86.9 ± 1.2	—	—	5.0 ± 0.8	87.0 ± 4.5
3	7.9 ± 1.6	90.2 ± 2.1	—	—	7.2 ± 2.0	88.9 ± 7.6
4	14.2 ± 1.2	94.4 ± 2.2	—	—	9.0 ± 2.1	92.1 ± 6.6
5	14.0 ± 1.5	91.1 ± 2.9	—	—	7.5 ± 2.5	89.2 ± 9.4

Table 3.5: Comparison between imaging and spectropolarimetry polarimetry results at the aperture positions for the continuum and the Hα region. The polarization angles are given in degrees.

Comparison between the Hα filter (i) and Hα filter (s) reveals that similar polarizations are measured in Apertures 2, 3, 4 and 5. The spectropolarimetry has a higher value in Aperture 1 which may again be caused by oscillation of the Stokes parameters about zero in the spectropolarimetry, increasing the polarization measured there.

In Aperture 4 continuum subtraction was repeated individually for the systemic velocity component and the blueshifted component. The blue-shifted line had a polarization of (4.8 ± 1.6)% and the systemic component had a polarization of (11.2 ± 1.4)%. This shows the depolarization caused by the lack of polarized intensity corresponding to the blue-shifted line.

The polarization angles were calculated using the Stokes parameters and were mainly found to vary around 90 degrees on average. The imaging polarimetry polarization angles are in general slightly less than 90 degrees, while the spectropolarimetry angles are slightly more. We would expect a polarization of around 90 degrees, since for Rayleigh and Mie scattering the polarization angle is always normal to the illuminating source in a cloud of scatterers. The errors on the polarization angles in the spectropolarimetry are

quite large, reflecting the variations seen in Figs 3.13 – 3.17. Note that for the imaging polarimetry, the polarization angle has been modified to give its angle with respect to the nucleus and not with respect to North. This means it can be compared directly with the spectropolarimetry results.

3.2.7 Conclusions

We have shown that the origin of the polarized light in M82 is quite complex, with components from different scattering geometries being present, mixed with unpolarized emission.

Evidence (Scarrott, Eaton & Axon 1991, and this work) suggests that the Hα polarization comes from a different scattering geometry than that of the broadband continuum polarization. The wavelength dependence of the B, V and C wavebands suggests Rayleigh or Mie scattering as the polarization mechanism and there is ample evidence for the existence of dust grains in M82. A dust halo exists around the galaxy out to 150″, suggested by the extent of the broadband polarizations. The spectropolarimetry clearly agrees with superwind models and we see evidence for a mixture of scattering and intrinsic emission from the walls of the superwind bubble/cavity. Since only the systemic component of M82 is seen in polarized intensity, the blueshifted component must be due to intrinsic emission only.

The decreases in the quite high continuum polarization at the positions of the emission lines are caused by two different effects, (1) depolarization by the intrinsic emission of the blueshifted peak, which in theory should be very low, and (2) the decrease caused the systemic peak could be due to the fact that it comes from a different polarizing geometry – the two mechanisms are not the same and therefore we would not expect identical polarizations.

It would be useful to confirm these results by observing the northern filaments of M82 in spectropolarimetric light. The northern filaments also display the line splitting in Hα and NII, with these lines being redshifted, but in the imaging polarimetry, the northern filaments are less polarized than the southern filaments. This could be an effect of the tilted nature of the galaxy.

A *direct* comparison between M82 and other starburst galaxies may not be particularly useful since M82 differs significantly from them in many ways. It is very disturbed and dusty, and has significant polarization at broadband optical wavelengths. Also, M82

is the only starburst galaxy which is optically thin in CO. However, NGC 1808 was recently found to show similar properties in its central region (Scarrott *et al.* 1993). It is seen mainly as a reflection nebula illuminated by the galactic nucleus but with minor contributions from hotspots. In the rest of the galaxy, the polarization pattern follows the spiral arms indicating polarization by dust grains aligned by the magnetic field in the arms. Forbes, Boisson and Ward (1992) found radial dust filaments in NGC 1808. They think that SNRs and other stellar and gaseous processes associated with starbursts can explain the optical and IR colours and line ratios in the nuclear region of NGC 1808 without need for a black hole, which has implications for AGN theory. Phillips (1993) looked at NGC 1808 and found evidence for a stellar bar and a wind from the nucleus which give it more similarity to M82.

A Hα imaging polarimetry study or a spectropolarimetric examination of other starburst galaxies may be of use in determining their geometries and the nature of their starburst centres since other starburst galaxies have similar bipolar Hα bubbles caused by superwinds.

Chapter 4

Review of NGC 5128 & grain alignment mechanisms

4.1 Introduction

NGC 5128, the optical counterpart to the radio galaxy Centaurus A, is a highly active nearby galaxy. Best known for its extensive radio jets and dramatic visual appearance, it has been intensively studied at most wavelengths. Its optical appearance is that of an elliptical galaxy bisected by a broad lane of obscuring matter. It has been proposed that this dust lane is in fact the remnants of a spiral galaxy which has collided with the elliptical galaxy. Its position is R.A.(1950) = $13^h\ 22^m\ 30^s$; Dec.(1950) = -42° 45′ 30″ and its distance is normally taken to be 5Mpc[1] giving a scale of 1″ equal to 25pc. In this chapter, we will review previous studies of NGC 5128, including previous polarization studies. We will also discuss possible alignment mechanisms of dust grains, which may play an important role in producing the polarization pattern observed in NGC 5128 and discuss wavelength dependence studies of polarization in other extragalactic objects.

4.2 Initial Investigations of NGC 5128

A detailed review of studies of NGC 5128 is given in Ebneter and Balick (1983) so we will highlight the more important of these and refer the reader to this paper and the references

[1] a recent study, Tonry and Schecter (1990), has put the distance at only 3Mpc.

therein for a more detailed discussion. Works published after this review will be discussed in more detail below.

It was originally proposed that NGC 5128 is a spiral galaxy silhouetted against a giant elliptical, but Baade and Minkowski (1954) identified it to be a single galaxy by its radial velocity, although they thought it to be a spiral and an elliptical in collision. The elliptical component is a normal E2 elliptical with a typical spectrum of an old stellar population of late F and early G type stars. Investigations of the velocities of the galaxy have shown that the elliptical part has a very low rotation velocity while the dust component is rotating rapidly at $\sim$ 300 km/sec about the major axis of the galaxy (Graham, 1979; Appenzeller and Mollenhoff, 1980; Hesser *et al.*, 1984). The dust lane is very perturbed and extends as far as $\sim 10'$ from the nucleus (Dufour *et al.* 1979) to the east, while to the west it ends more suddenly, closer to the nucleus. It contains a lot of compact HII regions in a diffuse envelope of low-ionization gas, large numbers of O and B stars, stellar clusters, neutral and molecular clouds of hydrogen and a patchy distribution of gas, as well as large quantities of obscuring dust. The young blue stars rotate with the dust and are responsible for the blue disk continuum. Rodgers (1978) found little reddening in the galaxy outside the dust lane and calculated a reddening law for the dust lane finding it to be similar to the Perseus region of our Galaxy which is normally taken to be representative of the general galactic reddening law for dust clouds which are not in intimate association with star forming regions and ionizing radiation.

The optical nucleus of the galaxy is lies behind the dust lane and Grasdalen and Joyce (1976) have calculated an extinction of (22 $\pm$ 5) magnitudes in that direction. Kunkel and Bradt (1971) discovered a "hot-spot" at 8000Å and proposed it as the nucleus. Adams *et al.* (1983) found an IR nucleus in the K waveband and decided it was the true nucleus. A radio nucleus was found by Burns *et al.* (1983) and it coincided with the IR nucleus within errors. Giles (1986) mapped the IR nucleus at high resolution in J, H and K and concluded that the 2.2μm nucleus is the true nucleus of the galaxy. Table 4.1 shows the positions at which these nuclei have been measured. The R.A. offset is $13^h\ 22^m$ and the Dec. offset is $-42°\ 45'$.

Dufour *et al.* (1979) found that gas in the dust lane could not have been produced by mass loss from stars in the elliptical component. Wilkinson *et al.* (1986) made a complete map of the stellar velocity field within $100''$ of the nucleus. They calculated the elliptical rotation to be $\sim$ 34km/sec and decided that the angular momentum of the central part of the disk is being directed away from us. They modelled possible geometries for the

Wavelength	R.A. (secs)	Dec. (arcsec)	References
8000Å	31.82 ± 0.07	30.3 ± 0.7	Kunkel & Bradt (1971)
Radio	31.65 ± 0.2	30.0 ± 3.0	Wade *et al.* (1971)
X-ray	31.46 ± 0.5	30.3 ± 5.0	Feigelson *et al.* (1981)
X-ray	31.95 ± 0.5	28.5 ± 5.0	Feigelson *et al.* (1981)
Radio	28.3 ± 3.0	31.76 ± 5.0	Burns *et al.* (1983)
2.2μm	32.16	30.0	Adams *et al.* (1983)
K	31.47 ± 0.04	34.6 ± 0.45	Giles (1986)
6000–8000Å	31.86 ± 0.04	30.53 ± 0.4	Giles (1986)
8500–10000Å	31.80 ± 0.04	30.37 ± 0.4	Giles (1986)
Radio	31.6	32.0	Bell & Seaquist (1988)
3.16μm	31.47 ± 0.04	34.6 ± 0.45	Turner *et al.* (1992)

Table 4.1: Estimates of nuclear positions in NGC 5128. The R.A. offset is 13^h 22^m and the Dec. offset is –42° 45′.

elliptical and dust lane. Bland *et al.* (1987) looked at the structure and kinematics of the ionized gas within NGC 5128 by observing the ionized gas in NIIλ6548 and Hα. Their results suggest that the dust lane is the projection of a severely warped thin disk of gas and dust. The velocity fields show well-ordered rapid circular motions within the ionized gas.

The IR morphology appears to be primarily determined by the presence of a thin absorbing warped disk (Quillen, Graham and Frogel, 1993). The geometry of this disk is consistent with it having evolved as a result of differential precession in a prolate potential. A scenario is proposed where a small gas-rich galaxy infalling under the force of dynamical friction is tidally stripped. Stripping occurs at different times during its infall. The orientation of the resulting gas disk depends on the angular momentum of the infalling galaxy. They find that it is probable that excess emission along the direction of the jet is necessary to account for the elongation.

4.2.1 Radio and X-ray Studies

NGC 5128 was identified as the optical counterpart of Cen A by Bolton, Stanley and Slee (1949). Although it is only 5Mpc away its radio structure stretches for over 1Mpc

and covers 10° of the sky. Since then extensive radio and X-ray investigations have been carried out. The nucleus is surrounded by three radio lobes. The outer pair seem to resemble a normal extragalactic radio source with extended X-ray emission associated with inverse Compton scattering of the microwave background by relativistic electrons in the radio lobe. The middle lobe is 23′ from the nucleus and the inner lobes are 12′ from the nucleus. The compact non-thermal nucleus (< 0.01pc) displays some variability at certain wavelengths and time-scales and its radio spectrum is strongly inverted. Connecting the northern inner lobe and the nucleus is a narrowly collimated channel of radio and X-ray emission known as the radio jet with a position angle of 55°. Figure 4.1 shows details of the radio structure.

Schreier *et al.* (1979) first mapped the X-ray structure of NGC 5128. They found a nucleus at the position of the IR nucleus, diffuse emission equivalent to the inner radio lobes, a 4′ extended region about the nucleus and an X-ray jet between the inner NE radio lobe and the nucleus, extending out to the inner optical jet. Schreier, Burns and Feigelson (1981) detected radio emission from the X-ray jet at 6 and 20cm and found the morphology to be very similar. Feigelson *et al.* (1981) found X-ray structure associated with the compact radio nucleus, an X-ray jet pointing at the NE inner radio lobe, emission associated with the middle lobe, the dust lane and diffuse emission around the nucleus. The X-ray nucleus is variable and is at the same position as the radio/optical nucleus within errors. The jet is a series of collimated knots from 8″ to 4′ between the nucleus and the inner NE radio lobe.

Burns, Feigelson and Schreier (1983) investigated the inner radio lobes and jet which are separated by ∼ 4′. The origin of the inner radio emission is most likely synchrotron radiation where electrons are captured and accelerated in a helical path around a line of force in a magnetic field. As the electron is accelerated it emits electromagnetic radiation normal to the helical path. This radiation is polarized. The inner lobes are asymmetric with the northern lobe more compact and slightly more powerful with higher polarizations than the southern lobe. Burns, Feigelson and Schreier (1983) suggest that perhaps the southern lobe is located behind the centre of the galaxy resulting in Faraday depolarization by a magnetic field in the clumpy ISM. The radio jet is clumpy with several knots. The inner jet has a moderate polarization at 6cm but little or no polarization at 20cm. This is perhaps due to internal Faraday effects. Burns, Feigelson and Schreier (1983) calculate the velocity of the jet to be ∼ 5000 km/sec.

The radiation has a curved S-like appearance perhaps due to the precession of the

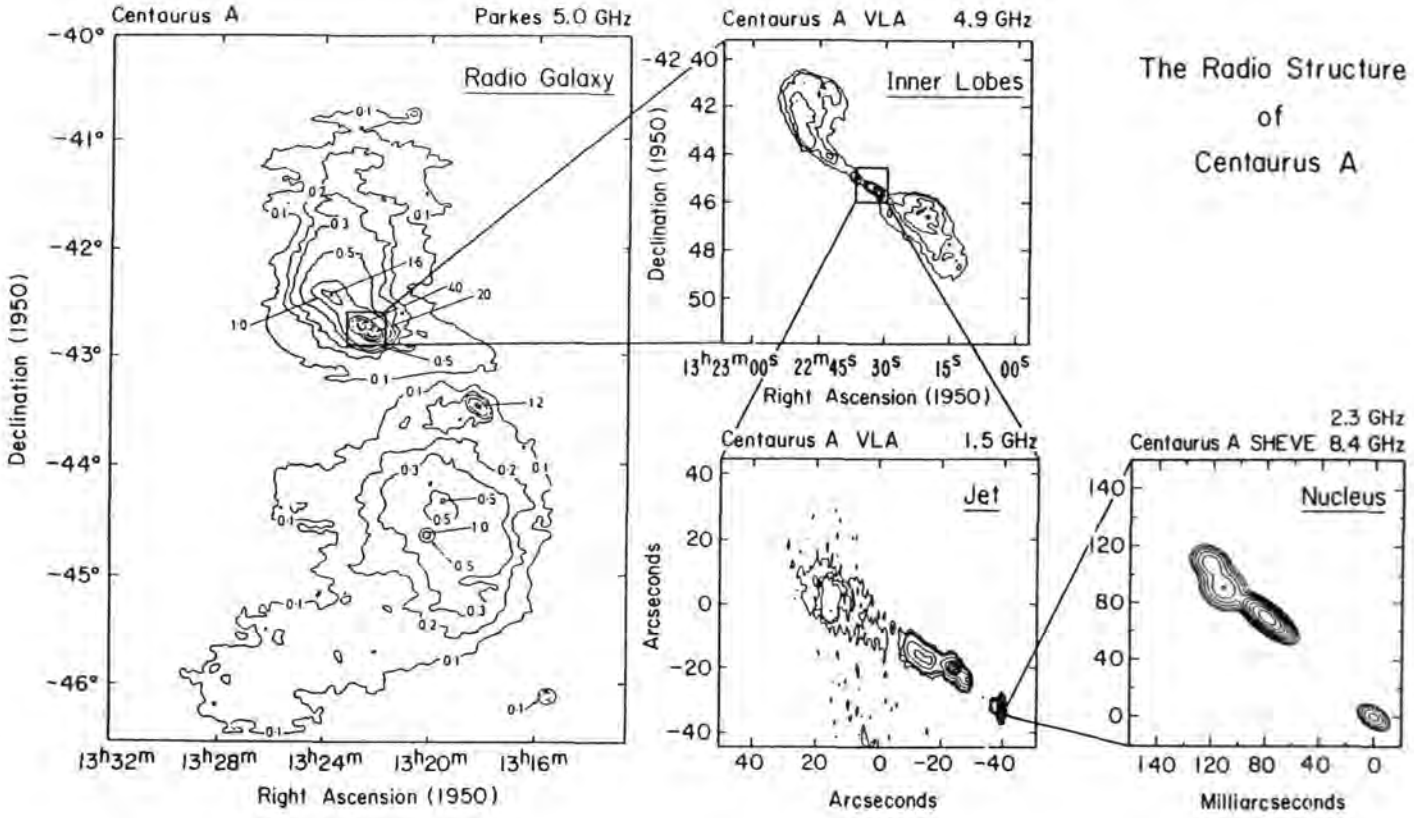

Figure 4.1: The radio structure of NGC 5128 (Centaurus A). The map is taken from Figure 4 of Burns, Feigelson and Schreier (1983) and Figure 11 of Meier *et al.* (1989). It shows the outer middle, middle and inner lobes at different wavelengths and resolutions, the radio jet and the nuclear structure down to milliarcseconds scales.

nucleus or an effect of the gas in the galaxy outside the nucleus pressing on the plasma beam. There is no counterjet in evidence, perhaps the emission from the jet pointing towards us is greatly enhanced and the emission from the jet pointing away from us is greatly reduced. The jet is $\sim$ 1kpc long (40″). The coincidence of the radio and the X-ray jet is another pointer toward synchrotron emission. The spectral index of the jet increases as one moves away from the nucleus indicating ageing of relativistic particles.

Clarke *et al.* (1986) obtained high resolution 2 and 6 cm observations of the inner radio jet and examined the filamentation and polarization in this region. The inner 40″ of the jet displays a side-to-side edge-brightened structure which had never been seen before in an extragalactic jet. They found limb brightening due to internal and external shocks which had been theorised for jets. Meier *et al.* (1989) made very high resolution radio observations of the nucleus of Cen A and resolved it into a compact core, a jet with three knots 100 – 160 milliarcseconds and a long component at the same P.A. as the knots (51° $\pm$ 3°). This is in agreement with the radio and X-ray data. The jet exhibited variability.

The 21cm observations of NGC 5128 showed that the HI is associated with the dust lane and is similarly warped (Van Gorkom *et al.*, 1990). The HI velocities of the inner parts agree with the optical emission line velocities and indicate that the dust lane is a warped rotating system. The outer parts however do not agree implying that in the outer regions the gas disk is unstable and not settled in its orbit. This implies that the dust and gas is recently captured.

The first indications of a counter-jet were found in two compact features in the southern lobe, roughly aligned with the northern jet (Clarke, Burns and Norman, 1992). There are differences between the polarizations in the lobes and the direction of the magnetic field inferred from the polarizations is generally aligned with the long axis of the filaments. The transition from lobe to jet occurs at the point of the first Malin shell (Gopal-krishna and Saripalli, 1984).

A recently published long-term (12 year) study of the nucleus of NGC 5128 by Botti and Abraham (1993) found that the behaviour of the radio flux densities at 22 and 43GHz was very similar to those of quasars and BL Lacs. They propose a model where the nuclear source is formed by a quiescent or slowly varying compact core, and one or more expanding components which are responsible for the observed variability. There is some evidence that the variable components are located in the milliarcsecond jet.

4.2.2 Infra-red Studies

Telesco (1978) examined the 10μm emission from the dust lane, showing that the composition of the dust lane seems to be ordinary interstellar dust with a silicate component. Harding *et al.* (1981) showed that the near-IR is dominated by the elliptical component and as one goes out to longer wavelengths vigorous star formation becomes apparent within the dust lane.

Adams *et al.* (1983) mapped the galaxy at 2.2μm. The nucleus shows up prominently on their map. The elliptical component can be clearly seen, with absorption features at the edges of the dust lane. The nuclear position is given in Table 4.1. Lepine *et al.* (1984) found underlying stellar emission at the nuclear position. They also found some evidence for variability in the L waveband. Giles (1986) mapped the nucleus at high resolution in J, H and K. He agreed with Adams *et al.* (1983) that the K nucleus is the true nucleus, offset from the hotspot of Kunkel and Bradt (1971) by 5.8″ to the NE. The hot-spot appears to be located at the position of the radio knot N1 of Burns *et al.* (1983).

Marston and Dickens (1988) observed NGC 5128 at 12, 25, 60 and 100μm. All maps show general disk-like emission with a peak at the nucleus and an extension to the SE and NW which coincides with starforming regions. This extension is more obvious at 12 and 25μm. They found extended far-IR emission across the whole dust lane, due to heating of grains by hot O and B stars. They calculated that about a third of the gaseous material in the dust lane is involved in star formation, and that there is a star formation efficiency of about 30% which is very high, or else there is an extra ionizing source heating the grains (probably the nucleus). Nearly all of the IR luminosity is produced by thermally emitting dust grains heated by massive young stars distributed through the optically thick dust lane.

Joy *et al.* (1991) looked at the central 40″ of the galaxy in J, H and K. In K they found a compact source superposed on a smooth profile of the underlying elliptical galaxy. In J and H they found an elongated 10″ emission feature to the NE and called it an IR jet. It has the same P.A. (55°) as the radio and X-ray jet and coincides with knot N1 of Burns *et al.* (1983) and the hotspot of Kunkel and Bradt (1971). It is most prominent in the J waveband. They infer that there is probably a physical connection between the IR, radio and X-ray emission mechanisms. Continuum emission processes dominate in the jet, i.e. there are no emission lines. They suggest near-IR imaging polarimetry of the nucleus as a means to discriminate between scattering and entrainment as the source of the emission.

In contrast to previously studied optical and IR jets in nearby active galaxies the short wavelength prominence of the jet indicates that it cannot be attributed to synchrotron emission from a beam of relativistic electrons. The observed properties of the IR jet are similar to those seen in distant radio galaxies.

Turner *et al.* (1992) obtained high-resolution images of the nucleus at J, H, K and 3.26μm. Their results are similar to those of Joy *et al.* (1991). The 3.26μm image shows a compact nuclear source (at the same position as that of Giles, 1986) with negligible galactic emission. The central source is $<$ 36pc in diameter (1.5″ at 5Mpc). A diffuse blue spot is visible to the NE of the nucleus on a J – H image. It is at the position of the IR jet and is 7.6″ from the nucleus at a P.A. of 45° NE. The J and H images are not resolved at the nuclear position which means there must be substantial extinction toward the nucleus *or* an intrinsically red nucleus. They conclude that the 3.26μm is the true nucleus and the blue spot to the NE of the nucleus is at the position of the Kunkel and Bradt (1971) hotspot. There is an alignment between the nucleus-to-blue spot line and the radio jet direction which leads them to assume that the blue spot is not caused by foreground emission.

The blue spot, if interpreted as emission from late-type giant stars, has 4 – 8 magnitudes less visual extinction than other regions close to the nucleus. No unique model has been postulated but one possible model involves the clearing of a cone of dust along the disk axial direction by a nuclear jet, close to the nucleus. In order to view the cleared region with little attenuation, either the foreground portion of the disk must be thin or the disk must be inclined to the line of sight. Such a geometry can also be used to explain the increasing extinction to the SW of the blue spot and the nucleus.

4.2.3 Optical Jets, Filaments and Shells

Blanco *et al.* (1975) found a faint optical filamentary structure extending in the form of a jet into the outer radio NE lobe. There were three components to this jet: an extended gaseous filaments with a few knot-like concentrations, isolated bright knots strong in Hα and the ultraviolet (UV), and a loose chain of resolved blue compact objects. This jet is at a position angle of 55° and passes 7.8″ from the Kunkel and Bradt hotspot. Dufour and Van den Bergh (1978) found a chain of faint diffuse elongated optical emission regions located between the nucleus and the "outer jet" of Blanco *et al.* (1975). Associated with this inner jet are two blue knots, a number of small dust patches and an elongated Hα

filament. They find that the jet is located on the nearside of the galaxy. Brodie and Bowyer (1985) made optical observations of the inner regions of the jet and showed that the optical features located at the site of the X-ray/radio knot B correspond in length and breadth to the X-ray and radio dimensions. The optical knot is a compact condensation confined to the region of the jet alone.

Malin *et al.* (1983) processed photographs of the galaxy and found a series of shells within the extended elliptical component. These shells are interpreted as being the aftermath of a merger with a smaller disk galaxy and have been observed in other merger galaxies. Gopal-krishna and Saripalli (1984) found that the bend in the inner radio jet occurs at the point of its intersection with the first shell of Malin *et al.* (1983), and there is also an X-ray emitter at the same position. They suggest that the jet is deflected by the shell and the bend in the jet is not due to precession of the galaxy as was previously thought.

Figure 4.2 shows the position of the knots and filaments. Spectroscopic observations of the optical filaments found that their velocity spread was such that they could not have travelled from the nucleus to their current position in their present state. This implies that they are temporary features and will disperse over 10^6 – 10^7yr (Graham 1983). Brodie, Konigl and Bowyer (1983) discovered three regions of intense optical emission in the inner 2 kpc of the jet. Two of these regions coincide with X-ray and radio knots and the third is situated between the other two at a low brightness interknot zone in X-ray and radio. The first two regions emit strong continuum radiation with superposed emission lines while the third has little continuum flux but intense emission lines. It is not a HII region but is probably caused by shock-heating or photo ionization. Nuclear UV flux can penetrate the dust lane through a tunnel excavated by the jet and photo-ionize those clumps which lie within the initial opening angle of the jet. Morganti *et al.* (1991) performed narrowband imaging and longslit spectroscopy of the inner and outer optical filaments and found them to be predominately photoionized by a continuum source with spectral properties characteristic of an AGN hidden from view. The nucleus shows blazar characteristics: radio and X-ray variability and intrinsic IR polarization (Bailey *et al.*, 1986) implying that the blazar is not beamed directly towards us. The beaming in their model is not brought about by obscuration of the core by, say a dusty torus, since the obscuration radiation would be re-radiated in the IR and the required IR flux is not observed. Thus the required beaming presumably corresponds to relativistic beaming in a UV/X-ray continuum. The filaments have complicated clumpy substructures with

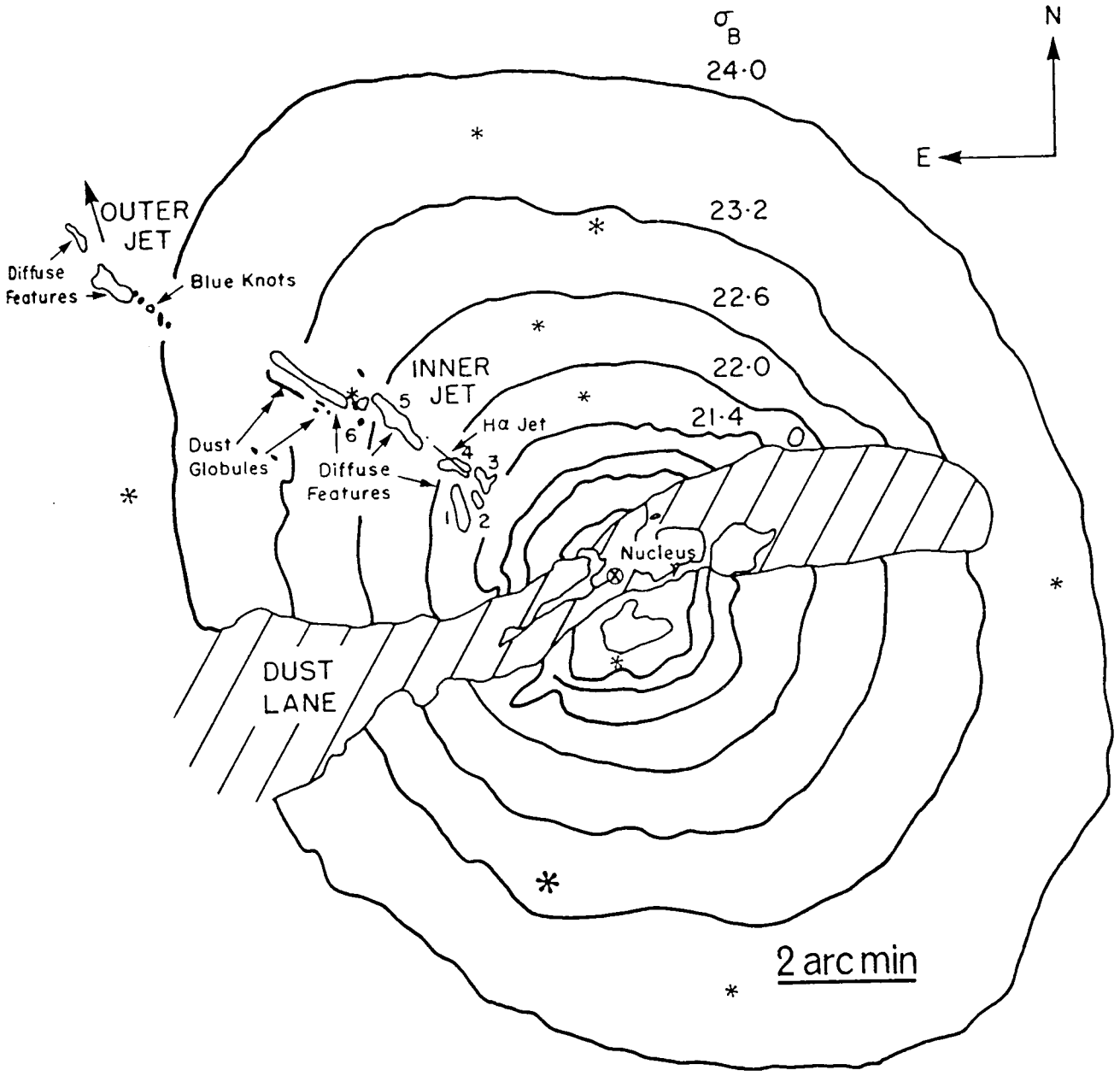

Figure 4.2: A line drawing of the knots and filaments in NGC 5128 (Ebneter and Balick, 1983).

significant velocity gradients in individual knots. Morganti *et al.* (1991) found no evidence for a counterjet. In Morganti *et al.* (1992) it is shown that there is an ionization gradient in the inner filaments and argue that the direction of the ionization gradient supports their model. The ionization source of the knots is not local but external and the most likely explanation is a photon stream from the direction of the nucleus.

Sutherland *et al.* (1993) modeled the excitation of the emission line filaments. Interaction of the northern radio jet with a dense cloud of material at the location of the filaments causes shock waves with velocities of $\sim$ 200-400km/s. The shocks produce a strong flux of EUV and X-ray radiation which photo-ionize the visible knots. The mechanical flux of a mildly supersonic low-density jet is sufficient to energise the shock waves through the production of supersonic turbulent velocities via the Kelvin-Helmholtz instability. They disagree with Morganti *et al.* (1991): a narrow ionizing radiation beam is not required to produce the observed phenomena.

4.2.4 Molecular Studies

Early molecular studies detected H_2CO in absorption in the direction of the nucleus (Gardener and Whiteoak, 1976) and found $^{12}CO(2-1)$ emission along the dust lane out to 2 arcmins from the nucleus (Phillips *et al.* 1987). The radial distribution of the H_2 is similar to that expected from small Sc galaxies. The molecular gas is concentrated most at the inner radii ($<$ 3kpc), the atomic gas is at larger radii. No infalling molecular gas was detected and the kinematics of the CO indicated circular rotation.

Bell and Seaquist (1988) detected several types of molecules in absorption, including C_3H_2, OH and H_2CO. They had previously detected C_3H_2 in absorption against the radio nucleus (Seaquist and Bell, 1986) and now found it in emission in the nuclear region in the dust lane. Seaquist and Bell (1990) obtained absorption spectra of OH, H_2CO and NH_3 against the nuclear continuum radio source and H_2CO against the radio jet. The dust lane absorption is due to a number of molecular clouds or the edge of a large molecular cloud. They detect OH gas falling toward the nucleus with a distinctive composition that has been shocked or excited by nuclear radiation.

Israel *et al.* (1990) detected molecular emission from H_2 and absorption of $^{12}CO(1-0)$ and $^{13}CO(1-0)$ towards the nucleus. They suggest that the H_2 is from an unresolved ($< 4''$) nuclear source which is perhaps collisionally excited. They also suggest a circum-nuclear disk with an outer radius of 160pc and thickness of 80pc and a density falloff

which goes as r^{-2}. Israel *et al.* (1991) looked at the emission spectra of $^{12}CO(1-0)$, $(2-1)$ and $(3-2)$ towards the nucleus and found two components, a broad plateau and underlying narrower emission due to extended emission from the dust lane. The plateau corresponds to a circumnuclear disk with a radius of $\sim$ 820pc. In absorption they examined $HCO^+(1-0)$, $^{12}CO(1-0)$, $(2-1)$, $(3-2)$, $^{13}CO(1-0)$ and $C^{18}O(1-0)$. They calculated an excitation temperature of $\sim$25K in the circumnuclear disk and found that some of the absorption features are redshifted, implying warm dense gas falling into the nucleus.

Eckart *et al.* (1990a) made maps of the $^{12}CO(1-0)$, the 50μm and 100μm continuum emission, and measured the $^{12}CO(2-1)$, $^{13}CO(1-0)$ and $C^{18}O(1-0)$ emission at certain points along the dust lane. The $^{12}CO(1-0)$ emission is concentrated along the dust lane with the centre of rotation at the IR/radio nucleus position. The velocities indicate a solid body rotating and not a rotating molecular ring. There is no strong velocity distribution at the centre. The UV emission and metallicity in the dust lane is equivalent to those from spiral galaxies and star forming regions in our Galaxy. About 50% of the 100μm emission is due to cold dust not associated intimately with star forming regions, with larger spatial extent than the molecular disk. Eckart *et al.* (1990b) looked at the absorption lines of ^{12}CO, ^{13}CO, HCO^+, HCN, CN and CS towards the nucleus. Abundances, excitation temperatures and densities of absorbed and emitted molecular gases in the disk are similar to values obtained for the disks of other galaxies.

Quillen *et al.* (1992) examined the kinematics of the $^{12}CO(2-1)$ emission along the inner dust lane. They found the molecular gas was distributed in a thin disk with a velocity dispersion of $\sim$ 10km/sec. They modelled this property and found that a warped disk with a prolate potential is a good fit to the profile shapes. The morphology and kinematics of the molecular gas is similar to that of the Hα (Bland *et al.* 1987). The best-fit warped disk model matches the optical appearance, the CO emission and the HI at larger radii.

4.2.5 Millimeter and sub-millimeter

Hawarden *et al.* (1993) presented maps of NGC 5128 at several millimeter and sub-millimeter wavelengths measured over a period of time. The nucleus is unresolved (6″) at 800 and 450 μm. The emission from the central source is non-thermal. The flat spectral shape of the nucleus is indicative of a blazar. A ridge of emission is apparent in the 800μm

data at 30″ on either side of the central source at P.A. 145°, parallel to the IR polarization vector of Bailey *et al.* (1986). It is also apparent at 450μm and has a thermal spectrum which indicates that it may be due to emission from warm dust in the circumnuclear torus suggested by Israel *et al.* (1990). They calculate the overall dust-to-gas ratio to be $\sim$ 330 which is higher than that for our Galaxy.

4.2.6 Collision

Tubbs (1980) modelled NGC 5128 as the partially relaxed product of a collision between a small, gas-rich spiral galaxy and a large, relatively gas-free, nearly prolate elliptical galaxy. Such a collision will result in the small, gas-rich galaxy smearing into a ring or annulus about the centre of the elliptical galaxy. From his model parameters he calculates that the distorted annulus most resembles the observations at 3.3 $\times$ 10^8 years.

Recent work by Thompson (1992) provides evidence in favour of the collision hypothesis, implying the dust lane is the remnant of the disc of a small gas-rich spiral galaxy that collided with the elliptical part $\sim$ 5 $\times$ 10^8 years ago. This galaxy shredding (Arp, 1967) occurs when a spiral galaxy undergoes a strong prograde interaction with a massive galaxy. The disk of the spiral is disrupted during the encounter and the massive galaxy captures up to half the disk material. Thompson (1992) has tentatively identified the nucleus of the spiral galaxy and the remains of the disk which continued past NGC 5128 after the interaction.

4.3 Previous Polarization Studies of NGC 5218

Initial polarization studies were carried out by Elvius and Hall (1964). They obtained estimates of the polarization at various positions within the dust lane using photoelectric photometry. They found dust lane polarization with values up to 6%, with the E vector parallel to the dust lane.

Jura (1982) modelled galaxies with pronounced dust lanes whose polarization vectors run parallel to the dust lane. Using an optically thin cloud of Rayleigh scatterers located at the centre of a thin disk he obtained model polarization values of up to 5% in the dust lane from simple scattering.

Berry (1985) mapped the polarization vectors of NGC 5128 in a broad V filter. This map showed that the dust lane is polarized with the vectors aligned parallel to the

dust lane and with polarization values of 4 – 5%. The elliptical component of the galaxy is not significantly polarized and the outer regions of the dust lane have polarization values of around 10%, with the vectors tangential to the line joining them to the nucleus. He calculated the extinction in the dust lane by subtracting a fitted model elliptical component from the dust lane and plotted measured polarization versus the extinction. The result was a scatter plot with a linear form which appeared to indicate that the polarization pattern included an aligned grain component. The slope was 2.5%/mag which compares with the value of 3%/mag obtained for our Galaxy. He tested whether simple scattering from spherical or unaligned grains could produce the observed polarizations and ruled out certain assumptions which could produce higher polarizations i.e. the dust lane is not an optically thin cloud of Rayleigh scatterers located at the centre of a thin disk. He modelled the scattering geometry using multiple scattering from Mie particles with an optically thick, more realistic geometry. The particles had a power-law grain size distribution.

His model produced polarizations that were significantly lower than those observed and despite varying model parameters such as the power law index and the refractive index of the dust grains he could not obtain polarizations of the observed values. Only by including the effect of extinction from elongated dust grains aligned in a toroidal magnetic field in the dust lane could he obtain polarizations as large as the observed values. The magnetic field was assumed to be similar in strength to that in our Galaxy. Previous studies of grain alignment and polarization (Purcell 1979; Cugnon 1983; Scarrott *et al.* 1986) lend credence to this proposal.

The polarization of the IR nucleus in the J, H, K and L wavebands was measured by Bailey *et al.* (1986) for a number of aperture sizes. The polarization in J in the largest aperture is similar to the dust lane component. As the size of the aperture decreases the polarization increases and the polarization angle changes. There is a residual polarization after removal of the component due to dichroic absorption in the dust lane. The remaining polarization is due to embedded thermal source polarization by interaction with additional dust near the nuclear region *or* an intrinsically polarized very red point source. Emission from sources without intrinsic polarization (accretion disk, small grains) would need to interact with dust grains in the nuclear vicinity to produce the observed polarization. The polarization angle is almost perpendicular to the radio angle and this leads them to suggest that the nucleus may well be a blazar.

Of the possible thermal sources, those most likely to relate to the radio AGN in-

clude thermal gas emission from an accreting black hole, starlight from a compact central starburst, and/or emission from transiently heated small grains (frequently associated with starburst regions). While a compact starburst cannot be eliminated as the AGN source, no starburst nucleus exhibits variability like this. The blackbody colour temperatures argue against any dust component except small transiently heated dust grains since larger dust grains typically exhibit lower temperatures than those found. If these hot grains are elongated and partially aligned they could produce intrinsically polarized light. Synchrotron emission is another possible inherently polarized source in the region.

Hough *et al.* (1987) have measured the wavelength dependence of the polarization at one point in NGC 5128, using the supernova SN1986G which went off behind the dust lane. Their results will be discussed in detail in Chap. 5. They found a fit to a Serkowski equation (see Sect. 4.5) with $\lambda_{max} = 0.43\mu$m and $P_{max} = 5.16\%$. This implies the polarization is caused by aligned non-spherical dust grains in a magnetic field.

4.4 Grain Alignment Mechanisms

In Chapter 5 we will undertake a multi-wavelength polarimetric study of NGC 5128. Following the work of Serkowski *et al.* (1975) the wavelength dependence of the polarization of an object can be used to calculate a number of properties of that object. Firstly, assuming the grains are aligned by a process similar to the Davis-Greenstein (DG) paramagnetic relaxation process (Davis and Greenstein, 1951), the position angle of the polarization vector gives the projected direction of the magnetic field aligning the grains. Secondly, the maximum value of polarization relative to the value $E(B-V)$ gives a measure of the efficiency of dust grain alignment and hence the strength of the magnetic field. Thirdly, the ratio of total to selective extinction, $R = A_v/E(B-V)$, can be calculated from the wavelength at which maximum polarization occurs since the two are strongly correlated.

4.4.1 The Davis-Greenstein Effect

An elongated or flattened dust grain, rotating at high speed, will undergo a dissipative torque originating in the coupling of its induced magnetic momentum with an external magnetic field and will tend to align its shortest axis of inertia along the field. The grain then scatters (or absorbs) starlight differently following the direction of polarization of

the incident radiation and because the grains are roughly aligned the same way, a net large scale effect is observed (Davis and Greenstein, 1951).

One assumes that the dust particles responsible for the polarization of light are elongated and dielectric and have paramagnetic properties. Interstellar grains are composites of very small grains. A small fraction of these particles are iron or superparamagnetic (SPM) material. If and only if a large grain contains one or more SPM inclusions then the grain aligns with the magnetic field. Since large grains are more likely to contain at least 1 SPM, they are more likely to be aligned that small grains. Non-dielectric grains are assumed to be not elongated and not aligned.

Davis and Greenstein (1951) examined the dynamical behaviour of the magnetic torque was examined in some detail and they emphasised the fundamental role of the imaginary part of the paramagnetic susceptibility, the real part giving rise to a conservative torque without real alignment efficiency. The dissipative torque associated with the imaginary susceptibility was shown to induce a slow angular momentum in the grain tending to align its shortest axis of inertia along the magnetic field, this orientation corresponds to a minimum dissipation of energy.

Jones and Spitzer (1967) made a detailed analysis of the possible magnetic behaviour of different types of grains and suggested superparamagnetism as a means to increase the imaginary part of the magnetic susceptibility by an important factor. They discussed the orientation of a grain in a magnetic field by paramagnetic relaxation. They predicted that grains can align quickly if the imaginary part of the magnetic susceptibility is greatly enhanced over that of most substances. Such enhancement (SPM), could be caused by small clusters of ferromagnetic atoms or molecules (e.g. metallic Fe, Fe_3O_4, etc.). If the inclusions of the ferromagnetic material are small enough, the grain has a normal paramagnetic susceptibility but with the imaginary part 10^6 times the usual value.

Another important feature for the orientation mechanism is the rotation of the particles. The grain is initially rotating due to random collisions with ambient atoms and molecules. Purcell (1975) proposed a method whereby the speed of rotation may be greatly increased. This suprathermal[2] spinup mechanism involves the nonthermal ejection of particles (molecules or electrons) from certain active sites on the surface of the grain. Small variations of surface properties of the dust particles may lead to incident hydrogen atoms wandering over the grains surface and combining into H_2 molecules preferentially

[2]It is called suprathermal because it is dependent on the temperature of the grain and the temperature of the ambient gas

at these active regions. The recoil from these ejections makes the grain spin rapidly and the Barnett effect quickly aligns the angular velocity of the grain with the angular momentum. If the active regions are sufficiently immobile on the surface, a 'rocket' effect arises which speeds up particle rotation (up to 10^9 s^{-1})

The axis of rotation is always the major axis of inertia because internal dissipation of rotational energy brings the grains principle axis of greatest inertia into line with the suprathermal angular momentum. The effect of suprathermal rotation on the magnetic alignment of interstellar grains is such that the DG process would bring the grains axis of spin slowly but surely into parallelism with the magnetic field. The alignment would eventually become complete, not partial as it must be without suprathermal rotation. A good review of this process is given in Ruzmaikin *et al.* (1988).

Alignment of dust grains by magnetic fields renders the interstellar medium optically anisotropic. The resulting ability to preferentially extinguish light whose electric vector is parallel to the major axes of oriented grains manifests itself in the linear polarization of light from distant objects.

4.4.2 The Barnett Effect

The Barnett effect is the opposite of the Einstein–de Hass effect in which magnetising a body causes it to rotate. A paramagnetic or ferromagnetic body rotating freely in a field-free space spontaneously develops a magnetic moment parallel to the axis of rotation.

An isolated cylinder rotating freely with angular momentum $I\Omega$ about a vertical axis contains N unpaired electrons with their spins initially half up and half down: $N_u = N_d = N/2$. The magnetisation M is zero. The rotational energy could be reduced while keeping the total angular momentum constant if some of the angular momentum $I\Omega$ could be transferred to the spin system by turning some of the electron spins over, thus $N_u \neq N_d$.

Given some coupling between the macroscopic rotation of the cylinder and the spin system, this readjustment must occur to a degree determined by the energetic cost of a spin flip and the temperature of the system. Coupling between the spin system and the rotation of the lattice provided by the angle-dependant terms in the dipole-dipole interaction of neighbouring spins. The strength of the coupling between the rotational degree of freedom and the spin of the system will only determine how quickly the equilibrium state is attained. For a paramagnetic material the magnetisation M (the magnetic moment

per unit volume) is $M = \chi\Omega/\gamma$ where Ω is the angular velocity of the rotating body, χ is the magnetic susceptibility of the material and γ is the magnetogyric ratio of electron spins, the ratio of magnetic momentum to angular momentum. This can be expressed in another way by introducing the "Barnett equivalent" field H_{Be}, defined as Ω/γ. We can then say that the rotating object is magnetised exactly as strongly as it would be if a rest in a field H_{Be}.

If the current appearance of NGC 5128 is due to a collision between an elliptical galaxy with a smaller spiral galaxy than a possible explanation for the magnetic field is that it belonged to the disk of the spiral galaxy and was flux frozen into the dust and gas. Charged particles moving in a magnetic field experience forces which tend to make the particles move in spiral paths around the magnetic flux lines. (Radiation emitted by the charged particles is known as synchrotron radiation if the particles are moving at relativistic speeds, and as cyclotron radiation otherwise). Uncharged particles do not experience these forces. However collisions between the charged and uncharged particles dampens the velocity components of the uncharged particles which are not parallel to the field lines. If gas and dust (uncharged particles) are forced to move normally to the flux lines (e.g. by strong gravitational forces) then the motion of the charged particles, which constitutes a current, will tend to set up a magnetic field such that the flux lines appear to be dragged along with the gas. Thus the flux lines appear to be frozen into the gas and dust.

4.5 The Serkowski equation

Serkowski *et al.* (1975) measured the linear polarization of about 180 stars for wavelengths of 0.45μm to 0.8μm and found that the normalized wavelength dependence of interstellar polarization follows a single empirical curve:

$$\frac{P(\lambda)}{P_{max}} = \exp(-K \ln^2 \frac{\lambda_{max}}{\lambda}),$$

where λ_{max} is the wavelength at which maximum interstellar linear polarization P_{max} occurs. They found a value of 1.15 for K fit their curve. λ_{max} was in the range 0.45 – 0.85μm and from the colour excesses they calculated that R, the ratio of total to selective extinction can be expressed by $R = 5.5\lambda_{max}$. R is usually given by $R = A_V/E(B-V)$. P(%)$/E(B-V)$ is a measure of the alignment of dust grains by a magnetic field. The

magnetic field has negligible influence on λ_{max} which, like R, is determined mainly by the average size of the dust grains. Serkowski *et al.* (1975) found that $P(\%)/E(B-V)$ is always less than or equal to 9%/mag for our Galaxy. Whittet and van Breda (1978) made further observations and found a linear correlation between λ_{max} and R, the ratio of total to selective extinction. They deduced that $R = (5.6 \pm 0.3)\lambda_{max}$.

Wilking *et al.* (1982) revised the Serkowski equation after studying the wavelength dependence of stars from UV to IR so that K varied with λ_{max} as

$$K = (-0.01 \pm 0.05) + (1.86 \pm 0.9)\lambda_{max},$$

and this was further revised by Whittet *et al.* (1992) to be

$$K = (0.01 \pm 0.05) + (1.66 \pm 0.09)\lambda_{max}.$$

Linear polarization caused by the alignment of dust grains, shows a λ_{max} which varies from star to star. It is usually in the range 0.1 - 1.0μm with an average of 0.55μm. The empirical law of Wilking *et al.* (1982) fits the form of $P(\lambda)$ very well. The correlation between λ_{max} and R can be understood in a reasonable but qualitative way by the idea that both large λ_{max} and R are associated with particles which are larger than average. There is no correlation between P_{max} and $E(B-V)$ except that their ratio never exceeds 9%/mag. This can be explained by the fact that a tangled magnetic field or imperfect grain alignment can easily lower $P_{max}/E(B-V)$. The largest values of $P_{max}/E(B-V)$ must be associated with those directions with the most uniform magnetic field and perfect alignment. The observed maximum value implies almost perfect spinning alignment.

Details of previous studies of wavelength dependence of polarization are given in Table 4.2. Martin and Shawl (1979) measured the dependence at one position in M31 and found a low value of λ_{max} which implies that the aligned grains in M31 are about 20% smaller than Galactic grains, assuming they have the same chemical composition. This in turn gives a low value of R. Their values for $P_{max}/E(B-V)$ are quite high implying there is a good alignment efficiency. Clayton *et al.* (1983) found an average λ_{max} of 0.58μm from 26 stars in the LMC. This gives R = 3.25 which compares well with a value of $R = 3.1 \pm 10\%$ calculated in an alternate manner. The range of λ_{max} shows a normal Galactic range. About two thirds of their stars are fitted well by a Serkowski curve, the remainder show considerable deviance. Scarrott *et al.* (1990) calculated $\lambda_{max} = 0.42\mu$m

Object	λ_{max} (μm)	R	Authors
Our Galaxy	0.545 (av.)	3	Serkowski *et al.* 1975
Our Galaxy	0.52 – 0.58	2.93 – 3.25	Whittet & van Breda 1978
ρ Oph,M78, NGC 2264	–	4 – 6	Whittet & van Breda 1978
M31	0.43 $\pm$ 0.06	2.41 $\pm$ 0.13	Martin & Shawl 1979
S78 in M31	0.45 $\pm$ 0.05	2.52 $\pm$ 0.14	Martin & Shawl 1982
LMC	0.49 – 0.65	3.25	Clayton *et al.* 1983
Our Galaxy	–	3.09 $\pm$ 0.03	Rieke & Lebofsky 1985
NGC 5128	0.43 $\pm$ 0.01	2.41 $\pm$ 0.13	Hough *et al.* 1987
M104	0.42	2.35 $\pm$ 0.13	Scarrott *et al.* 1990

Table 4.2: Wavelength dependence studies of extragalactic objects

for M104 and hence R_{M104} is 2.35. However, it must be remembered that the relation $R = (5.6 \pm 0.3)\lambda_{max}$ was derived from measurements of our Galaxy and may not be valid for other galaxies.

For each aligned grain the polarization is the difference in extinction along the minor and major axes, while the extinction is the average of the extinction along the two axes. This implies there is a close relationship between the wavelength dependence of the polarization and the extinction of an aligned grain, while the degree of alignment affects only the measured polarization. R is related to the mean size of the grains responsible for extinction but is not simply proportional. For $P_{max}/E(B-V)$, the linear upper limit is the value of P under the most favourable conditions possible for a column of dust. $P_{max}/E(B-V)$ is dependent on many factors including alignment efficiency, the orientation of the magnetic field along the line of sight, the fraction of aligned and unaligned grains and R. The normalized parameter P_{max}/A_V, is a better absolute measure of the magnitude of polarization from a certain column of dust and removes any colour dependence. The decline in P_{max}/A_V with increasing R can be produced if

1. grains grow by small grains sticking to larger grains thus increasing the mean size of the grain population while decreasing the number of small grains

2. as R increases the average grain size increases and the ability of these grains to polarize light drops with respect to their ability to extinguish light

3. larger grains increase A_V along a line of sight without affecting the polarization
4. larger aligned grains have become more spherical during the growth process and do not polarize light as efficiently
5. larger grains do not align as efficiently, increasing the fraction of unaligned grains.

Aannestad and Greenberg (1983) decided that the observed correlation of the width of polarization curve with λ_{max} is most likely caused by a variation in the size distribution of the interstellar grains. Models using infinite cylinders show that the data implies imperfect spinning alignment for the grains and also the DG thermal alignment mechanism is too inefficient in aligning the grains when they have acquired large mantles. Purcell's suprathermal alignment mechanism (rocket effect) is consistent with the observed data.

4.6 Summary

Most authors have drawn the conclusion that NGC 5128 only appears unusual because it is so close to us, and were it to be as distant as most other radio galaxies it's properties would be very typical. There are many known elliptical galaxies with dust lanes and the orientation of the dust lane tells us more about the elliptical than the origin and evolution of the dust. Recent authors have drawn the conclusion that NGC 5128 has a blazar as its nucleus.

In Chapter 5 we will perform a wavelength dependence study of polarization in an attempt to see whether the polarization in the dust lane is caused by extinction due to aligned grains in a magnetic field.

Chapter 5

Imaging Polarimetry of NGC 5128

5.1 Introduction

NGC 5128 appears to be a perfect galaxy in which to search for magnetic fields via polarization due to aligned grains. This work involves an optical multi-waveband study of the polarization in the galaxy, searching for wavelength dependence in the dust lane that bisects the galaxy. Four polarization maps are presented in B, V, R and I with the highest optical polarization resolution yet obtained for this object.

5.2 Observations

NGC 5128 was observed on the nights of 1992 March 4–8 using the Durham Imaging Polarimetry system on the 40 inch telescope at the South African Astronomical Observatory, Sutherland. The Durham Imaging Polarimeter (Scarrott *et al.*, 1983; Scarrott 1991) was used with a blue-sensitive coated GEC CCD to make a total of 32 exposures in the V waveband and 8 exposures in the B, R and I wavebands. Table 5.1 shows the observations made and the filter responses. The readout noise of the CCD is typically 7 – 9 electrons per pixel and the effective seeing of the combined data was 4 arcseconds. The image scale corresponds to 1.15 arcsecs per pixel.

Since the galaxy is greater than 20 arcminutes in size, not all of it fitted on the CCD in a single exposure. To obtain full coverage of the galaxy, observations were carried out by first placing the central region of the galaxy in the bottom right area of the CCD and observing the SE part of the galaxy, and then placing the central region in the top left

area of the CCD and observing the NW part of the galaxy. When the two sets of data were reduced, they were aligned with respect to each other to form an image of the whole galaxy, with better signal to noise in the central regions, where the two data sets overlap.

Filter	B	V	R	I
Number of exposures	8	32	8	8
Exposure Time (secs)	1000	1000	1000	1000
Peak Response (Å)	4385	5498	6287	7576
Mean wavelength (Å)	4400	5520	6630	8090
Bandwidth (Å)	1030	860	1640	1410

Table 5.1: Observation Details of NGC 5128

Because of the two channel nature of the polarimeter (Scarrott 1991), the B, R and I images consist of vertical strips of data with blank spaces in between, so only half of the galaxy is visible in these images. Full coverage of the galaxy was obtained in the V filter only, because of time constraints.

5.3 Results

In Fig. 5.1 we show a greyscale intensity image of NGC 5128 in the V waveband overlaid with a map of polarization vectors for the same wavelength. The origin of the co-ordinate system is at R.A.(1950) = $13^h\ 22^m\ 31.82^s$; Dec.(1950) = -42° 45′ 30.3″, coinciding with the hotspot of Kunkel and Bradt (1971). The polarization measurements are integrated over 11″ square bins, with a small overlap between adjacent bins. It can be seen that the polarization pattern consists of several distinct areas; the central dust lane, the elliptical galactic component, and the extremities of the dust lane. No correction has been applied for any contamination from foreground polarization in our Galaxy since previous studies have shown that this has little or no effect on the results (Hough *et al.*, 1987, hereafter referred to as H87).

The polarization vectors in the central dust lane run parallel to the dust lane at a position angle of 117 degrees and with a value of about 4 to 5%. This value gets slightly smaller towards the edges of the dust lane. The elliptical component appears to have randomly oriented polarization vectors with values of less than 1%.

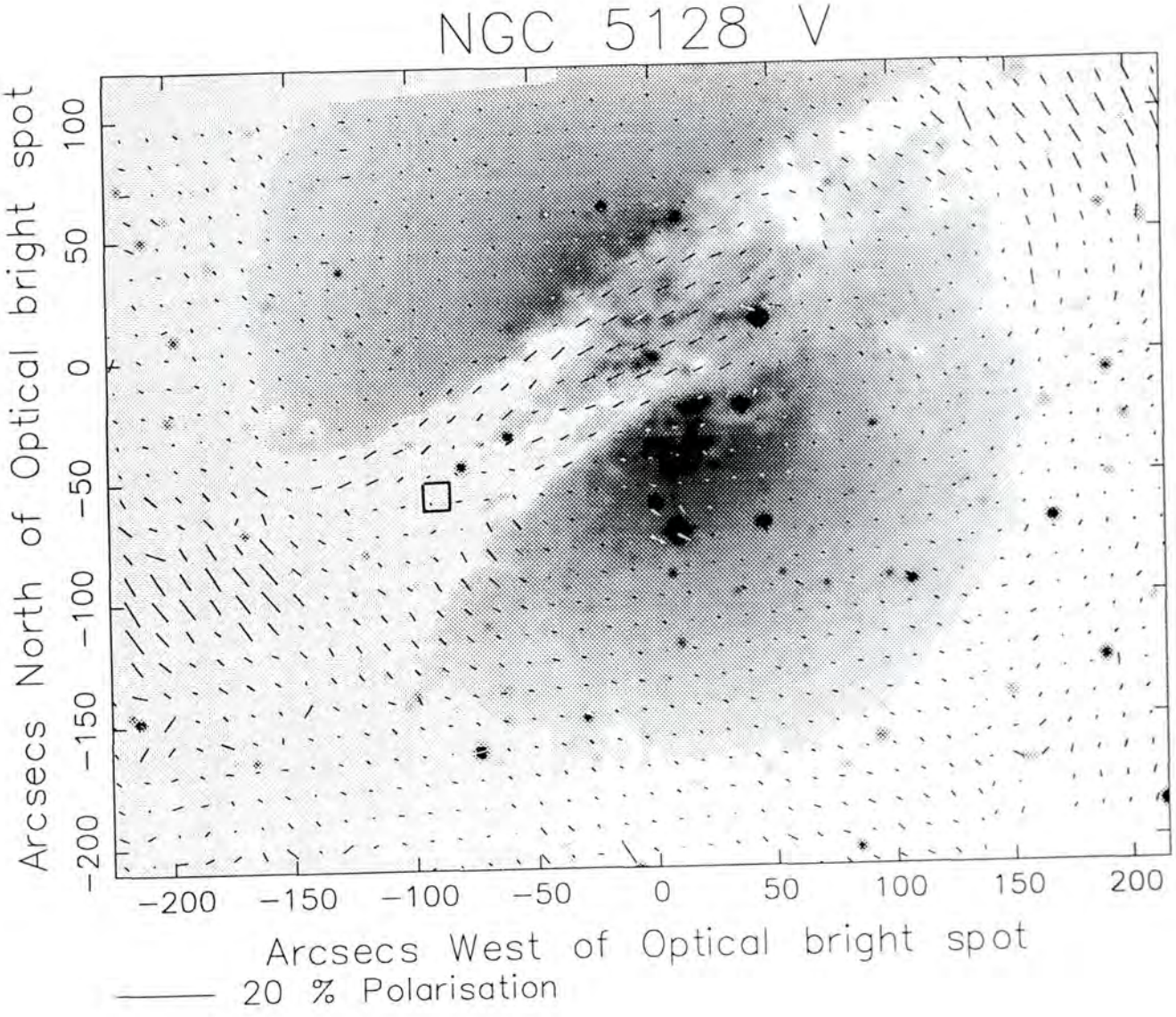

Figure 5.1: A reverse greyscale image of NGC 5128 in the V waveband overlaid with a map of the polarization vectors.

The galaxy is shown as an unsharp-masked image in photographic form in Fig. 5.2 to give the maximum contrast between the dusty areas and the background. It can be seen that the dust appears to sweep around in a loop as if it were encircling the galaxy and the angles of the polarization vectors follow the curve of the dust, with polarization values slightly larger than those in the central dust lane, 6 to 8%. If the dust lane contains a toroidal magnetic field then we would expect the angles of the polarization vectors to turn around in this manner. At the areas where the "cross-over" in polarization angle occurs i.e. where the vectors stop being parallel to the dust lane and start following the sweep of the dust lane the polarization values drop considerably, reaching a "nullpoint" on either side before rising in value again with position angles are perpendicular to the nuclear regions. Note the orientation of Fig. 5.2 as indicated by the compass.

Figure 5.3 shows a contour map of a greyscale image of NGC 5128 in the B waveband overlaid with a map of the polarization vectors. This map is similar to the V map, with parallel polarizations in the dust lane, and a change in polarization angle to follow the dust lane. Figure 5.4 shows the results for the R waveband and Fig. 5.5 those for the I waveband. The change of angle with the turning of the dust lane is more pronounced in R and I. The polarization values are on average slightly larger in the B waveband than in the R and I.

Berry (1985) modelled the polarization pattern in the dust lane of NGC 5128 and obtained a pattern which was similar to that observed, i.e. vectors parallel to the dust lane in the centre, reaching null points further along and turning through 90° to be perpendicular to the dust lane at its ends. However, the maximum value of polarization he could obtain with his model was 1.7%, despite extensive variation of the model parameters. Only with the introduction of non-spherical grains aligned by a magnetic field did he find values of 4 – 5% in his model polarizations.

5.4 Modelling the Wavelength Dependence of the Polarization

As discussed in Chapter 4, non-spherical dust grains can line up in a magnetic field with their axis of greatest inertia perpendicular to the magnetic field using a mechanism such as the Davis-Greenstein effect. This alignment allows a net extinction effect to accumulate; light whose electric vector is parallel to the major axis of the grain is preferentially

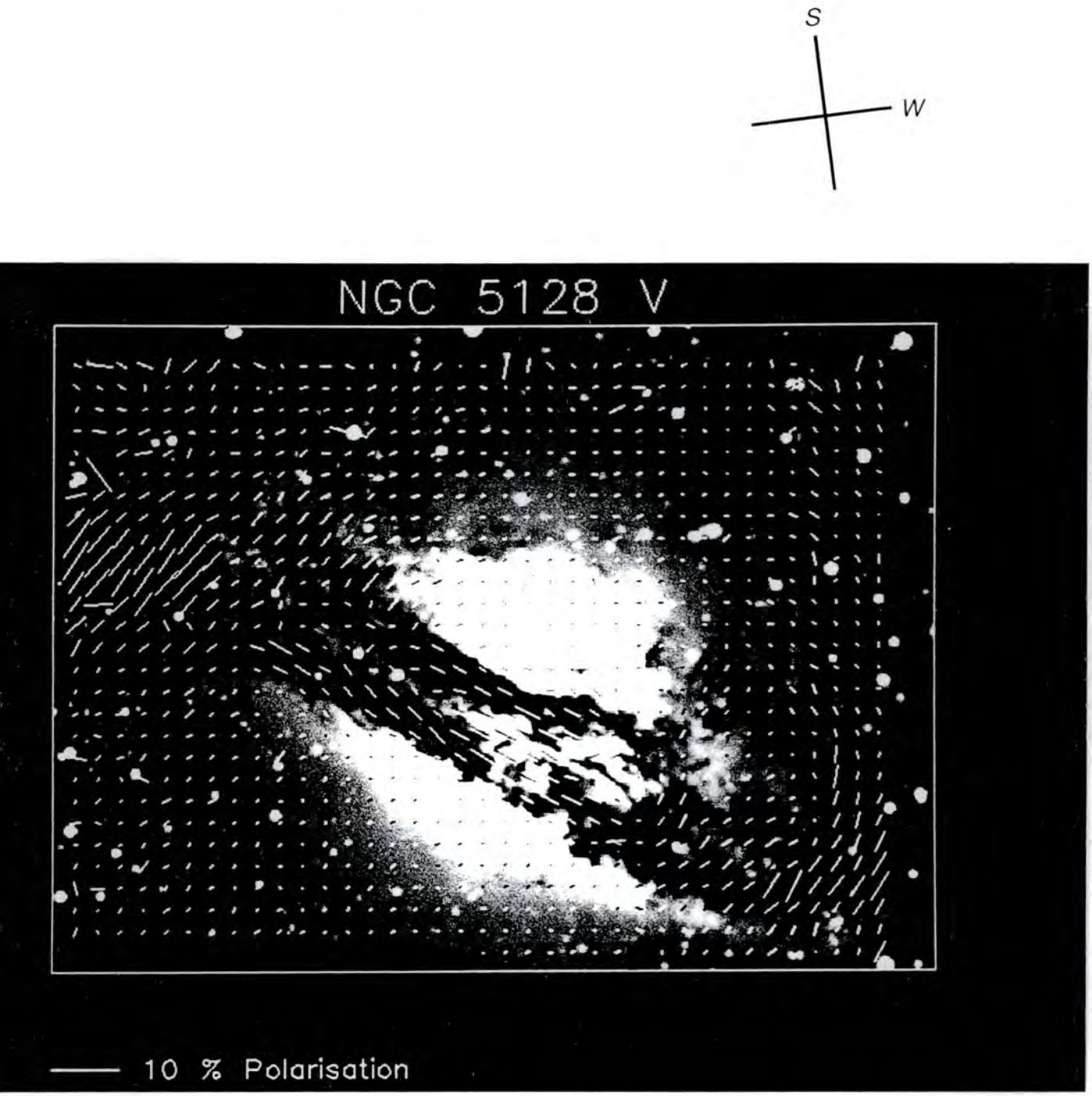

Figure 5.2: An unsharp masked greyscale photograph of NGC 5128 in the V waveband overlaid with a map of the polarization vectors. Note the orientation of the photograph as indicated by the compass.

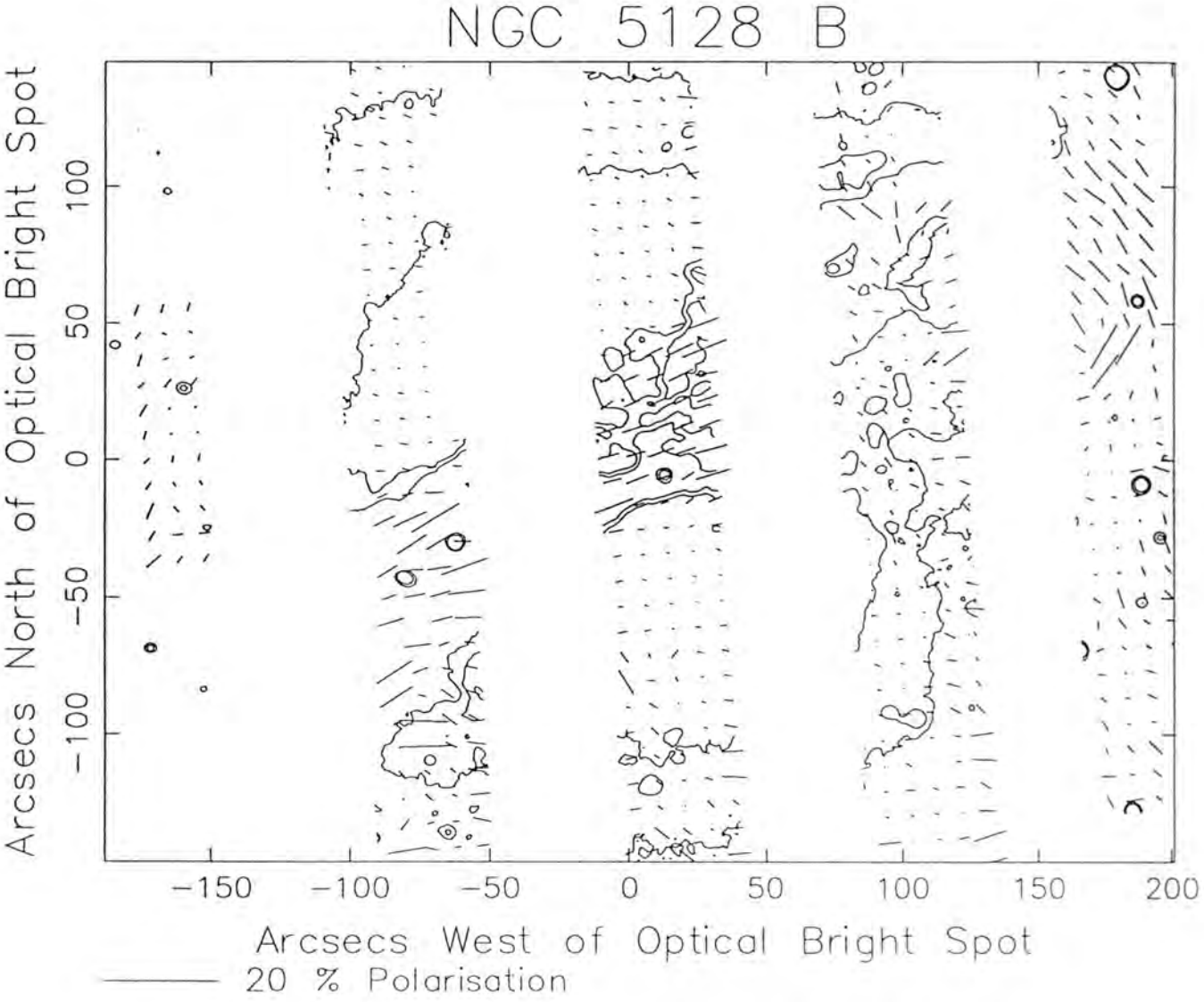

Figure 5.3: A contour map of NGC 5128 in the B waveband overlaid with a map of the polarization vectors.

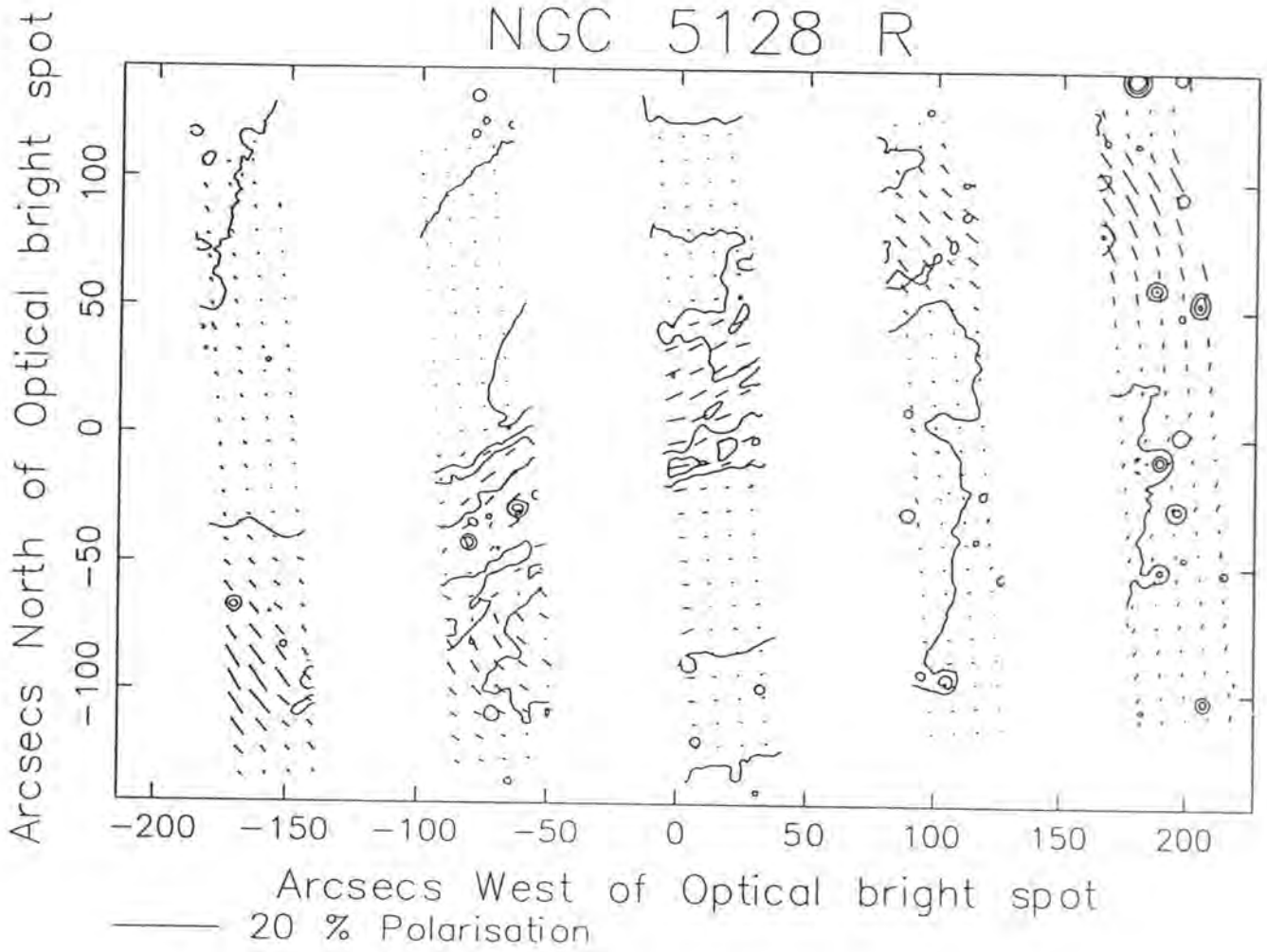

Figure 5.4: A contour map of NGC 5128 in the R waveband overlaid with a map of the polarization vectors.

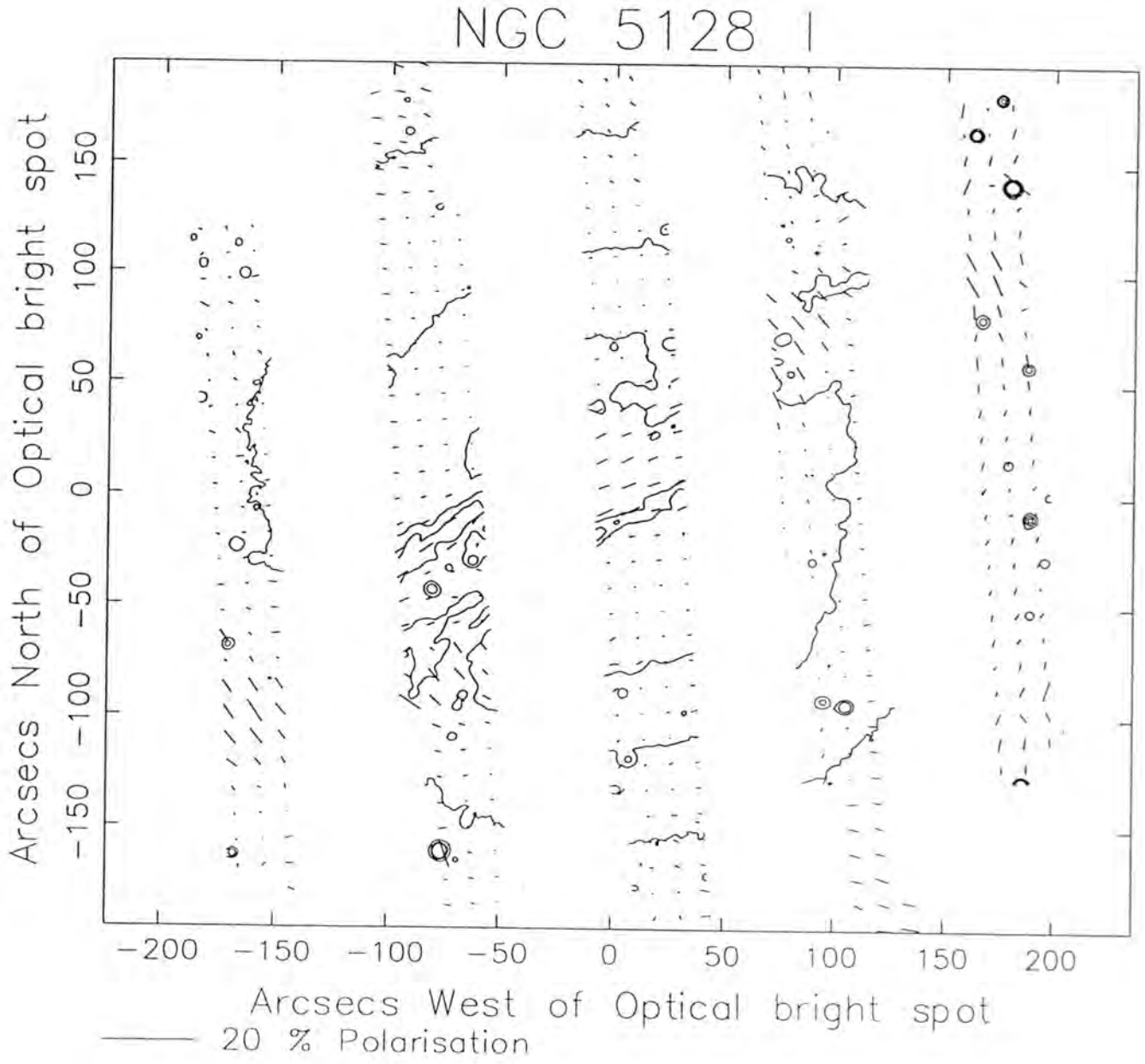

Figure 5.5: A contour map of NGC 5128 in the I waveband overlaid with a map of the polarization vectors.

extinguished, manifesting itself as linearly polarized light.

To test the dependence of linear polarization on wavelength in NGC 5128 a large number of apertures, 10″ in diameter, were selected along the dust lane and the polarization in each aperture was calculated for the four wavebands. For every aperture where polarization results could be measured in all four wavebands, a best-fit Serkowski curve was calculated to fit each set of (4) points by minimizing a parameter Q, the quality of fit, defined by

$$Q = \sum_{i=1}^{n} \frac{(O-E)^2}{O}$$

where O is the observed value, and E is the estimated value. The apertures are shown in Fig. 5.6a on a greyscale image in the V filter, with Fig. 5.6b showing a close up of the central regions for the sake of clarity.

Figure 5.7 (54 panels) shows the calculated best-fit for each of these apertures. In the central cases there are two results, one from the left hand data set and one from the right hand data set (see Section 5.1), this is indicated by the word *left* or *right* in the corner of the panel. The number refers to the aperture number. Table 5.2 shows the calculated P_{max} and λ_{max} for each aperture, as well the Q for that fit. The range P_{max} could take was limited to 1.1% – 11% in steps of 0.1%, and the range λ_{max} could take was limited to 3050Å – 8000Å in 50Å steps.

From Fig. 5.7 it can be seen that the central regions of the dust lane (Apertures 9, 11, 16, 19, 94, 95, 110) appear to follow the same Serkowski curve. The λ_{max} range for these apertures is 0.365μm to 0.6μm with an average of 0.441μm and the P_{max} range is 2.4% to 4.6% with an average of 3.49%.

Away from the centre of the dust lane (Apertures 33, 35, 43, 51, 52, 61, 84, 103, 105, 119, 120, 132, 133, 143, 144, 153, 154, 155) there appears to be little or no correlation between wavelength and polarization, however the percent polarization values are very low in this region. Out at the edges there seems to be a correlation which is not similar to the Serkowski curve calculated for the centre. The left hand apertures, 175 and 182, follow a much steeper curve within errors but the right hand apertures, 278 and 288, are more similar to the central curves, but only these two apertures have valid curves. One possible explanation for this is that at the "cross-over" areas there is a change in the principle polarizing mechanism. In the centre, polarization is caused by the extinction of light by aligned dust grains, whereas in the outer parts of the dust lane the polarization is caused by scattering from unaligned dust grains. Where the polarization drops off and

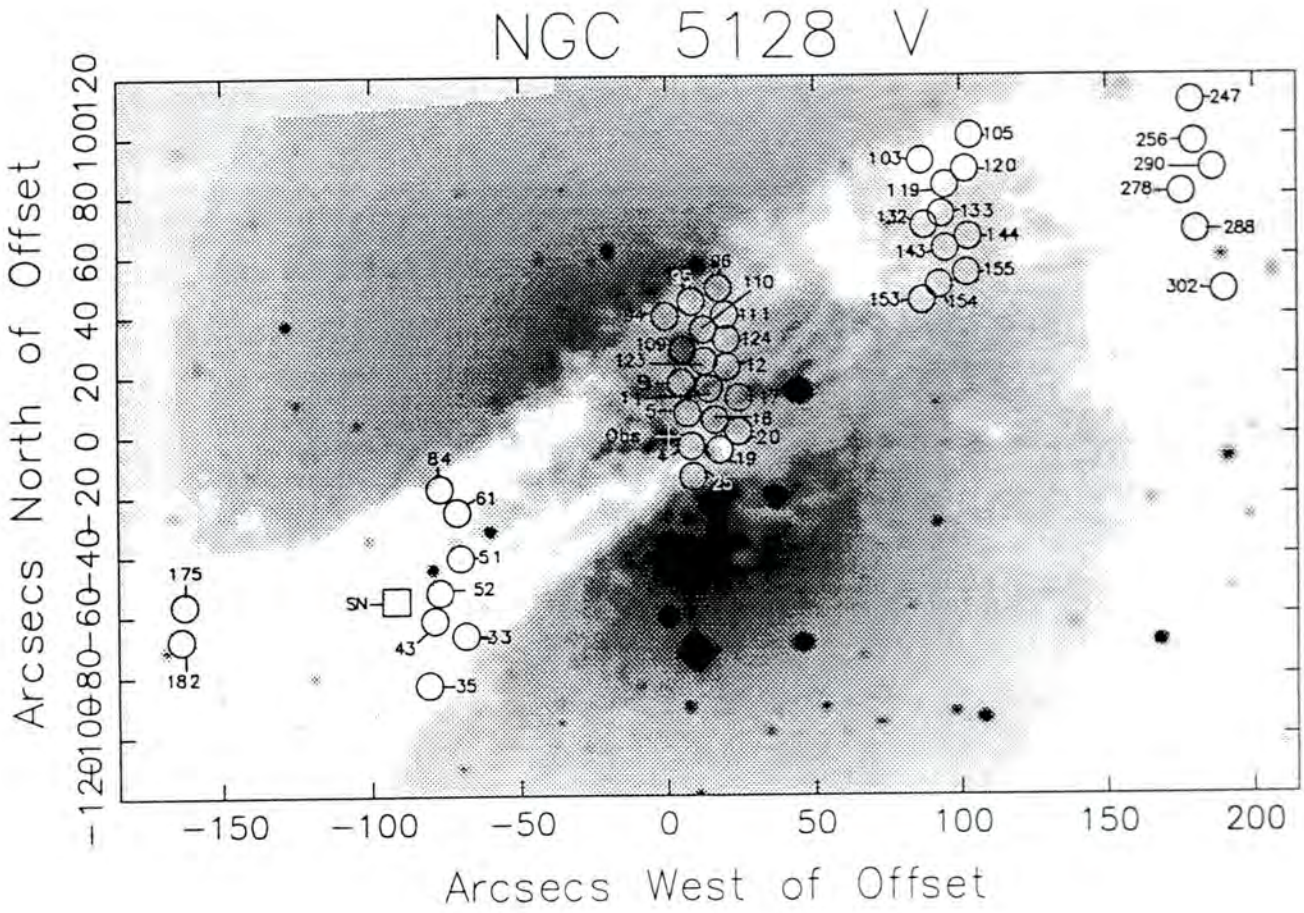

Figure 5.6: (a) Apertures where best-fit Serkowski curves were calculated, on a reverse greyscale image of NGC 5128 in the V waveband. The apertures are numbered and the position of SN1986G is marked by a square labelled **SN**. The optical bright spot is marked by a cross labelled **Obs**.

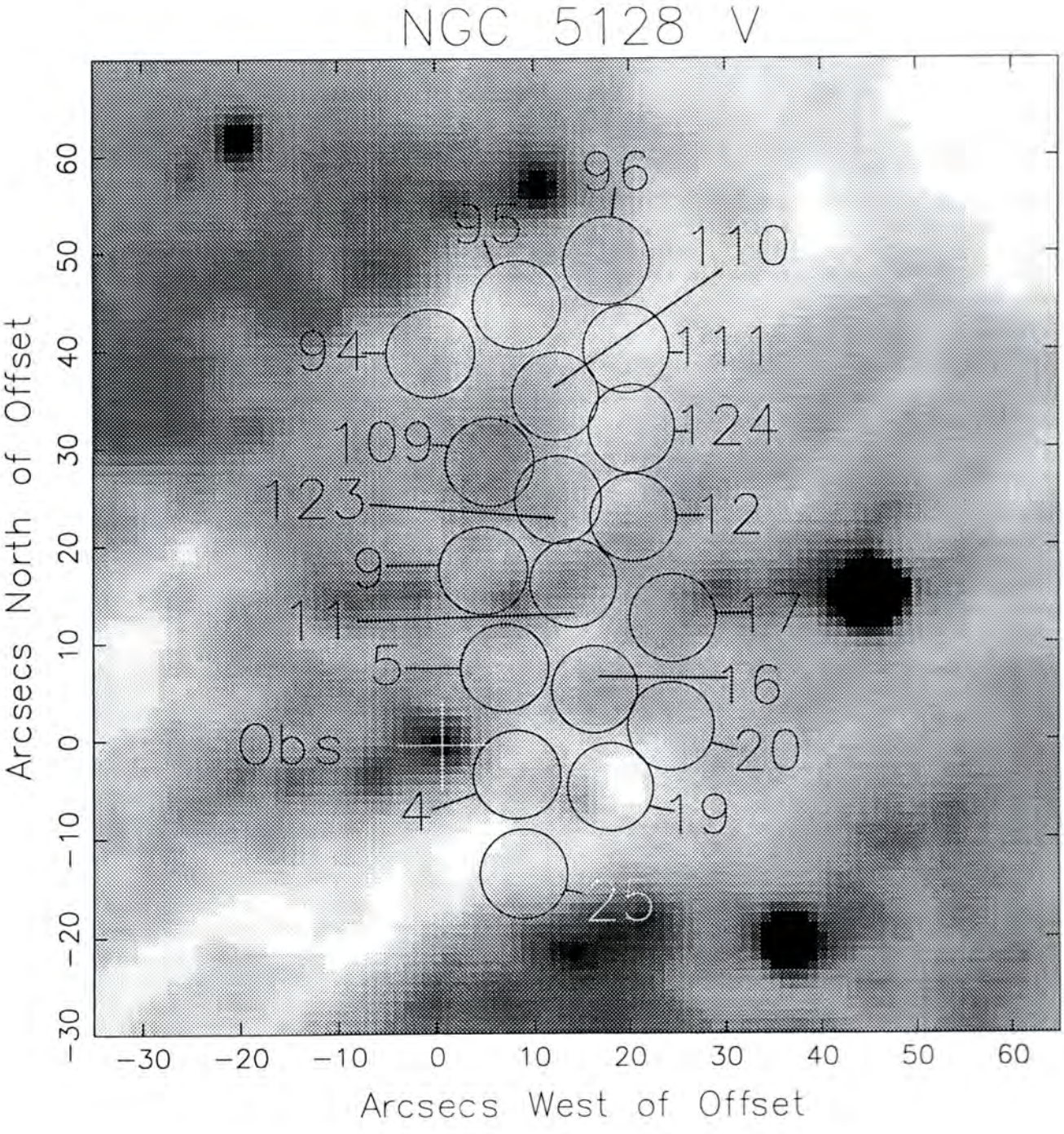

Figure 5.6: (b) As Fig. 5.6a, showing the central region of the galaxy.

Aper	Q	P_{max} (%)	λ_{max} (Å)	Aper	Q	P_{max} (%)	λ_{max} (Å)
L 4	3.4075	4.2	5350	L 143	1.0603	2.8	3200
L 5	0.1283	4.2	4650	L 144	1.4224	1.9	7100
L 9	0.0209	3.2	4850	L 154	0.1809	1.4	3050
L 11	0.0609	2.9	4850	L 155	0.4099	1.4	4550
L 12	0.2013	3.5	3500	L 175	1.2315	7.7	3050
L 16	0.0174	4.6	3650	L 182	0.2657	7.3	3050
L 17	0.2042	4.2	3050	R 4	0.2329	4.0	7600
L 19	0.2673	2.8	3900	R 5	0.0250	4.6	4300
L 20	0.9786	6.0	3050	R 9	0.0550	3.6	3900
L 25	0.1523	2.3	6000	R 25	0.2908	2.6	5400
L 33	1.7667	2.7	4300	R 95	0.2245	2.0	7750
L 35	3.0340	5.6	7350	R 103	1.1161	2.9	6500
L 43	3.5193	6.4	3050	R 109	0.0392	3.5	3750
L 51	3.0543	4.2	3050	R 110	0.0398	4.2	3850
L 52	3.4756	5.6	3050	R 119	0.7324	3.9	8000
L 61	2.2187	5.4	3050	R 132	0.7895	3.8	8000
L 84	2.4556	5.7	5200	R 133	0.4285	3.7	8000
L 94	0.1864	2.8	4500	R 143	0.3196	2.1	5000
L 95	0.0263	2.4	6000	R 153	2.5951	2.8	8000
L 96	0.0494	2.5	8000	R 154	0.2059	1.1	4050
L 105	7.9079	6.0	8000	R 247	2.5421	4.2	4700
L 109	0.1829	2.5	7000	R 256	0.0421	5.6	6000
L 110	0.0413	3.9	4450	R 257	0.3777	5.3	5550
L 111	0.5476	6.5	3050	R 278	0.2112	4.6	3750
L 120	4.3413	5.1	8000	R 288	0.0945	2.8	4050
L 123	0.1460	4.5	3500	R 290	1.4616	5.4	5450
L 124	0.7854	5.0	3050	R 302	0.8841	2.1	4600
L 133	0.7741	3.7	8000				

Table 5.2: Parameters in Serkowski best-fit.

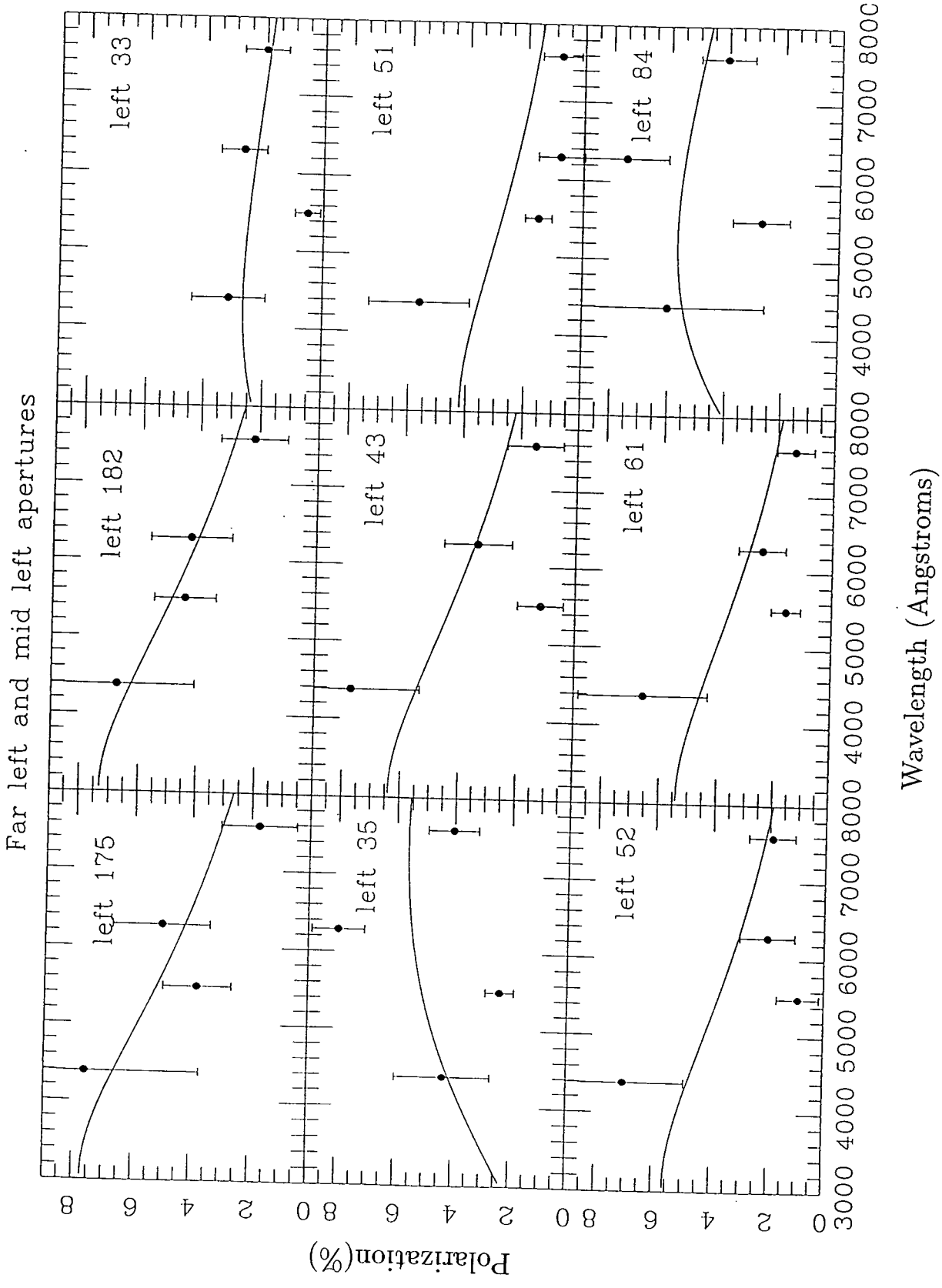

Figure 5.7: (a) Wavelength dependence on the apertures with best-fit Serkowski curve

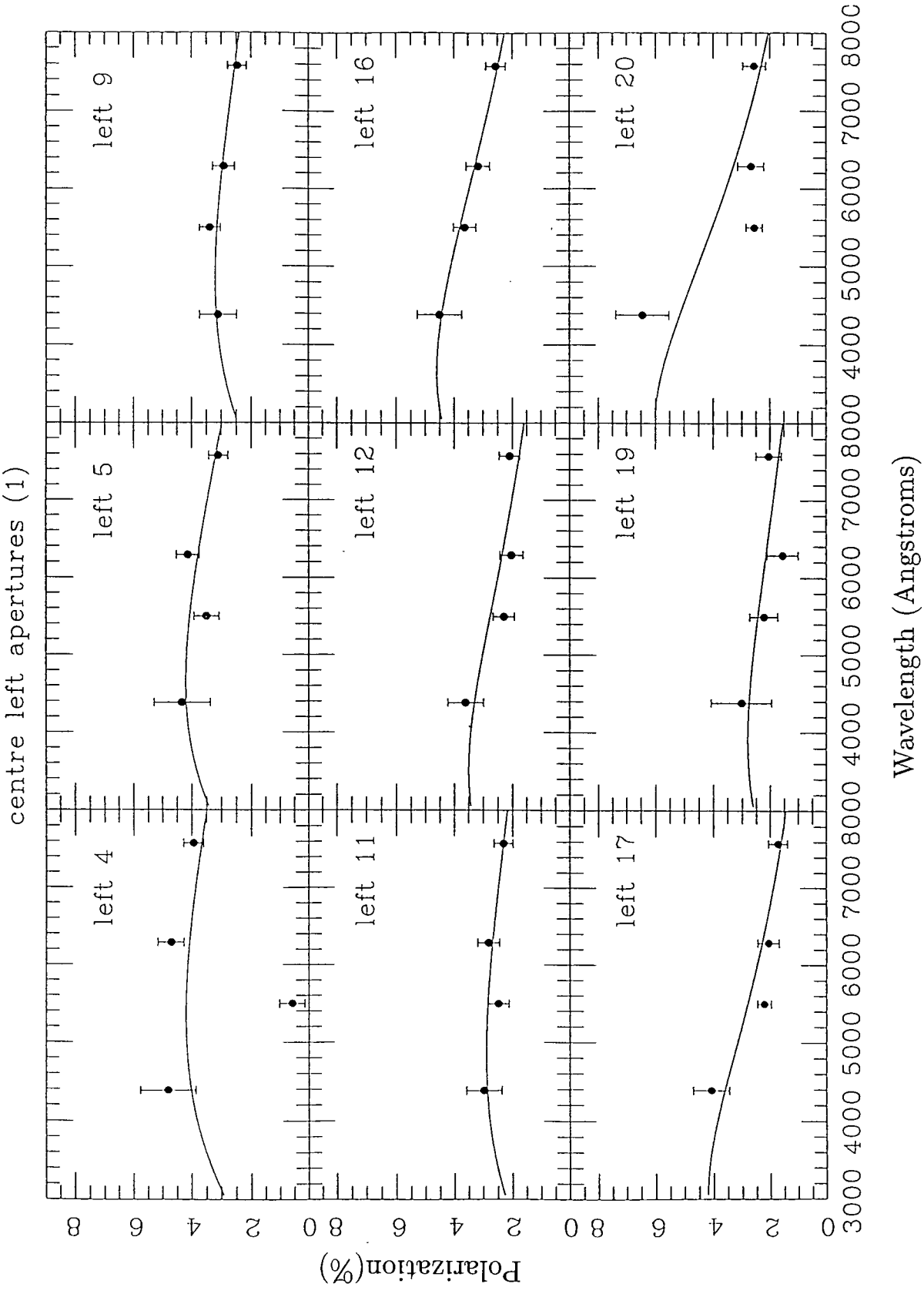

Figure 5.7: (b) Wavelength dependence on the apertures with best-fit Serkowski curve

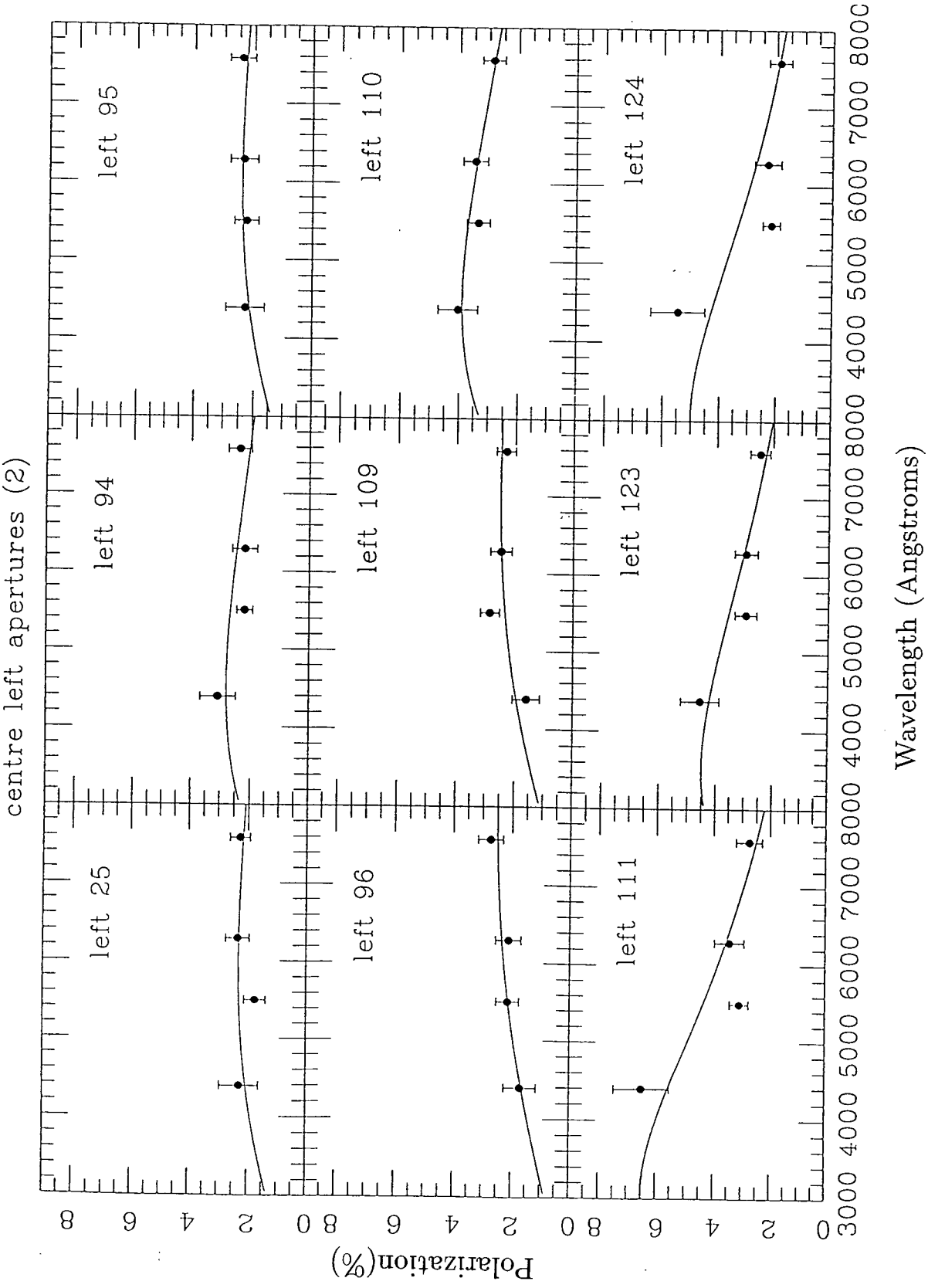

Figure 5.7: (c) Wavelength dependence on the apertures with best-fit Serkowski curve

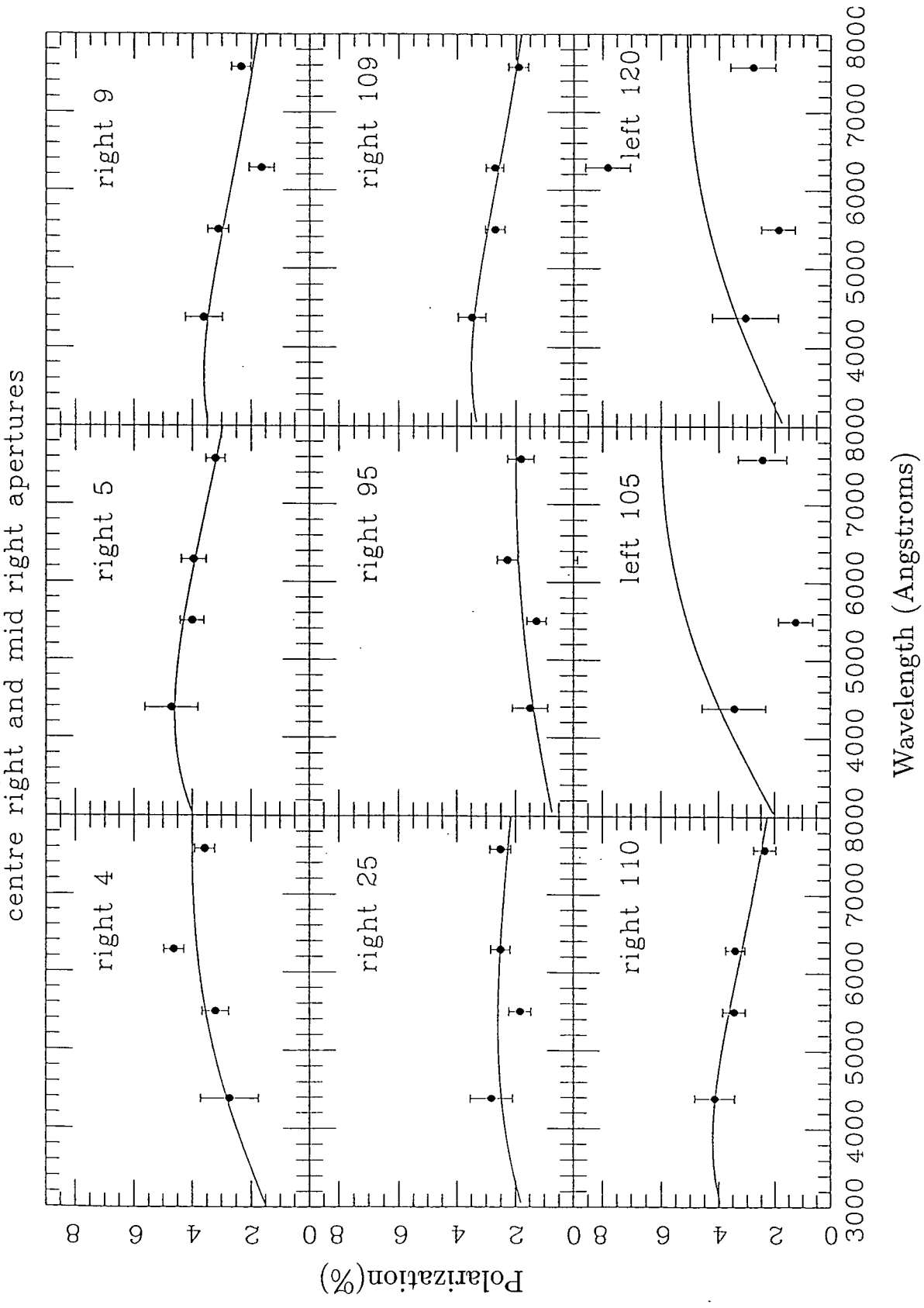

Figure 5.7: (d) Wavelength dependence on the apertures with best-fit Serkowski curve

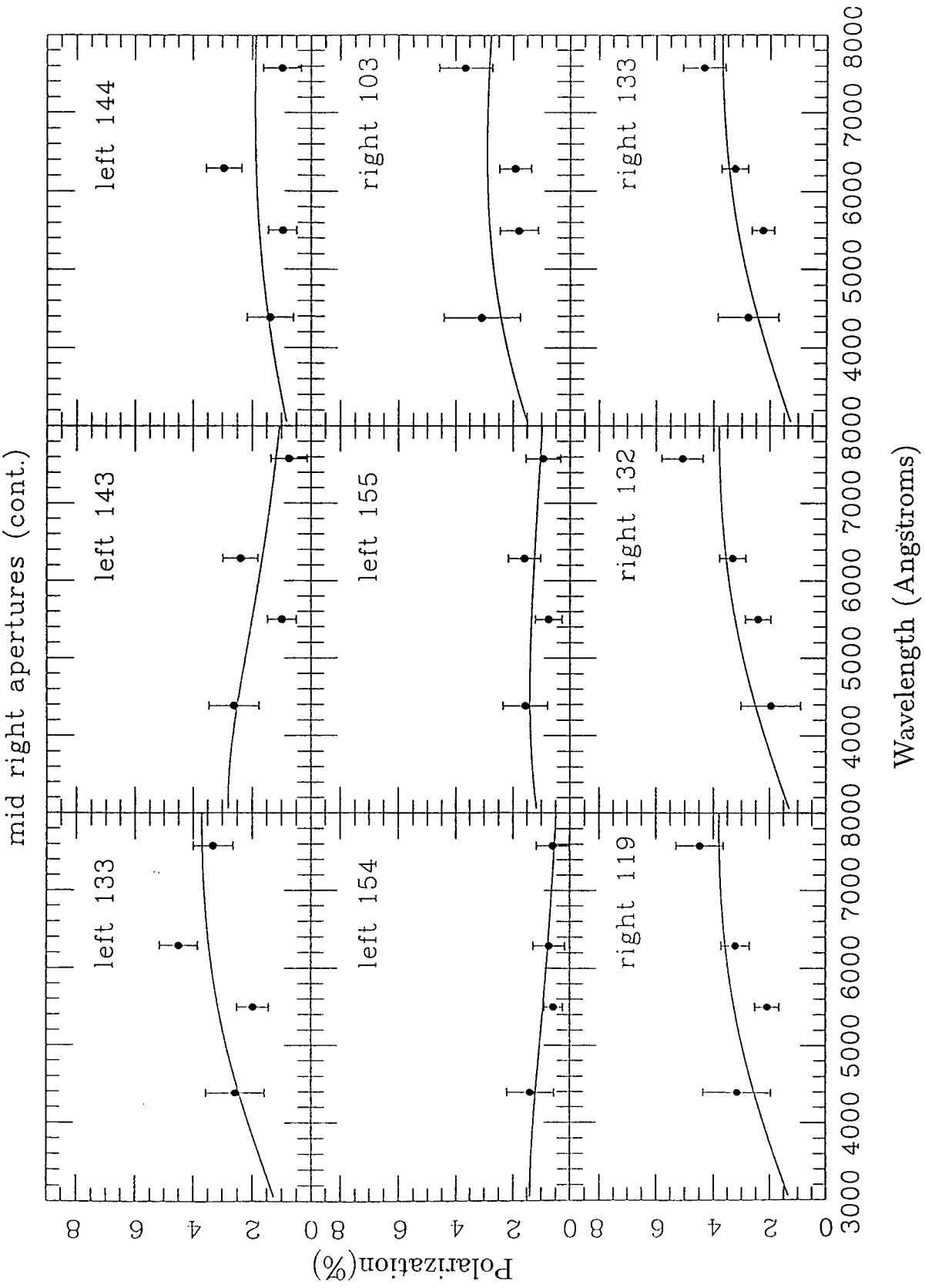

Figure 5.7: (e) Wavelength dependence on the apertures with best-fit Serkowski curve

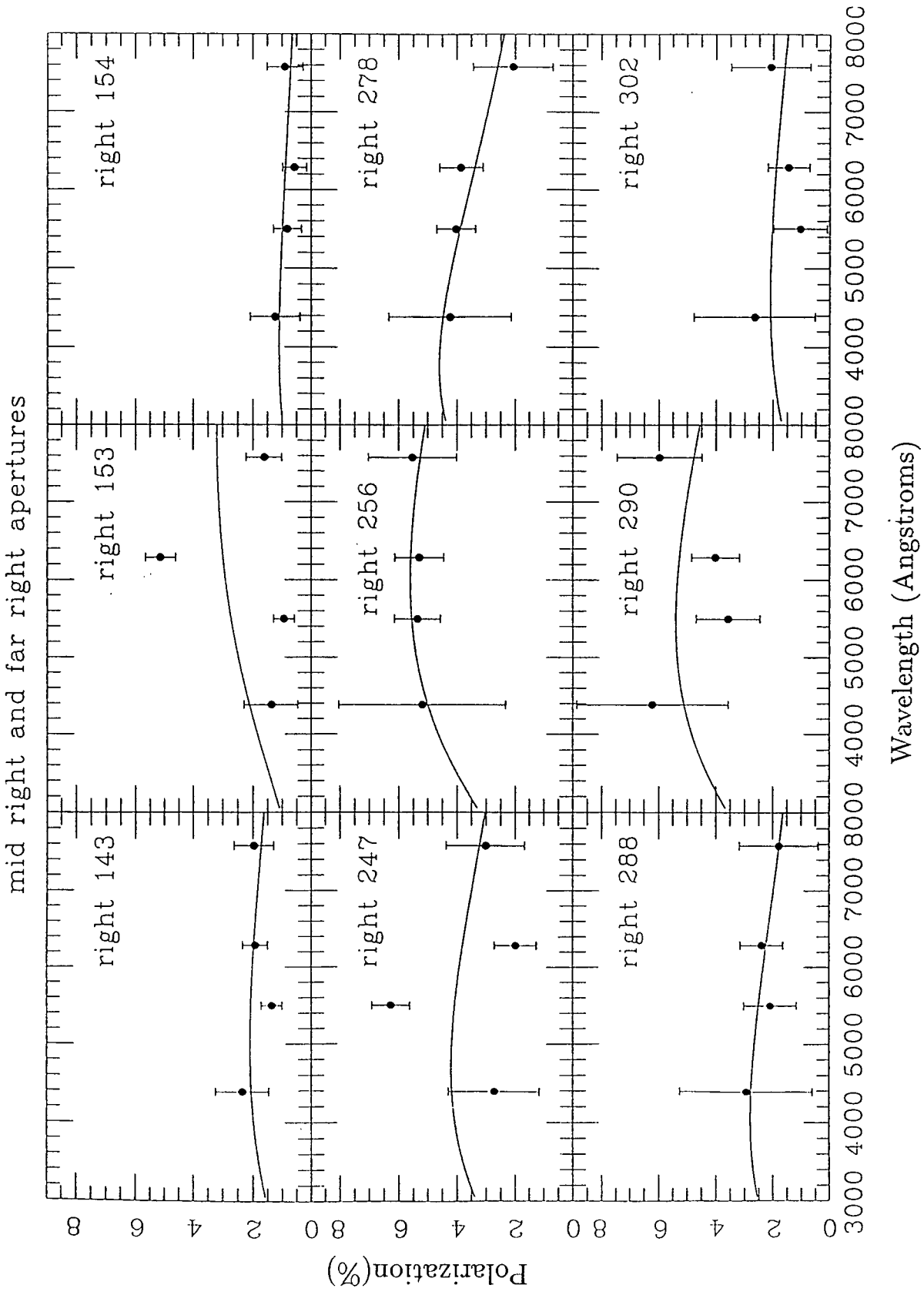

Figure 5.7: (f) Wavelength dependence on the apertures with best-fit Serkowski curve

the angles change is where these two mechanisms compete with each other, effectively cancelling the action of the other out.

The Serkowski curves were also calculated using the correction for K of Whittet *et al.* (1992),

$$K = (0.01 \pm 0.05) + (1.66 \pm 0.09)\lambda_{max}.$$

The best-fit curves were slightly worse, probably because this correction was calculated using IR measurements of stars in our galaxy and may not be appropriate for the optical part of an extragalactic object.

It can be seen from the data that other functional forms such as a straight line could be fitted to most of the data. It is unfortunate that we do not have any measurements at a wavelength bluer than the B filter, since this is where we would expect the polarizations to begin to decrease again, and give us clear evidence that the Serkowski equation is being followed. However the observations of Hough *et al.* (1987) showed a clear wavelength dependence with $\lambda_{max} = 0.43\mu$m, therefore we can assume that the dust lane does contain aligned grains.

Berry (1985) tested whether simple scattering from spherical or unaligned grains could produce the observed polarizations. He modelled the scattering geometry using multiple scattering from Mie particles, with a power-law grain size distribution, in an optically thick geometry. His model produced polarization values that were significantly lower than those observed and despite varying model parameters such as the power law index and the refractive index of the dust grains he could not obtain polarization values comparable to the observed values. Only by including the effect of extinction from elongated dust grains aligned in a magnetic field in the dust lane could he obtain polarizations as large as the observed values.

In order to test whether the apertures in the centre, where good fits to the Serkowski curve were obtained, were valid, the nuclear regions of the left and right data files were combined (only the nuclear regions were used because this is where the best-fits to the Serkowski curves were obtained.) and a new series of apertures were chosen at random that covered the area. Figure 5.8 (24 panels) shows the results and best-fit Serkowski curves and Fig. 5.9 shows the location of these apertures where good fits (a good fit being defined where $Q < 0.1$) were obtained in the nuclear region.

Aper	Q	P_{max} (%)	λ_{max} (Å)	Aper	Q	P_{max} (%)	λ_{max} (Å)
20	0.0633	1.6	5850	42	0.0562	1.6	5800
29	0.7106	1.1	3050	43	0.0030	3.8	4750
30	0.0362	2.9	4100	44	0.4767	1.1	8000
31	0.0060	3.2	3850	45	1.2149	7.3	3050
32	0.0141	4.0	4600	46	1.6636	6.3	3050
34	0.1800	1.3	5650	47	0.1045	3.8	3550
35	0.5928	3.6	8000	48	0.0214	4.0	3950
36	0.2580	5.5	3250	49	0.7623	3.1	4500
37	0.0414	3.7	5550	50	0.1217	2.6	4100
38	0.0797	3.3	3800	51	0.5933	2.8	8000
39	0.0009	2.8	4750	52	0.1889	1.1	8000
40	0.1260	1.8	6700	55	0.5418	4.1	3050

Table 5.3: Parameters in Serkowski best-fit for nuclear region, with the merged left and right data files.

It can seen that the same regions of the data fit Serkowski curves. Apertures 30, 31, 32, 43, 48 and especially 39 have very good fits to Serkowski curves.

As a further check, the test was repeated with smaller aperture sizes and the fitting Serkowski curves were still found in the same region. A central aperture was selected so that it encompassed the largest possible valid area in all four wavebands, with a diameter of 23″ (also shown in Fig. 5.8 and labelled 'Big') and the polarizations were calculated in each waveband. A best-fit Serkowski curve was calculated to fit these points, and a curve for the whole region was obtained with a $P_{max} = (3.16 \pm 0.01)\%$ and a λ_{max} of (4250 $\pm$ 21)Å, where Q equaled 0.0056. Note that these errors are on the fit and not on the polarization measurements at this point. This is shown in Fig. 5.10 as is the SN1986G curve of H87. The data points and their errors are given in Table 5.5 along with those for SN1986G of H87.

What characteristics does the area where agreement with the Serkowski equation have that differ from the other dust lane regions? Figure 5.11a compares maps of the intensity, polarized intensity, percentage polarization and polarization angle in the central (200″ × 200″) dust lane region taken in the V waveband. (Note both Fig. 5.11a and 5.11b have the same orientation as Fig. 5.2). We see strong polarized intensity in the centre

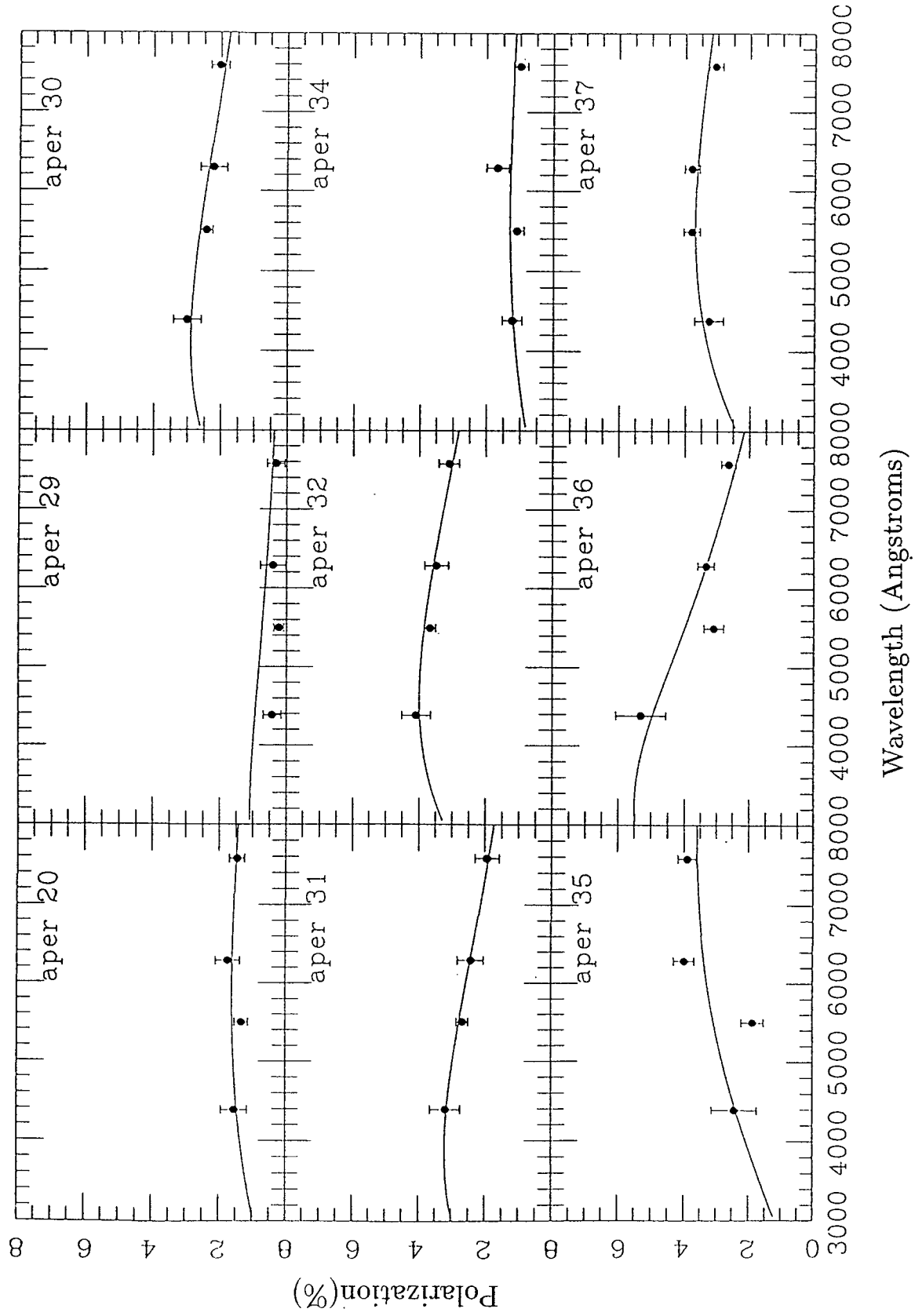

Figure 5.8: (a) Wavelength dependence on the apertures with best-fit Serkowski curve

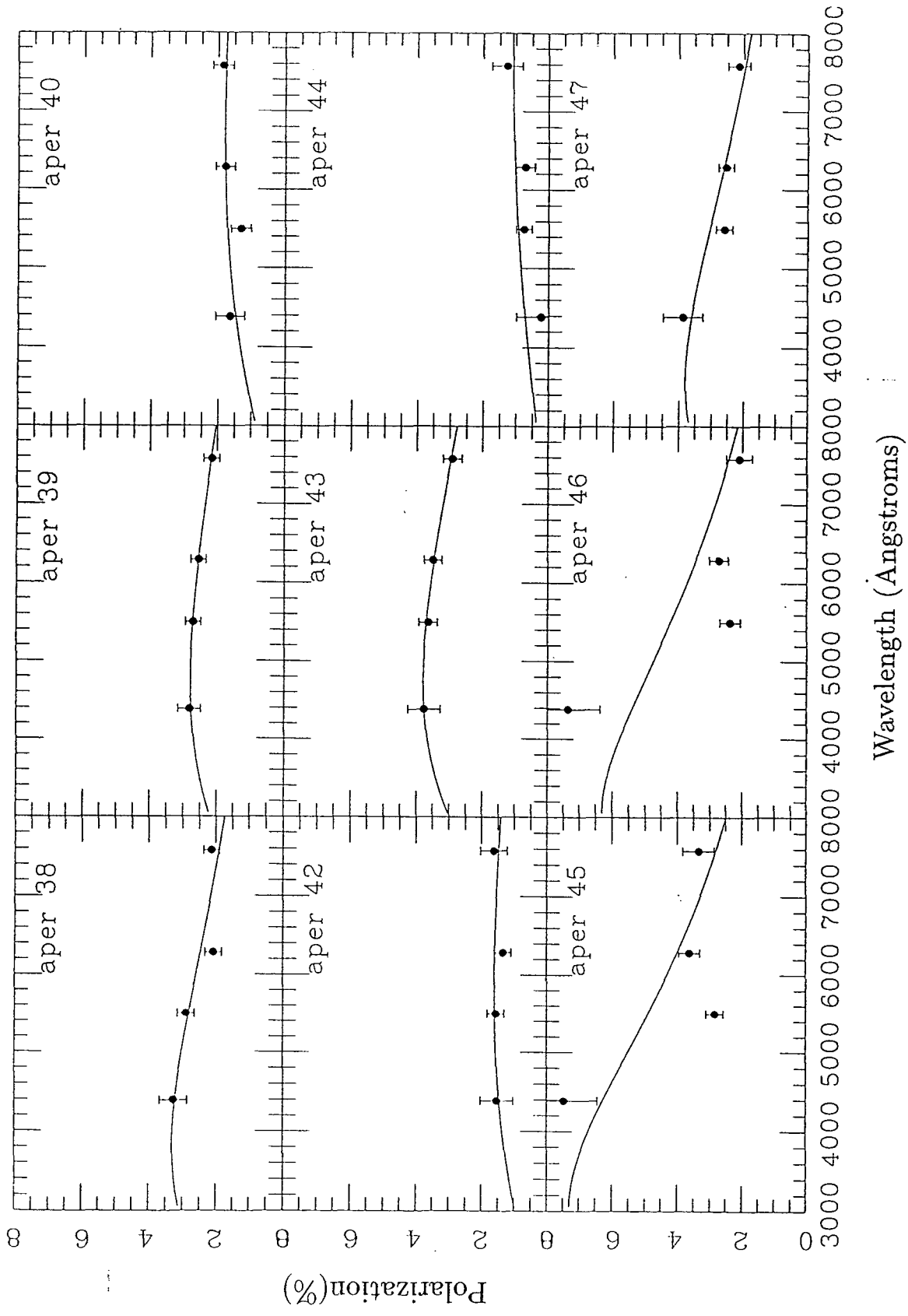

Figure 5.8: (b) Wavelength dependence on the apertures with best-fit Serkowski curve

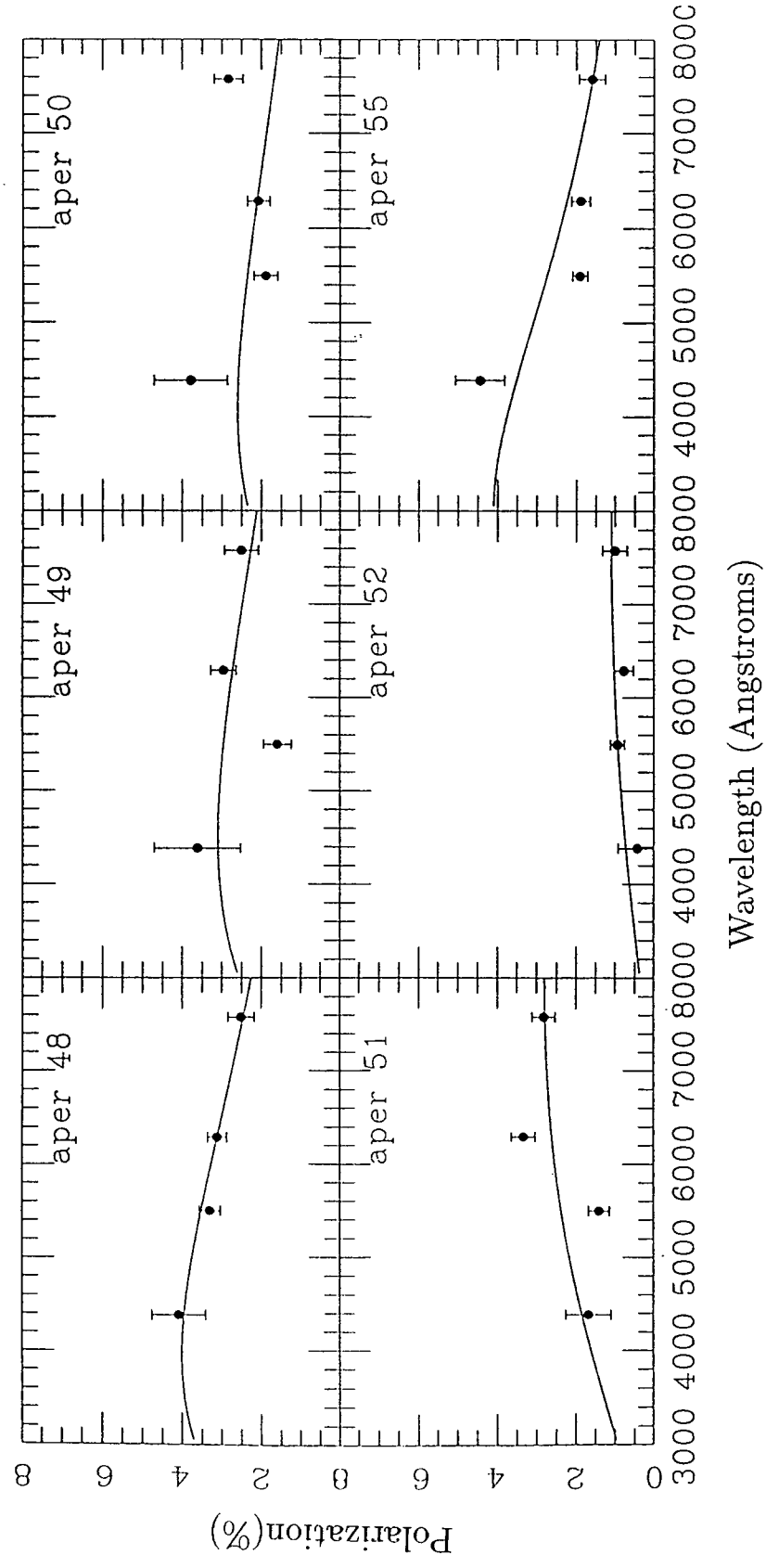

Figure 5.8: (c) Wavelength dependence on the apertures with best-fit Serkowski curve

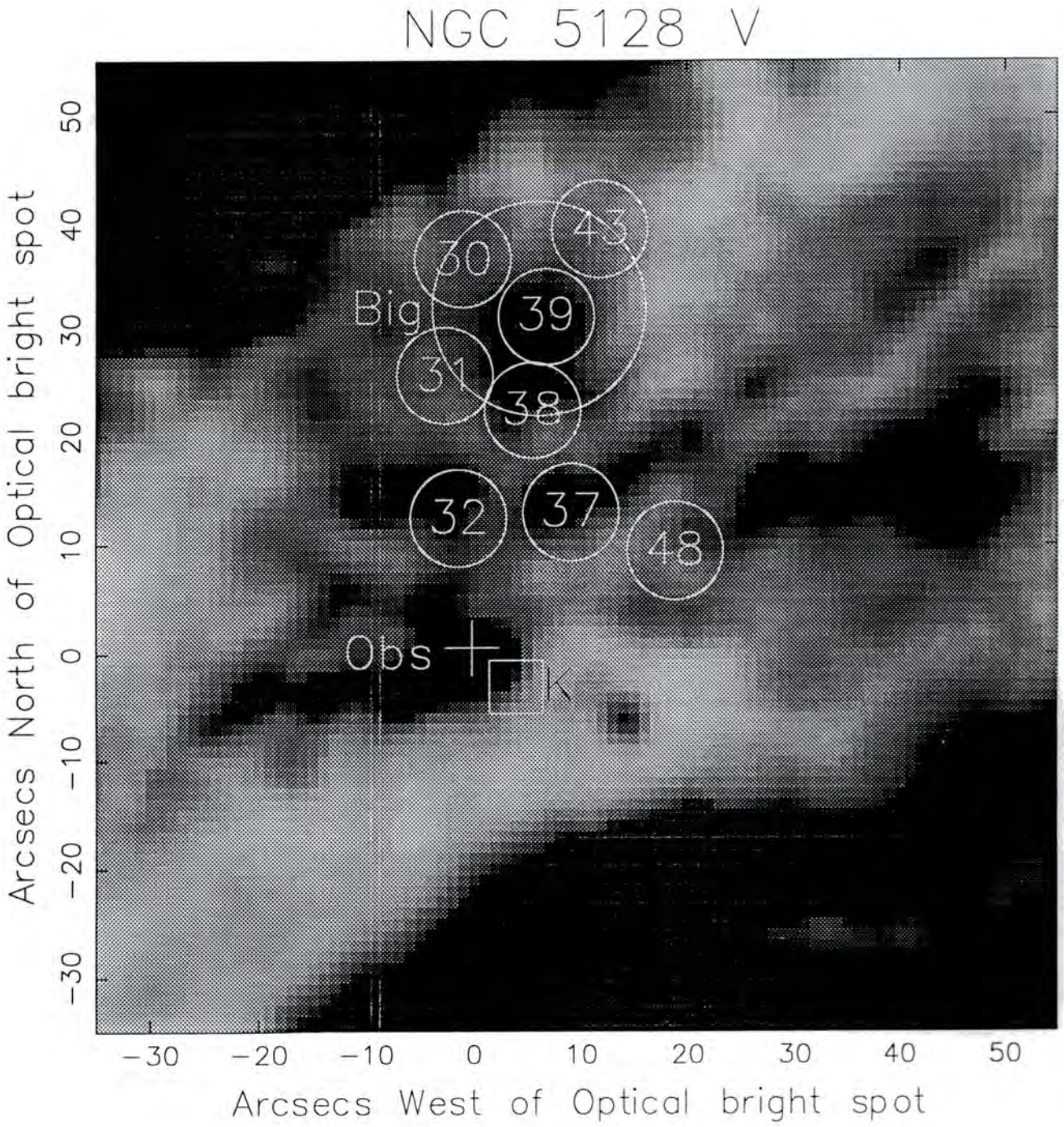

Figure 5.9: Second set of apertures on greyscale image of nuclear region in V waveband

of the dust lane, where we get the most polarization, and a consistent polarization angle parallel to the dust lane. We can also see the polarization after the turn-around region beginning to show in the top left corner. The map of polarization angles is displayed at a range which shows the parallel polarizations in the dust lane, with the dark regions being at polarization angles less than the dust lane and the white regions being greater. Figure 5.11b shows the positions of the best-fit apertures on a close up of the nuclear region (50″ × 80″.) These apertures are also shown on Fig. 5.9. It can be seen that the apertures with the best fits correspond to regions of moderate polarized intensity and percentage polarization (1.5 to 3.5%). On the intensity map there appears to be a large "spot" at the position of aperture 39 which is slightly brighter than the surroundings, and it is at and around this spot that the closest fits to Serkowski curves are obtained (with the exception of aperture 48).

It seems that where there is moderate, constant polarized intensity/percentage polarization in the dust lane we get good fits to Serkowski curves. Where there are higher levels or bright spots of polarized intensity/percentage polarization we do not get good fits. It could be that in the moderate regions there exist smoothly aligned grain regions, but where there are brighter regions there could either be excess illumination from additional sources or variations in the dust lane.

Berry (1985) calculated a curve for the variation of polarization from aligned grains with the density of grains in the path of a light wave. He found that the polarization will reach a maximum when there is only a very small quantity of dust in the light wave path (Fig. 5.12). Thus, if the thickness of the dust lane decreases the intensity of the transmitted light should increase as should the polarization, unless the dust lane becomes optically thin in which case the intensity would increase but the polarization would decrease. However it is extremely unlikely that the dust lane in the centre of NGC 5128 would become optically thin since extinctions of up to 45 magnitudes have been calculated there.

In the additional illumination scenario, the effect this would have on the polarization would depend on the nature of the additional source or sources. Jones and Klebe (1989) discuss different polarizing geometries such as a pure dust screen in front of an illuminating source, a dust screen with diluting emission, and a mix of dust and illuminating sources. The pure dust screen is the case one assumes occurs in the centre of NGC 5128 when calculating the Serkowski curves. The aligned grains in the dust lane are illuminated from behind by a bright source.

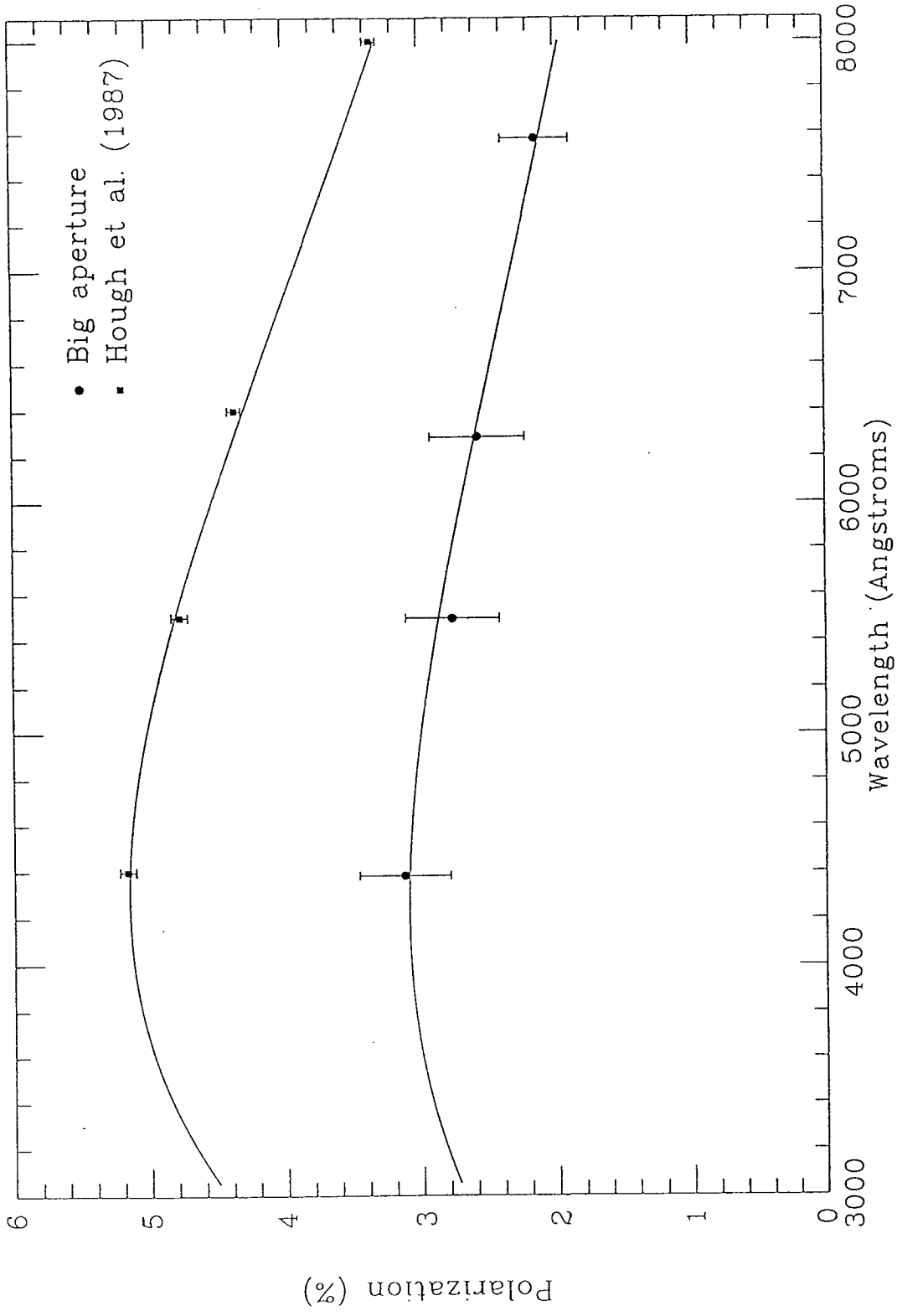

Figure 5.10: Wavelength dependence of big aperture with best-fit Serkowski curve and H87 curve

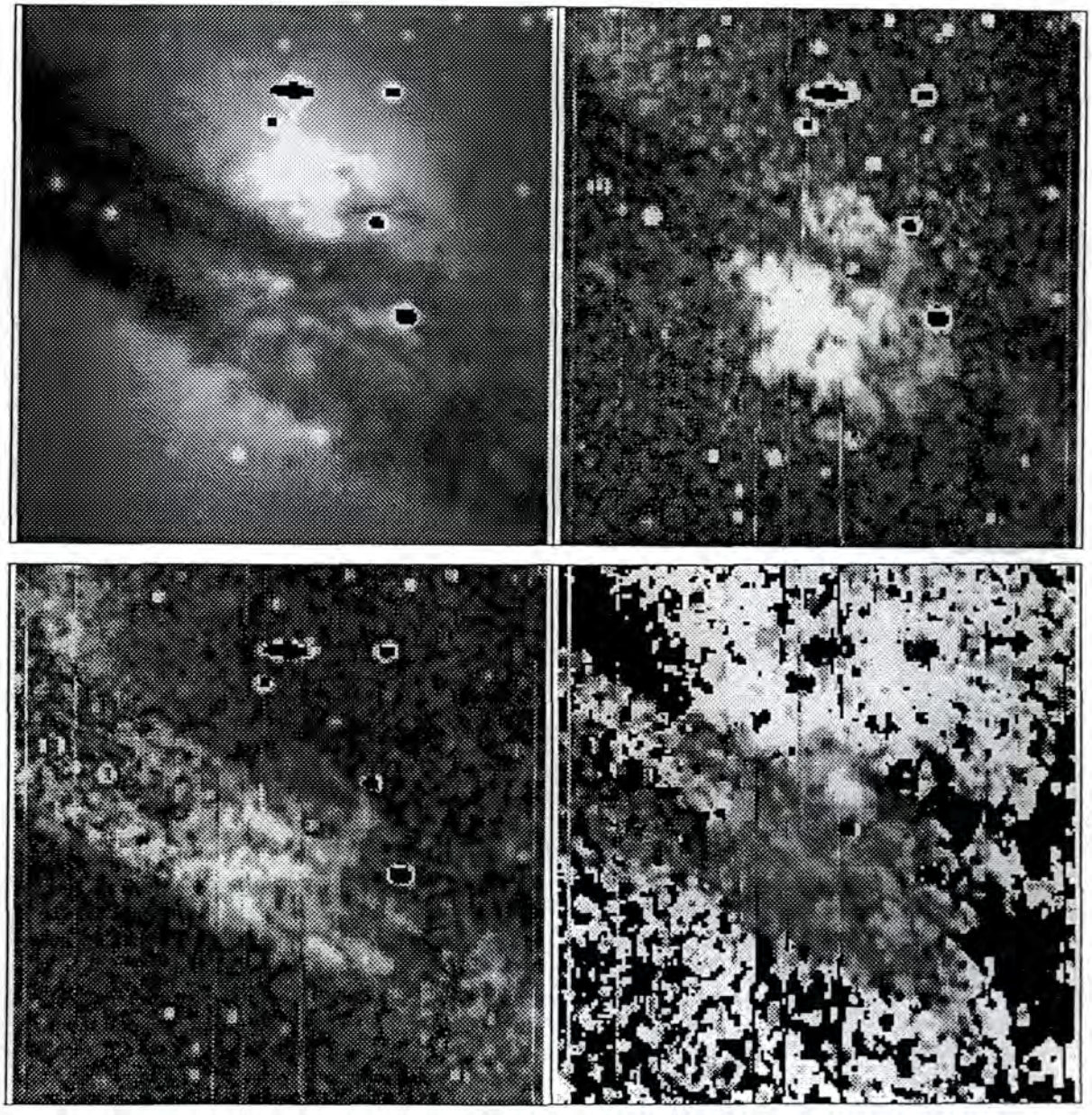

Figure 5.11: (a) Maps of intensity (top left), polarized intensity (top right), percentage polarization (bottom left) and polarization angle (bottom right) in the central 200″ × 200″ region of NGC 5128 in the V waveband.

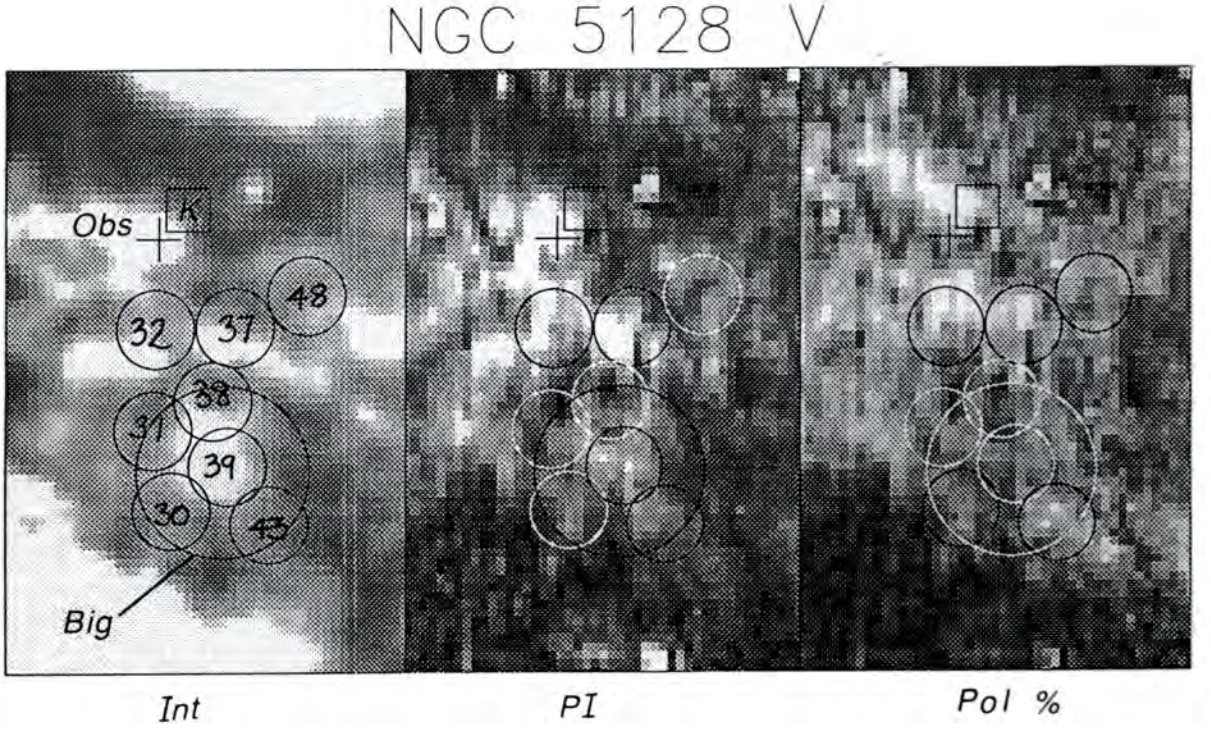

Figure 5.11: (b) Maps of intensity (left), polarized intensity (centre) and percentage polarization (right) the central 50″ × 80″ region of NGC 5128 in the V waveband. The apertures where good fits to Serkowski curves were calculated are shown.

For the diluting emission case, if intervening dust obscures only the central source and not the galactic bulge, the unpolarized light will dilute the polarization. If the optical depth to the nuclear source is substantial, dilution of the polarization by sources outside the nucleus would be significant. This effect is first seen at shorter wavelengths i.e the net B polarization would be significantly reduced with respect to the net R polarization. This may be the case seen in the turn-around regions where the polarization drops significantly.

For the mixed source and dust geometry, the sources are mixed in with the aligned dust grains. The less polarized sources near the front of the distribution contribute the most light since they are the least extinguished. As the total optical depth through the mixture increases, the contribution from stars at the back becomes weaker even though they become more highly polarized. Consequently the net polarization for a mixture of dust and sources would reach a maximum value when the total optical depth becomes large. The wavelength dependence of polarization can depart strongly from the value for normal interstellar polarization, especially when the optical depth exceeds unity.

Thus, for our data, a departure from the moderate polarization most likely indicates additional illumination which would change the wavelength dependence of polarization from that which fits a Serkowski curve.

Further tests for wavelength dependence of polarization of the turn-around regions at the extremities of the dust lane yielded no significance what-so-ever to a Serkowski curve. This is mainly because the B waveband data is poor in these regions owing to lack of signal. The evidence of the V, R and I wavebands showed that the fits obtained in these regions were poor anyway because the polarizing mechanism is no longer dominated by aligned grains in a magnetic field but instead scattering is assumed to become the main polarizing mechanism, since the polarization angles become perpendicular to the nuclear region.

Figure 5.13 shows a contour image of the central 50″ × 50″ of NGC 5128 in the V waveband overlaid with the polarizations calculated for individual pixels. The polarization angle can be seen to vary slightly across this region indicating variations in the projected magnetic field which runs through the dust lane. The only significant deviation from the roughly parallel polarization angles is at 12″W, –5″N of the offset where the polarization angles turns through 90°, at the position of a foreground star. At the optical bright spot and the K nucleus position there is no deviation from the general pattern so we are not seeing additional polarization from these features. The "swirling" variation in the polarization angle pattern may be symptomatic of a partially relaxed magnetic field in

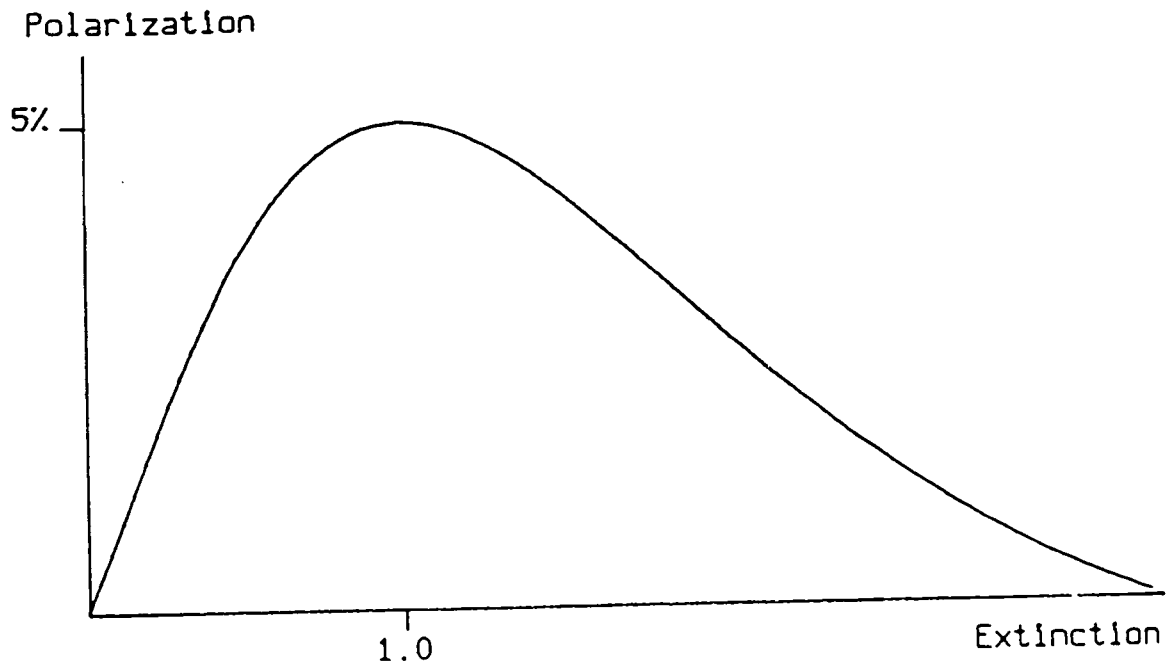

Figure 5.12: Expected form of polarization versus extinction curve for a simple scattering model of NGC 5128, from Berry (1985)

	Hough *et al.* (1987)		Big (23″) aperture	
Colour	P(%)	Angle (degs)	P(%)	Angle(degs)
B	5.17 ± 0.06	116 ± 1	3.17 ± 0.34	110.0 ± 3.1
V	4.78 ± 0.06	119 ± 1	2.77 ± 0.34	113.5 ± 3.6
R	4.37 ± 0.05	117 ± 1	2.57 ± 0.39	109.1 ± 4.3
I	3.35 ± 0.05	118 ± 1	2.14 ± 0.25	112.7 ± 3.4

Table 5.4: The results of H87 for SN1986G in the dust lane and for our big aperture

the dust lane which has been modelled by Quillen *et al.* (1992).

5.4.1 Supernova SN1986G

Using the supernova SN1986G, which went off behind the NE outer dust lane of NGC 5128, Hough *et al.* (1987) measured the wavelength dependence of polarization of a particular point in the dust lane, Their results are shown in Table 5.5. The supernova position is marked on Figs. 5.6a and 5.6b by a labelled square. There is an excellent fit to a Serkowski curve with $\lambda_{max} = 0.42\mu$m and $P_{max} = 5.19\%$, as shown in Fig. 5.10.

Comparing these results with those calculated for our big aperture, we see that although our λ_{max} is similar to that of H87, our P_{max} is much lower and our polarization angles differ by 5 – 8°. The difference in polarization angle is understandable given that our measurements are taken in a totally different part of the dust lane. The supernova provided the perfect opportunity to measure the wavelength dependence of the polarization in the dust lane but occurred away from the central regions.

5.4.2 Optical bright spot

We have measured the polarizations at the optical bright spot which is at the position of the hotspot of Kunkel and Bradt (1971) and the IR blue spot of Turner *et al.* (1992). Our results are shown in Table 5.6 for three different sized apertures which correspond to the aperture sizes of Bailey *et al.* (1986) and the largest of which is equal to that of H87. No results are available for the optical bright spot in the R waveband because of CCD saturation at that point. There is no evidence that the polarizations at the bright spot follow a Serkowski curve.

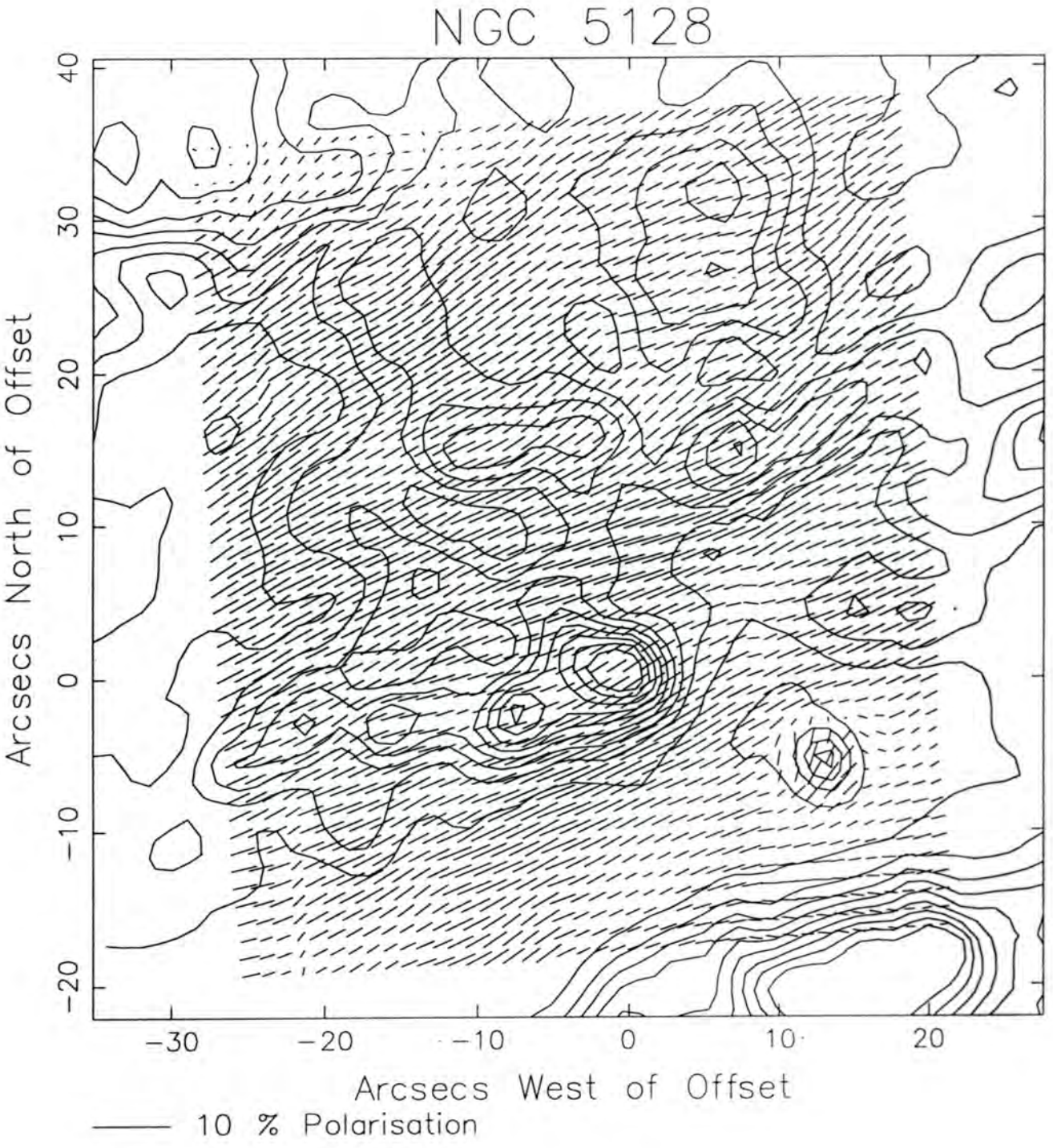

Figure 5.13: Contour image of the central 50″ × 50″ of NGC 5128 in the V waveband overlaid with the percentage polarizations calculated for individual pixels.

Aper. Size	8″	4.5″	2.3″
Filter	P(%)		
B	2.74 ± 0.39	2.01 ± 0.50	1.50 ± 0.84
V	3.22 ± 0.16	3.23 ± 0.16	3.28 ± 0.20
R	–	–	–
I	3.44 ± 0.30	3.23 ± 0.20	3.26 ± 0.22

Table 5.5: Polarization results for the optical bright spot

5.4.3 K nucleus

For the K nucleus position (Giles, 1986) our results are shown in Table 5.7. It can be seen that they do not fit a Serkowski curve. The K nucleus is greatly extinguished (by 22 magnitudes in IR (Grasdalen and Joyce, 1976) and 45 magnitudes in UV (Feigelson *et al.*, 1981)) so that we have low intensity there. No equivalent object is observable at optical wavelengths.

5.5 Extinction

The maximum value of polarization relative to the value $E(B-V)$ gives a measure of the efficiency of dust grain alignment and hence the magnetic field strength. The value of $R = A_v/E(B-V)$, the ratio of total to selective extinction can be determined directly from the wavelength of maximum polarization using the empirical relation $R = (5.6 \pm 0.3)\lambda_{max}$ (Whittet and van Breda, 1978). For our λ_{max} of 0.425μm we calculate $R_{CenA} = 2.4 \pm 0.13$, which agrees with the R_{CenA} of 2.4 calculated by H87. Unfortunately we have not got a calibrated value for $E(B-V)$ so we cannot calculate an exact value for A_v.

5.6 Conclusions

The presence of aligned grains in the dust lane of NGC 5128 is confirmed by the polarization angles observed in the broadband observations of NGC 5128. Extensive attempts to fit Serkowski curves to polarizations measured in different sized apertures along the dust lane were partially successful. There does appear to be some wavelength dependence of

Aper.	8″		4.5″		2.3″	
Filt.	P(%)	Angle	P(%)	Angle	P(%)	Angle
B	3.76 ± 0.71	104.9 ± 5.4	4.58 ± 1.19	103.7 ± 7.5	4.73 ± 2.34	106.3 ± 14.2
V	4.34 ± 0.22	115.4 ± 1.4	4.73 ± 0.28	116.1 ± 1.7	5.19 ± 0.45	117.1 ± 2.5
R	4.73 ± 0.40	114.3 ± 2.4	5.74 ± 0.32	113.8 ± 1.6	6.30 ± 0.32	117.2 ± 1.5
I	4.93 ± 0.21	115.3 ± 1.3	5.57 ± 0.22	116.1 ± 1.2	5.96 ± 0.26	116.6 ± 1.3

Table 5.6: Optical polarization results for the K nucleus

polarization in certain areas of the dust lane but not consistently so. Only in the central regions of the dust lane to we find polarization which fits the Serkowski equation. We conclude that for most of the dust lane the wavelength dependence one would expect to see from aligned dust grains is being distorted by extinction effects. For SN1986G, where H87 got an almost perfect fit to a Serkowski curve, the brightness of the supernova as illuminating point source dominated over the contribution from the rest of the galaxy. For most of the dust lane, other effects such as polarization from scattering and dilution from unaligned grains and unpolarized light sources must be considered, which can lead to deviation of the wavelength dependence of polarization from the Serkowski equation. Measuring the wavelength dependence of polarization in extragalactic objects is not easy. The integrated starlight of a galaxy will contain both scattered and transmitted components which cannot be separated easily.

Chapter 6

Conclusions

We began this thesis with the aim of examining the optical polarizations of two nearby active galaxies known for their unusual appearances. We obtained optical polarimetry images of these galaxies in a four waveband search, and also obtained spectropolarimetry for one of them. Reviews of previous studies of both these galaxies were presented.

6.1 Summary

M82 is an extremely well-studied object at most wavelengths, it is the most often cited example of a starburst galaxy; very active with a hidden energetic centre and has a very dusty appearance with wispy filaments protruding along its minor axis. There has been a lot of speculation as to the origin of the filaments – are they the result of a giant explosion in the galactic centre, or perhaps illumination effects, or maybe they have been blown out by a galactic superwind?

A multi-waveband imaging polarimetry study of M82 has been presented, showing elliptical and centrosymmetric polarization patterns with polarization values of up to 35%, which are indicative of Rayleigh or Mie scattering. A wavelength dependence of polarization is found along the minor axis of the galaxy with the southern side being more strongly polarized than the northern, and the bluer wavelengths more polarized than the redder wavelengths. This asymmetry can be explained if the galaxy is tilted with the northern side pointing towards us. Light from the southern part of the galaxy is scattered directly towards the observer but light from the northern part must travel through the galactic disk and is attenuated before reaching the observer.

Also presented are the results of a spectropolarimetry study of the southern filaments of M82. The Hα line is split along the minor axis indicating there is a hollow bubble on either side of the galaxy, and we see light coming from the front and back wall of this cavity but there is very little light coming from the centre. This suggests it has been blown out by a superwind from the nuclear starburst. The continuum spectrum is highly polarized with values similar to those obtained in the imaging polarimetry. Examination of the split Hα lines showed evidence for a mixture of scattering and intrinsic emission from the walls of the superwind bubble/cavity. Only the systemic component of M82 is seen in polarized intensity, the blueshifted component must be due to intrinsic emission only.

Observation details and results of a multi-waveband imaging polarimetry study of NGC 5128 are presented. The polarization pattern in the central dust lane is indicative of extinction by aligned non-spherical grains. Wavelength dependence of polarization is found in the central regions of the dust lane and appears to fit a Serkowski curve indicating that the polarization is due to extinction by grains aligned by a magnetic field in the dust lane. Elsewhere in the galaxy other effects such as polarization from scattering and dilution from unaligned grains occur, leading to deviation of the wavelength dependence of polarization from the Serkowski equation.

6.2 Conclusions

The results presented in this thesis illustrate two important causes of extragalactic polarization, scattering from dust grains and extinction by aligned non-spherical grains in a magnetic field. M82 clearly demonstrates polarization due to scattering on a galactic scale. It would interesting to observe the northern filaments of M82 with the spectropolarimeter to see they agree with the results of the southern filaments. NGC 5128 shows some evidence for polarization cause by extinction due to aligned grains but only in the central regions of the dust lane where the illumination from the elliptical galaxy is strong.

References

1. Aannestad P.A., Greenberg J.M., 1983. *Ap.J.,* **272,** 551.
2. Adams D.J., Adamson A.J., Giles A.B., 1983. *MNRAS,* **202,** 241.
3. Appenzeller I., Mollenhoff C., 1980. *A & A,* **81,** 54.
4. Appleton P.N., Davis R.D., Stephenson R.J., 1981. *MNRAS,* **195,** 327.
5. Arp H., 1967. *Ap.J.,* **148,** 321.
6. Artomonov B.P., 1978. *Sov. Astron.,* **22,** 7.
7. Axon D.J., Taylor K., 1978. *Nature,* **274,** 37.
8. Baade W., Minkowski R., 1954. *Ap.J.,* **119,** 215.
9. Baan W.A., Henkel C., Schilke P., Mauersberger R., Gusten R., 1990. *Ap.J.,* **353,** 132.
10. Bailey J., Hough J.H., Axon D.J., 1983. *MNRAS,* **203,** 339.
11. Bailey J., Sparks W.B., Hough J.H., Axon D.J., 1986. *Nature,* **322,** 150.
12. Ballard K.R., Mead A.R.G., Brand P.W.J.L., Hough J.H., 1990. *MNRAS,* **243,** 640.
13. Bartel N., Ratner M.I., Rogers A.E.E., Shapiro I.I., Bonometti R.J., Cohen N.L., Gorenstein M.V., Marcaide J.M., Preston R.A., 1987. *Ap.J.,* **323,** 505.
14. Bell M.B., Seaquist E.R., 1988. *Ap.J.,* **329,** L17.
15. Berry D.S., 1985. *Ph.D. Thesis,* University of Durham.
16. Bingham R.D., McMullan D., Pallister W.S., White C., Axon D.J., Scarrott S.M., 1976. *Nature,* **259,** 463.
17. Blanco V.M., Graham J.A., Lasker B.M.,Osmer P.S., 1975. *Ap.J.,* **198,** L63.
18. Bland J., Taylor K., Atherton P.D., 1987. *MNRAS,* **228,** 598.
19. Bland J., Tully R.B., 1988. *Nature,* **334,** 43.

20. Bohren C.F., Huffman D.R., 1983. *"Absorption and Scattering of Light by Small Particles"*, (Wiley).

21. Bolton J.G., Stanley G.J., Slee O.B., 1949. *Nature,* **164,** 101.

22. Botti L.C.L., Abraham Z., 1993. *MNRAS,* **264,** 807.

23. Brindle C., Hough J.H., Bailey J.A., Axon D.J., Hyland A.R., 1986. *MNRAS,* **221,** 739.

24. Brodie J., Bowyer S., 1985. *Ap.J.,* **292,** 447.

25. Brodie J., Konigl A., Bowyer S., 1983. *Ap.J.,* **273,** 154.

26. Burns J.O., Feigelson E.D., Schreier E.J., 1983. *Ap.J.,* **273,** 128.

27. Carlstrom J.E., 1988. in *Galactic and Extragalactic Star Formation,* ed. R.E. Pudritz and M. Fich, p. 571, (Kluwer Dordrecht).

28. Carlstrom J.E., Kronberg P.P., 1991. *Ap.J.,* **366,** 422.

29. Chandrasakhar S., 1960. *"Radiative Transfer"*, (Dover).

30. Chesterman J.F., Pallister W.S., 1980. *MNRAS,* **191,** 349.

31. Chevalier R.A., Clegg A.W., 1985. *Nature,* **317,** 44.

32. Clarke D.A., Burns J.A, Feigelson E.D., 1986. *Ap.J.,* **300,** L41.

33. Clarke D.A, Burns J.O., Norman M.L., 1992. *Ap.J.,* **395,** 444.

34. Clayton G.C., Martin P.G., Thompson I., 1983. *Ap.J.,* **265,** 194.

35. Collura, Reale, Schulman, Bregman, 1994. *Ap.J.,* **420,** L63.

36. Cottrell G.A., 1977. *MNRAS,* **178,** 577.

37. Cottrell G.A., 1978. *MNRAS,* **184,** 259.

38. Cox D.P., Smith B.W., 1974. *Ap.J.,* **189,** L105.

39. Crawford M.K., Genzel R., Townes C.H., Watson D.M., 1983. *Ap.J.,* **291,** 755.

40. Cugnon P., 1983. *A & A.,* **120,** 156.

41. Davis J., Greenstein J.L., 1951. *Ap.J.,* **114,** 206.

42. Dietz R.D., Smith J., Hackwell J.A., Gehrz R.D., Grasdalen G.L., 1986. *A.J.,* **91(4),** 758.

43. Dietz R.D., Gehrz R.D., Jones T.J., Grasdalen G.L., Smith J., Gullixson C., Hackwell J.A., 1989. *A.J.,* **98(4),** 1260.

44. Draper P.W., 1988. *Ph.D Thesis,* University of Durham.

45. Dufour R.J., van den Bergh S., 1978. *Ap.J.,* **226,** L73.

46. Dufour R.J., van den Bergh S., Harvel C.A., Margins D.H., Schiffer III F.H., Talbot Jr. R.J., Talent D.J., Wells D.C., 1979. *A.J.,* **84,** 284.

47. Eaton N., Scarrott S.M., Gledhill T.M., 1992. *MNRAS,* **258,** 384.

48. Eaton N., Scarrott S.M., Wolstencroft R.D., 1991. *MNRAS,* **250,** 654.

49. Ebneter K., Balick B., 1983. *PASP,* **95,** 675.

50. Eckart A., Cameron M., Rothermel H., Wild W., Zinnecker H., Rydbeck G., Olberg M., Wiklind T., 1990a. *Ap.J.,* **363,** 451.

51. Eckart A., Cameron M., Genzel R., Jackson J.M., Rothermel H., Stutzki J., Rydbeck G., Wiklind T., 1990b. *Ap.J.,* **365,** 522.

52. Elvius A., 1962. *Lowell Obs. Bull.,* **5,** 281.

53. Elvius A., 1967. *A.J.,* **72,** 794.

54. Elvius A., 1969. *Lowell Obs. Bull.,* **7,** 117.

55. Elvius A., 1972. *A & A,* **19** 193.

56. Elvius A., Hall J.S., 1964. *Lowell Obs. Bull.,* **6,** 123.

57. Fabbiano G.,1988, *Ap.J.,* **330,** 672.

58. Feigelson E.D., Schreier E.J., Delaville J.P., Giacconi R., Grindlay J.E., Lightman A.P., 1981. *Ap.J.,* **251,** 31.

59. Foley N.B., Scarrott S.M., Axon D.J., 1991. *Gemini,* **34,** 8.

60. Foley N.B., Gledhill T.M., Scarrott S.M., Wolstencroft R.D., 1993. *MNRAS,* **262,** 175.

61. Forbes D.A., Ward M.J., DePoy D.L., Boisson C., Smith M.S., 1992. *MNRAS,* **254,** 509.

62. Freedman W.L., Madore B.F., 1988. *Ap.J.,* **332,** L63.

63. Gaffney N.I., Lester D.F., Telesco C.M., 1993, *Ap.J.,* **407,** L57.

64. Gardner F.F., Whiteoak J.B., 1976. *MNRAS,* **175,** 9P.

65. Getov R.G., Georgiev Ts.B., 1989. *Sov. Astr. Lett.,* **14(5),** 345.

66. Giles A.B., 1986. *MNRAS,* **218,** 615.

67. Gopal-krishna, Saripalli L., 1984. *A & A,* **141,** 61.

68. Gottesman S.T., Weliachew L., 1977. *Ap.J.,* **211,** 47.

69. Gotz M., McKeith C.D., Downes D., Greve A., 1990. *A & A,* **240** 52.

70. Graham J.A., 1979. *Ap.J.,* **232,** 60.

71. Graham J.A., 1983. *Ap.J.,* **269,** 440.

72. Grasdalen G.L., Joyce R.R., 1976. *Ap.J.,* **208,** 317.

73. Gusten R., Serabyn E., Kasemann C., Schinkel A., Schneider G., Schulz A., Young K., 1993. *Ap.J.,* **402,** 537.

74. Harding P., Jones T.J., Rodgers A.W., 1981. *Ap.J.,* **251,** 53.

75. Hargrave P.J., 1974. *MNRAS,* **168,** 491.

76. Hawarden T.G., Sandell G., Matthews H.E., Friberg P., Watt G.D., Smith P.A., 1993. *MNRAS,* **260,** 844.

77. Hecht E. & Zajac A., 1974. "Optics", (Addison-Wesley Publishing Co.)

78. Heckathorn H.M., 1972. *Ap.J.,* **173,** 501.

79. Heckman T.M., Armus L., Miley G., 1987. *A.J.,* **92,** 276.

80. Heckman T.M., Armus L., Miley G., 1990. *Ap.J.S.,* **74,** 833.

81. Heckman T.M., Lehnert, Armus L., 1994. S.T.S.I Preprint No. 724.

82. Hesser J.E., Harris H.C., van den Bergh S., Harris G.H., 1984. *Ap.J.,* **276,** 491.

83. Holmes P.A., Brand P.W.J.L., Impey C.D., Williams P.M., 1984a. *MNRAS,* **210,** 961.

84. Hough J.H., Bailey J.A., Rouse M.F., Whittet D.C.B., 1987. *MNRAS,* **227,** 1P.

85. Hughes D.H., Gear W.K., Robson E.I., 1990. *MNRAS,* **244,** 759.

86. Impey C.D., Brand P.W.J.L., Wolstencroft R.D., Williams P.M., 1982. *MNRAS,* **200,** 19.

87. Impey C.D., Brand P.W.J.L., Wolstencroft R.D., Williams P.M., 1984. *MNRAS,* **209,** 245.

88. Impey C.D., Tapia S., 1990. *Ap.J.,* **354,** 125.

89. Impey C.D., Lawerence C.R., Tapia S., 1991. *Ap.J.,* **375,** 46.

90. Israel F.P., van Dishoeck E.F., Baas F., Koornneef J., Black J.H., de Graauw T., 1990. *A & A,* **227,** 342.

91. Israel F.P., van Dishoeck E.F., Baas F., de Graauw T., Phillips T.G., 1991. *A & A,* **245,** L13.

92. Jaffe D.T., Becklin E.E., Hildebrand R.H., 1984. *Ap.J.,* **285,** L31.

93. Jones R.V., Spitzer L.Jnr., 1967. *Ap.J.,* **147,** 943.

94. Jones T.J., Klebe P., 1989. *Ap.J.,* **341,** 707.

95. Joy M., Lester D.F., Harvey P.M., 1987. *Ap.J.,* **319,** 314.

96. Joy M., Lester D.F., Harvey P.M., Benton Ellis H., 1988. *Ap.J.,* **326,** 662.

97. Joy M., Harvey P.M., Tollestrup E.V., Sellgren K., McGregor P.J., Hyland A.R., 1991. *Ap.J.,* **366,** 82.

98. Jura M., 1982. *Ap.J.,* **258,** 59.

99. Killian D.J., Gottesmann S.T., 1979. in *Photometry, Kinematics and Dynamics of Galaxies,* ed. Evans D.S., (Austin, Univ. of Texas) p. 267.

100. Klein U., Wielebinski R., Morsi H.W., 1988. *A & A,* **190,** 41.

101. Knapp G.R., Phillips T.G., Huggins P.J., Leighton R.B., Wannier P.G., 1980. *Ap.J.,* **240,** 60.

102. Kronberg P.P., Biermann P., Schwab F.R., 1981. *Ap.J.,* **246,** 751.

103. Kronberg P.P., Biermann P., Schwab F.R., 1985. *Ap.J.,* **291,** 693.

104. Kronberg P.P., Emerson D.T., Klein U., Wielebinski R., 1979. *Ap.J.,* **230** L149.

105. Kronberg P.P., Sramek R.A., 1985. *Science,* **227,** 28.

106. Kronberg P.P., Sramek R.A., 1992. in *X-ray emission from AGNs and the Cosmic X-ray Background,* ed. Brinkman W. & Trumper J., 247.

107. Kronberg P.P., Pritchet C.J., van den Bergh S., 1972. *Ap.J,* **173,** L47.

108. Kronberg P.P., Wilkinson P.N., 1975. *Ap.J.,* **200,** 430.

109. Krugel E., Chini R., Klein U., Lemke R., Wielebinski R., Zylka R., 1990. *A & A,* **240,** 232.

110. Kunkel W.E., Bradt H.V., 1971. *Ap.J.,* **170,** L7.

111. Larkin J.E., Graham J.R., Matthews K., Soifer B.T., Backwith S., Herbst T.M., Quillen A.C., 1994. *Ap.J.,* **420,** 159.

112. Lawerence A., 1987. *PASP,* **99,** 615.

113. Lepine J.R.D., Braz M.A., Epchtein N., 1984. *A & A,* **131,** 72.

114. Lester D.F., Carr J.S., Joy M., Gaffney N., 1990. *Ap.J.,* **352,** 544.

115. Lo K.Y., Cheung K.W., Masson C.R., Phillips T.G., Scott S.L., Woody D.P, 1987. *Ap.J.,* **312,** 574.

116. Loiseau N., Reuter H.P., Wielebinski R., Klein U., 1988. *A & A,* **200,** L1.

117. Longair M.S., 1981. *"High Energy Astrophysics",* (Cambridge University Press), p. 259.

118. Lugten J.B., Watson D.M., Crawford M.K., Genzel R., 1986. *Ap.J.*, **311,** L51.

119. Lynds C.R., 1961. *Ap.J.,* **134,** 659.

120. Lynds C.R., Sandage A.R., 1963. *Ap.J.,* **137** 1005.

121. MacCarthy P.J., Heckman T., van Breugel W., 1987. *A.J.,* **92(2),** 264.

122. Malin D.F., Quinn P.J., Graham J.A., 1983. *Ap.J.,* **272,** L5.

123. Marston A.P., Dickens R.J., 1988. *A & A,* **193,** 27.

124. Martin P.G., Shawl S.J., 1979. *Ap.J.,* **231,** L57.

125. Martin P.G., Shawl S.J., 1982. *Ap.J.,* **253,** 86.

126. Mathis J.S., 1973. *Ap.J.,* **183,** 41.

127. McKeith C.D., Castles J., Greve A., Downes D., 1994. IRAM Preprint 278. accepted by *A & A*..

128. McLeod K.K., Rieke G.H., Rieke M.J., Kelly D.M., 1993. *Ap.J.,* **412,** 111.

129. Mead A.R.G., Ballard K.R., Brand P.W.J.L., Hough J.H.., Brindle C., Bailey J.A., 1990. *A & A Supp.* **83,** 183.

130. Meier D.L. *et al.*, 1989. *A.J.,* **98,** 27.

131. Moore R.L., Stockman H.S., 1984. *Ap.J.,* **279,** 465.

132. Morganti R., Robson A., Fosbury R.A.F., di Serego Alighieri S., Tadhunter C.N., Malin D.F., 1991. *MNRAS,* **249,** 91.

133. Morganti R., Fosbury R.A.F., Hook R.N., Robinson A., Tsvetanov Z., 1992. *MNRAS,* **256,** 1P.

134. Muxlow T.W.B., Pedlar A., Wilkinson P.N., Axon D.J., Sander E.M. & de Bruyn A.G., 1994. *MNRAS,* **266,** 455.

135. Nakai N., Hayashi M., Handa T., Sofue Y., Hasegawa T., Sasaki M., 1987. *Pub. Astr. Soc. Japan,* **39,** 685.

136. O'Connell R.W., Mangano J.J., 1978. *Ap.J.,* **221,** 62.

137. Olofsson H., Rydbeck G., 1984. *A & A,* **136,** 7.

138. Pallister W.S., 1976. *Ph.D. Thesis,* University of Durham.

139. Perkins H.G., 1978. *Ph.D Thesis,* University of Durham.

140. Phillips J.P., Mampaso A., 1989. *A & A,* **218,** 24.

141. Phillips T.G., Ellison B.N., Keene J.B., Leighton R.B., Howard P.J., Masson C.R., Sander D.B., Veidlt B., Young K., 1987. *Ap.J.,* **322,** L73.

142. Purcell E.M., 1975. in *The Dusty Universe,* ed. Field G.B., & Cameron A.G.W., (Neale Watson) p. 155.

143. Purcell E.M., 1979. *Ap.J.,* **231,** 404.

144. Puxley P.J., 1991. *MNRAS,* **249,** 11P.

145. Quillen A.C., de Zeeuw P.T., Phinney E.S., Phillips T.G., 1992. *Ap.J.,* **391,** 121.

146. Quillen A.C., Graham J.R., Frogel J.A., 1993. *Ap.J.,* **412,** 550.

147. Reuter H.P., Klein U., Lesch H., Wielebinski R., Kronberg P.P., 1992. *A & A,* **256,** 10.

148. Rickard L.J., Palmer P., Morris M., Zuckerman B., Turner B.E., 1975. *Ap.J.,* **199,** L75.

149. Rieke G.H., Lebofsky M.J., Thompson R.I., Low F.J., Tokunga A.T., 1980. *Ap.J.,* **238,** 24.

150. Rieke G.H., Lebofsky M.J., 1985. *Ap.J.,* **288,** 618.

151. Rieke G.H., Lebofsky M.J., Walker C., 1988. *Ap.J.,* **325,** 679.

152. Rodgers A.W., 1978. *Ap.J.,* **219,** L7.

153. Ruzmaikin A.A., Shukov A.M., Sokoloff D.D., 1988. *"Magnetic Fields of Galaxies",* (Kluwer Academic).

154. Sandage A.R., 1961. *"The Hubble Atlas of Galaxies",* (California Institute of Technology).

155. Scarrott S.M., Warren-Smith R.F., Pallister W.S., Axon D.J., Bingham R.G., 1983. *MNRAS,* **204,** 1163.

156. Scarrott S.M., Ward-Thompson D.W., Warren-Smith R.F., 1986. in *Proc. on Interstellar Mag. Fields,* ed. Beck R. & Grave R., p.71, (Springer Verlag).

157. Scarrott S.M., Ward-Thompson D., Warren-Smith R.F., 1987. *MNRAS,* **224,** 299.

158. Scarrott S.M., Draper P.W., Wolstencroft R.D., 1989 *MNRAS,* **237,** 621.

159. Scarrott S.M., Rolph C.D., Semple D.P., 1990. in *I.A.U. Symposium* **140,** p.245 (Kluwer Academic).

160. Scarrott S.M., Eaton N., Axon D.J, 1991. *MNRAS,* **252,** 12P.

161. Scarrott S.M., 1991. *Vistas in Astronomy,* **34,** 163.

162. Scarrott S.M., Draper P.W., Tadhunter C.N., 1993. *MNRAS,* **260,** 171.

163. Scarrott S.M., Draper P.W., Stockdale D.P., Wolstencroft R.D., 1993. *MNRAS,* **264,** L7.

164. Schaaf R., Pietsch W., Biermann P.L., Kronberg P.P., Schmutzler T., 1989. *Ap.J.,* **336,** 722.

165. Schike P., Carlstrom J.E., Keene J., Phillips T.G., 1993. *Ap.J.,* **417,** L67.

166. Schmidt G.D., Angel J.R.P., Cromwell R.H, 1975. *Ap.J,* **206,** 888.

167. Schreier E.J., Feigelson E., Delaville J., Giacconi R., Grindlay J., Schwartz D.A., 1979. *Ap.J.,* **234,** L39.

168. Schreier E.J., Burns J.O., Feigelson E.D., 1981. *Ap.J.,* **251,** 523.

169. Seaquist E.R., Bell M.B., Bignell R.C., 1985. *Ap.J.,* **294,** 546.

170. Seaquist E.R., Bell M.B., 1986. *Ap.J.,* **303,** L67.

171. Seaquist E.R., Bell M.B., 1990. *Ap.J.,* **364,** 94.

172. Seaquist E.R., Odegard N., 1991. *Ap.J.,* **369,** 320.

173. Serkowski K., Mathewson D.S., Ford V.L., 1975. *Ap.J.,* **196,** 261.

174. Steward J.F.L., Steward B.G., 1985, *A & A,* **142,** 100.

175. Smith P.A., Brand P.W., Puxley P.J., Mountain C.M., Nakai N., 1990. *MNRAS,* **243,** 97.

176. Sofue Y., 1988. in *Galactic and Extragalactic Star Formation,* ed. R.E. Pudritz and M. Fich, p. 409, (Kluwer Dordrecht).

177. Sofue Y., Reuter H.P., Krouse M., Wielebinski R., Nakai N., 1992. *Ap.J.,* **395,** 126.

178. Solinger A.B., 1969. *Ap.J.,* **155,** 403.

179. Solinger A.B., Markert T., 1975. *Ap.J.,* **197,** 309.

180. Solinger A.B., Morrison P., Markert T., 1977. *Ap.J.,* **211,** 707.

181. Solomon P.M., de Zafra P., 1975. *Ap.J.,* **199,** L79.

182. Stark A.A., Carlson E.R., 1982. *Ap.J,* **279,** 122.

183. Sutherland R.S., Bicknell G.V., Dopita M.A., 1993. *Ap.J.,* **414,** 510.

184. Sutton E.C., Masson C.R., Phillips T.G., 1983. *Ap.J.,* **275,** L49.

185. Telesco C.M., 1978. *Ap.J.,* **226,** L125.

186. Telesco C.M., Harper D.A., 1980. *Ap.J.,* **235,** 392.

187. Telesco C.M., 1988. *Ann. Rev. Astron. Astroph.,* **26,** 343.

188. Telesco C.M., Decher R., Joy M., 1989. *Ap.J.,* **343,** L13.

189. Telesco C.M., Campins H., Joy M., Dietz K., Decher R., 1991. *Ap.J.,* **369,** 135.

190. Telesco C.M., Gezari D.Y., 1992. *Ap.J.,* **395,** 461.

191. Terlevich R., Tenorio-Tagle G., Franco J., Melnick J., 1993. *MNRAS,* **255,** 713.

192. Thompson R.C., 1992. *MNRAS,* **257,** 689.

193. Thronson H.A. Jnr., Walker C.K., Walker C.E., Maloney P., 1989. *A & A,* **214,** 29.

194. Thronson H.A., Wilton C., Ksik A., 1991. *MNRAS,* **252,** 543.

195. Tilanus R.P.J., Tacconi L.T., Sutton E.C., Zhou S., Sander D.B., Wynn-Williams C.G., Lo K.Y., Stephens S.A., 1991. *Ap.J.,* **376,** 500.

196. Tomisaka K., Ikeuchi S., 1988. *Ap.J.,* **330,** 695.

197. Tonry J.L., Schecter P.L., 1990. *A.J.,* **100,** 1794.

198. Tubbs A.D., 1980. *Ap.J.,* **241,** 969.

199. Turner J.L, Martin N., Ho P.T.P., 1991. *Ap.J.,* **367,** 677.

200. Turner P.C., Forrest W.J., Pipher J.L., Shure M.A., 1992. *Ap.J,* **393,** 648.

201. Unger S.W., Pedlar A., Axon D.J., Wilkinson P.N., Appleton P.N., 1984. *MNRAS,* **211,** 783.

202. Van der Hulst H.C., 1957. *"Light Scattering by Small Particles"* (Dover).

203. Van der Hulst J.M., 1978. in *IAU Symposium* **77,** *Structures and Properties of Nearby Galaxies,* ed. E.M. Berkhuijsen, R. Wielebinski, (Reidel, Dordrecht) p.269.

204. Van der Hulst J.M., 1979. *A & A,* **75,** 97.

205. Van Gorkom J.H., Van der Hulst J.M., Haschick A.D., Tubbs A.D., 1990. *A.J.,* **99,** 1781.

206. Van der Werf P.P., Genzel R., Krabbe A., Blietz M., Lutz D., Drapatz S., 1993. *Ap.J.,* **405,** 522.

207. Verter F., Rickard L.J., 1989. *A & A,* **225,** 27.

208. Visvanathan N., Sandage A.R., 1972. *Ap.J.,* **176,** 57.

209. Wade C.M., Hjellming R., Kellermann K.I., Wardle C., 1971. *Ap.J.,* **170,** L11.

210. Waller W.H., Gurwell M. & Tamura M., 1992. *A.J.,* **104,** 63.

211. Ward M.J., 1988. *MNRAS,* **231,** 1P.

212. Wardle J.F.C., Moore R.L., Angel J.R.P., 1984. *Ap.J.,* **279,** 93.

213. Warren-Smith R.F., 1978. *Ph.D. Thesis,* University of Durham.

214. Watson M.G., Stanger V., Griffiths R.E., 1984. *Ap.J.,* **286,** 144.

215. Weliachew L., Fomalont E.D., Greisen E.W., 1984. *A & A,* **137,** 335.

216. Whittet D.C.B., van Breda I.G., 1978. *A & A,* **66,** 57.

217. Whittet D.C.B., Martin P.G., Hough J.H., Rouse M.F., Bailey J.A., Axon D.J., 1992. *Ap.J.,* **386,** 562.

218. Wild W., Harris A.I., Eckart A., Genzel R., Graf U.U., Jackson J.M., Russell A.P.G., Stutzki J., 1992. *A & A,* **265,** 447.

219. Wilking B.A., Lebofsky M.J., Rieke G.H., 1982. *A.J.,* **87,** 695.

220. Wilkinson A., Sharples R.M., Fosbury R.A.E., Wallace P.T., 1986. *MNRAS,* **218,** 297.

221. Williams T.B., Caldwell N., Schommer R.A., 1984. *Ap.J.,* **281,** 579.

222. Wright J.S., MacKay C.D., 1981. *Proc. Soc. Inst. Eng.,* **290,** 160.

223. Young J.S., Scoville N.Z., 1984. *Ap.J.,* **287,** 153.

224. Yun M.S., Ho P.T.P., Lo K.Y., 1993., *Ap.J.,* **411,** L17.

Acknowledgements

I must thank my supervisor Dr. Mike Scarrott for giving me the opportunity to do this Ph.D. with the Polarimetry Group at Durham. I thank Prof. Arnold Wolfendale and Prof. Alan Martin, the heads of Department at Durham during my time here for allowing me to use the departmental facilities. I am grateful to Dr. John Major for his help and advice when I was looking for a post-graduate position. I acknowledge SERC for funding the Polarimetry Group. I would also like to thank Alan Lotts for providing an excellent Starlink service and for keeping me supplied with paper for the laser printer.

I would like to thank my fellow polarimetrists, Peter Draper, Nick Eaton, Tim Gledhill and especially Chris Rolph, for teaching me everything I know about polarimetry, showing me how to use the polarimetry software and interpret polarization patterns (especially the centrosymmetric ones from galactic bipolar nebulae). I would also like to thank the rest of the group, in particular David Stockdale and Phil Armstrong, for their assistance in all matters to do with the polarimeter.

I thank Mike Lee and Vicki Greener in the Photographic Laboratory at the Department for producing the photographs in this thesis, and for patiently unjamming the photocopier for the n^{th} time after I broken it.

I am grateful to Dave Axon and Will Henney at Manchester for accompanying me on my first observing trip, and for helping me obtain the spectropolarimetry data.

Finally I would like to thank Pete, Gillian, Sue, Roger and the rest of the gang in the vaxroom and tea-room both past and present, for making the whole thing more bearable.